
Dynamic Land and Vegetation in a Global Earth System Model

Dissertation

zur Erlangung des akademischen Grades

Doctor rerum naturalium

(Dr. rer. nat.)

der Fachbereiche

08 - Physik, Mathematik und Informatik,
09 - Chemie, Pharmazie und Geowissenschaften,
10 - Biologie, und Universitätsmedizin
der Johannes Gutenberg-Universität Mainz

angefertigt am Max-Planck-Institut für Chemie
Max Planck Graduate Center

vorgelegt von

Anna Martin

geboren am 15. August 1996 in Bingen am Rhein

Mainz, den 01. September 2025

Betreuer

Prof. Dr. Jos Lelieveld

Max-Planck Institute for Chemistry, Mainz

Prof. Dr. Holger Tost

Johannes Gutenberg Universität Mainz

Nachnutzungslizenz: InC-1.0

Declaration

I hereby declare that I wrote the dissertation submitted without any unauthorized external assistance and used only sources acknowledged in the work. All textual passages which are appropriated verbatim or paraphrased from published and unpublished texts as well as all information obtained from oral sources are duly indicated and listed in accordance with bibliographical rules. In carrying out this research, I complied with the rules of standard scientific practice as formulated in the statutes of Johannes Gutenberg-University Mainz to insure standard scientific practice.

Anna Martin
Mainz, 01. September 2025

Acknowledgments

Abstract

Climate change, driven by anthropogenic greenhouse gas emissions, has profound impacts on the Earth system, including rising global temperatures, more frequent extreme weather events, and disruptions to ecosystems, agriculture, and human health. Understanding and projecting these impacts requires sophisticated Earth System Models (ESMs) that represent interactions between the atmosphere, oceans, land surface, and biosphere, including complex processes such as atmospheric chemistry, cloud–aerosol interactions, and land–atmosphere exchange of trace gases. This work presents the further development and application of the ECHAM5/MESy Atmospheric Chemistry (EMAC) model through the integration of the comprehensive land surface and vegetation model JSBACH Version 4 and the coupling of a newly developed submodel, BIODEP, to simulate terrestrial sinks for hydrogen (H_2) and methane (CH_4). These enhancements improve the representation of soil moisture, vegetation and energy fluxes, as well as trace gases such as methane and hydrogen. The evaluation is based on reanalyses, satellite data and direct ground measurements. EMAC is used to determine the influence of increased aerosol concentrations from biomass combustion on gross primary production. The model shows good agreement with observations of the distribution of diffuse and direct radiation. In addition, various feedback mechanisms have been isolated for the first time and their individual impact on plant productivity investigated. Additionally, the implementation of BIODEP enables dynamic simulation of soil uptake processes for H_2 and CH_4 with direct coupling to atmospheric chemistry. Here, too, the model shows good agreement with measured atmospheric mixing ratios and previously published soil deposition rates of H_2 and CH_4 . Overall, this work enhances EMAC’s capabilities to realistically simulate coupled biosphere–atmosphere processes, greenhouse gas budgets and climate feedbacks, providing a valuable tool for future analyses of climate projections and the development of effective strategies to mitigate climate change.

Zusammenfassung

Der durch anthropogene Treibhausgasemissionen verursachte Klimawandel hat weiterhin tiefgreifende Auswirkungen auf das Erdsystem. Dazu zählen unter anderem steigende globale Temperaturen, häufigere extreme Wetterereignisse, die Zerstörung von Ökosystemen, die Beeinträchtigung der Landwirtschaft sowie Folgen für die Gesundheit. Um diese Auswirkungen zu verstehen und zu prognostizieren, sind hochentwickelte Erdsystemmodelle (ESMs) erforderlich, die die Wechselwirkungen zwischen Atmosphäre, Ozeanen, Landoberfläche und Biosphäre modellieren. Sie integrieren komplexe Prozesse wie Atmosphärenchemie, die Wechselwirkungen zwischen Wolken und Aerosolen sowie den Austausch von Spurengasen zwischen Landoberfläche und Atmosphäre. Diese Arbeit dokumentiert die Weiterentwicklung und Anwendung des ECHAM5/MESy Atmospheric Chemistry (EMAC) Modells durch die Integration des umfassenden Landoberflächen- und Vegetationsmodells JSBACH Version 4 sowie die Kopplung eines neu entwickelten Submodells, BIODP, zur Simulation terrestrischer Senken für Wasserstoff (H_2) und Methan (CH_4). Diese Erweiterungen verbessern die Darstellung von Bodenfeuchte, Vegetation und Energieflüssen sowie von Spurengasen wie Methan und Wasserstoff. Die Evaluation erfolgt anhand von Reanalysen, Satellitendaten und direkten Bodenmessungen. EMAC wird genutzt, um den Einfluss erhöhter Aerosolkonzentrationen aus der Verbrennung von Biomasse auf die Bruttoprimärproduktion zu bestimmen. Das Modell zeigt eine gute Übereinstimmung mit den Beobachtungen der Verteilung von diffuser und direkter Strahlung. Darüber hinaus wurden erstmals verschiedene Rückkopplungsmechanismen isoliert und ihre individuellen Auswirkungen auf die Pflanzenproduktivität untersucht. Schließlich ermöglicht die Implementierung von BIODP eine dynamische Simulation der Bodenaufnahmeprozesse für H_2 und CH_4 mit direkter Kopplung an die Atmosphärenchemie. Auch hier zeigt das Modell eine gute Übereinstimmung mit den gemessenen atmosphärischen Mischungsverhältnissen und den zuvor veröffentlichten Depositionsraten von H_2 und CH_4 im Boden. Insgesamt erweitert diese Arbeit die Fähigkeiten von EMAC, gekoppelte Biosphären-Atmosphären-Prozesse, Treibhausgasbilanzen und Klimarückkopplungen realistisch zu simulieren, und stellt damit ein wertvolles Instrument für künftige Analysen von Klimaprojektionen sowie die Entwicklung wirksamer Strategien zur Eindämmung des Klimawandels dar.

Contents

Acknowledgments	vii
Abstract	ix
Zusammenfassung	xi
Contents	xiii
1 Introduction	1
1.1 Motivation	1
1.2 Surface energy balance and hydrology	2
1.3 Biogenic volatile organic compounds (BVOCs)	3
1.4 Aerosols	6
1.5 Methane (CH ₄)	8
1.6 Hydrogen (H ₂)	11
1.7 Summary of introduction	13
1.8 Thesis outline	14
2 Methodology	15
2.1 Modular Earth Submodel System (MESSy)	15
2.1.1 ECHAM5/MESSy atmospheric chemistry model (EMAC)	15
2.1.2 JSBACH submodel	16
2.1.3 BIODIP submodel	17
2.2 Summary of methodology	18
3 Results	19
3.1 Coupling of the JSBACH land surface and vegetation model and the ECHAM5/MESSy atmospheric chemistry model (EMAC)	19
3.2 Effects of biomass burning aerosols on plant productivity	48
3.2.1 Introduction	50
3.2.2 Methods	51
3.2.3 Results and discussion	58
3.2.4 Conclusion	69
3.2.5 Appendix	71

3.3	Biogenic soil deposition of methane and hydrogen in the ECHAM5/MESSy atmospheric chemistry model (EMAC)	73
3.3.1	Introduction	75
3.3.2	Evaluation datasets	77
3.3.3	Model description and setup	77
3.3.4	Results and discussion	84
3.3.5	Conclusion	92
3.3.6	Appendix	93
4	Contributions	105
4.1	Numerical simulation of the impact of COVID-19 lockdown on tropospheric composition and aerosol radiative forcing in Europe	105
4.1.1	Aerosol–cloud interactions	106
5	Conclusions & Outlook	111
	Bibliography	113
	List of Publications	133
	Appendix A	135
	Supplement of "Evaluation of the coupling of EMACv2.55 to the land surface and vegetation model JSBACH"	135
	Appendix B	153
	Supplement of "The effect of biomass burning aerosol emissions on global gross primary productivity"	153

1.1 Motivation

Following the 6th IPCC Assessment Report (IPCC 2023), we know that climate change caused by human activities leads to rising global temperatures, accelerated melting of glaciers, sea ice, and permafrost, as well as sea level rise and increased frequency of extreme weather events such as heatwaves, heavy precipitation, droughts, and wildfires. These climate change impacts are complemented by ocean acidification and ecosystem disruptions, all contributing to biodiversity loss. Water resources are under pressure due to more frequent droughts, declining snow-pack and glacier-fed flows, and worsening water quality and availability. In agriculture, climate change is linked to declining crop yields, increased livestock stress, and disrupted fisheries. Human health risks are rising due to heat-related illnesses, the spread of vector-borne diseases, respiratory issues from pollution and wildfires, and malnutrition driven by food insecurity. These impacts are also fueling displacement and migration, with growing numbers of climate refugees. Economically, the costs of infrastructure damage, disaster response, and losses in key sectors such as agriculture and tourism are increasing. Social and political effects include deepening inequalities, competition over scarce resources, and increased strain on governance systems. Long-term risks include exceeding climate tipping points and activating self-reinforcing feedback loops that could potentially trigger abrupt and irreversible changes. Those risks will increase if greenhouse gas emissions persist.

This knowledge is largely derived from simulations with comprehensive Earth System Models (ESMs). ESMs are advanced numerical tools developed to simulate the complex, dynamic interactions among the major components of the Earth system. These components include the atmospheric general circulation (analyzed by atmospheric general circulation models, or GCMs), land surface processes (analyzed by land surface models, or LSMs), and ocean dynamics (analyzed by ocean circulation models, or OCMs). Comprehensive ESMs also incorporate atmospheric chemistry and biological processes, which pursue a holistic picture of the entire Earth system. These integrated models help us understand the relationships and feedback mechanisms within the climate system across scales, interpret observed climate variability, identify future risks, and develop strategies to counteract them by providing projections of future climate evolution under different greenhouse

gas emission scenarios. It is especially challenging to model and analyze cloud microphysical processes, aerosol-cloud interactions and atmospheric chemistry. Cloud processes occur across a broad spectrum of spatial and temporal scales, ranging from the formation of droplets smaller than $1\ \mu\text{m}$ over a period of minutes, to wave patterns extending over thousands of kilometers and persisting for more than a week on a planetary scale. The same applies to chemical reactions in the atmosphere, the simulation of which is extremely computationally intensive and for which only a limited number of models can accurately represent these dynamics. Although atmospheric dynamics, ocean circulation and interactions between clouds and aerosols pose challenges for climate modeling, processes at the interface between land and atmosphere are equally crucial. These interactions play a central role in the Earth system and influence the composition of the atmosphere, cloud formation, surface temperatures and the global water cycle. To fully capture these dynamics, ESMs consider processes at the land surface that control the exchange of energy, water, and trace gases. In this context, the surface energy balance and hydrological processes are essential components of climate simulations, influencing both short-term weather conditions and long-term climate trends.

1.2 Surface energy balance and hydrology

Land surface processes strongly influence the surface energy balance and the hydrological cycle (Oke 2002). These include the control of soil moisture through infiltration and evaporation, as well as transpiration and carbon assimilation via vegetation (Flato 2011). Governed by the principles of mass and energy conservation, these processes determine how radiation is absorbed, reflected, and emitted by the surface. The energy balance for the interface between the surface and the atmosphere is given by the net radiation (R_{net}), sensible and latent heat fluxes (H_{sensible} and H_{latent}) and the ground heat flux (G), the conductive heat transfer between the surface and the ground below (Reick et al. 2013).

$$C \frac{\partial T_{\text{surf}}}{\partial t} = R_{\text{net}} + H_{\text{sensible}} + H_{\text{latent}} + G \quad (1.1)$$

With heat capacity (C) depending on soil type and the change in surface temperature per time ($\frac{\partial T_{\text{surf}}}{\partial t}$). Soil moisture and vegetation characteristics control latent heat fluxes via evapotranspiration, condensation, and sublimation, thereby modulating surface energy exchange. These same factors also affect surface albedo and aerodynamic roughness, influencing both radiative forcing and turbulent fluxes. Moreover, soil moisture dynamics regulate vertical mixing, cloud formation, and

chemical transformation rates, acting as key drivers of land–atmosphere coupling (Seneviratne et al. 2010; Koster et al. 2006; Seneviratne et al. 2006). One of the most important interactions is the influence of water vapor on atmospheric chemistry, which plays a central role in the formation of hydroxyl radicals (OH), the primary oxidants in the troposphere. OH is mainly produced via photolysis of ozone (O₃) by solar ultraviolet radiation, forming excited oxygen atoms (O(¹D)) that react with water vapor (Lelieveld et al. 2008; Seneviratne et al. 2010). Thus, near-surface H₂O concentrations—largely determined by land processes such as evapotranspiration—directly influence OH production (Monks 2005). Regions with high soil moisture or dense vegetation contribute to elevated water vapor levels, enhancing the local oxidative capacity of the atmosphere (Lelieveld et al. 2008). Land surface conditions also affect temperature, solar radiation, and the emission of reactive gases like VOCs and NO_x, all of which shape OH cycling. As a result, the hydrological state of the land exerts a strong influence not only on energy and moisture fluxes but also on atmospheric composition and chemical feedbacks. These interactions become even more complex when biogeochemical feedbacks are considered. Biological processes—such as photosynthesis, respiration, and microbial activity—further alter atmospheric chemistry. Vegetation emits BVOCs, serving as precursors to tropospheric ozone and secondary organic aerosols (see Section 1.3) (Guenther et al. 2006; Sanderson et al. 2003). Likewise, soil microbes, sensitive to moisture and temperature, release reactive nitrogen species (e.g., NO, N₂O, NH₃) and influence the uptake of greenhouse gases like methane CH₄ and carbon dioxide CO₂, thereby affecting radiative forcing (see Sections 1.5 and 1.6) (Saunio et al. 2025). Accurately capturing these intertwined physical and biogeochemical dynamics requires comprehensive land surface models that integrate energy balance, hydrology, vegetation, and microbial processes. Simultaneously, the land surface is continually influenced by atmospheric forcing. Variables such as shortwave and longwave radiation, precipitation, air temperature, wind, humidity, surface pressure, and CO₂ concentrations provide boundary conditions that drive or constrain land surface behavior. This ongoing exchange forms a tightly coupled system characterized by complex, nonlinear feedbacks between the physical and chemical states of the atmosphere and the land.

1.3 Biogenic volatile organic compounds (BVOCs)

Biogenic volatile organic compounds (BVOCs) are trace gases emitted by terrestrial vegetation (Guenther et al. 2006; Peñuelas et al. 2010a). These trace gases are part of a plant's adaptation to stress factors, as they can stabilize cell membranes and

protect the plant from heat damage (e.g. isoprene), serve as a defense mechanism against herbivore attacks, or attract pollinators (e.g. monoterpenes such as α -pinene, β -pinene and limonene, or sesquiterpenes) (Laothawornkitkul et al. 2008; Peñuelas et al. 2010a). Additionally, they can act as defense signals by attracting the natural enemies of herbivores and warning neighboring plants. Therefore BVOC emissions are strongly influenced by physiological responses to environmental conditions and stress factors, such as high temperatures, water deficits, strong winds, the presence of tropospheric ozone or herbivores (Peñuelas et al. 2010b; Yang et al. 2025; Emmerichs et al. 2024; Vella et al. 2023b). Once emitted, biogenic VOCs undergo rapid atmospheric oxidation and trigger a cascade of chemical reactions involving reactive nitrogen species and oxidants (Atkinson 2000; Atkinson et al. 2003) as illustrated in Figure 1.1.

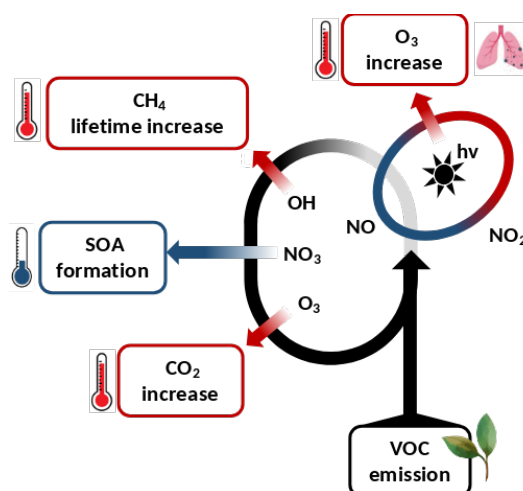


Figure 1.1: Schematic overview of atmospheric feedbacks triggered by biogenic VOC emissions, involving interactions with oxidants (e.g., OH, O₃) and reactive nitrogen species (e.g., NO, NO₂, NO₃). These processes contribute to the formation of secondary organic aerosols (SOA) and affect climate-relevant gases such as ozone, methane, and carbon dioxide. Symbols include Planck's constant (h) and photon frequency (ν). Adapted from Matyssek et al. (2014).

The dominant reaction pathway is initiated by hydroxyl radicals (OH):



The resulting peroxy radicals (RO_2) subsequently react with nitrogen monoxide (NO), forming nitrogen dioxide (NO_2):



NO_2 can be photolyzed under solar radiation by photons with photon frequency (ν), producing atomic oxygen, which then reacts with molecular oxygen to form tropospheric ozone:



Tropospheric ozone is a potent greenhouse gas contributing to global warming and as an irritant gas it affects human health, triggering diseases and damaging the respiratory system (Calfapietra et al. 2013; Ehhalt et al. 2009; Sand et al. 2023; Lippmann 1991; Pozzer et al. 2023; Ebi et al. 2009; McKee 1993). In addition, ozone poses a significant threat to plant health as it can destroy leaf structures, making plants more susceptible to attack by animals and impairing photosynthesis, which in turn increases plant stress and subsequent BVOC emissions (Yang et al. 2025). The oxidation of BVOCs also has implications for methane (CH_4) chemistry. As the oxidation of BVOCs reduces OH radicals, less OH is available to react with CH_4 , thereby increasing the atmospheric lifetime of methane (Lelieveld et al. 1998). As CH_4 is itself a potent greenhouse gas, this indirect mechanism contributes to warming through a reduction in the atmospheric CH_4 sink. An overview of the role of CH_4 in the earth system is given in Section 1.5. BVOCs are key precursors to secondary organic aerosols (Hallquist et al. 2009; Kulmala et al. 2004; Wang et al. 2018; Wu et al. 2020). During the daytime, BVOCs such as isoprene react with hydroxyl radicals, forming oxidized intermediates like ISOPOOH and isoprene-derived epoxydiols (IEPOX), which can undergo multiphase reactions and condense onto aerosols forming SOAs. At night, particularly monoterpenes, can react with nitrate radicals (NO_3) or ozone, leading to the formation of highly oxygenated organic molecules (HOMs), which also efficiently contribute to SOA formation. These aerosols influence climate through both direct radiative forcing (by scattering or absorbing solar radiation) and indirect effects (by altering cloud condensation nuclei properties and cloud albedo) (Peñuelas et al. 2003; Scott et al. 2014; Rap et al.

2013; Sporre et al. 2019). Section 1.4 provides a more detailed overview of the effects of aerosols on clouds and the climate. Additionally, BVOCs can react with ozone, resulting in the production of CO₂, further contributing to the greenhouse effect (Matyssek et al. 2014; Guenther 2002; Kesselmeier et al. 2002). These processes show the significant impact of BVOC emissions on the interactions between the biosphere and atmosphere, as they are strongly influenced by atmospheric and climatic conditions such as temperature, ozone levels and water availability. In turn, they influence atmospheric composition, oxidative capacity, and the formation of secondary pollutants such as ozone and aerosols. These interactions can alter radiative forcing, cloud properties and ecosystem health, thereby contributing to the overall climate response (Peñuelas et al. 2009; Peñuelas et al. 2010a; Calfapietra et al. 2013; Matyssek et al. 2014; Kulmala et al. 2004). Despite their significance, quantifying the BVOC–aerosol–cloud feedbacks within ESMs remains challenging. Key questions include how BVOC emissions will respond to plant stress in future climate scenarios with rising temperature and changed precipitation patterns or, how atmospheric oxidant concentrations will vary under elevated CO₂ concentrations and land use change (Kulmala et al. 2004; Monson et al. 2007). These factors highlight the need for ESMs that explicitly link vegetation dynamics, atmospheric chemistry, and hydrological processes in order to model the interactions that drive the Earth’s climate system.

1.4 Aerosols

Aerosols, which are microscopic solid or liquid particles suspended in the atmosphere, play a significant role in the Earth’s climate system and ecosystems. Their effects can be broadly categorized into radiative, cloud-related, and biogeochemical/ecosystem impacts:

1. Radiative effects (direct and semi-direct)

- **Direct effect:** Aerosols can scatter and absorb solar radiation. Scattering aerosols (e.g., sulfates, nitrates, sea salt) reflect sunlight back to space, producing a net cooling effect (Andreae et al. 2005; Lohmann et al. 2005; Haywood et al. 2000). Absorbing aerosols (e.g., black carbon, organic carbon) absorb solar energy, leading to heating of the atmosphere and potential surface dimming (Lohmann et al. 2005; Penner et al. 2001).
- **Semi-direct effect:** Absorbing aerosols heat the atmospheric column, potentially stabilizing it and thereby suppressing cloud formation and enhancing

cloud evaporation (Ackermann et al. 2001) which alters local circulation and precipitation patterns (Penner et al. 2001).

2. Cloud-related effects (indirect effects)

- **First indirect effect (cloud albedo effect):** Aerosols act as cloud condensation nuclei (CCN), resulting in clouds with more, but smaller, droplets. This increases cloud albedo and enhances shortwave reflection, contributing to a net cooling (Twomey 1959c; Twomey 1959a; Lohmann et al. 2005; Haywood et al. 2000). This effect is analyzed in more detail later in this work, Chapter 4, Part 4.1.
- **Second indirect effect (cloud lifetime effect):** Smaller cloud droplets coalesce less efficiently, thereby reducing precipitation efficiency and extending cloud lifetime, which can further affect radiation and regional water cycles (Lohmann et al. 2005; Haywood et al. 2000).

3. Biogeochemical and ecosystem effects

- **Surface radiation reduction:** Aerosols modify the amount of photosynthetically active radiation (PAR) reaching the surface, which can lead to changes in plant productivity (Carslaw et al. 2010; Zhou et al. 2020; Rap et al. 2015; Cohan et al. 2002). A detailed analysis of this feedback effect is presented later in this work, Chapter 3, Part 3.2.
- **Surface albedo change:** Aerosol deposition on snow and ice can reduce surface albedo, thereby increasing the amount of solar radiation absorbed by the surface and decreasing the fraction reflected back to space (Hansen et al. 2004).
- **Nutrient deposition:** Certain aerosols, such as mineral dust, nitrates, and iron-containing particles, can deposit essential nutrients onto terrestrial and ocean surfaces potentially enhancing primary productivity in nutrient-limited regions (Swap et al. 1992; Duce 1986).
- **Ozone formation:** Precursors of secondary organic aerosols participating in photochemical reactions can lead to increased tropospheric ozone concentrations, with negative impacts on the respiratory system, plant physiology and crop productivity. (Lelieveld et al. 1998; Rabl et al. 2000).
- **Toxicity and ecological damage:** Aerosols containing heavy metals or acidic compounds can alter soil and water chemistry, reduce biodiversity and plant growth. (Rabl et al. 2000).

Overall, aerosols can offset part of the warming caused by greenhouse gases through both direct (radiative scattering and absorption) and indirect (cloud-related) cooling effects. However, their short atmospheric lifetimes, spatial variability, and limited mixing lead to significantly greater uncertainty in their net climate forcing compared to other climate forcers (e.g., long-lived greenhouse gases).

1.5 Methane (CH₄)

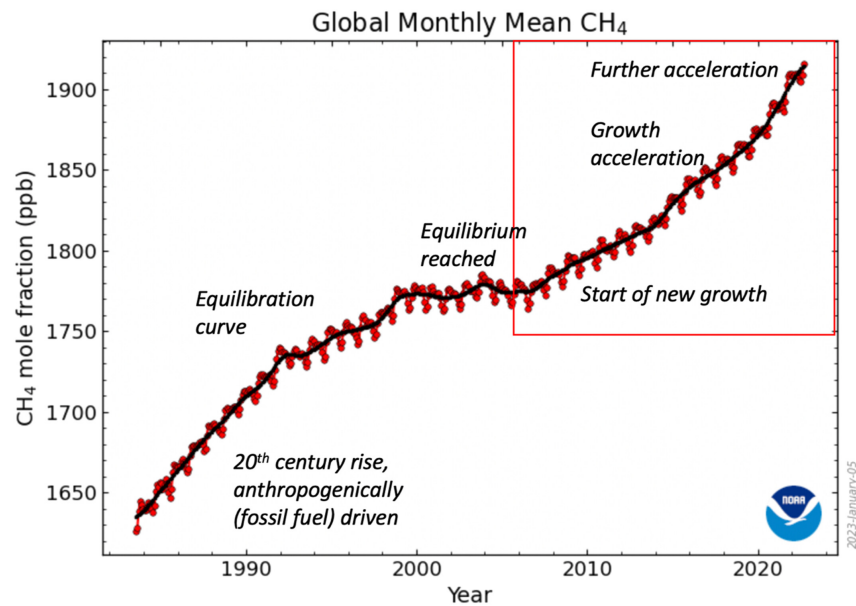


Figure 1.2: Global monthly mean atmospheric methane (CH₄) mole fractions (in ppb) from 1980 to 2023 (Nisbet et al. 2023)

Methane (CH₄) is the second most important anthropogenic greenhouse gas after CO₂, and both its emissions and atmospheric concentrations have been steadily rising in recent decades (Saunois et al. 2025). Methane emissions originate from a wide range of anthropogenic and natural sources. Anthropogenic sources include fossil fuel production and use, agriculture, waste management, and biomass combustion. Natural sources comprise wetlands, inland freshwater systems, geological emissions, oceans, termites, wild animals, thawing permafrost, and vegetation (Woodward et al. 2010; Fluet-Chouinard et al. 2023; Saunois et al. 2025). These emissions are spatially diffuse, temporally variable, and often poorly characterized, with leakage hot spots remaining difficult to detect and monitor (Zhao et al. 2019). The

primary atmospheric sink of CH₄ is oxidation by OH in the troposphere, accounting for roughly 90% of its removal. An additional 5–10% is removed via soil uptake, particularly in well-drained, aerobic soils through microbial oxidation (Saunio et al. 2025). Figure 1.2 shows the global monthly mean atmospheric methane mole fractions from the 1980 to 2023 (Nisbet et al. 2023). CH₄ concentrations have increased from approximately 1650 ppb in 1985 to over 1900 ppb by 2023, with an accelerating upward trend. The time series shows distinct phases: an initial 20th-century rise mainly driven by anthropogenic fossil fuel emissions, a stabilization period around 2000 where equilibrium appears to have been reached, and a renewed growth phase beginning around 2007. This growth has accelerated notably since 2014, with a further steep increase after 2020. The recent acceleration raises concerns about intensifying CH₄ emissions or weakening atmospheric sinks, reinforcing methane's importance in near-term climate forcing and the urgency of mitigation strategies. Although CH₄ has a much shorter atmospheric lifetime (~8.2 years) (Saunio et al. 2025) compared to CO₂, it is significantly more potent, with a 100-year global warming potential for fossil fuel emitted CH₄ of approximately 29.8 times that of CO₂ (Saunio et al. 2025; Armour et al. 2021). CH₄ plays a central role in several critical Earth system feedback mechanisms, many of which are of high relevance for understanding and projecting climate dynamics:

- **Atmospheric oxidation:** The atmospheric lifetime of CH₄ is controlled by its reaction with OH, whose concentrations are influenced by emissions of NO_x, CO, VOCs, and water vapor. This creates a dynamic chemical feedback that also affects tropospheric ozone (O₃) levels (Crutzen 1973; Crutzen 1979).
- **Stratospheric processes:** A fraction of CH₄ reaches the stratosphere, where its oxidation contributes to ozone depletion and increases stratospheric water vapor, both of which affect radiative forcing (Noël et al. 2018; Ehhalt et al. 1973).
- **Wetland, permafrost, and vegetation–soil moisture feedbacks:** CH₄ emissions from wetlands (saturated and anaerobic soils) and thawing permafrost are highly sensitive to temperature and moisture conditions. Warming accelerates microbial methanogenesis, and increased precipitation and permafrost thaw can expand wetland extent, enhancing CH₄ release. Concurrently, soil moisture and root exudates modulate methanogenic and methanotrophic microbial activity, influencing both CH₄ production and oxidation. These processes reinforce a positive climate–carbon feedback (Kleinen et al. 2023; Zhang et al. 2023; Schaefer et al. 2014; Nauta et al. 2015; Luo et al. 2013).

- **Soil CH₄ uptake:** Upland (dry and oxygen-rich) soils act as a modest but persistent CH₄ sink through oxidation by methanotrophic bacteria. This sink is sensitive to soil temperature, moisture, and land-use change (Liu et al. 2019; Murguia-Flores et al. 2021; Murguia-Flores et al. 2018).

Despite progress in satellite and ground-based observations, substantial uncertainties remain in quantifying CH₄ emissions, especially from natural sources such as wetlands and freshwater systems, which are often poorly represented in models due to limited data and uncertain spatial coverage (Kleinen et al. 2012; Kleinen et al. 2020; Kleinen et al. 2023). Anthropogenic emission inventories are also incomplete and biased toward mid-latitude regions in the Northern Hemisphere, with sparse observational coverage in the tropics (Dlugokencky et al. 2011). This can be partly improved by increased and improved satellite measurements, but their accuracy is still limited by cloud cover and surface heterogeneity (Buchwitz et al. 2005; Jacob et al. 2022). The atmospheric sink of CH₄ is dominated by oxidation with OH, which themselves are highly variable and difficult to quantify. OH has a short atmospheric lifetime (on the order of 1 second) and its concentrations exhibit strong spatial and temporal variability. Direct measurements are limited to local scales (1 km spatial and 30 minutes temporal resolution), making global observation infeasible (Saunois et al. 2025). Moreover, because the efficiency of the CH₄ sink depends on both OH concentration and temperature, OH concentration alone cannot serve as a reliable proxy for sink strength. Consequently, large-scale atmospheric chemistry models that simulate temperature and corresponding atmospheric OH concentration remain essential for global CH₄ budget assessments (Saunois et al. 2025). In addition to atmospheric loss processes, CH₄ is removed through uptake by upland soils, which serve as a modest but persistent sink via microbial oxidation. This terrestrial sink has roughly doubled from 1900 to 2015 and may increase further with rising atmospheric CH₄ concentrations (Murguia-Flores et al. 2021). Accurate representation of this sink is critical for improving global CH₄ budget estimates.

1.6 Hydrogen (H₂)

Molecular hydrogen (H₂) plays a critical role in atmospheric chemistry and the Earth's biogeochemical cycles. Despite its lower concentration in the atmosphere compared to CH₄, H₂ is involved in a variety of processes that connect the atmosphere with terrestrial ecosystems, including soils and vegetation. A comprehensive understanding of these interactions is essential, as they significantly influence atmospheric composition, oxidative capacity, and ultimately, climate dynamics. Key feedback mechanisms involving H₂ include:

- **Soil uptake:** Soils act as the largest sink for atmospheric H₂, mainly through microbial activity. Specialized microbes consume H₂, and this uptake depends strongly on soil conditions such as moisture, temperature, and the diversity and abundance of microbial communities. Variations in these factors lead to fluctuations in how much H₂ is removed from the atmosphere. Currently, soil uptake accounts for about 70–80% of H₂ removal (Constant et al. 2009; Ehhalt et al. 2009; Paulot et al. 2024). However, as hydrogen use expands, increased emissions may disrupt this balance, potentially triggering a cascade of climate and chemical feedbacks (Ehhalt et al. 2009; Trapani et al. 2025).
- **Vegetation interactions:** Vegetation affects atmospheric H₂ in multiple ways. Leaves can directly absorb H₂, while plants also influence soil properties—such as aeration and organic matter content—that affect microbial uptake rates. These plant-soil interactions create a dynamic environment that modulates H₂ exchange with the atmosphere.
- **Climate and environmental feedbacks:** Changes in climate, such as temperature and precipitation patterns, alter soil moisture and vegetation growth, which in turn affect microbial activity and H₂ uptake rates. This creates a feedback loop where environmental changes influence atmospheric H₂, which then impacts atmospheric chemistry and climate. Although H₂ is not a direct greenhouse gas, it influences climate indirectly by interacting with OH radicals. Elevated H₂ reduces OH availability, which slows the atmospheric removal of CH₄ leading to a significant warming effect (Ehhalt et al. 2009). Additionally, the reaction of H₂ with OH produces atomic hydrogen (H), which can increase tropospheric O₃ concentrations.
- **Coupling with atmospheric chemistry:** As illustrated in Figure 1.3, atmospheric H₂ influences the oxidative capacity of the atmosphere by interacting with OH. Variations in H₂ concentrations therefore affect the cycling of other

important greenhouse gases, including CH_4 , O_3 , and CO_2 . In the stratosphere, the oxidation of H_2 increases the level of water vapor, which affects ozone chemistry and potentially reduces the ozone layer's ability to shield the Earth from harmful ultraviolet radiation. (Sand et al. 2023; Solomon et al. 2010; Shindell 2001; Tromp et al. 2003; Feck et al. 2008). Elevated atmospheric H_2 may also affect aerosol chemistry. By reducing OH-driven oxidation of sulfur dioxide (SO_2), H_2 can decrease sulfate aerosol formation, which normally has a cooling effect through scattering sunlight and influencing cloud properties (Sand et al. 2023; Lohmann et al. 2005) (see 1.4). This contributes further to warming effects linked to increased hydrogen emissions.

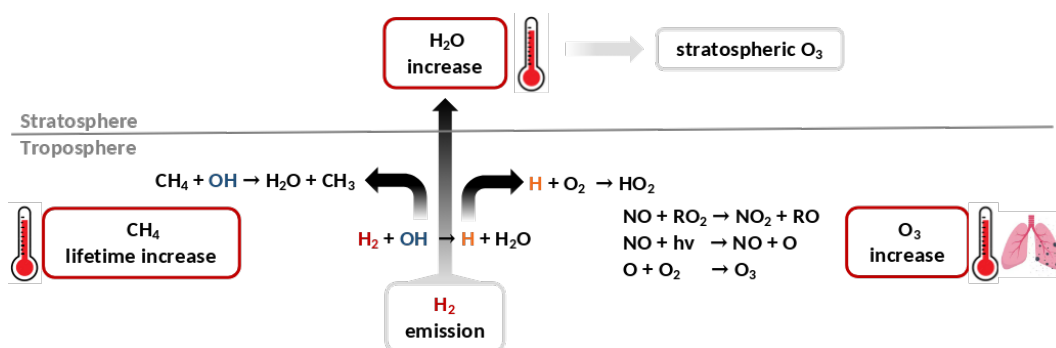


Figure 1.3: Schematic overview of key atmospheric feedback mechanisms associated with hydrogen (H_2) emissions. H_2 oxidation by OH reduces the oxidative capacity of the atmosphere, increases CH_4 lifetime, promotes O_3 formation, and raises stratospheric water vapor levels, with implications for both air quality and climate. Adapted from Sand et al. (2023).

Taken together, these natural and anthropogenic processes show that increased H_2 emissions and leakage have the potential to intensify global warming, despite H_2 itself not being a direct greenhouse gas. Direct measurements of soil H_2 fluxes are geographically sparse and mostly limited to temperate sites in the Northern Hemisphere (Tardito Chaudhri et al. 2024; Cowan et al. 2024). This makes the soil sink the largest source of uncertainty in the global hydrogen budget (Cowan et al. 2024; Ehhalt et al. 2009). Due to the limited observational coverage, ESMs are essential for estimating soil hydrogen fluxes in regions with sparse sampling, offering a consistent framework for quantifying their contribution to the global hydrogen cycle.

1.7 Summary of introduction

Human-induced climate change is intensifying and will persist if greenhouse gas emissions are not reduced. Understanding and quantifying these changes requires Earth System Models (ESMs), which represent the complex physical, chemical, and biological interactions within the climate system. Modeling small-scale processes—such as cloud microphysics, aerosol interactions, and atmospheric chemistry—remains computationally intensive, and only a few models can perform coupled simulations across different timescales. Among these, the ECHAM5/MESSy atmospheric chemistry model (EMAC) incorporates both cloud microphysics and aerosols coupled with atmospheric chemistry (Jöckel et al. 2005; Jöckel et al. 2006; Jöckel et al. 2010a; Jöckel et al. 2016). EMAC currently uses a simplified surface scheme and the dynamic vegetation model LPJ-GUESS, which simulates plant functional types, leaf area index, canopy structure, biomass, and vegetation cover (Forrest et al. 2020; Vella et al. 2023a). However, LPJ-GUESS provides only limited energy balance, soil hydrology, and land–atmosphere coupling, omitting key vegetation–hydrology–atmosphere feedbacks. Additionally, EMAC cannot fully represent methane–climate feedbacks or dynamic coupled sinks of methane and hydrogen, both strongly influenced by land and soil conditions and so far only available as offline fields. Improving model performance requires incorporating vegetation and soil feedbacks, which are essential for understanding long-term climate projections, nonlinear responses, and tipping points. This is also critical for evaluating climate intervention strategies, such as hydrogen-based energy systems or large-scale carbon dioxide removal, which introduce new feedbacks and uncertainties—from hydrogen leakage to land-use changes associated with bioenergy. Capturing these dynamics demands integration with socio-economic, energy, and policy frameworks, making enhanced ESMs essential not only supporting scientific understanding but also for climate risk management. This project addresses these gaps by coupling EMAC with the JSBACHv4 land surface model (Reick et al. 2013; Reick et al. 2021), improving the representation of energy, water, and trace gas fluxes, as well as biosphere–atmosphere interactions. Enhanced surface energy balance and soil hydrology affect vegetation growth, evapotranspiration, and biogenic volatile organic compound (BVOC) emissions, which influence atmospheric oxidative capacity, ozone and aerosol formation, and radiative forcing. Additionally a biogenic soil deposition submodel is added, calculating the online uptake of methane and hydrogen, processes highly sensitive to soil moisture, temperature, and vegetation. The primary goal is to develop EMAC into a fully coupled ESM that includes atmospheric chemistry and aerosol dynamics, enabling investigation of vegetation and microbial feedbacks, climate and ecosystem impacts

of methane, hydrogen, and aerosols, and their influence on atmospheric composition. In addition, this work applies the upgraded model to assess the effects of biomass burning aerosols on plant productivity and implements interactive soil sink parameterizations for CH₄ and H₂ in MESSy.

1.8 Thesis outline

The thesis is organized as follows:

- **Chapter 2** provides an overview of the ECHAM5/MESSy atmospheric chemistry model, the JSBACH land surface and vegetation model, and the BIODep submodel.
- **Chapter 3** presents one peer-reviewed publication and two publication drafts, each with own methodology, experimental design, and result section:
 - **Part 3.1:** Evaluation of the coupling of EMACv2.55 to the land surface and vegetation model JSBACHv4. (Peer-reviewed publication)
 - **Part 3.2:** The effect of biomass burning aerosol emissions on global gross primary productivity. (Publication draft)
 - **Part 3.3:** Methane and hydrogen soil deposition in the ECHAM5/MESSy atmospheric chemistry model (EMAC) v2.55 using the newly implemented submodel BIODep. (Publication draft)
- **Chapter 4** presents my contribution to the analysis of indirect aerosol effects, by the improved representation of aerosol–cloud interactions in EMAC in the study of Reifenberg et al. 2022.
- **Chapter 5** summarizes the key conclusions and outlines directions for future research.

2.1 Modular Earth Submodel System (MESSy)

2.1.1 ECHAM5/MESSy atmospheric chemistry model (EMAC)

The ECHAM5/MESSy Atmospheric Chemistry (EMAC) model is a comprehensive numerical system for simulating interactions between atmospheric chemistry and climate processes. It is based on the fifth-generation European Center Hamburg general circulation model (ECHAM5) (Roeckner et al. 2006), which has been restructured and re-implemented within the Modular Earth Submodel System (MESSy) framework (Jöckel et al. 2010a). The MESSy framework is a multi-institutional software infrastructure designed to flexibly connect general circulation models with a wide range of modular submodels that represent key Earth system components and processes. These include infrastructural tools, diagnostic modules, physical parameterizations, and atmospheric chemistry schemes. Submodels can be selectively activated depending on the scientific focus of the simulation, enabling applications that range from simplified box model simulations to fully interactive earth system and climate scenario simulations, including coupled ocean–atmosphere dynamics. While most of the original ECHAM physical routines have been replaced by MESSy-compatible submodels, a few core elements remain, specifically, the spectral transform dynamical core, the flux-form semi-Lagrangian advection scheme, and the nudging routines for Newtonian relaxation. Further technical documentation on EMAC is provided by Jöckel et al. 2016 and is available at the official MESSy website: <https://messy-interface.org/> (last accessed: 07 July 2025). For this study, simulations were conducted using the EMAC model with MESSy version 2.55.0, at a T63 horizontal resolution. This corresponds to a quadratic Gaussian grid with a spatial resolution of approximately 1.8° in both latitude and longitude. The vertical resolution includes 31 hybrid pressure levels, reaching up to roughly 10 hPa. Detailed descriptions of the specific model configurations and submodels applied in this work can be found in the respective studies referenced in Chapter 3.

2.1.2 JSBACH submodel

Main part of this work is the implementation of the JSBACHv4 land surface model (Reick et al. 2013; Reick et al. 2021), a key component of the Icosahedral Non-hydrostatic Earth System Model (ICON-ESM) (Jungclaus et al. 2022) and its predecessor (JSBACH3) in the Max Planck Institute Earth System Model, MPI-ESM (Mauritsen et al. 2019), within the EMAC model framework to improve the representation surface fluxes of energy, water, and carbon to the atmosphere. JSBACH includes dynamic vegetation, a comprehensive hydrological system, and biogeochemical cycles, providing a physically consistent interface between the land surface and the atmosphere. The version four of JSBACH applied here incorporates seven main process categories that contribute to a more realistic representation of land-atmosphere interactions within EMAC (Schneck et al. 2022). **Vegetation processes** are represented using 11 Plant Functional Types (PFTs) including tropical and extra-tropical broadleaf evergreen and deciduous trees, rain-green shrubs, deciduous shrubs, C_3 - and C_4 -grass, pasture, and crops, each simulated with a three-layer canopy radiation scheme. Key physiological and phenological processes are included, with dynamic calculation of the Leaf Area Index (LAI) and plant fractional coverage, all dependent on atmospheric boundary conditions and soil states (e.g., temperature, water stress, precipitation, and radiation). This configuration enables full coupling between vegetation and atmosphere. Furthermore, JSBACH can be interactively coupled with the MEGAN submodel (Guenther et al. 2006) to simulate biogenic volatile organic compound emissions, thereby linking vegetation processes directly to atmospheric chemistry and enabling feedbacks via emissions, evapotranspiration, and surface temperature changes. **The hydrology scheme** features a five-layer soil model that replaces the former single-layer bucket scheme in EMAC's SURFACE submodel. It simulates soil temperature and moisture profiles down to 9 meters, incorporating percolation and diffusion processes. This structure allows for the computation of soil moisture dynamics, runoff, and evaporation, and captures water availability across the rooting zone more realistically. **The surface energy balance** module calculates temperature profiles within all five soil layers as well as three snow layer temperatures on the surface. Heat and moisture fluxes are determined in conjunction with hydrological and thermal conditions. A dedicated **turbulence scheme** models surface roughness, controlling the exchange of energy and moisture between the land surface and the lowest atmospheric layer. **The radiation scheme** accounts for the transmission of radiation through the three vegetation canopy layers and dynamically computes surface albedo based on vegetation type, snow, and water cover. This module is also used to calculate photosynthetically active radiation, which directly influences photosynthesis rates. **Carbon cycling**

is represented through modules for vegetation productivity, carbon assimilation, and turnover, all influenced by stress factors, radiation availability, and vegetation type. Plant growth and biomass accumulation are thereby dynamically simulated. An additional component addressing **fuel load and disturbance processes** (e.g., biomass burning, wind-throw) has been included but not yet activated and evaluated in this version. It offers potential for future incorporation of disturbance-driven emissions and vegetation dynamics. JSBACH is under continuous development by the Max Planck Institute for Meteorology in Hamburg, and improvements can be progressively integrated into the JSBACH submodel in MESSy. A comprehensive description, tuning, and evaluation of JSBACH within MESSy are presented in Chapter 3, Part 3.1, constituting a central contribution of this PhD work.

2.1.3 BIODP submodel

As part of this work, the BIODP submodel was developed and implemented within the MESSy framework to simulate the biogenic soil uptake (deposition) of hydrogen (H_2) and methane (CH_4). BIODP represents an extension of EMAC, enabling the interactive coupling of trace gas soil deposition with land surface processes. The H_2 deposition scheme is based on parameterizations present in literature (Paulot et al. 2021; Ehhalt et al. 2013; Yonemura et al. 2000). It calculates the diffusion and uptake of H_2 in soil as a function of soil temperature and moisture, with these variables now provided online by the newly integrated JSBACH submodel. The H_2 deposition parameters were tuned to match a globally averaged deposition velocity of approximately 0.033 cm s^{-1} , consistent with previous studies (Surawski et al. 2025). In addition, BIODP includes an implementation of the MeMo v1.0 soil methanotrophy model (Murguia-Flores et al. 2018) to simulate CH_4 uptake in soils. Similar to the H_2 scheme, CH_4 uptake depends on soil temperature, moisture, and physical soil characteristics provided by JSBACH. Moreover, the rate of CH_4 consumption is influenced by nitrogen deposition, which can be dynamically provided by EMAC's atmospheric chemistry submodels, enabling a fully interactive coupling with atmospheric processes and human influence on the nitrogen cycle. Both H_2 and CH_4 deposition schemes compute deposition velocity, total uptake, and surface fluxes, which are fed back into the atmospheric chemistry modules of EMAC. This feedback updates the tendencies of atmospheric H_2 and CH_4 concentrations, thereby enabling fully coupled soil–atmosphere exchange simulations and supporting both short-term and long-term climate feedback analyses. A full technical description, evaluation against observations, and comparison with other models for both schemes is provided in Chapter 3, Part 3.3.

2.2 Summary of methodology

This work enhances the Modular Earth Submodel System by integrating an advanced land surface model and trace gas deposition processes into the ECHAM/MESMx Atmospheric Chemistry model. A key development is the implementation of JSBACH v4, a state-of-the-art land surface model which simulates key processes such as energy, water and carbon fluxes, vegetation, hydrology, canopy radiation, the surface energy balance and biogeochemical cycles. With this addition, EMAC can now represent physically consistent land–atmosphere interactions, enabling fully coupled Earth system simulations. Based on this improved surface representation, the newly developed BIODep submodel has been introduced to simulate the uptake of biogenic hydrogen (H_2) and methane (CH_4) by the soil. H_2 deposition is driven by soil properties provided by JSBACH and follows established parameterizations. CH_4 uptake is based on the MeMo v1.0 model and is further modulated by nitrogen deposition from EMAC’s atmospheric chemistry modules. Both deposition schemes feed back into atmospheric chemistry, thereby closing the surface–atmosphere exchange cycle for these trace gases. Together, JSBACH v4 and BIODep substantially extend EMAC’s Earth system modeling capabilities, providing a robust foundation for scenario-based simulations of hydrogen leakage and methane emissions in the context of a changing climate.

3.1 Coupling of the JSBACH land surface and vegetation model and the ECHAM5/MESSy atmospheric chemistry model (EMAC)

This chapter presents a research article published in the journal *Geoscientific Model Development*. I am the first author of and the main contributor to this paper. I coupled EMAC and JSBACH and performed the model simulations with Andrea Pozzer. I analyzed the model results and evaluated the simulations. I prepared the manuscript and made the figures. More detailed information on the Author contributions are provided at the end of the manuscript. The supplement to this work can be found in [Appendix A](#). How to cite:

Martin, A., Gayler, V., Steil, B., Klingmüller, K., Jöckel, P., Tost, H., Lelieveld, J., and Pozzer, A.: Evaluation of the coupling of EMACv2.55 to the land surface and vegetation model JSBACHv4, *Geosci. Model Dev.*, 17, 5705–5732, <https://doi.org/10.5194/gmd-17-5705-2024>, 2024.



Evaluation of the coupling of EMACv2.55 to the land surface and vegetation model JSBACHv4

Anna Martin¹, Veronika Gayler², Benedikt Steil¹, Klaus Klingmüller¹, Patrick Jöckel³, Holger Tost⁴, Jos Lelieveld^{1,5}, and Andrea Pozzer^{1,5}

¹Atmospheric Chemistry Department, Max Planck Institute for Chemistry, 55128 Mainz, Germany

²Climate Dynamics Department, Max Planck Institute for Meteorology, 20146 Hamburg, Germany

³Deutsches Zentrum für Luft- und Raumfahrt (DLR), Institut für Physik der Atmosphäre, Oberpfaffenhofen, Germany

⁴Institute for Atmospheric Physics, Johannes Gutenberg University Mainz, 55128 Mainz, Germany

⁵The Cyprus Institute, Climate and Atmosphere Research Center, Nicosia 1645, Cyprus

Correspondence: Anna Martin (a.martin@mpic.de)

Received: 18 December 2023 – Discussion started: 5 January 2024

Revised: 5 April 2024 – Accepted: 30 May 2024 – Published: 30 July 2024

Abstract. We present the coupling of the Jena Scheme for Biosphere–Atmosphere Coupling in Hamburg version 4 (JSBACHv4) to the ECHAM/MESSy Atmospheric Chemistry (EMAC) model. With JSBACH, the soil water bucket model in EMAC is replaced by a diffusive hydrological transport model for soil water that includes water storage and infiltration in five soil layers, preventing soil from drying too rapidly and reducing biases in soil temperature and moisture. A three-layer soil scheme is implemented, and phase changes in water in the soil are considered. The leaf area index (LAI) climatology in EMAC has been substituted with a phenology module calculating the LAI. Multiple land cover types are included to provide a state-dependent surface albedo, which accounts for the absorption of solar radiation by vegetation. Plant net primary productivity, leaf area index and surface roughness are calculated according to the plant functional types. This paper provides a detailed evaluation of the new coupled model based on observations and reanalysis data, including ERA5/ERA5-Land datasets, Global Precipitation Climatology Project (GPCP) data and Moderate Resolution Imaging Spectroradiometer (MODIS) satellite data. Land surface temperature (LST), terrestrial water storage (TWS), surface albedo (α), net top-of-atmosphere radiation flux (Rad_{TOA}), precipitation (precip), leaf area index (LAI), fraction of absorbed photosynthetic active radiation (FAPAR) and gross primary productivity (GPP) are evaluated in particular. The strongest correlation (r) between reanalysis data and the newly coupled

model is found for LST ($r = 0.985$, with an average global bias of -1.546 K), α ($r = 0.947$, with an average global bias of -0.015) and Rad_{TOA} ($r = 0.907$, with an average global bias of 3.56 W m⁻²). Precipitation exhibits a correlation with the GPCP dataset of 0.523 and an average global bias of 0.042 mm d⁻¹. The LAI optimisation yields a correlation of 0.637 with observations and a global mean deviation of -0.212 . FAPAR and GPP exemplify two of the many additional variables made available through JSBACH in EMAC. FAPAR and observations show a correlation of 0.663, with an average global difference of -0.223 , while the correlation for GPP and observations is 0.564 and the average global difference is -0.001 kg carbon km⁻¹. Benefiting from the numerous added features within the simulated land system, the representation of soil moisture is improved, which is critical for vegetation modelling. This improvement can be attributed to a general increase in soil moisture and water storage in deeper soil layers and a closer alignment of simulated TWS with observations, mitigating the previously widespread problem of soil drought. We show that the numerous newly added components strongly improve the land surface, e.g. soil moisture, TWS and LAI, while surface parameters, such as LST, surface albedo or Rad_{TOA} , which were mostly prescribed according to climatologies, remain similar. The coupling of JSBACH brings EMAC a step closer towards a holistic comprehensive Earth system model and extends its versatility.

1 Introduction

Earth system models (ESMs) are needed to analyse current and future climate scenarios, and particularly in view of ongoing climate change (IPCC, 2021), it is crucial to include the main Earth system components to identify and quantify potential feedback mechanisms. These numerical models are based on a mathematical formulation of the physical and chemical processes, accounting for interactions between the atmosphere, oceans and biogeochemical processes on land (Flato, 2011). Common ESMs contain an atmospheric general circulation model (A-GCM), an ocean general circulation model (O-GCM) and a land surface model (LSM). A comprehensive list of existing ESMs can be found, for instance, in “Annex II: Models” of the Sixth Assessment Report of the Intergovernmental Panel on Climate Change (Gutiérrez et al., 2021).

The ECHAM5/MESy Atmospheric Chemistry (EMAC) general circulation model is based on an underlying A-GCM; more specifically, the spectral dynamical core, the large-scale advection and the “nudging” method are originally from ECHAM5 (the fifth generation of the European Centre Hamburg general circulation model; Roeckner et al., 2006). The physical parameterisations from ECHAM have been modularized between respective further-developed MESy submodels. These include a simplified surface model (SURFACE); O-GCM MPIOM (Pozzer et al., 2011a); and several other submodels which address atmospheric chemistry, cloud and transport processes (Roeckner et al., 2003; Jöckel et al., 2005, 2010). The coupling is achieved via the Modular Earth Submodel System (MESy2) framework, gradually refined and expanded during the past 2 decades to provide an infrastructure of submodel and process combinations with a wide range of applications. EMAC is a community model with a growing number of users contributing to developments in various research areas, e.g. studies on particle concentrations and aerosols (Kohl et al., 2023; Righi et al., 2023), oxidation capacity (Nussbaumer et al., 2023; Friedel et al., 2023), atmospheric dynamics (Eichinger et al., 2023; Charlesworth et al., 2023) and environmental consequences for human health (Pozzer et al., 2023; Milner et al., 2023). Furthermore, an alternative dynamic vegetation scheme (LPJ-GUESS; Forrest et al., 2020) has been coupled to EMAC, allowing for climate–vegetation interactions (e.g. Vella et al., 2023b). In the following, the implementation and evaluation of the LSM Jena Scheme for Biosphere–Atmosphere Coupling in Hamburg (JSBACH), a substitute of EMAC’s current surface model, is documented. JSBACH is implemented into the MESy framework following the relevant coding standards. The dynamical land–surface model JSBACH was first developed as the land model for ECHAM at the Max Planck Institute for Meteorology (MPI-M) (Reick et al., 2021). Originally, it emerged from the combination of all ECHAM5 land processes in a separate land model and was further developed and refined, now providing

a large repertoire of biogeochemical processes of the ecosystem. The latest version (JSBACHv4) is part of the Icosahedral Nonhydrostatic Land (ICON-Land) model and has not yet been coupled to models simulating atmospheric chemistry (Pham et al., 2021).

The implementation of JSBACH represents significant progress in the development of the ESM EMAC. As climate change progresses and the occurrence of extreme weather events increases, the influence of surface processes and vegetation becomes more prominent (Domeisen et al., 2022). Vegetation and soil water balance are the driving factors for surface fluxes of heat and moisture, affecting temperature, precipitation, atmospheric dynamics and chemistry (Miralles et al., 2019; Lauwaet et al., 2009; Matyssek et al., 2014; Mellouki et al., 2015). JSBACH replaces the soil water bucket model included in the MESy submodel SURFACE by a more comprehensive five-layer hydrological soil model. This substitution aims at improving the representation of surface energy fluxes of heat and moisture, reducing biases in surface temperature and subsequent plant stress and their impact on biogenic emissions. JSBACH enables the analysis of biogeochemical processes on much smaller timescales, including not only climatic scales, but also days and hours. This allows for the analysis of the impact of vegetation on atmospheric chemistry, plant stomatal uptake, volatile organic compound (VOC) emissions and associated feedback mechanisms and enables a more detailed understanding of land–atmosphere interactions. Furthermore, the impact on the surface energy budget allows for a more consistent representation of chemical and transport processes in the atmospheric boundary layer. In Sect. 2, we give a short description of JSBACH and describe the coupling of EMAC and JSBACH via MESy, including the tuning of the newly coupled model. In Sect. 3, the evaluation variables and corresponding observation and reanalysis datasets are introduced. The results and the discussion of the corresponding evaluation are presented in Sect. 4.

2 Model description

2.1 JSBACH

In this work, we implemented the most recent version of JSBACH (JSBACHv4, Schneck et al., 2022). A detailed description of the parameterisations used in JSBACH can be found in Reick et al. (2013, 2021), while Schneck et al. (2022) present features of the version JSBACHv4 in comparison with the previous one (JSBACHv3) along with an assessment of the results of both versions. On the technical side, JSBACHv4 has been improved with modernised source codes and software infrastructure, while on the application side, it offers an improved soil scheme with a dynamic calculation of ground heat conductivity and capacity, taking phase change in water and organic fractions within soil layers into

account (Jungclaus et al., 2022; Schneck et al., 2022; Ekici et al., 2014). It provides a complex soil hydrological transport model that includes percolation and storage of water in several soil depths, reaching down to 9.8 m with increasing layer thickness of 0.065, 0.254, 0.913, 2.902 and 5.7 m for the first to the fifth layer, respectively. This gives a realistic estimate of soil desiccation and corresponding soil temperature and moisture. Additionally, the new version introduces a fractional lake mask, a three-layer snow scheme and the forest age structures (Schneck et al., 2022; de Vrese et al., 2021; Nabel et al., 2020). The implemented version of JSBACHv4 does not include the natural vegetation dynamics, land-use transitions and nitrogen cycle from JSBACH3. Those mechanisms have only recently been adopted in JSBACHv4 and will be added to MESSy in the near future. However, on the climate timescale, the interactions between climate and vegetation are already available in MESSy through the LPJ-GUESS interactive vegetation module (Vella et al., 2023a).

In the case of the ICON-Land infrastructure, a clear separation of the physical processes used in JSBACHv4 is allowed. The processes used in this study include the vegetation coverage, phenology and plant productivity (defined via gross primary productivity, GPP, and net primary productivity, NPP, and photosynthesis); a turbulence and radiation scheme; surface energy balance; and the exchange fluxes of heat and moisture, soil and vegetation carbon turnover, and disturbances due to wildfires or windthrow. The processes are listed in Table 1. In JSBACH, subgrid-scale heterogeneity is taken into account by a tile approach; i.e. grid boxes are divided into tiles associated with a specific land cover type (Reick et al., 2021). All available land cover types are listed in Table A1. The concept allows us to define processes specific to the different land cover types. For example, processes only related to vegetation (such as photosynthesis) are calculated only on vegetated tiles. Based on Reick et al. (2021), water, carbon, nitrogen, and area are conserved with numerical accuracy. Energy conversion is not fully achieved yet since the temperature of rainwater and heat produced by heterotrophic respiration are not accounted for (Reick et al., 2013, 2021).

To couple JSBACH with EMAC, it is implemented as a new submodel within the MESSy framework, following its well-described coding standards (Jöckel et al., 2010). Each process of the JSBACHv4 source code (listed in Table 1) is implemented as an individual Fortran module in the MESSy submodel core layer (SMCL) and complemented by a newly created submodel core layer file. A schematic overview of JSBACH as a new submodel in EMAC and corresponding process calls are given in the Supplement. In addition to the individual JSBACH processes, the file “*messy_jsbach.f90*” is created, which includes the definitions of land-cover specifications (originally taken from *lctlib_nlct21.def*), the tile aggregation subroutines and the subroutine to read the JSBACH namelist. The namelist (*jsbach.nml*) serves as a user interface, where input and coupling variables are specified. The full namelist is available in the Supplement; the cou-

pled variables are listed from line 152 to 206 of the namelist. Parameters can be defined, and logical switches to modify and adjust the simulation can be set. The module subroutines are called from a newly created JSBACH interface (*messy_jsbach_si.f90*), which is implemented in the MESSy submodel interface layer (SMIL). Besides the process calls, the interface includes the creation of new “representations” to expand the EMAC model grid to new dimensions, for soil, snow and canopy layers and vegetation tiles, and the JSBACH output variables are saved as new “channel objects”. Both representations and channel objects are elements defined in the submodel CHANNEL, which handles the memory, data output (including checkpointing) and internal data exchange (Jöckel et al., 2010).

JSBACH was chosen as the LSM for EMAC since it has already been successfully implemented and tested in other models like the Icosahedral Nonhydrostatic Earth System Model (ICON-ESM) and its predecessor (JSBACH3) in the Max Planck Institute Earth System Model, MPI-ESM 1.2 (Mauritsen et al., 2019), which took part in the Coupled Model Intercomparison Project phases 5 and 6 (Giorgetta et al., 2013). Furthermore, in JSBACH, specific ecosystem processes, like carbon cycling, are included. Those mechanisms will, in combination with an atmospheric chemistry model, provide new and interesting insights into the interactions and feedback mechanisms between vegetation and atmospheric composition. The combination of EMAC and JSBACH makes it possible to analyse biogeochemical processes at various spatial and temporal resolutions, from small-scale experiments of local sub-daily effects to global-scale climate change experiments, in contrast to the coupling of the dynamic vegetation model LPJ-GUESS to EMAC (Forrest et al., 2020), in which the vegetation–atmosphere coupling is restricted by the diurnal time step of the vegetation scheme.

2.2 The EMAC model

The ECHAM/MESSy Atmospheric Chemistry (EMAC) model is a numerical chemistry and climate simulation system that includes submodels describing tropospheric and middle-atmosphere processes and their interaction with oceans, land and human influences (Jöckel et al., 2010). It uses the second version of the Modular Earth Submodel System (MESSy2) to link multi-institutional computer codes. The core atmospheric model is the fifth-generation European Centre Hamburg general circulation model (ECHAM5; Roeckner et al., 2006). The physics subroutines of the original ECHAM code have been modularised and reimplemented as MESSy submodels and have continuously been further developed. Only the spectral transform core, the flux-form semi-Lagrangian large-scale advection scheme, and the nudging routines for Newtonian relaxation remain from ECHAM. Further details on EMAC are documented by Jöckel et al. (2016) and can be found on the MESSy web-

Table 1. JSBACH file overview.

JSBACH process	MESSy filename (SMCL)	Short description
Fuel	<i>messy_jsbach_fuel.f90</i>	Availability of carbon fuel to wildfires.
Disturbance	<i>messy_jsbach_dist.f90</i>	Carbon relocation due to windthrow and vegetation fires.
Phenology	<i>messy_jsbach_pheno.f90</i>	Leaf area index and foliage projected cover.
Hydrology	<i>messy_jsbach_hydro.f90</i>	Soil hydrology.
Surface energy balance	<i>messy_jsbach_seb.f90</i>	Surface latent and sensible heat fluxes.
Snow and soil energy	<i>messy_jsbach_sse.f90</i>	Soil characteristics and ground heat fluxes.
Turbulence	<i>messy_jsbach_turb.f90</i>	Surface roughness affecting the distribution of surface fluxes.
Carbon	<i>messy_jsbach_carb.f90</i>	Carbon pools above and below ground.
Assimilation	<i>messy_jsbach_assim.f90</i>	Net primary productivity (NPP) and carbon assimilation.
Radiation	<i>messy_jsbach_rad.f90</i>	Surface albedo and light absorption in canopy.
JSBACH LCT library	<i>messy_jsbach_lctlib.f90</i>	JSBACH land cover type (LCT) library.
Core file (SMCL)	<i>messy_jsbach.f90</i>	JSBACH core file for MESSy.
Interface (SMIL)	<i>messy_jsbach_si.f90</i>	Interface for MESSy.
Namelist	<i>jsbach.nml</i>	User interface.

site (<https://www.messy-terrace.org>, last access: 12 October 2023).

2.3 Parameter optimisation

JSBACH is an alternative to the standard submodel used, SURFACE. In the case JSBACH is used, the SURFACE submodel must be switched off. Using JSBACH, a more complex scheme for land temperature and hydrology is adopted, and with that, the dynamical lower-boundary conditions of ECHAM5 are modified. Since the EMAC dynamics were optimised for the specific combination of ECHAM5 and SURFACE (Kern, 2013), the new combination of ECHAM5 and JSBACH requires a refined parameter optimisation (“re-tuning”), with respect to radiation balance, land surface temperature and clouds. Such a parameter optimisation is generally performed to adjust the model results to be as close as possible to observations and to prevent the model climate from drifting, for example, due to a large radiative imbalance. It is achieved by small variations in specific parameters for processes with a high degree of uncertainty or a high level of parameterisation, such as the ones related to clouds and convection. A more detailed description of the optimisation process is provided by Mauritsen et al. (2012). The five parameters optimised in this study are the correction factor for asymmetries of ice clouds (*zasic*), the homogeneity factors for ice and liquid water clouds (*zinhomi* and *zinhoml*), the convective mass flux at the level of neutral buoyancy (*cmfctop*), and the conversion factor from cloud water to rain (*cpcon*; in $\text{s}^2 \text{m}^{-2}$). Simulations for the same period from 1990 to 2010 were carried out with gradually changing parameters. The simulation using JSBACH based on the default parameters is from now on referred to as CTRL. The climatically optimised simulation is from here on referred to as EMAC/JSBACH, while the simulation without JSBACH (and with SURFACE

activated instead) is referred to as EMAC/SRF. The simulations with the according parameter setups are listed in Table S2 in the Supplement (simulations 2 and 31 were not completed due to server failures and were excluded from the analysis). Subsequently, the global and temporal averages of LST; top-of-atmosphere (TOA); and surface (SRF) radiation including net, solar and terrestrial parts; heat flux including net, sensible and latent parts; total column fractional cloud coverage; total column cloud liquid and ice water content; and TWS are calculated and compared to ERA5 and ERA5-Land monthly averaged data (Muñoz Sabater, 2019). Additionally, the global and temporal average of precipitation is compared to the Global Precipitation Climatology Project (GPCP) monthly precipitation dataset (Adler et al., 2003). These datasets are from here on referred to as reference data REF. The results of the global and time averages of the previously mentioned parameters for each simulation are listed in Table S3 in the Supplement. The corresponding RMSE and NRMSE (RMSE normalised by the range of the reference data) are shown in Table S4 in the Supplement. The criteria used for the selection of the optimised tuning parameters were, on the one hand, the smallest deviation from the reference data paired with the lowest normalised root mean square error (NRMSE) sum and, on the other hand, the change in as few parameters as possible to stay as close as possible to the tuning of EMAC/SURF. The sets of parameters of CTRL and EMAC/JSBACH are listed in Table 2. As shown here, only one parameter needed to be adjusted via the replacement of the calculation of *zinhoml* dependent on model level (*lev*) and liquid water path (*lwp*) by a constant value of 0.92. The default value of *zinhoml* is calculated based on Eqs. (11.52)–

(11.53) in Roeckner et al. (2003), viz.

$z_{\text{inhoml}}_{\text{default}} =$

$$\begin{cases} (\sum_0^{\text{nlev}} I_{\text{wp}\partial\text{lev}})^{-0.1} & \text{if } (\sum_0^{\text{nlev}} I_{\text{wp}\partial\text{lev}}) > 1, \\ 1 & \text{otherwise,} \end{cases} \quad (1)$$

with nlev being the number of model levels.

The temporally and spatially averaged results of REF, EMAC/SRF, CTRL and EMAC/JSBACH are shown in Table 3, with values that could be improved with respect to CTRL indicated in bold.

3 Evaluation

3.1 Model setup

For the present study, we applied EMAC (MESSy version 2.55.0) at the T63L31ECMWF resolution, i.e. with a spherical truncation of T63 (corresponding to a quadratic Gaussian grid of approx. 1.8° by 1.8° spacing in latitude and longitude), with 31 vertical hybrid pressure levels up to 10 hPa. An overview of the submodels used in the reference simulation EMAC/SRF is given in Table 4 along with a brief description of each. In the simulation EMAC/JSBACH, the submodel SURFACE is replaced by the new submodel, JSBACH, and the tuning parameters are updated, while the remaining setup is unchanged. Both simulations were performed from January 1970 to January 2011 and include tracer nudging of CO_2 , CH_4 , N_2O , CFC11 and CFC12 based on tracer profiles derived from Atmospheric Chemistry and Climate Model Intercomparison Project (ACCMIP) historical lower-boundary condition datasets (Lamarque et al., 2010, 2013). JSBACH is operated on three snow layers, three canopy layers and five soil layers, reaching a depth of 9.8 m below the surface. From 21 possible land cover types (LCTs), 11 plant functional types (PFTs) are taken into account for the standard tile setup (Table A1 in the Appendix). Those are tropical and extra-tropical broadleaf evergreen and deciduous trees, raingreen shrubs, deciduous shrubs, C_3 and C_4 grass, C_3 and C_4 pasture, and C_3 and C_4 crops. This evaluation focuses only on the dynamical coupling between EMAC and JSBACH; thus, all calculations of atmospheric chemistry and the O-GCM are deactivated. Aerosol concentrations are prescribed for all simulations based on Tanré et al. (1997). A list of all coupled variables can be found in the namelist attached in the electronic Supplement. Coupled variables include surface temperature, latent and sensible fluxes, ground heat fluxes, soil water content, surface albedo, and specific humidity at the lowest atmospheric level. Atmospheric Model Intercomparison Project (AMIP)-type simulations were performed with prescribed monthly sea surface temperature and sea ice concentration to identify systematic errors in the model (Gates et al., 1999). The sea surface temperature and ice concentration are based on ERA5 6-hourly data from 1940 to present

(Hersbach et al., 2020) and are the same for all performed simulations. JSBACH was initialised with carbon pool, soil and land property data from the year 2005 (in the Supplement), which are estimated to stabilise within 5 years. This is possible since we perform AMIP-type simulations in which the land–carbon interaction remains inactive. Atmospheric variables stabilise within days, and the soil moisture is estimated to be the slowest variable to adjust to equilibrium, with a maximum adjustment time of 1 year (Hagemann and Stacke, 2015; Schneck et al., 2022). Therefore, the first year (1970) is considered the spin-up time and is not taken into account for the evaluation.

3.1.1 Evaluation variables and reference datasets

The selected variables to be assessed are variables representing not only the land surface, like land surface temperature (LST), terrestrial water storage (TWS) and surface albedo (α), but also other atmospheric variables, like precipitation (precip), top-of-atmosphere radiation balance (Rad_{TOA}), fraction of absorbed photosynthetic active radiation (FAPAR), leaf area index (LAI) and gross primary productivity (GPP), in line with the study of Schneck et al. (2022). These variables are compared either to ERA5/ERA5-Land reanalysis datasets or directly to observational datasets of the GPCP or MODIS satellite data (Table 5). The ERA5/ERA-Land reanalysis data are a combination of synthesised estimates of the climate state, which are calculated based on as many observations as possible, and a numerical model due to either direct assimilation of the observations or forcings (Muñoz Sabater, 2019). A comprehensive overview of the limitations and uncertainties in the MODIS data is provided by Disney et al. (2016). The MODIS standard deviations of LAI, FAPAR and GPP are displayed in the Appendix (Figs. A2, A3 and A4) together with the GPCP precipitation error (Fig. A1).

4 Results and discussion

To get an overview of the model performance compared to the reference data, their statistical metrics of the monthly and globally averaged results are presented in Fig. 1 as a Taylor diagram (Taylor, 2001). For the classification of the results of the coupled model, the statistical measures of the model results without the coupling to JSBACH are added. Results of the EMAC/JSBACH are shown as dots, while the results of the EMAC/SRF simulation are displayed as crosses. The Taylor plot shows the Pearson correlation coefficient between simulated and reference data on straight lines stemming from the origin, with arcs around the origin indicating the standard deviation normalised by the reference standard deviation and arcs around the value of 1 indicating the root mean square error normalised by the range of the reference data (NRMSE). The Pearson correlation coefficient (r) and

Table 2. List of the optimised parameters of the simulation without JSBACH (EMAC/SRF), the control simulation including JSBACH (CTRL) and the simulation best fitting the requirements (EMAC/JSBACH).

Parameter (default)	zasic (0.85)	zinhomi (0.85)	zinhoml (zinhoml _{default} ; Eq. 1)	cmfctop (0.3)	cprcon ($\times 10^{-4} \text{ s}^2 \text{ m}^{-2}$) (1)
EMAC/SRF	default	default	default	default	default
CTRL	default	default	default	default	default
EMAC/JSBACH	default	default	0.92	default	default

Table 3. Table of the temporally and globally averaged results, with inter-annual variability as the standard deviation of CTRL, EMAC/SRF and EMAC/JSBACH from 1990 to 2010. The corresponding reanalysis or observational results are listed as REF. For precipitation, REF refers to the GPCP monthly precipitation dataset (Adler et al., 2003), while for the remaining variables, REF refers to ERA5 and ERA5-Land reanalysis datasets (Hersbach, 2023; Muñoz Sabater, 2019, 2021). TOA_{net} refers to the sum of shortwave (TOA_{sw}) and longwave (TOA_{lw}) top-of-atmosphere radiation flux, while SRF_{*} refers to the same at surface level. HFLX_{net} refers to the sum of the sensible (HFLX_{sensible}) and latent (HFLX_{latent}) heat fluxes. Clouds are assessed based on the accumulated cloud cover (ACLC), the liquid water content (LWC) and the ice water content in clouds (IWC).

Run	LST [K]	TOA _{net} [W m ⁻²]	TOA _{sw} [W m ⁻²]	TOA _{lw} [W m ⁻²]	SRF _{net} [W m ⁻²]
	282.25 ± 0.27	0.45 ± 0.65	242.67 ± 0.65	-242.22 ± 0.29	105.91 ± 0.45
EMAC/SRF	283.09 ± 0.27	3.56 ± 0.39	234.33 ± 0.27	-230.77 ± 0.34	107.92 ± 0.24
	280.66 ± 0.26	6.61 ± 0.5	237.22 ± 0.3	-230.61 ± 0.42	108.08 ± 0.28
EMAC/JSBACH	280.48 ± 0.23	3.23 ± 0.38	233.86 ± 0.29	-230.63 ± 0.38	104.43 ± 0.3
Run	SRF _{sw} [W m ⁻²]	SRF _{lw} [W m ⁻²]	HFLX _{net} [W m ⁻²]	HFLX _{sensible} [W m ⁻²]	HFLX _{latent} [W m ⁻²]
	163.76 ± 0.54	-57.85 ± 0.31	-69.92 ± 0.57	-28.15 ± 0.68	-41.76 ± 0.43
EMAC/SRF	161.74 ± 0.31	-53.83 ± 0.3	-104.24 ± 0.35	-16.74 ± 0.18	-87.5 ± 0.42
	165.97 ± 0.36	-57.88 ± 0.35	-110.92 ± 0.65	-11.59 ± 0.15	-99.33 ± 0.6
EMAC/JSBACH	162.14 ± 0.34	-57.71 ± 0.35	-110.47 ± 0.67	-11.67 ± 0.14	-98.79 ± 0.61
Run	Precip [mm d ⁻¹]	ACLC	LWC [kg m ⁻²]	IWC [kg m ⁻²]	TWS [m]
	2.7 ± 0.03	0.553 ± 0.00405	0.04707 ± 0.00098	0.02166 ± 0.00033	1.06012 ± 0.00947
EMAC/SRF	2.83 ± 0.02	1.06067 ± 0.00444	0.10394 ± 0.00115	0.04972 ± 0.00068	0.34995 ± 0.00425
	2.77 ± 0.02	0.6462 ± 0.0025	0.09594 ± 0.00114	0.04945 ± 0.00067	1.00362 ± 0.00761
EMAC/JSBACH	2.76 ± 0.02	0.6464 ± 0.0028	0.09519 ± 0.0009	0.04936 ± 0.00054	1.00385 ± 0.00815

NRMSE are listed in Table 6, together with the weighted global average, with standard deviations for the model simulations ($\overline{\text{MOD}}$) and reference data ($\overline{\text{REF}}$). The correlation and NRMSE are based on monthly averages for the available time period of the reference datasets, with the correlation conducted over time and location (see Table 6). This covers the years 1971–2010 for LST, Rad_{TOA}, α and TWS. Precipitation is analysed for the period 1980–2010 and LAI, FAPAR and GPP for 2000–2010.

LST has the highest correlation with REF – namely 0.985 for EMAC/JSBACH and 0.989 for EMAC/SRF – whereas the global average EMAC/JSBACH LST is, on average, 1.546 K colder than REF and EMAC/SRF and 0.816 K warmer than REF (see Fig. 1 and Table 6). The second-

highest correlation between REF and the model simulations is found for the surface albedo (shown in black in Fig. 1) is 0.947 for EMAC/JSBACH and 0.944 for EMAC/SRF. Also for this parameter, EMAC/JSBACH has a slightly lower global average than REF, with an average difference of -0.015, and EMAC/SRF differs by -0.013 from the global average. The third-highest correlation is found for Rad_{TOA} (shown in orange in Fig. 1) and is 0.907 for EMAC/JSBACH compared to REF and 0.909 for EMAC/SRF compared to REF. The net radiative flux at the top of the atmosphere (TOA) between EMAC/JSBACH and REF differs by 3.56 and 3.045 W m⁻² from EMAC/SRF. FAPAR (shown in yellow in Fig. 1) is only available for the EMAC/JSBACH simulation, with a correlation of 0.663 with REF.

Table 4. List of the submodels comprising the EMAC/SRF simulation including short description and reference.

Process submodels	Short description	Reference
AEROPT	Calculation of aerosol optical properties	Dietmüller et al. (2016)
CLOUD	ECHAM5 cloud scheme as MESSy submodel	Roeckner et al. (2006); Tost (2023)
CLOUDOPT	Calculation of cloud optical properties.	Dietmüller et al. (2016)
CONVECT	Convection parameterisations	Tost et al. (2006)
E5VDIFF	Land–atmosphere exchange and vertical diffusion based on ECHAM5	MESSy (2023a); Roeckner et al. (2003)
GWAVE	ECHAM5 non-orographic gravity wave routines plus additional drag parameterisations	MESSy (2023a); Hines (1997)
HD	Hydrological discharge model for present-day rivers	Pozzer et al. (2011a)
TNUDGE	Newtonian relaxation of species as pseudo-emission	Kerkweg et al. (2006)
ORBIT	Calculation of orbital parameters of the Earth's orbit around the Sun	Dietmüller et al. (2016)
OROGW	Parameterisation of drag due to subgrid-scale orography blocking and orographic gravity wave forcing	Chap. 7 of Roeckner et al. (2003)
PTRAC	User-defined initialised prognostic tracers	Jöckel et al. (2008)
RAD	ECHAM5 radiation code with extended features	Dietmüller et al. (2016)
SURFACE	Modularised version of the ECHAM5 subroutines SURF, LAKE, LICETEMP and SICETEMP	Chap. 6 of Roeckner et al. (2003)

Table 5. Table of the evaluation variables, the corresponding reference dataset and the time period of the evaluation analysed.

Variable	Dataset	Time period	Reference
LST	ERA5-Land monthly averaged data from 1950 to the present	1971–2010	Muñoz Sabater (2019)
TWS			
Surface albedo			
Rad _{TOA}	ERA5 monthly averaged data from 1940 to the present	1971–2010	Hersbach et al. (2023)
Precipitation	GPCP monthly precipitation dataset from 1979 to 2021	1980–2010	Adler et al. (2003)
LAI	MOD15A2H MODIS/Terra Leaf Area Index/FPAR 8-Day L4 Global 500m SIN Grid V061 regridded to global data at 0.5 resolution derived by ICDC	2000–2010	Kern (2023); Myneni (2021)
FAPAR			
GPP	MOD17A2H MODIS/Terra gross primary productivity 8-Day L4 Global 500m SIN Grid V006 regridded to global data at 0.5 resolution derived by ICDC	2000–2010	Kern (2021); Running et al. (2015)
Further datasets used for LST evaluation			
HFLX _{latent}	ERA5-Land monthly averaged data from 1950 to the present	1971–2010	Muñoz Sabater (2019)
Evaporation	ERA5 monthly averaged data from 1940 to the present	1971–2010	Hersbach et al. (2023)

The global average difference is 0.223. The correlation of simulated and observed LAI (shown green in Fig. 1) is 0.637 for the EMAC/JSBACH simulation and 0.864 for the climatology used in EMAC/SRF. EMAC/JSBACH underestimates the global vegetation LAI by 0.212, while the EMAC/SRF climatology overestimates LAI by 0.768. As for FAPAR, GPP (shown in dark green in Fig. 1) is only available for EMAC/JSBACH, leading to a correlation with REF of 0.564, with an average global difference to REF of $-0.001 \text{ kg carbon km}^{-2}$. The correlation between simulated precipitation (shown in dark blue in Fig. 1) and REF is 0.523 for EMAC/JSBACH and 0.614 for EMAC/SRF.

EMAC/JSBACH overestimates the global mean precipitation by 0.042 mm d^{-1} and EMAC/SRF does the same by 0.316 mm d^{-1} . The lowest correlation between model results and reference data is found for TWS (shown in light blue in Fig. 1). EMAC/JSBACH and REF correlate with a value of 0.223, while EMAC/SRF and REF correlate with 0.257. EMAC/JSBACH overestimates the mean global TWS by 0.029 m, and EMAC/SRF underestimates it by 0.69 m.

For a more comprehensive assessment, in the following subsections, each variable derived from the new coupled model is evaluated individually via comparison to the reference dataset and the EMAC/SRF simulation. Monthly aver-

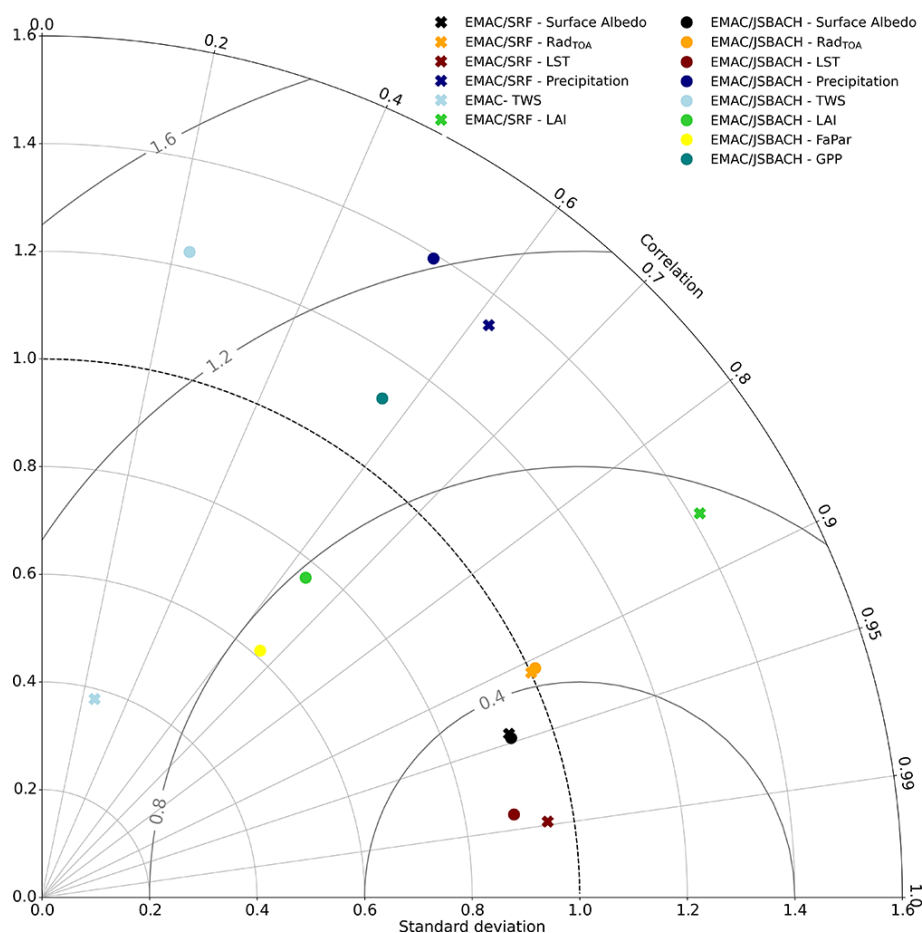


Figure 1. Taylor plots of the Pearson correlation coefficient; root mean square error (RMSE); and standard deviation normalised with the reference data standard deviation of monthly means of LST (1971–2010), Rad_{TOA} (1971–2010), surface albedo (1971–2010), precipitation (1980–2010), TWS (1971–2010), LAI (2000–2010), FAPAR (2000–2010) and GPP (2000–2010). The statistical measures of the EMAC/JSBACH are displayed as dots, while the EMAC/SRF values are shown as crosses. As EMAC does not provide FAPAR and GPP output; both are only shown for the EMAC/JSBACH simulation. Straight lines from the origin represent the correlations, while the arcs around the origin represent the standard deviations. The arcs around the value 1 on the horizontal axis show the RMSE normalised to the standard deviation. The correlation and RMSE are based on monthly average values, with the correlation conducted over time and location.

ages over the corresponding analysis period were calculated and, subsequently, the average values for the spring and summer months (March, April, May, June, July and August) and the autumn and winter months (September, October, November, December, January and February) were determined. The same was done for the MODIS, GPCP and ERA5 datasets.

4.1 Land surface temperature (LST)

The land surface temperature is one of the main drivers in determining the habitat conditions for the vegetation and living organisms in ecosystems. It is one of the most important drivers of all land processes as it controls the surface energy and radiation balance as well as the hydrological and thermal exchange fluxes between the surface and the atmosphere. Furthermore, it determines the freezing and thawing of the snow and ice covers. It is the upper-boundary condi-

tion for the soil temperature calculation within the five-layer soil scheme and one of the lower-boundary conditions for EMAC. LST is calculated in JSBACH via the surface energy balance equation and the values for saturated humidity and dry static energy based on the Richtmyer–Morton coefficients derived from the vertical diffusion scheme of ECHAM (Reick et al., 2021). Here, LST is compared with monthly averaged reanalysis data from ERA5-Land, available for the period from 1950 to the present (Muñoz Sabater, 2019), with only the simulated years (1971–2010) included in the comparison. The ERA5-Land dataset is provided at a 0.1° -by- 0.1° spatial resolution and is interpolated into the T63L31 EMAC output grid.

The geographical distribution of the LST difference between ERA5 and EMAC/JSBACH is shown in Fig. 2. Figures 3 and 4 show the LST time series and seasonality analysis and Fig. 5 shows the LST seasonality and correspond-

Table 6. Summary of the comparison between model results and reference data. The Pearson correlation coefficient is listed as r , and NRMSE shows the root mean square error normalised by the range of the reference data. The simulations were performed at T63L31 resolution and with a model time step of 600 s. The columns MOD and REF are the weighted global averages, with the standard deviation of the model simulation results and the reference data.

Variable	Period	r	NRMSE	MOD	REF
EMAC/JSBACH vs. REF					
LST [K]	1971–2010	0.985	0.045	280.434 ± 23.207	281.98 ± 26.258
TWS [m]	1971–2010	0.223	0.18	1.123 ± 0.701	1.094 ± 0.552
Surface albedo	1971–2010	0.947	0.127	0.301 ± 0.268	0.316 ± 0.292
Rad _{TOA} [W m^{-2}]	1971–2010	0.907	0.099	3.948 ± 65.664	0.388 ± 62.201
Precipitation [mm d^{-1}]	1980–2010	0.523	0.083	2.738 ± 2.479	2.696 ± 1.78
LAI	2000–2010	0.637	0.175	1.187 ± 1.049	1.399 ± 1.257
FAPAR	2000–2010	0.663	0.271	0.161 ± 0.137	0.384 ± 0.196
GPP [kg carbon km^{-2}]	2000–2010	0.564	0.203	0.02 ± 0.017	0.021 ± 0.013
EMAC/SRF vs. REF					
LST [K]	1971–2010	0.989	0.037	282.796 ± 24.933	281.98 ± 26.258
TWS [m]	1971–2010	0.257	0.211	0.404 ± 0.202	1.094 ± 0.552
Surface albedo	1971–2010	0.944	0.129	0.303 ± 0.267	0.316 ± 0.292
Rad _{TOA} [W m^{-2}]	1971–2010	0.909	0.098	3.434 ± 65.327	0.388 ± 62.201
Precipitation [mm d^{-1}]	1980–2010	0.616	0.074	3.025 ± 2.186	2.696 ± 1.78
LAI (climatology)	2000–2010	0.864	0.263	2.165 ± 1.945	1.399 ± 1.257

ing latent heat flux at the surface separated for three climate zones. The polar zone is defined as latitudes over 66.5° , the temperate zone as latitudes between 40° and 66.5° , and the tropical and subtropical zones as latitudes under 40° . As shown in Fig. 2, the EMAC/JSBACH LST is lower than REF everywhere throughout the year except for the polar regions, the Himalaya and over the Amazon Basin. The largest LST underestimations are found over the Rocky Mountains and the Taklamakan and Gobi deserts, being most pronounced in the Northern Hemispheric summer. The largest overestimation of LST occurs over the Antarctic Ross Ice Shelf (up to 20 K); along the coast of the Greenland Sea (up to 15 K); and in the Hindu Kush, Himalayan, Kunlun and Tien Shen mountain ranges (up to 15 K). As result, the zonal mean shows a slightly warmer surface in the polar regions and a colder surface in the subtropics and temperate zones. In the temporal and global average, the LST of EMAC/JSBACH is 1.546 K colder compared to the reanalysis data. The general trend of steadily increasing LST is reproduced by EMAC/JSBACH (Fig. 3). Nevertheless, in both the time series analysis and seasonality analysis, the overall difference of 1.546 K between EMAC/JSBACH and ERA5 LSTs is clearly visible. When comparing the geographical difference between EMAC/SRF and ERA5 LSTs, as displayed in Fig. 2, overestimations of the LST are found over the Antarctic Ross Ice Shelf, along the coast of the Greenland Sea, and over the same mountain ranges as previously found for the EMAC/JSBACH results. Here, too, are the polar regions in general warmer than indicated by ERA5. Overall, the LST derived from EMAC/SRF is 0.743 K warmer than the reanal-

ysis data. This is also visible in the trend analysis, which shows the overall warmer global land surface of EMAC/SRF in comparison to ERA5. In the zonal mean, the differences largely cancel out, leading to a similar zonal progression of the EMAC/SRF results compared to the ERA5 LST.

Comparing EMAC/JSBACH and the ERA5 LST, larger differences than 1.546 K are found for the tropics/subtropics and temperate zone (latitudes $> 66.5^\circ$), while in the polar climate zone, the LST is overestimated in the EMAC/JSBACH and the EMAC/SRF simulation, as shown in Fig. 5. The lower LST of EMAC/JSBACH compared to EMAC/SRF in non-polar regions can be explained by variations in the latent heat flux, where EMAC/JSBACH simulated consistently higher values than EMAC/SRF. Here, the main driver is evapotranspiration, the process by which water vapour is released from the surface and vegetation. Evapotranspiration, the sum of evaporation and transpiration, has, in general, a cooling effect on the evaporating surface due to energy absorption during the phase change in water. Figure 5 displays, besides LST and latent heat flux, the surface evaporation, which is strongest in the tropics and subtropics. This is in line with cooler LST values in those regions. The partially overestimated TWS (Sect. 4.2) could be the cause of the stronger latent heat flux, as more water is available for evaporation. As the moisture content of the soil in EMAC/JSBACH is, in general, much larger than in EMAC/SRF, increased evaporation in the coupled simulation is plausible. In the polar regions, where vegetation is sparse or absent, the difference in latent heat flux between EMAC/JSBACH and EMAC/SRF is less significant, as shown in Fig. 5, resulting in less variation in

the LST between simulations. The strong overestimation of LST along the Antarctic coast is visible in both simulations and might be an artifact of sea ice occurrence and the variability of snow and ice cover. Despite local variations, the overall temporal and spatial correlation between EMAC/JSBACH and ERA5 is large (0.985; Table 6), indicating that LST is, in general, realistically reproduced and that the representations of seasonal patterns and overall trends are plausible.

4.2 Terrestrial water storage (TWS)

The variation in soil depth of the reanalysis data and the model datasets complicates direct comparisons of the soil water content per layer. To overcome this problem, TWS is chosen as the evaluation variable. TWS is defined as the vertically integrated water content on land and the subsurface, including groundwater, rivers, lake water, soil moisture (also in the root zone), snow and ice (including permafrost), wet biomass, and water stored in vegetation (Giroto and Rodell, 2019). It depends on the amount of precipitation and the air temperature as well as on the soil type and infiltration, vegetation cover, surface and soil temperature, and runoff (Schneek et al., 2022).

For this assessment, however, we exclude water that drains from the land surface into rivers, streams or other waterbodies in order to focus only on the part of the water that is stored in the soil and vegetation. The TWS therefore includes all the water stored in a grid box; this total amount of water is comparable between the models and reanalysis.

In EMAC/JSBACH, the TWS is the sum of water content and runoff, calculated separately. The water content is calculated as the sum of all water reservoirs above and below ground, down to the bedrock. Everything below the bedrock, like deep groundwater and aquifers, is not represented in JSBACH and thus not taken into account (Reick et al., 2021). In EMAC/JSBACH, the soil water column is segmented into five layers, with a maximum depth of 9.834 m. The above-groundwater includes the wet skin reservoir (water on the canopy and surface) and snow on canopy and surface, both depending on and exchanging moisture between surface and atmosphere via precipitation, evaporation, sublimation, melting and windblow. TWS does not include any fluxes (such as evaporation). Water infiltrating the ground either percolates by gravitational movement (ending up as drainage if it reaches bedrock) or diffuses. Depending on its phase, it is defined as one of the EMAC/JSBACH below-groundwater reservoirs: soil moisture or soil ice. At the surface, the moisture exchange with the atmosphere occurs through evapotranspiration, dew formation or evaporation of bare soil, controlled by the specific humidity and temperature of the surrounding air. Furthermore, these processes strongly depend on vegetation coverage and, with that, plant productivity, which is also assessed via the gross primary productivity (GPP) (Sect. 4.8). TWS is compared to the ERA5-

Land TWS, derived as the sum of the integrated volumetric soil water content, skin reservoir content and snow depth in metres water equivalent. The ERA5 soil water column is distributed over four layers, with a maximum depth of 2.89 m. Here, too, is the ERA5 dataset interpolated into the EMAC grid. Since TWS is not calculated for glaciers within EMAC/JSBACH, glaciated polar areas are excluded from this analysis.

In Fig. 6, the difference in TWS between EMAC/JSBACH and EMAC/SRF to ERA5 is shown. The annual global average of EMAC/JSBACH TWS weighted by latitudes is 0.029 m larger than the global mean of the ERA5. The maximum overestimation of TWS is found in western Russia (up to 3.0 m). EMAC/JSBACH overestimates TWS almost everywhere, independent of the season, except for high, elevated regions such as the Tibetan Plateau and Tien Shen, central and eastern Siberia, India (Deccan Plateau), the Ethiopian highlands, and Patagonia. Additionally, TWS is underestimated in the Amazon Basin.

The zonal mean of the EMAC/JSBACH TWS, as shown in Fig. 6 (right panels), does not exactly reproduce the zonal mean of the TWS from ERA5, but its absolute values are in better agreement with the ERA5 data than the EMAC/SRF results. This is also visible in Fig. 7, where the globally averaged TWS time series is illustrated. Since there are no snow cover data available from ERA5-Land for the year 1974, this year was excluded from the analysis. The TWS of the EMAC/SRF simulation (Fig. 6) is lower everywhere compared to the ERA5 dataset, except for deserts, where the TWS is low anyway. This leads to an annual global average of the EMAC/SRF TWS of 0.404 ± 0.202 m, which is different by -0.69 m than the one derived from reanalysis data (see Table 6). In EMAC/JSBACH, the global average of TWS is 1.123 ± 0.701 m, which is, with a difference of 0.029 m, significantly closer to ERA5 (1.094 ± 0.552 m).

The soil hydrology module that comes with EMAC/JSBACH offers the possibility of improving the representation of the soil water. The soil moisture in EMAC/SRF was simulated based on a simple bucket model. Following Seneviratne et al. (2010), this is now replaced by a more complex five-layer diffusive hydrological transport model that includes water storage and infiltration in five soil layers, preventing soil from drying too rapidly. While EMAC/SRF tends to strongly underestimate soil moisture levels everywhere, the integration of JSBACH results in larger and more spatially diverse soil moisture content. However, de Vrese et al. (2023) found that in the JSBACH version used here, infiltration only takes place if the temperature of the first soil layer is at or above the melting point. In combination with the five-layer snow scheme presented by Ekici et al. (2014), this becomes problematic. During spring snowmelt, soil temperatures are below the 0°C of the overlying snow cover, causing all the meltwater to run off at the surface, while, in reality, a considerable amount should percolate into the soil (de Vrese et al., 2023). This contributes to the strong under-

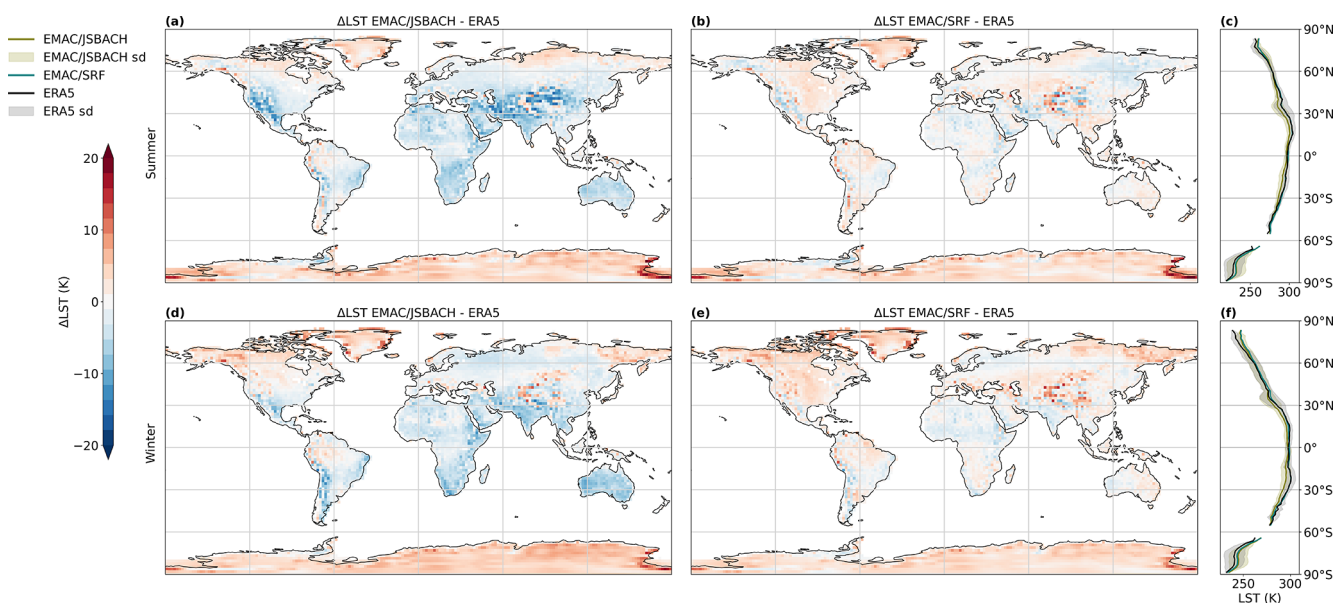


Figure 2. Difference in land surface temperature (LST) between EMAC/JSBACH and ERA5-Land during Northern Hemispheric (NH) summer (a) and NH winter (d) months, with data averaged over the years 1971 to 2010. Analogously, the difference between EMAC/SRF and ERA5-Land LST during summer (b) and winter (e) months is displayed. Positive values represent an overestimation of the simulated LST, while negative values indicate an underestimation. Additionally, the zonal average of all three datasets for both summer (c) and winter (f) months is shown. Here, LST from EMAC/JSBACH is depicted in green, LST from EMAC/SRF is shown in blue and LST from the ERA5-Land dataset is represented in black. The shaded area within the zonal mean plot illustrates the standard deviations along longitudes.

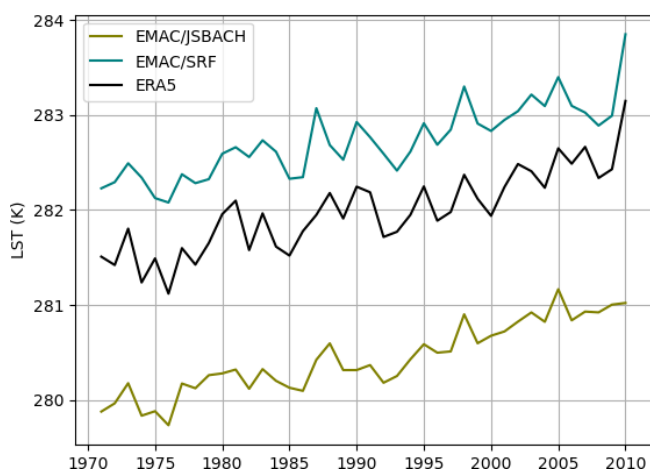


Figure 3. Globally averaged LST time series (in K) of EMAC/JSBACH (green), EMAC/SRF (blue) and ERA5 (black).

estimation of TWS in permafrost regions, e.g. Siberia. Despite this, the global average time series analyses show that EMAC/JSBACH TWS aligns much more closely with the TWS from the ERA5 reanalysis compared to the EMAC/SRF results (Fig. 7).

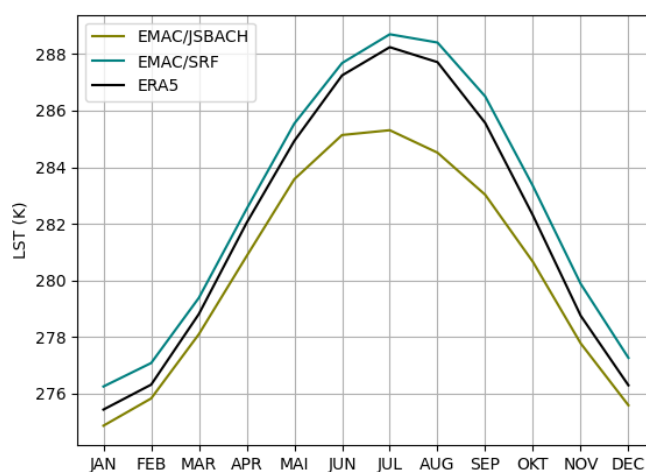


Figure 4. Globally averaged seasonal LST (in K) of EMAC/JSBACH (green), EMAC/SRF (blue) and ERA5 (black) for the years 1971 to 2010.

4.3 Surface albedo (α)

Another key factor in Earth system modelling is the surface albedo as it is a fundamental input for the radiation scheme and strongly influences the energy budget of the planet. Generally defined as the reflected fraction of incoming solar radiation, it depends on the type of land cover and the extent and thickness of the snow cover or ice sheet. Especially over

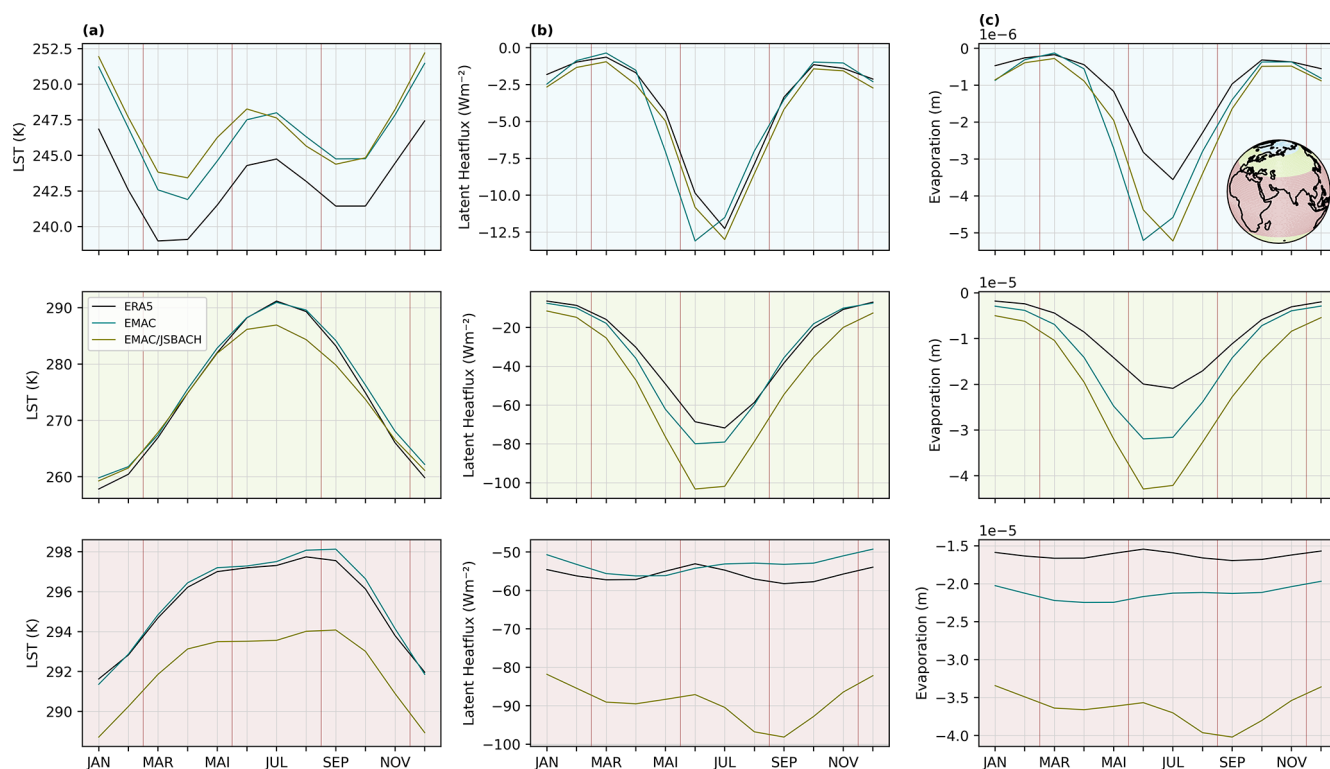


Figure 5. Averaged seasonal LST (in K), surface latent heat flux (in W m^{-2}) and evaporation (without transpiration) (in m) of EMAC/JSBACH (green), EMAC/SRF (blue) and ERA5 (black) for the years 1971 to 2010. The upper panels indicate values averaged over the polar climate zone (latitudes $> 66.5^\circ$), the mid panels values averaged over the temperate climate zone (latitudes between 40° and 66.5°) and the bottom panels values averaged over the tropical and subtropical climate zones (latitudes $< 40^\circ$).

the continental area of the Northern Hemisphere and the sea ice cover in the Southern Hemisphere, the surface albedo can exert a strong feedback effect (Hall, 2004). Since the surface coverage of snow and ice can vary on small scales and is strongly coupled to atmospheric and oceanic dynamics, the computation of the surface albedo is still a challenging factor for GCMs (Bony et al., 2006). In EMAC/JSBACH, the surface albedo on glaciers is calculated for grid boxes either with ice sheets or without them, where these boxes are either completely or not at all covered with ice. For ice sheets, the albedo is calculated according to ECHAM5 (Roeckner et al., 2003). Every other surface is treated with a new albedo scheme based on the current state of snow cover, LAI, vegetation distribution and the spectral composition of solar downward radiation for each grid box, as described by Reick et al. (2021).

The surface albedo is compared to the ERA5-Land albedo variable. The ERA5-Land albedo is based on a 5-year MODIS climatology. These satellite observations are a combined Terra and Aqua retrieval (Schaaf and Wang, 2015). From the 16 d level-3 data of a 0.05° climate modelling grid (approx. 5.6 km at the Equator), monthly averages are calculated and interpolated into the EMAC T63 grid. The surface albedo of EMAC/JSBACH is, in general, in good agree-

ment with the ERA5 surface albedo (Fig. 8). During summer, EMAC/JSBACH shows a slight overestimation over Europe and Asia between 45° and 75° N and parts of Canada. Between 25° S and 15° N, an underestimation is visible. During the northern winter months, North America and Canada show underestimated surface albedo along with Scandinavia, eastern Europe, northern Russia and elevated regions in Asia. The average annual global difference between EMAC/JSBACH and ERA5 is -0.015 . The same geographical patterns are visible for the EMAC/SRF compared to ERA5 surface albedo comparison with average annual global difference of -0.012 . The zonal mean shows a slight overestimation of surface albedo for both simulations in the southern subtropics during summer and winter. During winter, there is a minimum of the surface albedo at about 45° N, which is not seen in the reference data (Fig. 8, right panels).

The land surface albedo remains almost unchanged in the new model version. This is presumably due to the fact that in EMAC/SRF the background albedo is temporally constant except for changes in ice and snow cover (Nützel et al., 2023). In EMAC/JSBACH, a simplified ground albedo scheme was used to obtain a comparable result. However, there is a slight improvement compared to the reference data for EMAC/JSBACH, which is particularly noticeable during

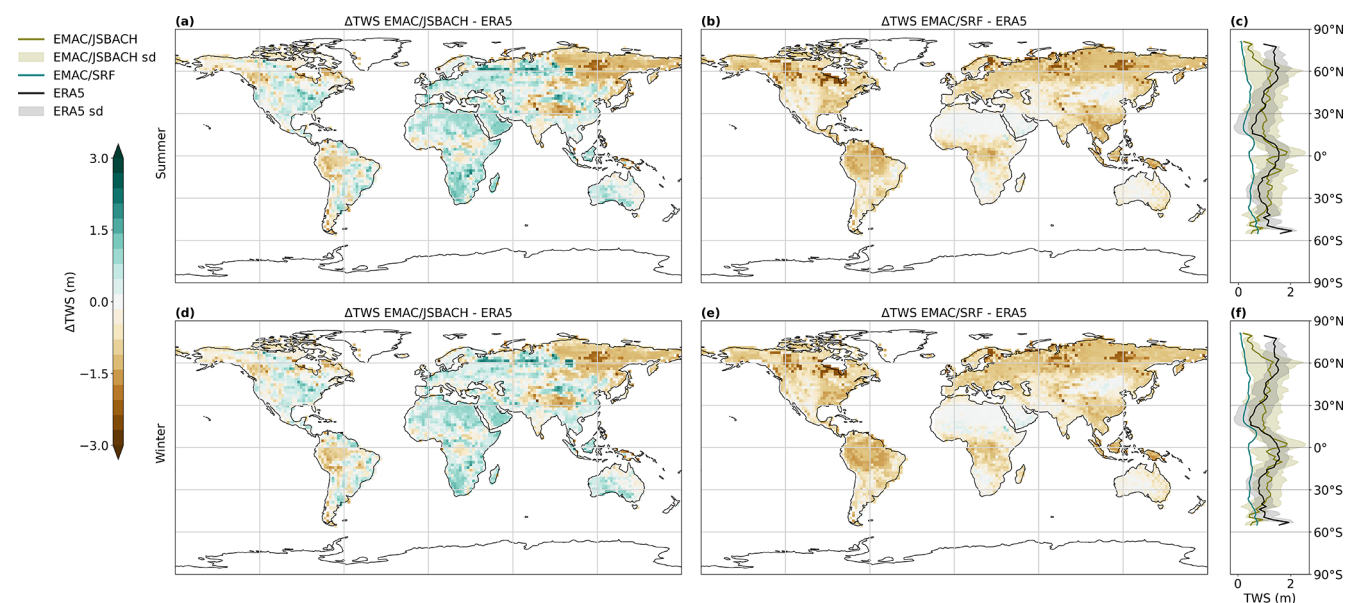


Figure 6. Difference in terrestrial water storage (TWS) between EMAC/JSBACH and ERA5-Land during NH summer (a) and NH winter (d) months, with data averaged over the years 1971 to 2010. Analogously, the difference between EMAC/SRF and ERA5-Land TWS during summer (b) and winter (e) months is displayed. Positive values represent an overestimation of the simulated TWS, while negative values indicate an underestimation. Additionally, the zonal average of all three datasets for both summer (c) and winter (f) months is shown. Here, TWS from EMAC/JSBACH is depicted in green, TWS from EMAC/SRF is shown in blue and TWS from the ERA5-Land dataset is represented in black. The shaded areas within the zonal mean plots illustrate the standard deviations of the datasets. Glaciated polar regions are excluded.

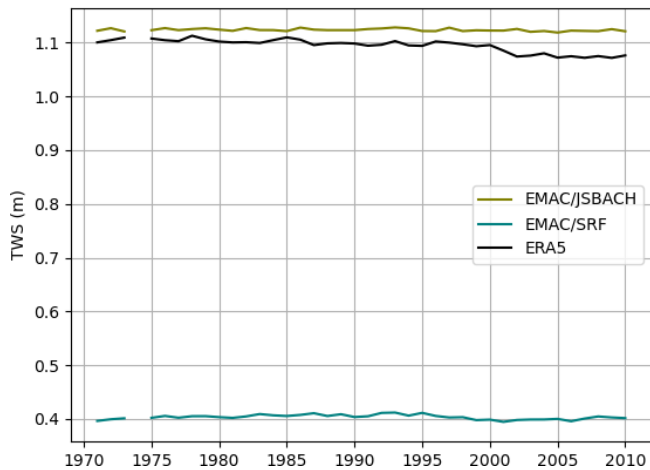


Figure 7. Globally averaged TWS time series (in m.w.e.) of EMAC/JSBACH (green), EMAC/SRF (blue) and ERA5 (black).

the summer in eastern Siberia, where the model overestimation is reduced. In this region, the LST and LAI derived from EMAC/JSBACH align more closely to the reference data than EMAC/SRF alone. This suggests that the slightly warmer surface and less vegetation in this region may contribute to the improved surface albedo representation.

4.4 Top-of-atmosphere radiation balance (Rad_{TOA})

The top-of-atmosphere (TOA) net radiation can be defined as the difference between the incoming solar radiation; outgoing solar radiation backscattered and reflected by clouds, aerosols, air and the land surface; and the terrestrial radiation emitted by the surface, atmosphere and clouds. In total and in equilibrium, the multi-year global mean sum should be zero. However, as climate change continues and the amount of greenhouse gases in the atmosphere increases, this effect exceeds zero; i.e. more radiation is trapped in the atmosphere than is emitted, leading to global warming. In climate modelling, the amounts of radiative energy absorbed and emitted in and by the atmosphere are key factors in the Earth's energy balance. The concentration of water vapour in the atmosphere and the surface albedo are important factors (Loeb et al., 2009). It is important to reproduce these factors correctly and to detect possible biases. The radiation fluxes are calculated by the MESSy submodel RAD, which is a new implementation of the ECHAM5 radiation scheme (Dietmüller et al., 2016). Rad_{TOA} is compared to the ERA5 monthly averaged reanalysis data of TOA solar and terrestrial radiation interpolated into the EMAC T63 grid (Hersbach et al., 2023).

The average temporal and spacial correlation between EMAC/JSBACH and ERA5 Rad_{TOA} is 0.907 (Table 6). The largest differences and overestimation of EMAC/JSBACH Rad_{TOA} in comparison to ERA5 during the summer

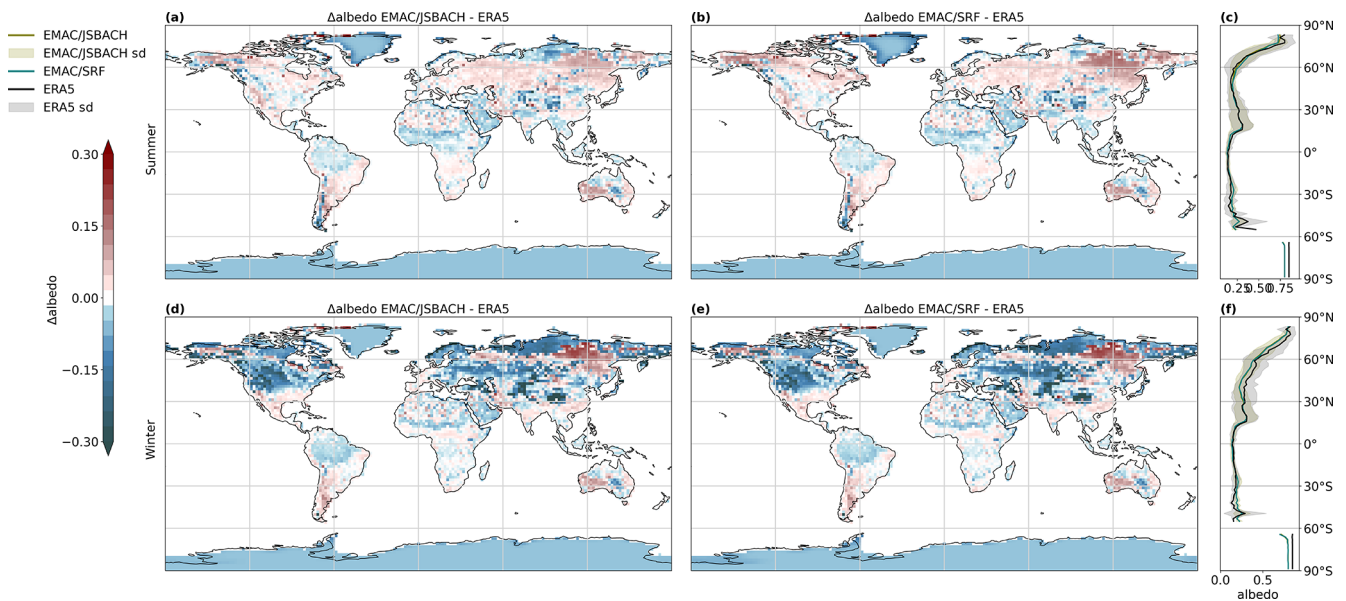


Figure 8. Difference in surface albedo (α) between EMAC/JSBACH and ERA5-Land during Northern Hemispheric (NH) summer (a) and NH winter (d) months, with data averaged over the years 1971 to 2010. Analogously, the difference between EMAC/SRF and ERA5-Land α during summer (b) and winter (e) months is displayed. Positive values represent an overestimation of the simulated α , while negative values indicate an underestimation. Additionally, the zonal average of all three datasets for both summer (c) and winter (f) months is shown. Here, α from EMAC/JSBACH is depicted in green, α from EMAC/SRF is shown in blue and α from the ERA5-Land dataset is represented in black. The shaded area within the zonal mean plot illustrates the standard deviations along longitudes.

months occur over north and west Africa and the Middle East (Fig. 9). The best agreement is found during summer over western Russia. The largest underestimations are found over central Africa and northern South America. During winter, the largest overestimation occurs over the Himalayas and the largest underestimation over the northern and southern Andes, central Africa, and Indonesia. During this time period, the best agreement is found over the polar and sub-polar regions. The average annual global difference between EMAC/JSBACH and ERA5 is 3.56 W m^{-2} . The zonal mean of the simulation is well in line with the zonal mean of the reanalysis data, and the overestimation of the simulation only occurs at 30° N and between 0 and 30° S . Comparing EMAC/SRF and ERA5, a similar geographical distribution is discernable and, especially in winter, there is almost no difference to the EMAC/JSBACH simulation. However, almost everywhere at high latitudes, the TOA radiative flux is lower during summer. The same applies for the zonal average. The average annual global difference between EMAC/SRF and ERA5 is 3.045 W m^{-2} , and the overall correlation is 0.909.

The TOA radiation derived from EMAC/JSBACH shows noticeable regional variations when compared to reanalysis data, yet its overall balance remains comparable to the one derived from EMAC/SRF. Moreover, these regional differences in Rad_{TOA} closely align with those observed for EMAC/SRF and do not significantly change when EMAC is in operation without JSBACH. Rad_{TOA} shows a strong anti-correlation with the surface albedo ($\rho = -0.86$), which de-

termines the amount of absorbed radiation on the surface (Table A2 in the Appendix). Since there are no significant differences between the EMAC/SRF and EMAC/JSBACH surface albedo, no significant differences in Rad_{TOA} are expected.

4.5 Precipitation (precip)

Since precipitation is one of the most important and challenging climate variables to reproduce for coupled global climate models (Dai, 2006), we are interested in analysing the general performance of the coupled EMAC/JSBACH and EMAC/SRF simulations to reproduce regional and temporal variations as well as the amount and intensity of precipitation. Problems of the simulation of precipitation can be an indication of issues of the processes that drive precipitation, such as large- and small-scale atmospheric dynamics, cloud micro-physics, and aerosol formation (Dai, 2006). Precipitation is calculated by the submodels CLOUD and CONVECT and is one of the standard input parameters for EMAC/JSBACH, forcing many processes in the land system. The simulated precipitation is compared to the Global Precipitation Climatology Project (GPCP) dataset of monthly precipitation spanning 1979 to 2021 (Adler et al., 2003). The observational precipitation data are available at a grid resolution of $2.5^\circ \times 2.5^\circ$, which is approximately 280 km at the Equator, and is regridded to the EMAC Gaussian T63 grid ($1.8^\circ \times 1.8^\circ$, approximately 210 km at the Equator) using bi-linear interpolation. The dataset provides an error estimate, which is defined

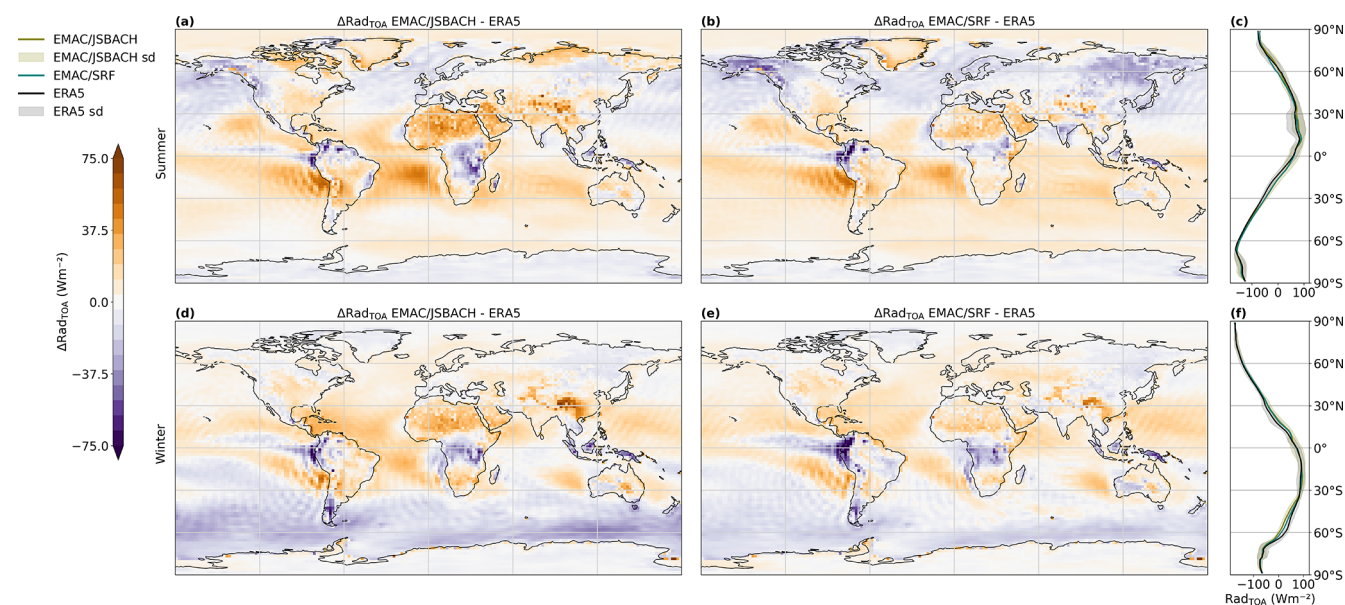


Figure 9. Difference in top-of-atmosphere radiation (Rad_{TOA}) between EMAC/JSBACH and ERA5 during Northern Hemispheric (NH) summer (a) and NH winter (d) months, with data averaged over the years 1971 to 2010. Analogously, the difference between EMAC/SRF and ERA5 Rad_{TOA} during summer (b) and winter (e) months is displayed. Positive values represent an overestimation of the simulated Rad_{TOA} , while negative values indicate an underestimation. Additionally, the zonal average of all three datasets for both summer (c) and winter (f) months is shown. Here, Rad_{TOA} from EMAC/JSBACH is depicted in green, Rad_{TOA} from EMAC/SRF is shown in blue and Rad_{TOA} from the ERA5 dataset is represented in black. The shaded area within the zonal mean plot illustrates the standard deviations along longitudes.

for every data point present in the dataset. This assessment considers solely the stochastic error and relies on both the mean rainfall rate and the quantity of samples utilized for its computation (Huffman, 1997). The differences between global precipitation distributions are shown in Fig. 10. The subtropical and tropical equatorial zones over land appear drier in the EMAC/JSBACH simulation in comparison to the GPCP data. This shifts from the Northern Hemisphere during summer to the Southern Hemisphere during winter. Over the oceans, regions of heavy precipitation are intensified in the simulation. The average annual global difference between EMAC/JSBACH and ERA5 is 0.042 mm d^{-1} (2.738 to 2.696 mm d^{-1} ; see Table 6). For the GPCP dataset, the error is shown as a grey-shaded area within the zonal mean plot. Zonally averaged, EMAC/JSBACH summer precipitation is within the GPCP precipitation error for the tropics and mid-latitudes, with EMAC/JSBACH underestimating precipitation at high latitudes. In the tropical region of the Northern Hemisphere, EMAC/JSBACH also slightly overestimates precipitation during winter. The northern Inter-Tropical Convergence Zone (ITCZ) is reproduced in agreement with the observations by the EMAC/SRF and EMAC/JSBACH simulations. The comparison between EMAC/SRF and GPCP shows that the simulated precipitation amounts are higher than the observed ones, with an average annual global deviation of 0.329 mm d^{-1} . Similar to EMAC/JSBACH, this simulation shows lower precipitation over Indonesia com-

pared to the GPCP data. Particularly noticeable is the tendency to overestimate precipitation over land, especially in the Himalayas in summer and in the Andes in winter. This is also evident in the zonal mean, although EMAC/SRF remains within the margin of error in the observations in summer. The only exception is the tropical regions of the Northern Hemisphere, where there is more precipitation in winter and less around 60° S .

Overall, EMAC/JSBACH is capable of reproducing global precipitation to a similar extent as EMAC/SRF. It exhibits a distinct wet bias zone, extending from 20° S to the Equator during winter and from 20° N to the Equator during summer (Fig. 11). This wet bias band is adjacent to a dry bias region, ranging from 0 – 10° N during NH winter and from 0 – 25° S during NH summer. The same is found for the precipitation derived from EMAC/SRF (Fig. 11) and leads to the assumption that there is no major change in the large-scale atmospheric dynamics of the new coupled model. The wet bias will be corrected by further “tuning” microphysical parameters in upcoming model versions. The dry biases over the Arctic and Antarctic regions throughout the year may be attributed to relatively low sea surface temperatures. This relationship has previously been documented by Pozzer et al. (2011a).

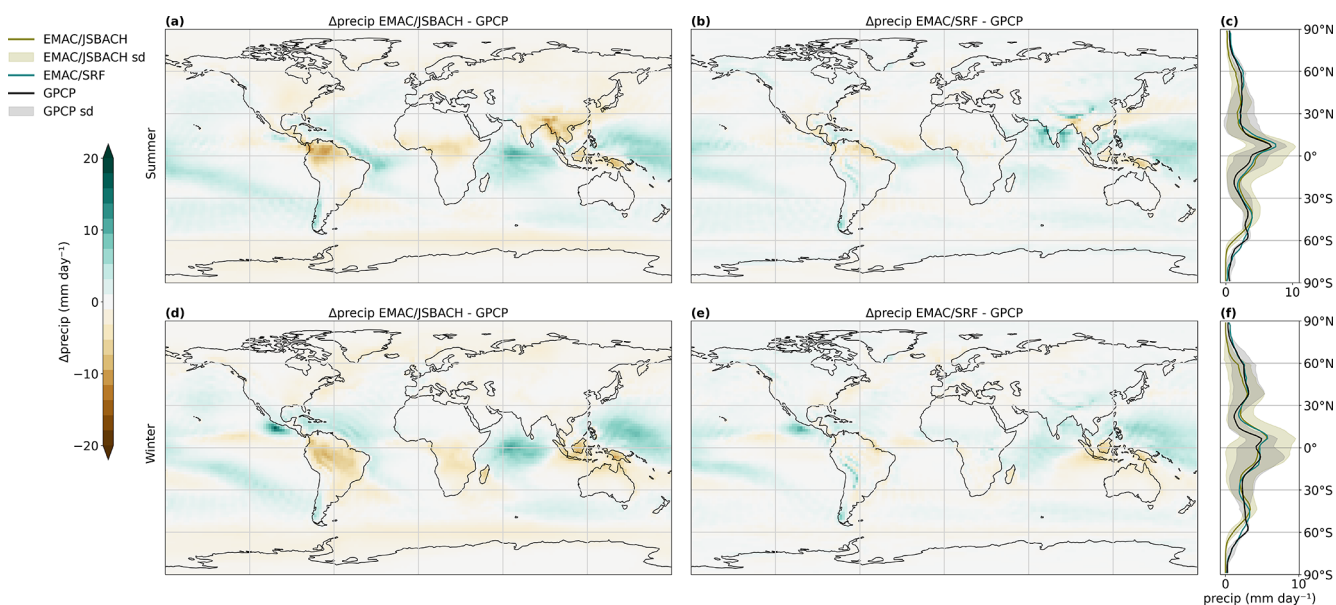


Figure 10. Difference in precipitation between EMAC/JSBACH and GPCP during Northern Hemispheric (NH) summer (a) and NH winter (d) months, with data averaged over the years 1980 to 2010. Analogously, the difference between EMAC/SRF and GPCP precipitation during summer (b) and winter (e) months is displayed. Positive values represent an overestimation of the simulated precipitation, while negative values indicate an underestimation. Additionally, the zonal average of all three datasets for both summer (c) and winter (f) months is shown. Here, precipitation from EMAC/JSBACH is depicted in green, precipitation from EMAC/SRF is shown in blue and precipitation from the GPCP dataset is represented in black. The shaded area within the zonal mean plot in black illustrates the GPCP dataset error and in green the standard deviation of the EMAC/JSBACH precipitation.

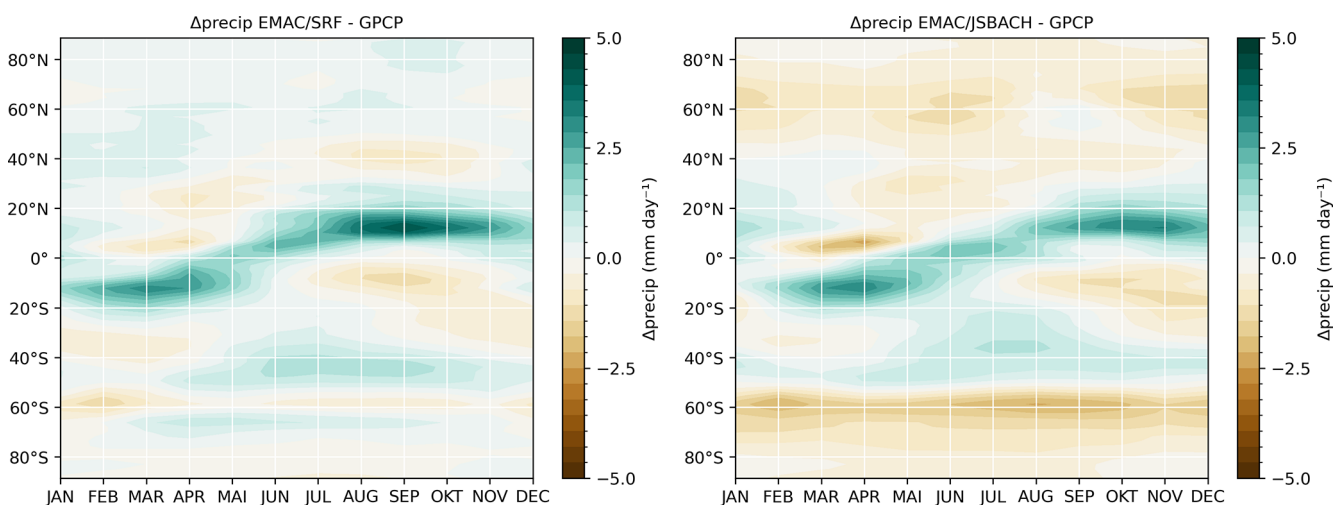


Figure 11. Zonally averaged monthly difference in EMAC/JSBACH (a) and EMAC/SRF (b) compared to GPCP precipitation in millimetres per day, averaged over the years 1980 to 2010.

4.6 Leaf area index (LAI)

The leaf area index is defined by Watson (1947) as the total one-sided area of leaf tissue per unit of ground surface area. It is an important quantity for estimating the gas exchange between vegetation and the atmosphere in particular (e.g. photosynthetic production or transpiration) and represents the canopy–atmosphere interface (Bréda, 2003). It has

a strong spatial and temporal variability, which makes it difficult to properly measure and simulate it. The default scheme to calculate the LAI in JSBACHv4 is an implementation of the Logistic Growth Phenology (LoGro-P) model, which is described in detail by Böttcher et al. (2016) and Reick et al. (2021). Within LoGro-P, the LAI is calculated depending on the phenology type of the plant functional types (PFTs),

which are either evergreen, summergreen, raingreen, grasses, or tropical or extratropical crops. Due to the prescribed geographical PFT distribution, there is no seasonal or inter-annual variability in plant functional types, limiting LAI variability. The phenology types are linked to certain phenology phases. For the summergreen type, these are, in turn, associated with seasons. Spring corresponds to the growth phase, summer to the vegetative phase, and winter and autumn to the resting phase (Schneck et al., 2022). Raingreen, grass, and tropical crop phenology types are only linked to a growth phase determined by environmental conditions like soil moisture, temperature and NPP, growing whenever those conditions are beneficial (Schneck et al., 2022). Tropical or extratropical crops are not linked to a vegetative phase. The LAI changes primarily due to temperature, soil moisture and NPP, and the maximum possible value is limited for each phenology type individually (Schneck et al., 2022). The LAI is compared to the 8-Day global MODIS/Terra Leaf Area Index dataset, regridded to 0.5° resolution (Kern, 2023; Myneni, 2021). Monthly averages are calculated and interpolated into the EMAC T63L31 grid.

The LAI difference between the EMAC/JSBACH and MODIS observations is shown in Fig. 12. The annual global average LAI within EMAC/JSBACH is $-0.212 \text{ m}^2 \text{ m}^{-2}$ (1.187 to $1.399 \text{ m}^2 \text{ m}^{-2}$; see Table 6) lower than the one estimated using MODIS satellite data. In particular, the LAI of tropical rainforests is underestimated throughout the year in the simulation, as are deciduous forests and boreal forests over eastern Siberia in summer. Otherwise, vegetation LAI tends to be overestimated, with peaks in India, south Africa and northern Canada throughout the year and in northern Europe during the winter. The zonal average (Fig. 12, right panels) shows that EMAC/JSBACH follows the MODIS LAI trend but with lower peak values at the Equator. EMAC/SRF overestimates LAI in comparison to the MODIS dataset almost everywhere, and the annual global average LAI is $0.768 \text{ m}^2 \text{ m}^{-2}$ larger than the satellite-instrument-based estimate. Maximum overestimations are found for the Amazon rain forest and Canadian boreal forest throughout the year. The same is found for the zonal average, of which the EMAC/SRF LAI peaks at the Equator at $7.5 \text{ m}^2 \text{ m}^{-2}$.

Discrepancies between EMAC/SRF and EMAC/JSBACH LAI are expected, due to EMAC/SRF's reliance on a LAI climatology, whereas in EMAC/JSBACH LAI is a prognostic variable. In JSBACH, the calculation of LAI for raingreen and crop phenology strongly depends on water availability. Tropical raingreen phenology is found in regions such as the Amazon, Indonesia and central Africa. These regions exhibit low TWS and coincide with regions of underestimated LAI. Over India, the phenology only consists of tropical broadleaf deciduous forests and both C_3 and C_4 crops. Given that the water deficit in India is not as pronounced as in other areas, the overestimation of LAI in India may be partly attributed to sufficient moisture content in the soil. In addition, GPP is enhanced in this area. This results in a feedback loop as more

vegetation leads to greater LAI, which in turn increases GPP and NPP, thus stimulating plant growth. The overestimation of LAI of extratropical evergreen and summergreen phenology, such as in northern Canada and Europe, is not determined by water availability since those LAI calculations are only based on parameterisations governing phenology and a set of parameters defining growth rate and the length of the growth season. Schneck et al. (2022) stated that an unlucky choice of those parameters can have a major effect on LAI estimation. However, Lin et al. (2023) found that the MODIS version 6.1 leaf area index product tends to underestimate LAI particularly in northern latitudes, which may contribute to the bias found over northern Canada and Europe.

4.7 Fraction of absorbed photosynthetic active radiation (FAPAR)

Together with the LAI, the fraction of absorbed photosynthetic active radiation is required to estimate the ecosystem productivity. It is a state variable that describes the amount of incoming solar radiation which is absorbed by leaves and available for photosynthesis. The absorption happens in the photosynthetic active radiation (PAR) band of 400–700 nm (Sellers, 1985) and depends on the solar zenith angle, the canopy thickness, the types of leaves, their optical properties, the orientation and the soil underneath (Reick et al., 2021).

In EMAC/JSBACH FAPAR is calculated in three canopy layers by the canopy radiation module, which is described by Loew et al. (2014) and Reick et al. (2021) in detail. After the calculation, FAPAR is handed over to the photosynthesis module and used to estimate the gross and net primary productivity and carbon fixation in the plants.

We compare our results to 8-Day Global MODIS/Terra Leaf Area Index dataset, regridded to global data at 0.5 resolution derived by the Integrated Climate Data Center (ICDC) (Kern, 2023; Myneni, 2021). Monthly averages are calculated and interpolated into the EMAC T63 grid.

The fraction of absorbed photosynthetic active radiation (FAPAR) is a newly introduced variable that was not available as EMAC output before the coupling to JSBACH. When compared to MODIS, the simulated FAPAR in EMAC/JSBACH is systematically underestimated across most regions, with the exception of India and northern Canada (Fig. 13). This underestimation is also evident in the zonal average. The annual global average FAPAR simulated by EMAC/JSBACH is 0.161 ± 0.137 , whereas MODIS data indicate a higher average of 0.384 ± 0.196 . Disney et al. (2016) conducted a comparison between the MODIS product and FAPAR and LAI measurements obtained from the ESA GlobAlbedo product. GlobAlbedo aligns with the 1D radiative transfer schemes used in EMAC/JSBACH and other large-scale ESMs. Their findings indicated overall good agreement in terms of timing between the datasets. Nevertheless, notable discrepancies in peak values were detected, with GlobAlbedo-derived values generally registering as lower

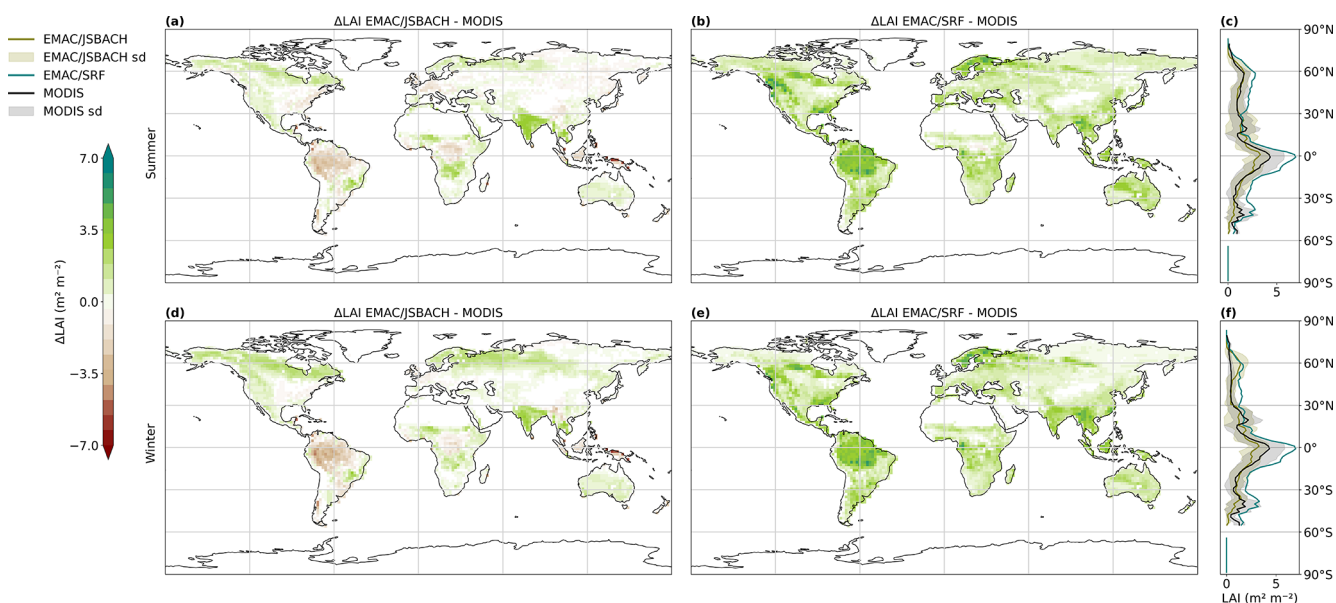


Figure 12. Difference in LAI between EMAC/JSBACH and MODIS during Northern Hemispheric (NH) summer (a) and NH winter (d) months, with data averaged over the years 2000 to 2010. Analogously, the difference between EMAC/SRF and MODIS LAI during summer (b) and winter (e) months is displayed. Positive values represent an overestimation of the simulated LAI, while negative values indicate an underestimation. Additionally, the zonal average of all three datasets for both summer (c) and winter (f) months is shown. Here, LAI from EMAC/JSBACH is depicted in green, LAI from EMAC/SRF is shown in blue and LAI from the MODIS dataset is represented in black. The shaded area within the zonal mean plot illustrates the standard deviations along longitudes.

compared to MODIS. They also state that the method used to determine FAPAR can result in variations of up to an order of magnitude difference. Loew et al. (2014) found a difference of up to 25 % when comparing models and satellite observations. These biases can be attributed, in part, to uncertainties in total cloud cover and snow cover that may affect satellite-based measurements. However, they may also result from the underlying definitions and algorithms used to determine the FAPAR product by satellite instruments (Loew et al., 2014). Within EMAC/JSBACH, the largest potential cause of uncertainty is the bias of the LAI, which, for example, most likely leads to the overestimation of FAPAR over India. Additionally, it cannot be ruled out that the representation of the surface albedo and the radiative transfer scheme might lead to the general underestimation of FAPAR, as was also documented in former studies (Loew et al., 2014; Disney et al., 2016). The differences in EMAC and observations in the radiative fluxes (mentioned above), especially the short-wave components, might also substantially contribute to the bias in FAPAR.

4.8 Gross primary productivity (GPP)

Gross primary productivity is the total rate of organic carbon gained via photosynthesis. This includes autotrophic respiration, which can be divided into maintenance respiration (driving basic functionalities of the plant, like water and nutrient transport, defence mechanisms, or repairs) and

growth respiration. GPP is a key parameter in estimating the net primary productivity (NPP), which describes the actual amount of carbon (sugars) stored in vegetation and is, therefore, an important quantity for the terrestrial carbon cycle. It is highly dependent on radiation, temperature, precipitation, LAI, TWS and water usage efficiency (the amount of water used by the plant to assimilate carbon). In EMAC/JSBACH, GPP is calculated via carbon assimilation (based on the plant water stress), FAPAR and LAI. The full and detailed description of the dynamics of vegetation carbon is provided by Reick et al. (2021).

GPP is compared to the MOD17A2H MODIS/Terra gross primary productivity 8-Day L4 Global 500m SIN Grid V006 regridded to global data at 0.5 resolution derived by ICDC (Kern, 2021; Running et al., 2015). Monthly averages are calculated and interpolated into the EMAC T63 grid.

Similar to FAPAR, gross primary productivity is a new diagnostic introduced in EMAC by JSBACH. GPP shows the largest differences to MODIS observations during NH summer over India, where GPP is strongly overestimated (Fig. 14). These are slightly lower during winter, when the GPP overestimation is larger over Australia and central South America. The largest underestimation is found during summer month over northeastern Siberia, the Amazon region and central Africa, while, during summer, the largest underestimation is found in the Amazon Basin and the Andes. The annual global average GPP of EMAC/JSBACH

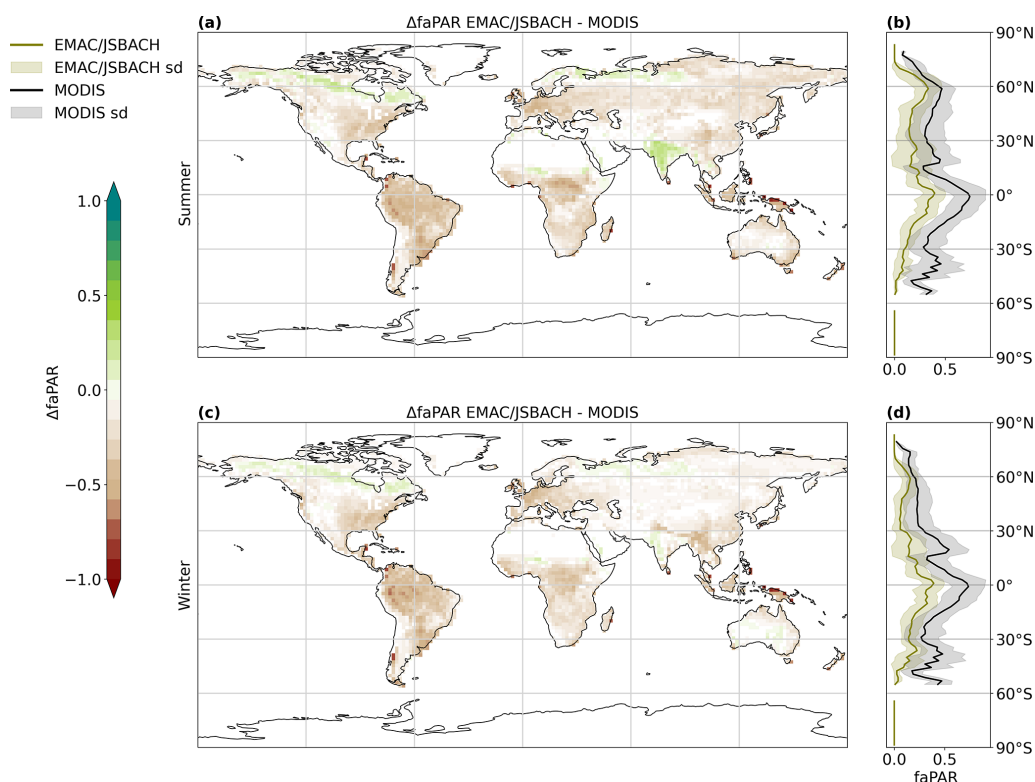


Figure 13. Difference in the fraction of absorbed photosynthetic active radiation (FAPAR) between EMAC/JSBACH and MODIS during Northern Hemispheric (NH) summer (a) and NH winter (c) months, with data averaged over the years 2000 to 2010. Positive values represent an overestimation of the simulated FAPAR, while negative values indicate an underestimation. Additionally, the zonal average of both datasets for both summer (b) and winter (d) months is shown. Here, FAPAR from EMAC/JSBACH is depicted in green and FAPAR from the MODIS dataset is represented in black. The shaded area within the zonal mean plot illustrates the standard deviations along longitudes.

is $0.02 \pm 0.017 \text{ kg carbon km}^{-2}$, while that of MODIS is $0.021 \pm 0.013 \text{ kg carbon km}^{-2}$.

GPP underestimations are mostly found in areas where TWS and FAPAR are also underestimated. The correlation between TWS and GPP is $\rho = 0.79$, indicating a monotonic relationship (Table A2 in the Appendix). The correlation between FAPAR and GPP is, as expected, high, with 0.94, since the GPP calculation is based on FAPAR. However, in this study, GPP demonstrates a notably better agreement with MODIS observations than FAPAR. The pronounced overestimation of GPP over India can be largely attributed to the concurrent overestimation of FAPAR in that region, which, in turn, can be traced back to the high LAI values that are prevalent there. In the global mean, FAPAR derived from EMAC/JSBACH and MODIS are in good agreement.

5 Conclusions

We have implemented the land surface model JSBACH version 4 as a new submodel into EMAC following the MESSy coding standards. The new addition aims to replace of the former, simplified submodel SURFACE, in which many parameters have been prescribed based on pre-determined cli-

matologies. JSBACH comprises numerous new features, including a comprehensive hydrology model and an improved soil scheme, enhancing the overall versatility of EMAC. It enables the possibility of performing new experiments that analyse not only the fundamental physical processes of the land surface within the Earth system on climatic timescales, but also the effects of atmospheric chemical components and associated feedback mechanisms on short timescales of hours and days. In this assessment, we demonstrate that the implementation, various modifications, and newly added features to EMAC have not degraded the overall model performance and stability. This is done based on a comparison of the new coupled model results to observational and reanalysis data and in comparison to results from a simulation conducted without JSBACH (i.e. based on climatologies). The newly coupled land–atmosphere model, however, required re-tuning to optimise the radiation budget via adjusted cloud parameters. The usage of JSBACH instead of SURFACE increases the runtime, on average, by $0.056 \% \pm 4 \times 10^{-4} \%$ for simulations carried out on two computing nodes of the DKRZ (German Climate Computing Centre) supercomputer LEVANTE.

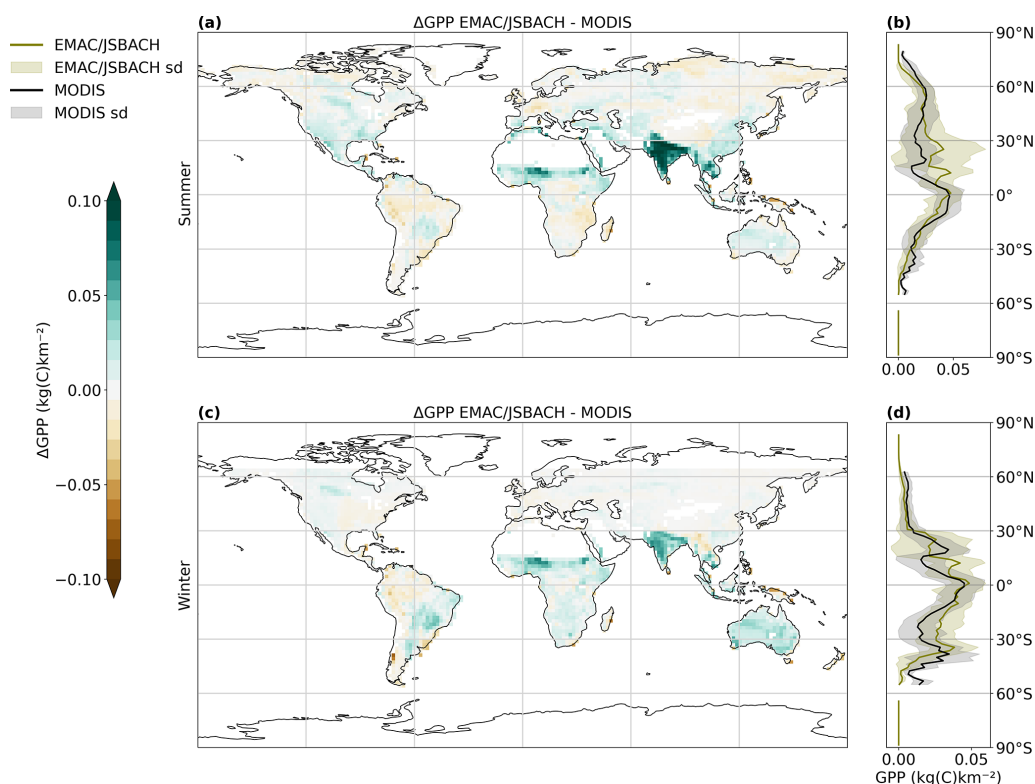


Figure 14. Difference in gross primary productivity (GPP) between EMAC/JSBACH and MODIS during Northern Hemispheric (NH) summer (a) and NH winter (c) months, with data averaged over the years 2000 to 2010. Positive values represent an overestimation of the simulated GPP, while negative values indicate an underestimation. Additionally, the zonal average of both datasets for both summer (b) and winter (d) months is shown. Here, GPP from EMAC/JSBACH is depicted in green and GPP from the MODIS dataset is represented in black. The shaded area within the zonal mean plot illustrates the standard deviations along longitudes.

Results indicate that the LST derived from the newly coupled EMAC/JSBACH model is, on average globally, 1.546 K colder compared to the LST derived from ERA5 (using the old SURFACE submodel, the globally averaged LST was 0.816 K warmer). The change from SURFACE to JSBACH improves the representation of TWS by generally increasing soil moisture and groundwater storage. This improves the agreement of the absolute global average TWS with the ERA5-Land reanalysis data and reduces the NRMSE. Surface albedo and Rad_{TOA} balance show no significant changes after the implementation of JSBACH. While seasonal and regional precipitation patterns are preserved, the global mean precipitation is slightly reduced in EMAC/JSBACH. The average global LAI of the EMAC/JSBACH simulation agrees better with the average LAI of MODIS than the climatological standard LAI present in EMAC/SRF; nevertheless, the spacial and temporal correlation of 0.637 between simulated LAI and observed LAI is still not very high. FAPAR and GPP are among many other newly introduced variables that were not available in previous EMAC versions (a selection of the additional output variables is included in the Supplement). They are now provided as diagnostic parameters. FAPAR shows the largest deviation from the observations,

which could partly be due to challenges in observing and quantifying FAPAR. Nevertheless, FAPAR as a fundamental parameter within the GPP calculations seems realistic, as the GPP and observational global average difference are only $-0.001 \text{ kg carbon km}^{-1}$.

We plan to implement the remaining JSBACH4 features, such as the closed carbon cycle and dynamic vegetation. The latter can be achieved before these updates are available by linking JSBACH with the dynamic vegetation of the LPJ-GUESS module that is already coupled with EMAC (Forrest et al., 2020). The model will be further refined to increase its capabilities and accuracy. This ongoing model development is crucial to striving towards the more comprehensive and realistic numerical modelling of the intricate interactions between the atmosphere and land along with the associated feedback mechanisms. It marks a significant advancement for EMAC, bringing it one step closer to the realisation of a comprehensive Earth system model.

Appendix A

Table A1. EMAC/JSBACH land cover types (lct) and corresponding tile in the EMAC/JSBACH simulation.

LCT	Description	Tile
lct01	glacier	1
lct02	tropical broadleaf evergreen	1
lct03	tropical broadleaf deciduous	2
lct04	extratropical evergreen	3
lct05	extratropical deciduous	4
lct10	raingreen shrubs	5
lct11	deciduous shrubs	6
lct12	C ₃ grass	7
lct13	C ₄ grass	8
lct15	C ₃ pasture	9
lct16	C ₄ pasture	10
lct20	C ₃ crops	11
lct21	C ₄ crops	11

Table A2. Spearman rank correlation (ρ) of the assessed variables derived from monthly means of EMAC/JSBACH for the years 1971 to 2010. A positive Spearman rank correlation suggests a monotonously increasing relationship, while a negative correlation indicates a monotonously decreasing relationship. All correlations were tested for statistical significance at the $p < 0.05$ level.

	LST	TWS	Surface albedo	Rad _{TOA}	Precipitation	LAI	FAPAR	GPP
LST	1.0							
TWS	0.69	1.0						
Surface albedo	-0.89	-0.77	1.0					
Rad _{TOA}	0.87	0.44	-0.86	1.0				
Precipitation	0.75	0.65	-0.87	0.68	1.0			
LAI	0.67	0.73	-0.79	0.66	0.78	1.0		
FAPAR	0.75	0.83	-0.85	0.74	0.84	0.95	1.0	
GPP	0.84	0.79	-0.90	0.84	0.82	0.91	0.94	1.0

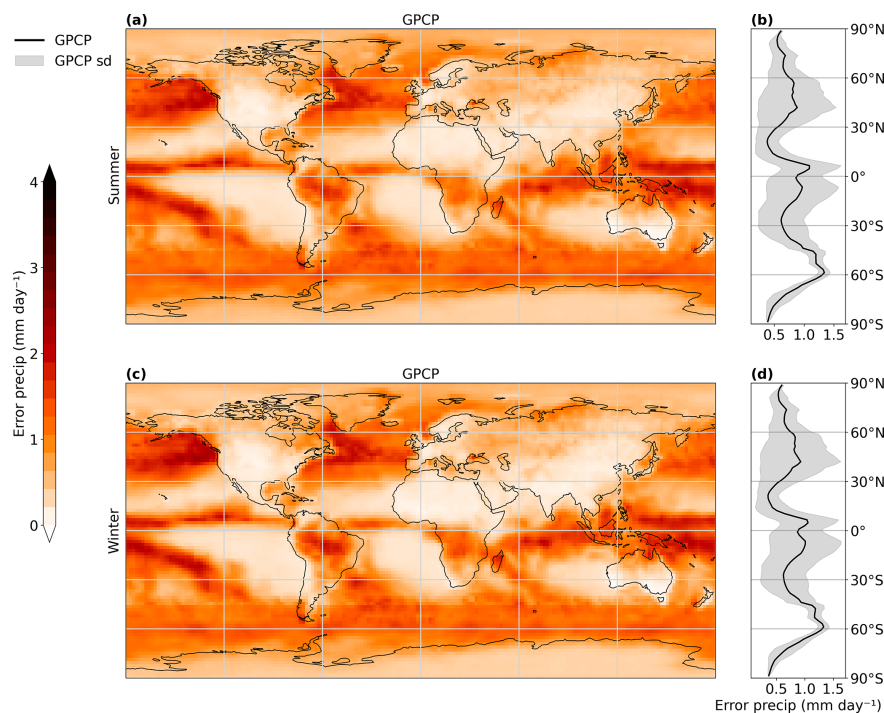


Figure A1. GPCP precipitation error during Northern Hemispheric (NH) summer (a) and NH winter (c) months, with data averaged over the years 2000 to 2010. Additionally, the zonal average of summer (b) and winter (d) months is shown. The shaded area within the zonal mean plot illustrates the standard deviations along longitudes.

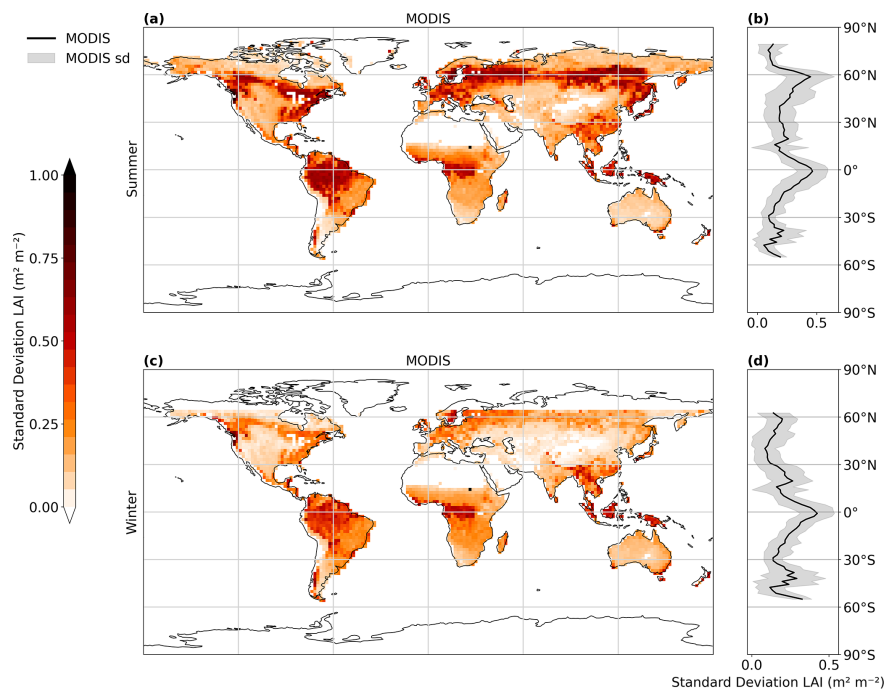


Figure A2. MODIS standard deviation of the leaf area index (LAI) during Northern Hemispheric (NH) summer (a) and NH winter (c) months, with data averaged over the years 2000 to 2010. Additionally, the zonal average of summer (b) and winter (d) months is shown. The shaded area within the zonal mean plot illustrates the standard deviations along longitudes.

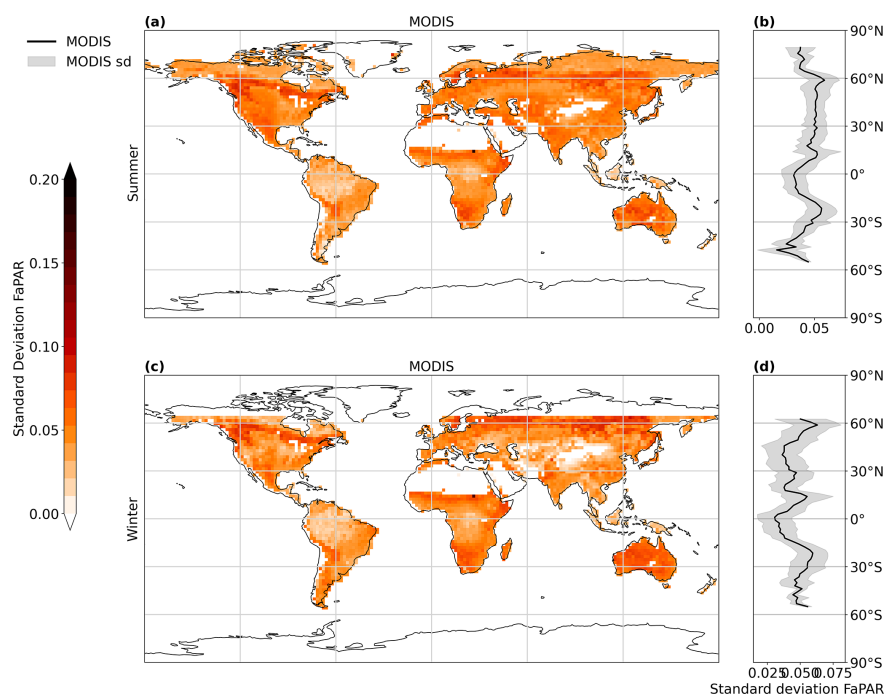


Figure A3. MODIS standard deviation of the fraction of absorbed photosynthetic active radiation (FaPAR) during Northern Hemispheric (NH) summer (a) and NH winter (c) months, with data averaged over the years 2000 to 2010. Additionally, the zonal average of summer (b) and winter (d) months is shown. The shaded area within the zonal mean plot illustrates the standard deviations along longitudes.

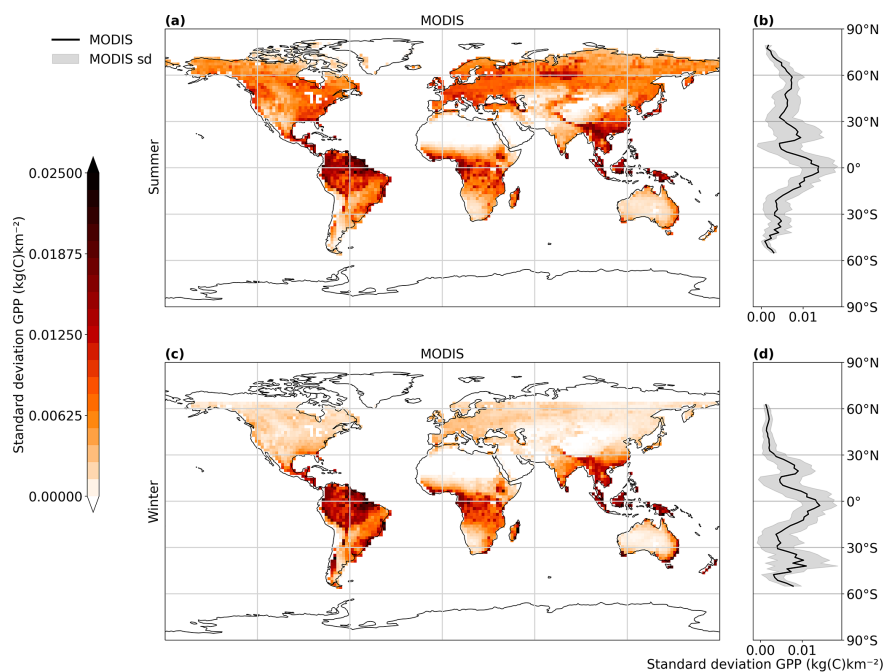


Figure A4. MODIS standard deviation of the gross primary productivity (GPP) during Northern Hemispheric (NH) summer (a) and NH winter (c) months, with data averaged over the years 2000 to 2010. Additionally, the zonal average of summer (b) and winter (d) months is shown. The shaded area within the zonal mean plot illustrates the standard deviations along longitudes.

Code availability. The Modular Earth Submodel System (MESSy; <https://doi.org/10.5281/zenodo.8360186>; The MESSy Consortium, 2024) is continuously further developed and applied by a consortium of institutions. The usage of MESSy and access to the source code are licensed to all affiliates of institutions which are members of the MESSy Consortium. Institutions can become a member of the MESSy Consortium by signing the MESSy Memorandum of Understanding. More information can be found on the MESSy Consortium website (<http://www.messy-interface.org>). The code presented/used here is available at <https://doi.org/10.5281/zenodo.10084186> (The MESSy Consortium, 2023) and will be part of the next official release. It is based on MESSy version d2.55.2 and JSBACH version 4 that is available via the jsbach repository on GitLab (no. 7de0f9bf3b50910655f474bc23d647c6ba2a7b6f). The model outputs relevant for this study are permanently stored in the Zenodo repository and are accessible via <https://doi.org/10.5281/zenodo.10084186> (The MESSy Consortium, 2023). The ERA5-Land monthly averaged data from 1950 to the present can be downloaded from <https://doi.org/10.24381/cds.68d2bb30> (Muñoz Sabater, 2019). The ERA5 monthly averaged data from 1940 to the present can be downloaded from <https://doi.org/10.24381/cds.f17050d7> (Hersbach et al., 2023). The GPCP monthly precipitation dataset from 1979 to 2021 can be downloaded from <https://downloads.psl.noaa.gov/Datasets/gpcp/> (last access: 19 January 2023, Adler et al., 2003). The MODIS/Terra 8-Day data product can be downloaded from <https://doi.org/10.25592/uhhfdm.8880> (Kern, 2021) and <https://doi.org/10.25592/uhhfdm.8880> (Kern, 2023).

Supplement. The supplement related to this article is available online at: <https://doi.org/10.5194/gmd-17-5705-2024-supplement>.

Author contributions. AM and AP planned the research. AM developed the model code and performed the simulations with the help of AP. AP, VG and PJ contributed to the overall model development. KK provided the MODIS datasets. BS provided the ERA5 datasets. AM wrote the paper with the help of AP, VG, PJ, KK, BS, HT and JL. AP, HT and JL supervised the project. All authors discussed the results and contributed to the review and editing of the paper.

Competing interests. At least one of the (co-)authors is a member of the editorial board of *Geoscientific Model Development*. The peer-review process was guided by an independent editor, and the authors also have no other competing interests to declare.

Disclaimer. Publisher's note: Copernicus Publications remains neutral with regard to jurisdictional claims made in the text, published maps, institutional affiliations, or any other geographical representation in this paper. While Copernicus Publications makes every effort to include appropriate place names, the final responsibility lies with the authors.

Acknowledgements. The model simulations have been performed at the German Climate Computing Centre (DKRZ) through support from the Max Planck Society.

Financial support. The article processing charges for this open-access publication were covered by the Max Planck Society.

Review statement. This paper was edited by Nathaniel Chaney and reviewed by two anonymous referees.

References

- Adler, R. F., Huffman, G. J., Chang, A., Ferraro, R., Xie, P.-P., Janowiak, J., Rudolf, B., Schneider, U., Curtis, S., Bolvin, D., Gruber, A., Susskind, J., Arkin, P., and Nelkin, E.: The Version-2 Global Precipitation Climatology Project (GPCP) Monthly Precipitation Analysis (1979–Present), *J. Hydrometeorol.*, 4, 1147–1167, [https://doi.org/10.1175/1525-7541\(2003\)004<1147:TVGPCP>2.0.CO;2](https://doi.org/10.1175/1525-7541(2003)004<1147:TVGPCP>2.0.CO;2), 2003.
- Bony, S., Colman, R., Kattsov, V. M., Allan, R. P., Bretherton, C. S., Dufresne, J.-L., Hall, A., Hallegatte, S., Holland, M. M., Ingram, W., Randall, D. A., Soden, B. J., Tselioudis, G., and Webb, M. J.: How Well Do We Understand and Evaluate Climate Change Feedback Processes?, *J. Climate*, 19, 3445–3482, <https://doi.org/10.1175/JCLI3819.1>, 2006.
- Böttcher, K., Markkanen, T., Thum, T., Aalto, T., Aurela, M., Reick, C. H., Kolari, P., Arslan, A. N., and Pulliainen, J.: Evaluating Biosphere Model Estimates of the Start of the Vegetation Active Season in Boreal Forests by Satellite Observations, *Remote Sens.*, 8, 580, <https://doi.org/10.3390/rs8070580>, 2016.
- Bréda, N. J. J.: Ground-based measurements of leaf area index: a review of methods, instruments and current controversies, *J. Exp. Bot.*, 54, 2403–2417, <https://doi.org/10.1093/jxb/erg263>, 2003.
- Charlesworth, E., Plöger, F., Birner, T., Baikhadzhaev, R., Abalos, M., Abraham, N. L., Akiyoshi, H., Bekki, S., Dennison, F., Jöckel, P., Keeble, J., Kinnison, D., Morgenstern, O., Plummer, D., Rozanov, E., Strode, S., Zeng, G., Egorova, T., and Riese, M.: Stratospheric water vapor affecting atmospheric circulation, *Nat. Commun.*, 14, 3925, <https://doi.org/10.1038/s41467-023-39559-2>, 2023.
- Dai, A.: Precipitation Characteristics in Eighteen Coupled Climate Models, *J. Climate*, 19, 4605–4630, <https://doi.org/10.1175/JCLI3884.1>, 2006.
- de Vrese, P., Stacke, T., Kleinen, T., and Brovkin, V.: Diverging responses of high-latitude CO₂ and CH₄ emissions in idealized climate change scenarios, *The Cryosphere*, 15, 1097–1130, <https://doi.org/10.5194/tc-15-1097-2021>, 2021.
- de Vrese, P., Georgievski, G., Gonzalez Rouco, J. F., Notz, D., Stacke, T., Steinert, N. J., Wilkenskjeld, S., and Brovkin, V.: Representation of soil hydrology in permafrost regions may explain large part of inter-model spread in simulated Arctic and subarctic climate, *The Cryosphere*, 17, 2095–2118, <https://doi.org/10.5194/tc-17-2095-2023>, 2023.
- Dietmüller, S., Jöckel, P., Tost, H., Kunze, M., Gellhorn, C., Brinkop, S., Frömming, C., Ponater, M., Steil, B., Lauer, A., and Hendricks, J.: A new radiation infrastructure for the Mod-

- ular Earth Submodel System (MESSy, based on version 2.51), *Geosci. Model Dev.*, 9, 2209–2222, <https://doi.org/10.5194/gmd-9-2209-2016>, 2016.
- Disney, M., Muller, J.-P., Kharbouche, S., Kaminski, T., Voßbeck, M., Lewis, P., and Pinty, B.: A New Global fAPAR and LAI Dataset Derived from Optimal Albedo Estimates: Comparison with MODIS Products, *Remote Sens.*, 8, 275, <https://doi.org/10.3390/rs8040275>, 2016.
- Domeisen, D. I., White, C. J., Afargan-Gerstman, H., Muñoz, Á. G., Janiga, M. A., Vitart, F., Wulff, C. O., Antoine, S., Ardilouze, C., Batté, L., Bloomfield, G. C., Brayshaw, D. J., Camargo, S. J., Charlton-Pérez, A., Collins, D., Cowan, T., del Mar Chaves, M., Ferranti, L., Gómez, R., González, P. L. M., González Romero, C., Infanti, J. M., Karozis, S., Kim, H., Kolstad, E. W., LaJoie, E., Lledó, L., Magnusson, L., Malguzzi, P., Manrique-Suñén, A., Mastrangelo, D., Materia, S., Medina, H., Palma, L., Pineda, L. E., Sftos, A., Son, S.-W., Soret, A., Strazzo, S., and Tian, D.: Advances in the subseasonal prediction of extreme events: relevant case studies across the globe, *B. Am. Meteorol. Soc.*, 103, E1473–E1501, 2022.
- Eichinger, R., Rhode, S., Garny, H., Preusse, P., Pisoft, P., Kuchař, A., Jöckel, P., Kerkweg, A., and Kern, B.: Emulating lateral gravity wave propagation in a global chemistry–climate model (EMAC v2.55.2) through horizontal flux redistribution, *Geosci. Model Dev.*, 16, 5561–5583, <https://doi.org/10.5194/gmd-16-5561-2023>, 2023.
- Ekici, A., Beer, C., Hagemann, S., Boike, J., Langer, M., and Hauck, C.: Simulating high-latitude permafrost regions by the JSBACH terrestrial ecosystem model, *Geosci. Model Dev.*, 7, 631–647, <https://doi.org/10.5194/gmd-7-631-2014>, 2014.
- Flato, G. M.: Earth system models: an overview, *WIREs Clim. Change*, 2, 783–800, <https://doi.org/10.1002/wcc.148>, 2011.
- Forrest, M., Tost, H., Lelieveld, J., and Hickler, T.: Including vegetation dynamics in an atmospheric chemistry-enabled general circulation model: linking LPJ-GUESS (v4.0) with the EMAC modelling system (v2.53), *Geosci. Model Dev.*, 13, 1285–1309, <https://doi.org/10.5194/gmd-13-1285-2020>, 2020.
- Friedel, M., Chiodo, G., Sukhodolov, T., Keeble, J., Peter, T., Seeber, S., Stenke, A., Akiyoshi, H., Rozanov, E., Plummer, D., Jöckel, P., Zeng, G., Morgenstern, O., and Josse, B.: Weakening of springtime Arctic ozone depletion with climate change, *Atmos. Chem. Phys.*, 23, 10235–10254, <https://doi.org/10.5194/acp-23-10235-2023>, 2023.
- Gates, W. L., Boyle, J. S., Covey, C., Dease, C. G., Doutriaux, C. M., Drach, R. S., Fiorino, M., Gleckler, P. J., Hnilo, J. J., Marlais, S. M., Phillips, T. J., Potter, G. L., Santer, B. D., Sperber, K. R., Taylor, K. E., and Williams, D. N.: An Overview of the Results of the Atmospheric Model Intercomparison Project (AMIP I), *B. Am. Meteorol. Soc.*, 80, 29–56, [https://doi.org/10.1175/1520-0477\(1999\)080<0029:AOTRO>2.0.CO;2](https://doi.org/10.1175/1520-0477(1999)080<0029:AOTRO>2.0.CO;2), 1999.
- Giorgetta, M. A., Jungclaus, J., Reick, C. H., Legutke, S., Bader, J., Böttinger, M., Brovkin, V., Crueger, T., Esch, M., Fieg, K., Glushak, K., Gayler, V., Haak, H., Hollweg, H.-D., Ilyina, T., Kinne, S., Kornbluh, L., Matei, D., Mauritsen, T., Mikolajewicz, U., Mueller, W., Notz, D., Pithan, F., Raddatz, T., Rast, S., Redler, R., Roeckner, E., Schmidt, H., Schnur, R., Segschneider, J., Six, K. D., Stockhause, M., Timmreck, C., Wegner, J., Widmann, H., Wieners, K.-H., Claussen, M., Marotzke, J., and Stevens, B.: Climate and carbon cycle changes from 1850 to 2100 in MPI-ESM simulations for the Coupled Model Intercomparison Project phase 5, *J. Adv. Model. Earth Sy.*, 5, 572–597, <https://doi.org/10.1002/jame.20038>, 2013.
- Giroto, M. and Rodell, M.: Chapter Two- Terrestrial water storage, in: *Extreme Hydroclimatic Events and Multivariate Hazards in a Changing Environment*, edited by Maggioni, V. and Massari, C., Elsevier, ISBN 978-0-12-814899-0, 41–64, <https://doi.org/10.1016/B978-0-12-814899-0.00002-X>, 2019.
- Gutiérrez, J. M., Tréguier, A.-M., Durack, P. J., Emori, S., Meinhausen, M., Nowicki, S., Ruiz, L., Sierra, J. D., Guilyardi, E., Satoh, Y., and Stockhause, M.: Annex II: Models, Cambridge University Press, Cambridge, United Kingdom and New York, NY, USA, 2087–2138, <https://doi.org/10.1017/9781009157896.016>, 2021.
- Hagemann, S. and Stacke, T.: Impact of the soil hydrology scheme on simulated soil moisture memory, *Clim. Dynam.*, 44, 1731–1750, <https://doi.org/10.1007/s00382-014-2221-6>, 2015.
- Hall, A.: The Role of Surface Albedo Feedback in Climate, *J. Climate*, 17, 1550–1568, [https://doi.org/10.1175/1520-0442\(2004\)017<1550:TROSAF>2.0.CO;2](https://doi.org/10.1175/1520-0442(2004)017<1550:TROSAF>2.0.CO;2), 2004.
- Hersbach, H., Bell, B., Berrisford, P., Hirahara, S., Horányi, A., Muñoz-Sabater, J., Nicolas, J., Peubey, C., Radu, R., Schepers, D., Simmons, A., Soci, C., Abdalla, S., Abellan, X., Balsamo, G., Bechtold, P., Biavati, G., Bidlot, J., Bonavita, M., De Chiara, G., Dahlgren, P., Dee, D., Diamantakis, M., Dragani, R., Flemming, J., Forbes, R., Fuentes, M., Geer, A., Haimberger, L., Healy, S., Hogan, R. J., Hólm, E., Janisková, M., Keeley, S., Laloyaux, P., Lopez, P., Lupu, C., Radnoti, G., de Rosnay, P., Rozum, I., Vamborg, F., Villaume, S., and Thépaut, J.-N.: The ERA5 global reanalysis, *Q. J. Roy. Meteor. Soc.*, 146, 1999–2049, 2020.
- Hersbach, H., Bell, B., Berrisford, P., Biavati, G., Horányi, A., Muñoz Sabater, J., Nicolas, J., Peubey, C., Radu, R., Rozum, I., Schepers, D., Simmons, A., Soci, C., Dee, D., and Thépaut, J.-N.: ERA5 monthly averaged data on single levels from 1940 to present, Copernicus Climate Change Service (C3S) Climate Data Store (CDS) [data set], <https://doi.org/10.24381/cds.f17050d7>, 2023.
- Hines, C. O.: Doppler-spread parameterization of gravity-wave momentum deposition in the middle atmosphere. Part 1: Basic formulation, *J. Atmos. Sol.-Terr. Phys.*, 59, 371–386, 1997.
- Huffman, G. J.: Estimates of Root-Mean-Square Random Error for Finite Samples of Estimated Precipitation, *J. Appl. Meteorol.*, 36, 1191–1201, [https://doi.org/10.1175/1520-0450\(1997\)036<1191:EORMSR>2.0.CO;2](https://doi.org/10.1175/1520-0450(1997)036<1191:EORMSR>2.0.CO;2), 1997.
- IPCC: Annex II: Models, in: *Climate Change 2021: The Physical Science Basis. Contribution of Working Group I to the Sixth Assessment Report of the Intergovernmental Panel on Climate Change*, edited by: Masson-Delmotte, V., Zhai, P., Pirani, A., Connors, S. L., Péan, C., Berger, S., Caud, N., Chen, Y., Goldfarb, L., Gomis, M. I., Huang, M., Leitzell, K., Lonnoy, E., Matthews, J. B. R., Maycock, T. K., Waterfield, T., Yelekçi, O., Yu, R., and Zhou, B.: Cambridge University Press, Cambridge, United Kingdom and New York, NY, USA, 2087–2138, <https://doi.org/10.1017/9781009157896.016>, 2021.
- Jöckel, P., Sander, R., Kerkweg, A., Tost, H., and Lelieveld, J.: Technical Note: The Modular Earth Submodel System (MESSy) – a new approach towards Earth System Modeling, *Atmos.*

- Chem. Phys., 5, 433–444, <https://doi.org/10.5194/acp-5-433-2005>, 2005.
- Jöckel, P., Kerkweg, A., Buchholz-Dietsch, J., Tost, H., Sander, R., and Pozzer, A.: Technical Note: Coupling of chemical processes with the Modular Earth Submodel System (MESSy) submodel TRACER, *Atmos. Chem. Phys.*, 8, 1677–1687, <https://doi.org/10.5194/acp-8-1677-2008>, 2008.
- Jöckel, P., Kerkweg, A., Pozzer, A., Sander, R., Tost, H., Riede, H., Baumgaertner, A., Gromov, S., and Kern, B.: Development cycle 2 of the Modular Earth Submodel System (MESSy2), *Geosci. Model Dev.*, 3, 717–752, <https://doi.org/10.5194/gmd-3-717-2010>, 2010.
- Jöckel, P., Kerkweg, A., Pozzer, A., Sander, R., Tost, H., Riede, H., Baumgaertner, A., Gromov, S., and Kern, B.: Development cycle 2 of the Modular Earth Submodel System (MESSy2), *Geosci. Model Dev.*, 3, 717–752, <https://doi.org/10.5194/gmd-3-717-2010>, 2010.
- Jöckel, P., Tost, H., Pozzer, A., Kunze, M., Kirner, O., Brenninkmeijer, C. A. M., Brinkop, S., Cai, D. S., Dyroff, C., Eckstein, J., Frank, F., Garny, H., Gottschaldt, K.-D., Graf, P., Grewe, V., Kerkweg, A., Kern, B., Matthes, S., Mertens, M., Meul, S., Neumaier, M., Nützel, M., Oberländer-Hayn, S., Ruhnke, R., Runde, T., Sander, R., Scharffe, D., and Zahn, A.: Earth System Chemistry integrated Modelling (ESCiMo) with the Modular Earth Submodel System (MESSy) version 2.51, *Geosci. Model Dev.*, 9, 1153–1200, <https://doi.org/10.5194/gmd-9-1153-2016>, 2016.
- Jungclaus, J. H., Lorenz, S. J., Schmidt, H., Brovkin, V., Brüggemann, N., Chegini, F., Crüger, T., De-Vrese, P., Gayler, V., Giorgetta, M. A., Gutjahr, O., Haak, H., Hagemann, S., Hanke, M., Ilyina, T., Korn, P., Kröger, J., Linardakis, L., Mehlmann, C., Mikolajewicz, U., Müller, W. A., Nabel, J. E. M. S., Notz, D., Pohlmann, H., Putrasahan, D. A., Raddatz, T., Ramme, L., Redler, R., Reick, C. H., Riddick, T., Sam, T., Schneek, R., Schnur, R., Schupfner, M., von Storch, J.-S., Wachsmann, F., Wieners, K.-H., Ziemann, F., Stevens, B., Marotzke, J., and Claussen, M.: The ICON Earth System Model Version 1.0, *J. Adv. Model. Earth Sy.*, 14, e2021MS002813, <https://doi.org/10.1029/2021MS002813>, 2022.
- Kerkweg, A., Sander, R., Tost, H., and Jöckel, P.: Technical note: Implementation of prescribed (OFFLEM), calculated (ONLEM), and pseudo-emissions (TNUDGE) of chemical species in the Modular Earth Submodel System (MESSy), *Atmos. Chem. Phys.*, 6, 3603–3609, <https://doi.org/10.5194/acp-6-3603-2006>, 2006.
- Kern, B.: Chemical interaction between ocean and atmosphere, PhD thesis, Johannes Gutenberg University, Mainz, chapter 5.1, https://www.bastiankern.de/files/kern_2013_print.pdf (last access: 27 October 2023), 2013.
- Kern, S.: MODIS Collection 6 global 8-daily Gross Primary Production, Universität Hamburg [data set], <https://doi.org/10.25592/uhhfdm.8880>, 2021.
- Kern, S.: MODIS Collection 6.1 global 8-daily LAI and FAPAR, Universität Hamburg [data set], <https://doi.org/10.25592/uhhfdm.11777>, 2023.
- Kohl, M., Lelieveld, J., Chowdhury, S., Ehrhart, S., Sharma, D., Cheng, Y., Tripathi, S. N., Sebastian, M., Pandithurai, G., Wang, H., and Pozzer, A.: Numerical simulation and evaluation of global ultrafine particle concentrations at the Earth's surface, *Atmos. Chem. Phys.*, 23, 13191–13215, <https://doi.org/10.5194/acp-23-13191-2023>, 2023.
- Lamarque, J.-F., Bond, T. C., Eyring, V., Granier, C., Heil, A., Klimont, Z., Lee, D., Liousse, C., Mieville, A., Owen, B., Schultz, M. G., Shindell, D., Smith, S. J., Stehfest, E., Van Aardenne, J., Cooper, O. R., Kainuma, M., Mahowald, N., McConnell, J. R., Naik, V., Riahi, K., and van Vuuren, D. P.: Historical (1850–2000) gridded anthropogenic and biomass burning emissions of reactive gases and aerosols: methodology and application, *Atmos. Chem. Phys.*, 10, 7017–7039, <https://doi.org/10.5194/acp-10-7017-2010>, 2010.
- Lamarque, J.-F., Shindell, D. T., Josse, B., Young, P. J., Cionni, I., Eyring, V., Bergmann, D., Cameron-Smith, P., Collins, W. J., Doherty, R., Dalsoren, S., Faluvegi, G., Folberth, G., Ghan, S. J., Horowitz, L. W., Lee, Y. H., MacKenzie, I. A., Nagashima, T., Naik, V., Plummer, D., Righi, M., Rumbold, S. T., Schulz, M., Skeie, R. B., Stevenson, D. S., Strode, S., Sudo, K., Szopa, S., Voulgarakis, A., and Zeng, G.: The Atmospheric Chemistry and Climate Model Intercomparison Project (ACCMIP): overview and description of models, simulations and climate diagnostics, *Geosci. Model Dev.*, 6, 179–206, <https://doi.org/10.5194/gmd-6-179-2013>, 2013.
- Lauwaet, D., van Lipzig, N., and De Ridder, K.: The effect of vegetation changes on precipitation and Mesoscale Convective Systems in the Sahel, *Clim. Dynam.*, 33, 521–534, 2009.
- Lin, W., Yuan, H., Dong, W., Zhang, S., Liu, S., Wei, N., Lu, X., Wei, Z., Hu, Y., and Dai, Y.: Reprocessed MODIS Version 6.1 Leaf Area Index Dataset and Its Evaluation for Land Surface and Climate Modeling, *Remote Sens.*, 15, 1780, <https://doi.org/10.3390/rs15071780>, 2023.
- Loeb, N. G., Wielicki, B. A., Doelling, D. R., Smith, G. L., Keyes, D. F., Kato, S., Manalo-Smith, N., and Wong, T.: Toward Optimal Closure of the Earth's Top-of-Atmosphere Radiation Budget, *J. Climate*, 22, 748–766, <https://doi.org/10.1175/2008JCLI2637.1>, 2009.
- Loew, A., van Bodegom, P. M., Widlowski, J.-L., Otto, J., Quaife, T., Pinty, B., and Raddatz, T.: Do we (need to) care about canopy radiation schemes in DGVMs? Caveats and potential impacts, *Biogeosciences*, 11, 1873–1897, <https://doi.org/10.5194/bg-11-1873-2014>, 2014.
- Matyssek, R., Kozovits, A. R., Schnitzler, J.-P., Pretzsch, H., Dieler, J., and Wieser, G.: Forest trees under air pollution as a factor of climate change, *Trees in a Changing Environment: Ecophysiology, Adaptation, and Future Survival*, 9, 117–163, 2014.
- Mauritsen, T., Stevens, B., Roeckner, E., Crueger, T., Esch, M., Giorgetta, M., Haak, H., Jungclaus, J., Klocke, D., Matei, D., Mikolajewicz, U., Notz, D., Pincus, R., Schmidt, H., and Tomassini, L.: Tuning the climate of a global model, *J. Adv. Model. Earth Sy.*, 4, 3, <https://doi.org/10.1029/2012MS000154>, 2012.
- Mauritsen, T., Bader, J., Becker, T., Behrens, J., Bittner, M., Brokopf, R., Brovkin, V., Claussen, M., Crueger, T., Esch, M., Fast, I., Fiedler, S., Fläschner, D., Gayler, V., Giorgetta, M., Goll, D. S., Haak, H., Hagemann, S., Hedemann, C., Hohengger, C., Ilyina, T., Jahns, T., Jimenez-de-la-Cuesta, D., Jungclaus, J., Kleinen, T., Kloster, S., Kracher, D., Kinne, S., Kleberg, D., Lasslop, G., Kornbluh, L., Marotzke, J., Matei, D., Meraner, K., Mikolajewicz, U., Modali, K., Möbis, B., Müller, W. A., Nabel, J. E. M. S., Nam, C. C. W., Notz, D., Nyawira, S.-S., Paulsen, H.,

- Peters, K., Pincus, R., Pohlmann, H., Pongratz, J., Popp, M., Raddatz, T. J., Rast, S., Redler, R., Reick, C. H., Rohrschneider, T., Schemann, V., Schmidt, H., Schnur, R., Schulzweida, U., Six, K. D., Stein, L., Stemmler, I., Stevens, B., von Storch, J.-S., Tian, F., Voigt, A., Vrese, P., Wieners, K.-H., Wilkenskjeld, S., Winkler, A., and Roeckner, E.: Developments in the MPI-M Earth System Model version 1.2 (MPI-ESM1.2) and its response to increasing CO₂, *J. Adv. Model. Earth Sy.*, 11, 998–1038, 2019.
- Mellouki, A., Wallington, T. J., and Chen, J.: Atmospheric Chemistry of Oxygenated Volatile Organic Compounds: Impacts on Air Quality and Climate, *Chem. Rev.*, 115, 3984–4014, <https://doi.org/10.1021/cr500549n>, 2015.
- MESSy: Modular Earth Submodel System (MESSy), <https://messy-interface.org/messy/submodels/>, last access: 12 October 2023.
- Milner, J., Hughes, R., Chowdhury, S., Picetti, R., Ghosh, R., Yeung, S., Lelieveld, J., Dangour, A. D., and Wilkinson, P.: Air pollution and child health impacts of decarbonization in 16 global cities: Modelling study, *Environ. Int.*, 175, 107972, <https://doi.org/10.1016/j.envint.2023.107972>, 2023.
- Miralles, D. G., Gentine, P., Seneviratne, S. I., and Teuling, A. J.: Land–atmospheric feedbacks during droughts and heatwaves: state of the science and current challenges, *Ann. NY Acad. Sci.*, 1436, 19–35, 2019.
- Muñoz Sabater, J.: ERA5–Land monthly averaged data from 1950 to present, Copernicus Climate Change Service (C3S) Climate Data Store (CDS) [data set], <https://doi.org/10.24381/cds.68d2bb30>, 2019.
- Myneni, R., Knyazikhin, Y., and Park, T.: MODIS/Terra Leaf Area Index/FPAR 8-Day L4 Global 500m SIN Grid V061, NASA EOSDIS Land Processes Distributed Active Archive Center [data set], <https://doi.org/10.5067/MODIS/MOD15A2H.061>, 2021.
- Nabel, J. E. M. S., Naudts, K., and Pongratz, J.: Accounting for forest age in the tile-based dynamic global vegetation model JSBACH4 (4.20p7; git feature/forests) – a land surface model for the ICON-ESM, *Geosci. Model Dev.*, 13, 185–200, <https://doi.org/10.5194/gmd-13-185-2020>, 2020.
- Nussbaumer, C. M., Fischer, H., Lelieveld, J., and Pozzer, A.: What controls ozone sensitivity in the upper tropical troposphere?, *Atmos. Chem. Phys.*, 23, 12651–12669, <https://doi.org/10.5194/acp-23-12651-2023>, 2023.
- Nützel, M., Stecher, L., Jöckel, P., Winterstein, F., Dameris, M., Ponater, M., Graf, P., and Kunze, M.: Updating the radiation infrastructure in MESSy (based on MESSy version 2.55), *EGU-sphere* [preprint], <https://doi.org/10.5194/egusphere-2023-2140>, 2023.
- Pham, T. V., Steger, C., Rockel, B., Keuler, K., Kirchner, I., Mertens, M., Rieger, D., Zängl, G., and Früh, B.: ICON in Climate Limited-area Mode (ICON release version 2.6.1): a new regional climate model, *Geosci. Model Dev.*, 14, 985–1005, <https://doi.org/10.5194/gmd-14-985-2021>, 2021.
- Pozzer, A., Jöckel, P., Kern, B., and Haak, H.: The Atmosphere–Ocean General Circulation Model EMAC–MPIOM, *Geosci. Model Dev.*, 4, 771–784, <https://doi.org/10.5194/gmd-4-771-2011>, 2011.
- Pozzer, A., Anenberg, S., Dey, S., Haines, A., Lelieveld, J., and Chowdhury, S.: Mortality attributable to ambient air pollution: A review of global estimates, *GeoHealth*, 7, e2022GH000711, <https://doi.org/10.1029/2022GH000711>, 2023.
- Reick, C., Raddatz, T., Brovkin, V., and Gayler, V.: Representation of natural and anthropogenic land cover change in MPI-ESM, *J. Adv. Model. Earth Sy.*, 5, 459–482, <https://doi.org/10.1002/jame.20022>, 2013.
- Reick, C. H., Gayler, V., Goll, D., Hagemann, S., Heidkamp, M., Nabel, J. E. M. S., Raddatz, T., Roeckner, E., and Schnur, R.: S. Wilkenskjeld: JSBACH 3 – The land component of the MPI Earth System Model: documentation of version 3.2, Hamburg, MPI für Meteorologie, <https://doi.org/10.17617/2.3279802>, 2021.
- Righi, M., Hendricks, J., and Brinkop, S.: The global impact of the transport sectors on the atmospheric aerosol and the resulting climate effects under the Shared Socioeconomic Pathways (SSPs), *Earth Syst. Dynam.*, 14, 835–859, <https://doi.org/10.5194/esd-14-835-2023>, 2023.
- Roeckner, E., Bäuml, G., Bonaventura, L., Brokopf, R., Esch, M., Giorgetta, M., Hagemann, S., Kirchner, I., Kornblüeh, L., Manzini, E., Rhodin, A., Schlese, U., Schulzweida, U., and Tompkins, A.: The atmospheric general circulation model ECHAM 5. PART I: Model description, Report, Max-Planck-Institut für Meteorologie, 349, <https://hdl.handle.net/11858/00-001M-0000-0012-0144-5> (last access: 24 July 2024), 2003.
- Roeckner, E., Brokopf, R., Esch, M., Giorgetta, M., Hagemann, S., Kornblüeh, L., Manzini, E., Schlese, U., and Schulzweida, U.: Sensitivity of simulated climate to horizontal and vertical resolution in the ECHAM5 atmosphere model, *J. Climate*, 19, 3771–3791, 2006.
- Running, S., Mu, Q., and Zhao, M.: MOD17A2H MODIS/Terra Gross Primary Productivity 8-Day L4 Global 500m SIN Grid, NASA LP DAAC, NASA EOSDIS Land Processes Distributed Active Archive Center [data set], <https://doi.org/10.5067/MODIS/MOD17A2H.006>, 2015.
- The MESSy Consortium: The Modular Earth Submodel System (2.55.2_711-jsbach), Zenodo [data set], <https://doi.org/10.5281/zenodo.10084186>, 2023.
- Schaaf, C. and Wang, Z.: MCD43C3 MODIS/Terra+Aqua BRD-F/Albedo Snow-free Model Parameters Daily L3 0.05Deg CMG. NASA LP DAAC, University of Massachusetts Boston – NASA GSFC and MODAPS SIPS – NASA, NASA EOSDIS Land Processes Distributed Active Archive Center [data set], <https://doi.org/10.5067/MODIS/MCD43C3.006>, 2015.
- Schneck, R., Gayler, V., Nabel, J. E. M. S., Raddatz, T., Reick, C. H., and Schnur, R.: Assessment of JSBACHv4.30 as a land component of ICON-ESM-V1 in comparison to its predecessor JSBACHv3.2 of MPI-ESM1.2, *Geosci. Model Dev.*, 15, 8581–8611, <https://doi.org/10.5194/gmd-15-8581-2022>, 2022.
- Sellers, P. J.: Canopy reflectance, photosynthesis and transpiration, *Int. J. Remote Sens.*, 6, 1335–1372, <https://doi.org/10.1080/01431168508948283>, 1985.
- Seneviratne, S. I., Corti, T., Davin, E. L., Hirschi, M., Jaeger, E. B., Lehner, I., Orlowsky, B., and Teuling, A. J.: Investigating soil moisture–climate interactions in a changing climate: A review, *Earth-Sci. Rev.*, 99, 125–161, 2010.
- Tanré, D., Kaufman, Y., Herman, M., and Mattoo, S.: Remote sensing of aerosol properties over oceans using the MODIS/EOS spectral radiances, *J. Geophys. Res.-Atmospheres*, 102, 16971–16988, 1997.

- Taylor, K. E.: Summarizing multiple aspects of model performance in a single diagram, *J. Geophys. Res.-Atmos.*, 106, 7183–7192, 2001.
- The MESSy Consortium: The Modular Earth Submodel System, Zenodo [code], <https://doi.org/10.5281/zenodo.10084186>, 2023.
- The MESSy Consortium: The Modular Earth Submodel System, Zenodo [code], <https://doi.org/10.5281/zenodo.12089833>, 2024.
- Tost, H.: ECHAM5 cloud scheme, <https://envmodel.ipa.uni-mainz.de/submodels-cloud/>, last access: 12 October 2023.
- Tost, H., Jöckel, P., and Lelieveld, J.: Influence of different convection parameterisations in a GCM, *Atmos. Chem. Phys.*, 6, 5475–5493, <https://doi.org/10.5194/acp-6-5475-2006>, 2006.
- Vella, R., Forrest, M., Lelieveld, J., and Tost, H.: Isoprene and monoterpene simulations using the chemistry–climate model EMAC (v2.55) with interactive vegetation from LPJ-GUESS (v4.0), *Geosci. Model Dev.*, 16, 885–906, <https://doi.org/10.5194/gmd-16-885-2023>, 2023a.
- Vella, R., Pozzer, A., Forrest, M., Lelieveld, J., Hickler, T., and Tost, H.: Changes in biogenic volatile organic compound emissions in response to the El Niño–Southern Oscillation, *Biogeosciences*, 20, 4391–4412, <https://doi.org/10.5194/bg-20-4391-2023>, 2023b.
- Watson, D.: Comparative physiological studies in the growth of Field crops. I. Variation in net assimilation rate and leaf area between species and varieties, and within and between years, *Ann. Botany*, 11, 41–76, 1947.

3.2 Effects of biomass burning aerosols on plant productivity

This chapter contains a complete manuscript draft. I am the first author of and the main contributor to this work. I built the setups for the individual feedback analysis and performed the model simulations. I analyzed the model results and compared the simulation results to observational dataset. I prepared the manuscript and made the figures. More detailed information on the Author contributions are provided at the end of the manuscript. The supplement to this work can be found in Appendix B. After further coauthor exchange and optimization, it will be submitted to a peer-reviewed journal as:

Martin, A., Vella, R., Cirino, G., Tost, H., Lelieveld, J., and Pozzer, A.: The effect of biomass burning aerosol emissions on global gross primary productivity, Manuscript in preparation, 2025.

The effect of biomass burning aerosol emissions on global gross primary productivity

Abstract Wildfires are expected to increase in frequency and intensity by the end of the century, posing significant challenges for ecosystems, climate systems, and human activities. Aerosols from biomass burning, such as organic aerosols and brown carbon, influence air quality, radiation dynamics, and ecosystem productivity. Biomass burning aerosols (BBA) can alter photosynthetically active radiation (PAR), impacting plant productivity and carbon sequestration. Light-scattering aerosols enhance diffuse radiation, which may increase photosynthesis in shaded leaves, while absorbing aerosols reduce direct light, limiting productivity. Previous observational and model studies have analyzed the local effect of aerosols on Gross Primary Productivity (GPP), but comprehensive global assessments including and quantifying feedback mechanisms like greenhouse gas emissions and aerosol-cloud interactions are not available. These feedbacks introduce significant uncertainties, making it challenging to predict the net impact of increased aerosols on global ecosystems. This study addresses the effects of a factor of two increase of biomass burning aerosol (BBA) emissions and associated feedback mechanisms on global GPP using the ECHAM/MESSy Atmospheric Chemistry (EMAC) model recently coupled to the land surface and vegetation model JSBACH. We find that increased BBA emissions reduce GPP by $-0.87 \pm 0.05 \text{gCm}^{-2}\text{y}^{-1}$ by altering the balance between direct and diffuse PAR, if all related feedback mechanisms are switched off. Including aerosol feedback mechanisms alter the effects of increased BBA emissions on GPP with expected large uncertainties. In particular, the greenhouse gas feedback contributes to a GPP change of $0.57 \pm 11.1 \text{gCm}^{-2}\text{y}^{-1}$, while induced evapotranspiration changes, denoted as water vapor feedback, contribute with $2.49 \pm 5.36 \text{gCm}^{-2}\text{y}^{-1}$. Modified volatile organic compound (VOC) emissions, the VOC feedback, cause a reduction in GPP of $-3.4 \pm 8.45 \text{gCm}^{-2}\text{y}^{-1}$ and aerosol-cloud feedbacks contribute $-0.01 \pm 11.16 \text{gCm}^{-2}\text{y}^{-1}$. In addition to the quantification, the study highlights regional variability's: in mid and high latitudes, dominated by boreal forests, changes in GPP are primarily correlated with variations in precipitation. In contrast, in tropical and subtropical ecosystems, the strongest correlation with GPP is found with land surface temperature changes, and only secondarily with precipitation and evapotranspiration changes. It is important to understand the impact of aerosol emissions on ecosystems and the carbon cycle, given the increase in emissions from both natural and human sources. This study provides a global perspective on the complex feedback mechanisms by which aerosols affect GPP, including the interplay between aerosols, radiative forcing and vegetation productivity, using emissions from biomass burning as a case study.

3.2.1 Introduction

Biomass burning aerosols (BBA) are a major contributor to particulate matter in the atmosphere, primarily originating from forest fires, agricultural burning, and other combustion activities (Reid et al. 2005). As wildfires are projected to increase globally, regional organic aerosol loading could rise by up to 40% (Carslaw et al. 2010). These aerosols have multiple impacts on the Earth's climate and ecosystems by altering atmospheric composition, radiative forcing, cloud properties and nutrient deposition (Reid et al. 2005; Carslaw et al. 2010). BBAs can directly and indirectly affect the carbon cycle, particularly Gross Primary Production (GPP) – the total carbon fixed by plants through photosynthesis. GPP is a critical measure of ecosystem health and carbon sequestration potential, responding sensitively to changes in atmospheric conditions, water availability, and radiation. Wildfire aerosols affect the amount of solar radiation reaching the surface, especially in the wavelength range from 0.45–0.75 μm , which is referred to as photosynthetically active radiation (PAR) (Carslaw et al. 2010). This effect can vary depending on several factors including aerosol type, concentration, size distribution, and atmospheric conditions. BBA like black carbon mostly absorb incoming solar radiation, reducing the amount of direct PAR available for photosynthesis. However, organic aerosols, such as organic carbon, sulfate particles and biogenic secondary organic aerosols, tend to scatter radiation more effectively, resulting in an increase in diffuse radiation. This increased diffuse radiation is found to penetrate deeper into the canopy and reach shaded leaves more effectively, potentially enhancing photosynthesis (Zhou et al. 2020; Unger et al. 2017; Strada et al. 2016; Rap et al. 2015). Previous studies have analyzed the relationship between aerosol-induced changes in radiation and GPP, primarily focusing on isolating the effects of fires on vegetation through changes in diffuse radiation (Bian et al. 2021; Rap et al. 2015; Ezhova et al. 2018; Moreira et al. 2017; Rap et al. 2018; Malavelle et al. 2019; Rodrigues et al. 2023; Cirino et al. 2014; Carslaw et al. 2010; Gu et al. 2002). However, these studies do not specifically account for other critical interactions associated with increased biomass burning aerosol emissions. For example, BBA can alter surface ozone concentrations (Pacifico et al. 2014; Delany et al. 1985; Desservettaz et al. 2023), influence evapotranspiration and precipitation patterns through changes in vegetation (Spracklen et al. 2012), and modify volatile organic compound (VOC) concentrations (Desservettaz et al. 2023; Yao et al. 2023). Additionally, they lead to shifts in cloud cover and induce surface cooling (Chang et al. 2024; Lohmann et al. 2005; Forster et al. 2007; Haywood et al. 2000; Andreae et al. 2004; Tosca et al. 2013). These processes, in turn, can significantly affect GPP, complicating the overall understanding of fire impacts on ecosystems. This study aims to account

for those interactions by disentangling the multiple feedback mechanisms through which BBAs affect GPP. Using a fully coupled Earth-System model, we examine the isolated and combined effects of BBA emissions on GPP, focusing on changes in radiation, water vapor, GHG concentrations, VOC emissions, and aerosol-cloud and aerosol-radiation interactions on a global scale. This work is organized as follows: Section 3.2.2 is divided a description of the EMAC model and the simulation setups and an overview of the observational data sets used for the model validation, in particular FLUXNET and AERONET data sets. The results are presented in section 3.2.3, while first the model validation based on the observational datasets are discussed followed by an analysis of the feedback effects of a twofold increase in BBA on GPP. Finally, section 3.2.4 provides a summary of the main findings and conclusions of the study.

3.2.2 Methods

The EMAC Model

The ECHAM/MESSy Atmospheric Chemistry (EMAC) model is a numerical chemistry and climate simulation system that includes sub-models describing tropospheric and middle atmosphere processes and their interaction with oceans, land and human influences (Jöckel et al. 2010a). It uses the second version of the Modular Earth Submodel System (MESSy2) to link multi-institutional computer codes. The core atmospheric model is the fifth-generation European Center Hamburg general circulation model (ECHAM5, (Roeckner et al. 2006)). The physics subroutines of the original ECHAM code have been modularized and re-implemented as MESSy submodels and have continuously been further developed. Only the spectral transform core, the flux-form semi-Lagrangian large-scale advection scheme, and the nudging routines for Newtonian relaxation remain from ECHAM. Further details on EMAC are documented by (Jöckel et al. 2016) and can be found on the MESSy website*. In this study, we utilized EMAC (MESSy version 2.55.0) at a resolution of T63L31ECMWF. This configuration corresponds to a spherical truncation of T63, which translates to a quadratic Gaussian grid with approximately 1.8 by 1.8 degrees spacing in latitude and longitude, and includes 31 vertical hybrid pressure levels extending up to 10 hPa. Each simulation conducted in this study includes 30 years of simulation data from January 1992 to December 2020. The simulations are nudged towards meteorological reanalysis data (ERA-Interim, (Berrisford et al. 2011)) from the European Center for Medium-Range Weather Forecasts (ECMWF) (Jeuken et al. 1996; Jöckel et al. 2006). An overview of the utilized submodels

* <https://www.messy-interface.org>

and a concise description of each can be found in the Supplement, Table S1. This work employs the same model setup presented in Kohl et al. 2023. The Biomass burning and agricultural waste burning emissions are based on burned dry matter and fire type data from the GFED (Global Fire Emissions Database) database (Randerson et al. 2017) using the BIOBURN submodel (Andreae 2019; Kaiser et al. 2012). EMAC was recently coupled to the Jena Scheme for Biosphere-Atmosphere Coupling in Hamburg (JSBACH) version four (Martin et al. 2024). JSBACH is a land-surface model designed to represent a wide range of biogeochemical processes in ecosystems (Reick et al. 2021; Schneck et al. 2022). It replaces the soil water model of the former surface model SURFACE with a more comprehensive hydrological model, improving the representation of surface energy fluxes and reducing biases in surface temperature and plant stress. JSBACH enables the analysis of biogeochemical processes on time scales from minutes to decades, allowing for a detailed understanding of land-atmosphere interactions and their impact on atmospheric chemistry. It operates on five snow layers and three canopy layers. Additionally it comprises five soil layers that reach depths of up to 9.8 meters below the surface. It incorporates 11 plant functional types (PFTs), including tropical and extra-tropical broadleaf evergreen and deciduous trees, rain-green shrubs, deciduous shrubs, C_3 - and C_4 -grass, as well as C_3 - and C_4 -pasture, and crops (those PFTs are listed together with the model validation datasets in section 3.2.2 and the PFTs in Supplement Table S2). The JSBACH initialization utilizes carbon pools, soil, and land property data from 2005, expected to stabilize within five years (Martin et al. 2024). While atmospheric variables stabilize rapidly within days, soil moisture is projected to adjust the slowest, with a maximum adjustment time of one year (Hagemann et al. 2015; Schneck et al. 2022). Consequently, the initial years (1990 and 1991) serve as a spin-up period and are excluded from the study. The version of JSBACH used here contains a simple representation of the nitrogen cycle in the soil which, according to the photosynthesis model following Farquhar et al. 1980, is independent of nutrient availability and only describes nitrogen limitation due to changes in atmospheric CO_2 (Reick et al. 2021). The temperature dependence of the electron transport capacity also follows Farquhar et al. 1980, assuming a linear temperature dependence corresponding to the vegetative temperature (Reick et al. 2021). Plant damage caused by tropospheric ozone is not included in this study. Light interception within the three canopy layers follows the two stream approximation by Sellers 1985 with absorption and scattering losses of incident radiation (including direct and diffuse) through the canopy. The absorbed Photosynthetic Active Radiation (PAR) is dependent on LAI and solar zenith angle.

Simulation setups

To investigate the feedback of BBA on GPP, five pairs of simulation setups were designed. Each pair consists of a reference simulation with standard BBA emissions (S_{REF}^*) and a simulation with twofold BBA emissions (S_{INC}^*). In the first pair of simulations ($S1_{\text{REF}}$ and $S1_{\text{INC}}$), all feedbacks from increased BBA emissions, except for changes in the direct and diffuse components of photosynthetically active radiation reaching vegetation, are turned off. This setup is implemented using two radiation calls: one that accounts for BBA-induced changes in diffuse radiation and passes this information to the JSBACH submodel, and a second, BBA-independent call that ensures the overall atmospheric dynamics remain identical in both runs. Additionally, the LAI is nudged towards a climatology, ensuring that changes in GPP do not affect vegetation growth. Greenhouse gas concentrations are held constant at their concentration in 2009 and are unaffected by BBA emissions, ensuring identical climate dynamics in both simulations. As a result, the availability of soil water and the leaf canopy temperature remains the same in the two simulations. These runs isolate the BBA feedback on GPP through changes in PAR_{dir} and PAR_{dif} , labeled F_{BBA} , which is calculated as the difference between $S1_{\text{INC}}$ and $S1_{\text{REF}}$:

$$F_{\text{BBA}} = S1_{\text{INC}} - S1_{\text{REF}} \quad (3.1)$$

The aim of the second pair of simulations ($S2_{\text{REF}}$ and $S2_{\text{INC}}$) is to isolate the feedback of water vapor changes due to LAI variations from changing GPP. For this, LAI can vary in response to changes in GPP, while VOC emissions remain constant. This setup includes both F_{BBA} and the feedback of water vapor changes due to LAI variations from changing GPP, labeled F_{WV} . F_{WV} can then be computed as:

$$F_{\text{WV}} = (S2_{\text{INC}} - S2_{\text{REF}}) - F_{\text{BBA}} \quad (3.2)$$

The third simulation pair ($S3_{\text{REF}}$ and $S3_{\text{INC}}$) follows the S1 setup, but allows GHG concentrations to be affected by BBA emissions. This setup accounts for F_{BBA} and the feedback of GHG changes due to BBA emissions, denoted as F_{GHG} . The value of F_{GHG} is calculated as follows:

$$F_{\text{GHG}} = (S3_{\text{INC}} - S3_{\text{REF}}) - F_{\text{BBA}} \quad (3.3)$$

In the fourth pair of simulations ($S4_{\text{REF}}$ and $S4_{\text{INC}}$), the feedbacks F_{BBA} , F_{WV} , and F_{GHG} are included, along with biogenic VOC emission changes due to LAI variations caused by BBA emissions, labeled F_{VOC} . The F_{VOC} feedback is given by:

$$F_{\text{VOC}} = (S4_{\text{INC}} - S4_{\text{REF}}) - F_{\text{GHG}} - F_{\text{WV}} - F_{\text{BBA}} \quad (3.4)$$

The fifth and final pair of simulations ($S5_{\text{REF}}$ and $S5_{\text{INC}}$) includes all previous feedbacks from $S4$, and additionally accounts for the direct and indirect effects of BBA on clouds and radiation. These feedbacks combined, labeled $F_{\text{CLOUD\&RAD}}$, are calculated as:

$$F_{\text{CLOUD\&RAD}} = (S5_{\text{INC}} - S5_{\text{REF}}) - F_{\text{VOC}} - F_{\text{GHG}} - F_{\text{WV}} - F_{\text{BBA}} \quad (3.5)$$

The total BBA feedback on GPP is the sum of all individual feedbacks, denoted as F_{sum} , which corresponds to the difference between $S5_{\text{INC}}$ and $S5_{\text{REF}}$:

$$F_{\text{sum}} = (S5_{\text{INC}} - S5_{\text{REF}}) = F_{\text{BBA}} + F_{\text{WV}} + F_{\text{GHG}} + F_{\text{VOC}} + F_{\text{CLOUD\&RAD}} \quad (3.6)$$

It should be noted that the feedbacks in the physical climate–biosphere system are not inherently additive, since radiation, hydrology, vegetation, and atmospheric chemistry interact nonlinearly. However, our subtraction-based experimental design enforces an additive partitioning of the total BBA feedback into the individual components (F_{BBA} , F_{GHG} , F_{WV} , F_{VOC} , and $F_{\text{CLOUD\&RAD}}$), which makes them diagnostically additive even though they are coupled in reality. An overview of the simulation setups and the included feedback mechanisms is provided in Table 3.1. Figure 3.1 provides a highly simplified graphical overview of the individual feedback mechanisms and the total feedback sum.

Table 3.1: Simulation setups and included feedback mechanisms of BBA emissions on GPP

	BBA emissions	F_{BBA}	F_{GHG}	F_{WV}	F_{VOC}	$F_{\text{CLOUD \& RAD}}$
<i>Simulation Setup</i>						
$S1_{\text{REF}}$	1xBBA	X	-	-	-	-
$S1_{\text{INC}}$	2xBBA	X	-	-	-	-
$S2_{\text{REF}}$	1xBBA	X	-	X	-	-
$S2_{\text{INC}}$	2xBBA	X	-	X	-	-
$S3_{\text{REF}}$	1xBBA	X	X	-	-	-
$S3_{\text{INC}}$	2xBBA	X	X	-	-	-
$S4_{\text{REF}}$	1xBBA	X	X	X	X	-
$S4_{\text{INC}}$	2xBBA	X	X	X	X	-
$S5_{\text{REF}}$	1xBBA	X	X	X	X	X
$S5_{\text{INC}}$	2xBBA	X	X	X	X	X

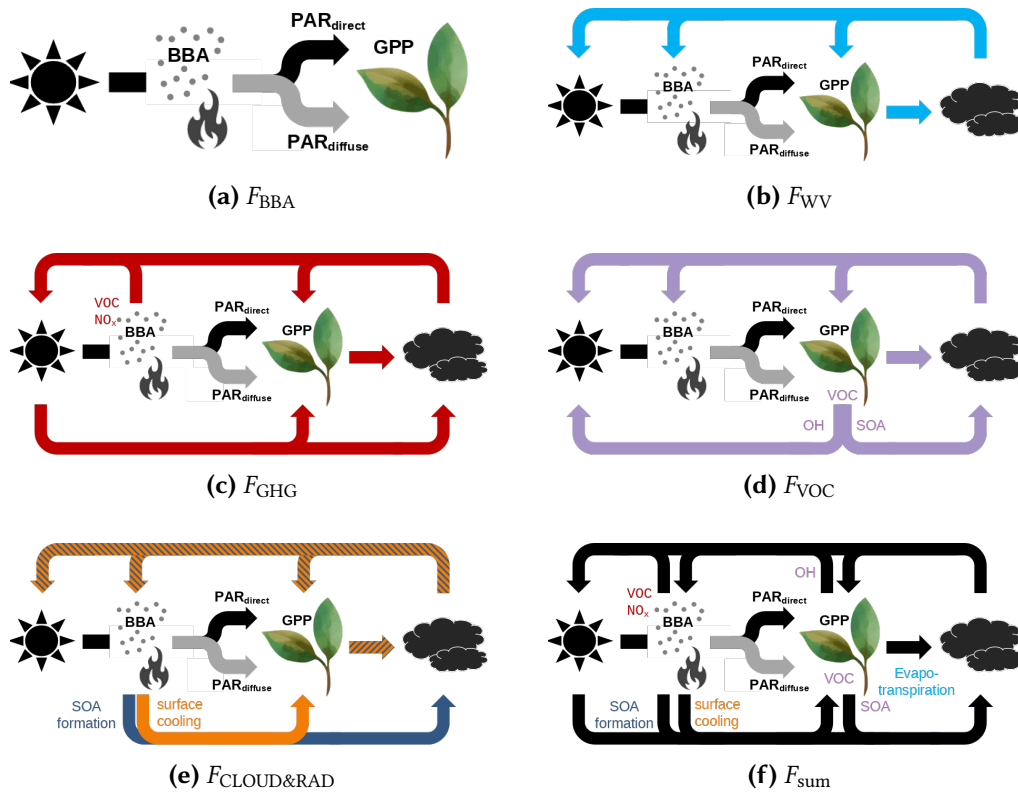


Figure 3.1: Simplified graphical schematics of the individual feedback mechanisms F_{BBA} (a), F_{WV} (b), F_{GHG} (c), F_{VOC} (d), $F_{CLOUD\&RAD}$ (e) and their sum F_{sum} (f).

Observations

The model output is validated using FLUXNET and AERONET datasets between January 2007 and December 2010. Five measurement sites with different PFTs were selected based on their data coverage and the availability of both FLUXNET and AERONET measurements. A list of all sites with their corresponding PFTs and detailed percentages of PFT coverage is provided in Table S2 of the Supplement. Figure 3.2 shows a corresponding map of the predominant PFTs within the EMAC/JSBACH simulation with the measurement sites marked by crosses. To assess the model results, we compare PAR) in correlation with aerosol optical depth (AOD) and the fraction (f) of incoming shortwave radiation (I) to the incoming shortwave radiation under clear sky conditions (I_{clr}), accounting for cloud effects in the measurements, viz.

$$f = \frac{I(\text{AOD} \geq 0.1, \text{all sky})}{I_{clr}(\text{AOD} < 0.1, \text{clear sky})} \quad (3.7)$$

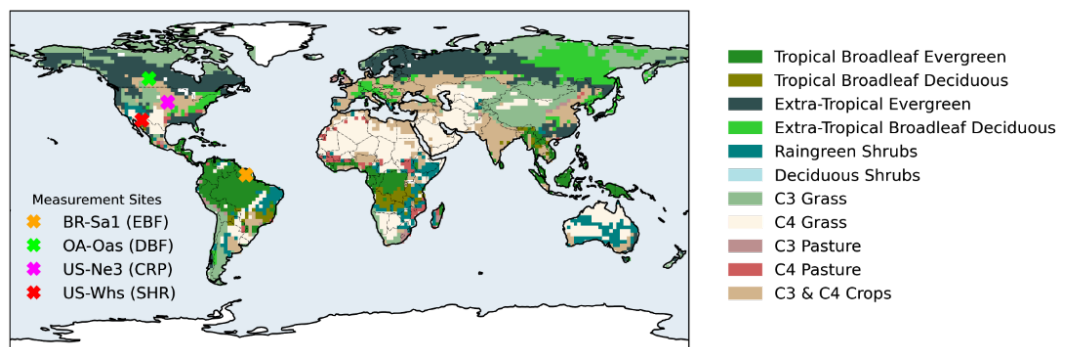


Figure 3.2: Measurement Sites and corresponding predominant plant Type in EMAC/JS-BACH

The relative irradiance (f) is used here as a proxy for sky coverage observations when direct measurements of clouds and aerosol smoke are unavailable. ($AOD < 0.1$, *clear sky*) was considered a background condition for clear-sky (i.e., cloudless and free of biomass burning aerosols). I_{clr} is obtained following Gu et al. 1999, applied by several previous studies (e.g., Oliveira et al. 2007; Cirino et al. 2014; Rodrigues et al. 2023).

FLUXNET

The FLUXNET datasets are a collection of observations from a global network of micro-meteorological tower sites that measure ecosystem exchange of carbon dioxide, water vapor, and energy using the eddy covariance technique (Baldocchi et al. 2001). These datasets provide continuous, long-term, and high-frequency data on the fluxes of these components between the biosphere and the atmosphere. Depending on the measurement site, the fluxes are provided in half-hourly or hourly frequency. For all locations the Subset Data Product was used, a close description of which can be found in at the Fluxnet data product website[†]. An overview and assessment of statistical and random errors of the FLUXNET datasets is given in Williams et al. 2009. All stations have an open data policy and incorporate at least two years of measurements of the incoming shortwave radiation (I), PAR and GPP. PAR_{dif} is not available for the listed Fluxnet site used in this study, therefore the fraction of PAR_{dif} ($f_{PAR,dif}$) is calculated based on the widely used method of Gu et al. 1999 (applied by Rodrigues et al. 2023; Jing et al. 2010; Zhang et al. 2010; Bai et al. 2012). Gu et al. 1999 combined the work of Reindl et al. 1990 and Spitters et al. 1986 to partition the diffusive and direct parts of the incoming shortwave

[†] <https://fluxnet.org/data/fluxnet2015-dataset/subset-data-product/>, Accessed on 08-04-2024

radiation. This can be done using the measured incoming shortwave radiation at the surface I , the solar zenith angle (SZA) and the current day of the year (t_d). First the extraterrestrial irradiance at horizontal plane parallel to earth I_{ext} is calculated following Spitters et al. 1986:

$$I_{ext} = SC \left[1 + 0.033 \cos\left(360 \cdot \frac{t_d}{365}\right) \right] \sin(\beta) \quad (3.8)$$

with the solar constant $SC = 1370 \text{ W m}^{-2}$ and the solar elevation angle $\beta = 90 - \text{SZA}$. Using the clearness index k_t , with $k_t = \frac{I}{I_{ext}}$, the fraction of the total diffusive radiation (visible and near-infrared) at the horizontal plane on Earth's surface I_{dif} and I can be determined following Reindl et al. 1990:

$$\frac{I_{dif}}{I} = \begin{cases} 1.020 - 0.254k_t + 0.0123 \sin(\beta) & \text{for } 0 \leq k_t \leq 0.3 \text{ and } \frac{I_{dif}}{I} \leq 1.0 \\ 1.400 - 1.749k_t + 0.177 \sin(\beta) & \text{for } 0.3 < k_t < 0.78 \text{ and } 0.1 \leq \frac{I_{dif}}{I} \leq 0.97 \\ 0.486k_t - 0.182 \sin(\beta) & \text{for } k_t \geq 0.78 \text{ and } 0.1 \leq \frac{I_{dif}}{I} \end{cases} \quad (3.9)$$

Lastly, following Spitters et al. 1986 the fraction of diffusive incoming PAR is given as:

$$f_{PAR,dif} = \frac{[1 + 0.3(1 - \frac{I_{dif}}{I})\frac{I_{dif}}{I}]}{1 + (1 - \frac{I_{dif}}{I}) \cos(90 - \beta) \cos(\beta)} \quad (3.10)$$

AERONET

The Aerosol Robotic Network (AERONET) dataset is a global network of ground-based solar photometers and radiometers designed to measure the optical properties of aerosols (<https://AERONET.gsfc.nasa.gov/>, Holben et al. 1998). Managed by the National Aeronautics and Space Administration (NASA) and international partners, AERONET provides long-term, continuous, and easily accessible data to support aerosol research and validate satellite observations. Column AOD is calculated from solar photometer measurements of direct solar radiation. We use the Level 2.0 AOD data product with automatic cloud clearance and quality assurance and pre- and post-field calibration applied. The Criterion for level 2.0 data, is at least three wavelength combinations must include 440 nm, 870 nm and either 490 nm, 500 nm or 675 nm, outliers are removed and the AOD for each channel must be greater than or equal to 0.02 m, where m is the optical air mass. The assessment of potential

measurement errors in the AOD datasets is for example provided in Sinyuk et al. 2012 and Dubovik et al. 2000. Sinyuk et al. 2012 indicate an average calibration uncertainty of 0.01 for the AOD measurements. For evaluating the AERONET AOD against the modeled AOD, values at a reference wavelength of 500 nm are used, while for the calculation of $f_{PAR,dif}$ SZA is taken.

3.2.3 Results and discussion

Validation results

Figure 3.3 shows the hourly averages of PAR and its diffuse and direct parts against f (the fraction of incoming shortwave radiation and incoming shortwave radiation at the surface under clear sky conditions, Eq. 3.7) for the four different measurement sites: BR-Sa1 (a), OA-Oas(b), US-Wkg (c) and US-Ne3 (d) (Figure 3.2). The data is filtered for solar zenith angles (SZA) between 30° and 60° , and the corresponding SZA is indicated by the color of the data points. The left panels show the data derived from the measurements (color-coded in blue), while the right panels show the same data derived from the EMAC/JSBACH simulation (color-coded in red). Both measured and modeled data show a positive correlation between PAR and f for all sites. PAR increases almost linearly with f , while the diffuse and direct parts of PAR show non-linear behavior with increasing f . After SZA filtering, the model tends to slightly overestimate PAR compared to the measurements, especially for higher values of f and clearer sky conditions. This overestimation is reflected in PAR_{dir} . In contrast, PAR_{dif} is slightly underestimated by the model compared to the observations for all four PFTs. The maximum amount of radiation reaching the surface is of the same order of magnitude for all four sites in the modeled data, while the observed PAR is slightly higher at the BR-Sa1 site than at the other sites. The variability of the data increases with increasing f for both methods, although the scatter of the observed data is somewhat more pronounced. For all locations and data types, the higher solar zenith angles correspond to lower PAR values, which is clearly shown by the color variations. Overall, there is good agreement between measured and modeled PAR values for all sites and corresponding plant function types. Both the measurements and the models show a clear positive relationship between PAR and f . Especially the distribution of PAR_{dif} with f is similar in the modeled results as in the observations, indicating a generally good performance of the model in predicting PAR_{dif} across different PFT's and for different solar zenith angles.

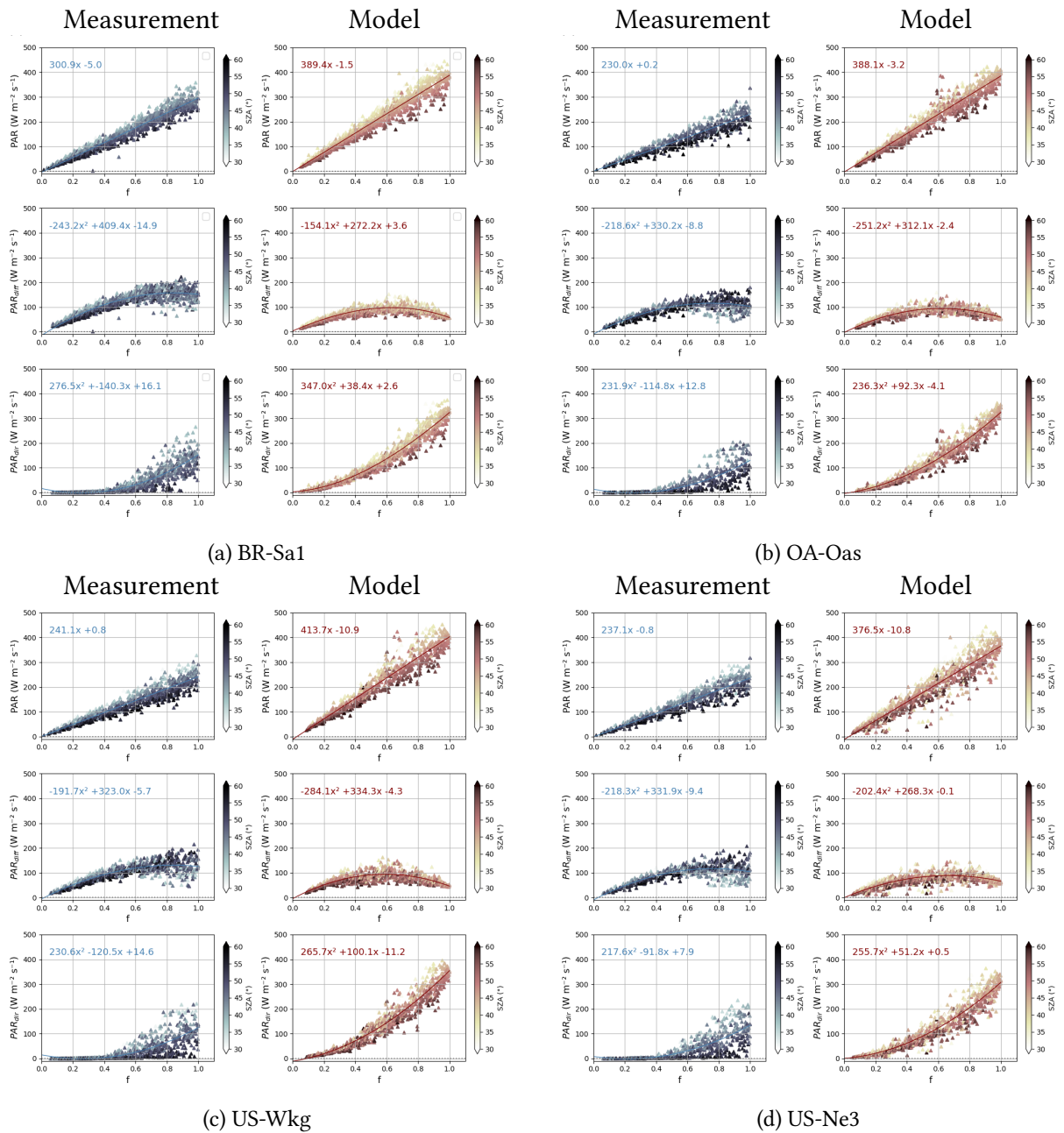


Figure 3.3: Hourly averages of PAR and its diffuse and direct components plotted against fraction f for BR-Sa1 (a), OA-Oas (b), US-Wkg (c), and US-Ne3 (d). Left panels show measured data (blue), while right panels show simulation results (red). Data are filtered for 30° – 60° solar zenith angles and are from 2007–2010. Simulation results are based on S4REF.

Feedbacks

In the following section, each of the GPP feedbacks resulting from a factor of two increase of BBA emissions - namely F_{BBA} , F_{GHG} , F_{WV} , F_{VOC} , $F_{\text{CLOUD\&RAD}}$ and F_{sum} - are analyzed individually. All standard deviations are computed as the area-weighted, year-to-year standard deviation of the differences between the simulation including BBA and the reference simulation with standard BBA, integrated over all grid cells. Figure 3.4 shows global maps illustrating the spatial distribution of GPP changes in $\text{g C m}^{-2} \text{ yr}^{-1}$ due to these feedback mechanisms. The feedback of BBA on GPP (F_{BBA}), scaled by a factor of 10 to match the color bar used for the other feedbacks, is shown in panel (a). Panel (b) shows the feedback of water vapor changes due to leaf area index changes caused by BBA on GPP (F_{WV}). Panel (c) shows the feedback of greenhouse gas concentration changes due to BBA on GPP (F_{GHG}). The feedback of volatile organic compound changes due to leaf area index changes caused by BBA on GPP is shown in panel (d) (F_{VOC}). Panel (e) shows the feedback of cloud cover and radiation changes due to BBA on GPP ($F_{\text{CLOUD\&RAD}}$). Finally, the total feedback sum (F_{sum}) is shown in panel (f). The data are based on monthly averages from 1992 to 2020. Figures 3.4 and the following figures use color coding to indicate positive (red) and negative (blue) changes.

Feedback of biomass burning aerosol on GPP via changes in PAR_{dir} and PAR_{dif}

The spatial distribution of changes in AOD (a), PAR_{dir} (b), and PAR_{dif} (c) due to a factor of two increase of BBA emissions is shown in Figure 3.5, based on monthly averages from 1992 to 2020. The data is derived from simulation setup S1, in which the vegetation is only affected by the change in ratio of direct to diffuse PAR due to BBA emission doubling. All other parameters are fixed. The model suggests a significant yearly-averaged AOD increase over biomass burning regions in Central Africa, parts of South America and East Asia, with a weaker signal over North America, Africa, Siberia and Australia. Regions with the least change are Europe and the Middle East. The overall global AOD is increased by $15.36\% \pm 1.57\%$. The detailed distribution of the modified aerosol types based on the S1 setup are listed in Appendix 3.8, with the largest changes found for black carbon (64%) and organic carbon (71%). As aerosols scatter and absorb sunlight, the amount of direct PAR reaching the surface is reduced by $1.04 \text{ W m}^{-2} \pm 0.12 \text{ W m}^{-2}$, corresponding to a decrease in direct PAR in all regions in which AOD increases of $1.37\% \pm 0.17\%$. Diffuse PAR is increased by $1.04 \text{ W m}^{-2} \pm 0.12 \text{ W m}^{-2}$ in those regions, corresponding to a global average change of PAR_{dif} of $3.52\% \pm 0.45\%$.

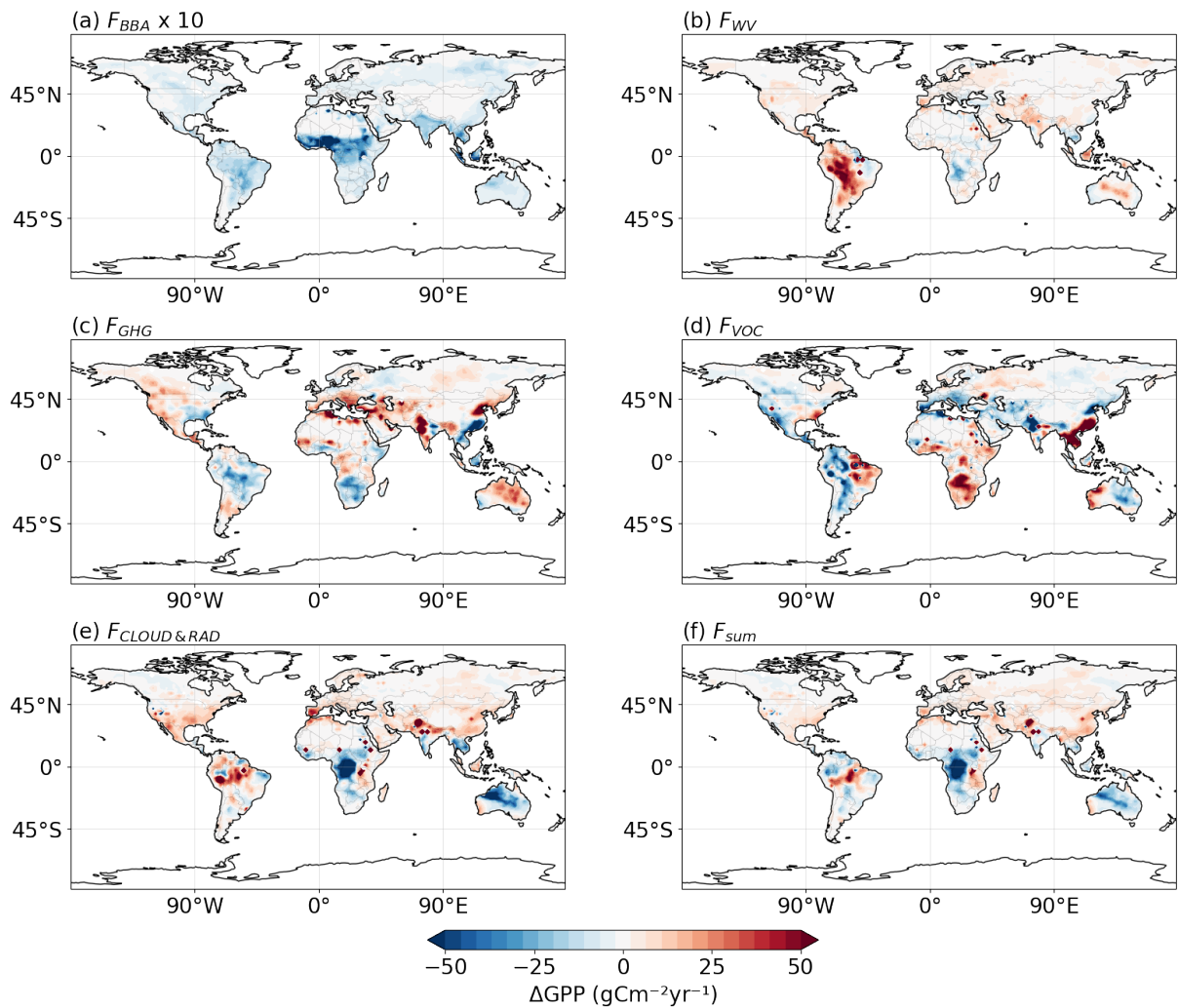


Figure 3.4: GPP change in ($\text{gCm}^{-2}\text{yr}^{-1}$) due to twofold BBA emissions. The feedback of BBA on GPP (F_{BBA}), scaled by a factor of 10 to adapt it to the same color-bar as the other feedbacks, is shown in (a), the feedback of water vapor changes due to leaf area index variation caused by BBA on GPP (F_{WV}) is shown in (b), the feedback of greenhouse gas concentration change due to BBA on GPP (F_{GHG}) is shown in (c), the feedback of volatile organic compound changes due to leaf area index variation caused by BBA on GPP (F_{VOC}) is shown in (d) and feedback of cloud cover and radiation changes due to BBA on GPP ($F_{CLOUD\&RAD}$) is shown in (e). The total feedback sum (F_{sum}) is displayed in (f). The data is based on monthly averages from 1992 to 2020.

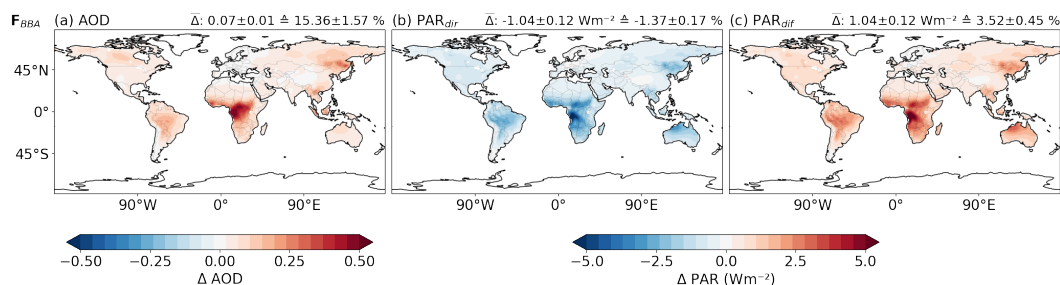


Figure 3.5: Annual average change in AOD (a), PAR_{dir} (b) and PAR_{dif} (b) due to twofold BBA emissions for F_{BBA} . The data is based on monthly averages from 1992 to 2020.

Figure 3.4a shows the isolated feedback of BBA on GPP (F_{BBA}). F_{BBA} is relatively small compared to the remaining feedbacks; for better comparison it is scaled by a factor of 10 to adapt it to the same color bar as the other feedbacks. Increasing the BBA emissions by a factor of two leads to an overall reduction in GPP by $-0.87 \pm 0.05 \text{ g C m}^{-2} \text{ yr}^{-1}$. The most pronounced reduction is found over Central Africa, consistent with the largest increase in AOD (Figure 3.4a). Weaker but still significant changes are visible over South America, Siberia, Southeast Asia, and Australia. The results indicate a negative correlation between changes in BBA and GPP. BBA emissions consistently reduce GPP across various locations and plant functional types, with the most significant impact occurring near the emission source, where AOD is increased. Separating the feedbacks by regions (Table 3.2) and by PFT (Table B7), F_{BBA} consistently shows a negative effect of the changing ratio of diffuse and direct PAR on GPP, with the largest values found for Africa ($-1.96 \pm 0.08 \text{ g C m}^{-2} \text{ yr}^{-1}$), northwest Amazon ($-1.44 \pm 0.06 \text{ g C m}^{-2} \text{ yr}^{-1}$), and central Amazon ($-1.28 \pm 0.05 \text{ g C m}^{-2} \text{ yr}^{-1}$). The strongest effect on PFTs is found for C3&C4 crops ($-0.58 \pm 0.08 \text{ g C m}^{-2} \text{ yr}^{-1}$), rain-green shrubs ($-0.16 \pm 0.01 \text{ g C m}^{-2} \text{ yr}^{-1}$), and tropical broadleaf evergreen forest ($-0.11 \pm 0.05 \text{ g C m}^{-2} \text{ yr}^{-1}$). Direct sunlight reaching the surface is decreased by increasing AOD. While the total amount of PAR remains the same for both emission scenarios, PAR_{dir} decreases by 1.32% globally. Conversely, the amount of diffuse light reaching the surface increases, resulting in a global increase in PAR_{dif} of 3.61%. Despite the greater increase in diffuse radiation compared to the decrease in direct radiation, the reduction in direct sunlight cannot be fully compensated by the increased diffuse light. This suggests that the diffuse fertilization effect — a phenomenon where enhanced diffuse light can boost photosynthesis — does not sufficiently counterbalance the reduced direct radiation caused by higher aerosol emissions in this scenario. The effect of diffuse radiation fertilization refers to the

concept of scattering aerosols increasing the amount of diffuse sunlight reaching the lower levels of the canopy and thus more leaves potentially improving photosynthesis, especially in densely vegetated environments (Unger et al. 2017; Strada et al. 2016; Rap et al. 2015). In JSBACH, photosynthesis is calculated based on the radiation penetration depth, which depends on the solar zenith angle, without differentiating between sunlit and shaded leaves. Consequently, due to the parameterization, it is to be expected that in tropical regions, most of the radiation reaching and being absorbed by the canopy is direct radiation due to the high zenith angle. A reduction in direct light would therefore reduce the amount of radiation reaching the canopy, leading to less absorption by the canopy and consequently lower GPP. Conversely, in mid to high latitudes, the zenith angle is more variable, so less direct and more diffuse radiation reaches the canopy layers. An increase in diffuse radiation would be expected to increase absorption in the lower layers and thus increase GPP. Under a twofold BBA emission scenario, the model predicts an increase of absorbed PAR (*aPAR*) in the lowest canopy layer, and a decrease of *aPAR* in the top canopy layers (Figure 3.6a). Corresponding to the changes in *aPAR*, GPP decreases in the top canopy layers, while it shows a weak increase in the lowest canopy layer (Figure 3.6b). The reduction in GPP in the top layers compensates for the increase in the lowest layer. This could be explained by the presence of the nitrogen-rich enzyme Rubisco, essential for carbon assimilation. The enzyme is predominantly concentrated in the well-lit leaves at the upper part of the canopy. In JSBACH, this variation in photosynthetic capacity across the canopy is addressed using a nitrogen scaling approach (see Section 5.3 of Reick et al. 2021; Farquhar et al. 1980). Consequently, in JSBACH photosynthesis is more effective in the upper layers than in the lower layers, and thus a reduction of light at the top of the canopy has a stronger effect on GPP than the increase in diffuse light absorption in the bottom canopy layer.

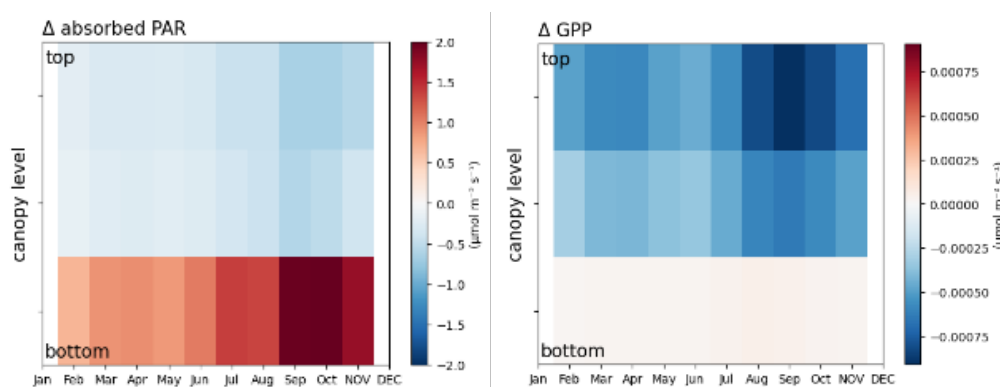


Figure 3.6: Zonally averaged monthly relative difference of absorbed PAR (*aPAR*) (a) and GPP (b) of the three canopy level averaged over the years 1992 to 2020.

Feedback of water vapor changes due to LAI variation caused by BBA on GPP

Figure 3.4c shows the feedback of atmospheric water vapor changes due to LAI variation caused by BBA on GPP (F_{WV}). Whereas F_{BBA} leads to a negative effect on GPP everywhere, F_{WV} shows several regions of increasing GPP. The most dominant increase is found in the Amazon region. Isolated areas of strong increase in GPP are found in northeastern Brazil, close to the mouth of the Amazon River, and in central Sudan. The latter coincides with an area dominated by crops whose growth can be triggered by changes in precipitation. A comparison of the feedback in the different regions (Table 3.2) shows that some regions, such as the central Amazon ($27.89 \text{ g C m}^{-2}\text{yr}^{-1} \pm 78.93 \text{ g C m}^{-2}\text{yr}^{-1}$) and the northwest Amazon ($5.53 \text{ g C m}^{-2}\text{yr}^{-1} \pm 44.17 \text{ g C m}^{-2}\text{yr}^{-1}$), have potential for positive water vapor feedback, but with considerable uncertainty. In contrast, regions like Africa ($-6.68 \text{ g C m}^{-2}\text{yr}^{-1} \pm 27.54 \text{ g C m}^{-2}\text{yr}^{-1}$) show negative water vapor feedback, suggesting that these areas might experience more droughts or reduced humidity under higher BBA emissions and warming conditions. When analysing F_{WV} for each plant type, the multi-year mean F_{WV} is positive for all plant types except tropical broadleaf deciduous; however, it is not possible to unambiguously link the effects of F_{WV} feedback to different plant types, as the uncertainties remain too large (Table B7). Although the inter-annual average of F_{WV} is $2.49 \text{ g C m}^{-2}\text{yr}^{-1}$, the high inter-annual variability of $\pm 5.36 \text{ g C m}^{-2}\text{yr}^{-1}$ indicates that the result is not statistically significant. Consequently, no definitive conclusions regarding the actual feedback can be drawn. The effect of changes in LAI on climate — through its impact on evapotranspiration and atmospheric water vapor content, which subsequently affects cloud formation and GHG changes — has a stronger effect on GPP than the effect of twofold BBA emissions.

Feedback of greenhouse gas (GHG) concentration change due to BBA on GPP

The changes in GPP due to F_{GHG} are more pronounced than those observed for F_{BBA} and F_{WV} (Figure 3.4d). GPP increases in South America and the Congo Basin, with a hotspot in India and northeastern Australia. GPP is reduced in northeastern India and over Europe. Upon multi-annual average doubling, BBA increases GPP by $0.56 \text{ g C m}^{-2}\text{yr}^{-1}$ with comparably large annual variability of $\pm 11.1 \text{ g C m}^{-2}\text{yr}^{-1}$. This feedback, like F_{WV} , is not significant due to the large variability caused by changing greenhouse gas concentrations, which affect the overall radiative balance. Biomass burning releases VOCs and NO_x, precursors for tropospheric ozone formation — a potent greenhouse gas. Furthermore, BBAs

contain absorbing aerosols, such as black carbon. Increased sunlight absorption contributes to a reduction of hydroxyl radical (OH) formation by inhibiting the reaction of water vapor with ultraviolet light. This leads to a decrease in the OH burden, subsequently extending the lifetime of methane – another potent greenhouse gas. Increased GHG concentrations intensify the greenhouse effect, resulting in a greater radiative imbalance at the Top of the Atmosphere, with a global average increase in RAD_{TOA} of 18.27%, equivalent to 0.58 W m^{-2} . The shift in the radiation balance introduces significant variability in the global climate, making it difficult to clearly attribute changes in GPP solely to the doubling of BBA. The resulting climate dynamics mask the direct effects of BBA on GPP, complicating any clear differentiation between BBA effects and changes in global climate dynamics. When comparing F_{GHG} across different plant types, the multi-annual mean F_{GHG} is highest for C3 and C4 crops ($0.82 \text{ g C m}^{-2}\text{yr}^{-1} \pm 7.55 \text{ g C m}^{-2}\text{yr}^{-1}$). This trend is also evident in regional comparisons, where a notable increase in GPP is observed in India. However, again the uncertainty remains too large to draw definitive conclusions about the effect of F_{GHG} on GPP (Table B7).

Feedback of volatile organic compound (VOC) changes due to LAI variation caused by BBA on GPP

The feedback of Volatile Organic Compounds (VOC) changes due to LAI variation caused by twofold BBA emissions on GPP (F_{VOC}) is illustrated in Figure 3.4e. In the Southern Hemisphere, F_{VOC} shows positive values at the northwest Amazon ($7.13 \text{ g C m}^{-2}\text{yr}^{-1} \pm 17.97 \text{ g C m}^{-2}\text{yr}^{-1}$), central and southern Africa ($8.47 \text{ g C m}^{-2}\text{yr}^{-1} \pm 10.63 \text{ g C m}^{-2}\text{yr}^{-1}$), parts of India, and southwest Australia, while it remains negative in central Amazon ($-31.27 \text{ g C m}^{-2}\text{yr}^{-1} \pm 65.6 \text{ g C m}^{-2}\text{yr}^{-1}$), northwest India ($-2.89 \text{ g C m}^{-2}\text{yr}^{-1} \pm 136.44 \text{ g C m}^{-2}\text{yr}^{-1}$), and northwest Australia. In the Northern Hemisphere, it is negative over Siberia ($-2.02 \text{ g C m}^{-2}\text{yr}^{-1} \pm 9.34 \text{ g C m}^{-2}\text{yr}^{-1}$) and positive over northern Europe ($2.08 \text{ g C m}^{-2}\text{yr}^{-1} \pm 22.27 \text{ g C m}^{-2}\text{yr}^{-1}$). On a multi-annual average, F_{VOC} is negative across all PFTs (see Table B7) and on a global mean, $-3.4 \text{ g C m}^{-2}\text{yr}^{-1}$ (see Table 3.2) with a large inter-annual variability of $\pm 8.45 \text{ g C m}^{-2}\text{yr}^{-1}$. Similar to the greenhouse gas feedback, altered VOC emissions lead to a shift in OH-burden and consequently to a change in methane lifetime and ozone formation in the troposphere (Weber et al. 2022). Altered GHG concentrations affect the radiation budget and thus the climate and dynamical patterns, which again outweigh the change in GPP due to the twofold increase of BBA emissions.

Feedback of cloud cover and radiation changes due to BBA on GPP

Figure 3.4f shows the feedback of cloud cover and radiation changes due to twofold BBA emissions on GPP. In this feedback, the direct and indirect aerosol effects are accounted for. The direct effects include absorption and scattering of sunlight by aerosols, while the indirect effect includes the effect of aerosol particles on cloud albedo, droplet concentration, formation processes, precipitation patterns, and lifetimes (Haywood et al. 2000; Bellouin et al. 2020; Christensen et al. 2020; Twomey 1959b; Lohmann et al. 2005). Haywood et al. 2000 estimate the combined effect of black carbon and organic carbon from biomass burning on radiative forcing to cooling of -0.14 to -0.74 W m^{-2} . Increasing BBA emissions by a factor of two is thus expected to change the radiative balance, in turn influencing climate and weather patterns and subsequent GPP. The largest decrease in GPP due to $F_{\text{CLOUD\&RAD}}$ is found over the Congo Basin in Central Africa, the northwest Amazon region, and Australia. The largest increase in GPP is found for the northeast Amazon region, south of the Congo Basin in Africa, Western Europe, the Middle East, and Southeast Asia. Isolated areas of strong increase in GPP are found over the Himalayas, the Ethiopian Highlands, and Tanzania. Tropical evergreen broadleaf forests and raingreen shrubs show a negative response in GPP due to $F_{\text{CLOUD\&RAD}}$, while the remaining PFTs show, on average, a positive feedback effect (Table B7). Overall, the annual average of $F_{\text{CLOUD\&RAD}}$ is $-0.01 \text{ g C m}^{-2}\text{yr}^{-1}$ with an annual variability of $\pm 11.16 \text{ g C m}^{-2}\text{yr}^{-1}$. As with F_{WV} , F_{GHG} , and F_{VOC} , the results are not significant since the effect of doubled BBA emissions on GPP is masked by changes in overall climate dynamics.

Total feedback of twofold BBA emissions on GPP

The total feedback (F_{sum}) is displayed in Figure 3.4g. It shows the total change in GPP due to all included feedback mechanisms (F_{BBA} , F_{WV} , F_{GHG} , F_{VOC} , and $F_{\text{CLOUD\&RAD}}$) and mostly follows the patterns visible for $F_{\text{CLOUD\&RAD}}$ (Figure 3.4f). The total global feedback sum of doubled BBA emissions on GPP is $-1.23 \text{ g C m}^{-2}\text{yr}^{-1}$ with an annual variability of $\pm 10.42 \text{ g C m}^{-2}\text{yr}^{-1}$. As the overall feedback also shows large variability, it cannot be considered statistically significant. To identify possible correlations between environmental variables and the total GPP feedback, Figure 3.7a shows the spatial distribution of regions where certain variable anomalies (e.g., cloud cover, soil moisture, diffuse PAR) have strong correlations ($\geq |0.5|$) with the GPP feedback. Each pixel on the maps represents a geographical location, with color-coded shading indicating the types of variable anomalies most strongly correlated with GPP feedback in that pixel. Variables include AOD, PAR_{dir} , PAR_{dif} , land surface temperature (LST), soil moisture, evapotranspiration, LAI, pre-

precipitation, low cloud cover ($\text{Cloud}_{\text{low}}$), medium cloud cover ($\text{Cloud}_{\text{mid}}$), and high cloud cover ($\text{Cloud}_{\text{high}}$). Since changes in LST show the strongest correlation with changes in GPP across large areas, it was excluded from the analysis in Figure 3.7b to highlight correlations between changes in other variables and GPP. Six distinct regions were selected based on levels of biomass burning activity, varying climatic conditions, and diverse ecosystems, each characterized by a different predominant PFT: Central Amazon, Northwest Amazon, Central Africa, North Europe, India, and Siberia. The GPP feedback to twofold BBA emissions within these regions is listed in Table 3.2. Over Northern Europe and Siberia, the GPP feedback shows the largest correlation with precipitation anomalies. This is related to the critical role of water availability in regulating plant productivity in extra-tropical evergreen and deciduous forests dominant in these areas (Figure 3.2). Precipitation directly influences soil moisture, essential for photosynthesis and overall plant growth. In regions with distinct seasonal precipitation variations, GPP is affected by changes in water availability, especially during the growing phase. Additionally, a reduction in direct light, as indicated by small areas showing the largest correlation with PAR_{dir} , may play a major role in regulating GPP. A decrease in direct sunlight, caused by clouds or aerosols, limits the amount of available PAR and therefore reduces GPP, which, alongside precipitation changes, is a key determinant of plant productivity in mid and high latitudes. In tropical and subtropical regions, changes in LST are most strongly correlated with changes in GPP (Figure 3.7a), suggesting that plant growth is particularly sensitive to surface temperature in these areas. Warm and stable climates may result in even small changes in temperature having substantial effects on photosynthesis. Increases in LST can intensify water stress by increasing evaporation and vapor pressure deficit, reducing canopy conductivity and regulating GPP.

These factors could explain why GPP is particularly sensitive to LST variations in the tropics and subtropics. Excluding LST from the analysis (Figure 3.7b) reveals that in the Central Amazon, GPP feedback shows a strong correlation with precipitation and direct PAR availability anomalies. This region is dominated by tropical evergreen broadleaf forests (Figure 3.2) and experiences the highest annual rainfall globally. In the Northwest Amazon, which consists of tropical broadleaf deciduous forest and raingreen shrubs, the correlation with changes in evapotranspiration dominates. This indicates that water balance and transpiration rates play a more important role in regulating GPP in these ecosystems. A similar pattern is observed in Central Africa, where changes in GPP are most strongly correlated with precipitation and PAR_{dir} in the northern areas—dominated by tropical evergreen broadleaf forests and stronger precipitation events—whereas changes in evapotranspiration have a stronger influence in the southern areas dominated by tropical deciduous

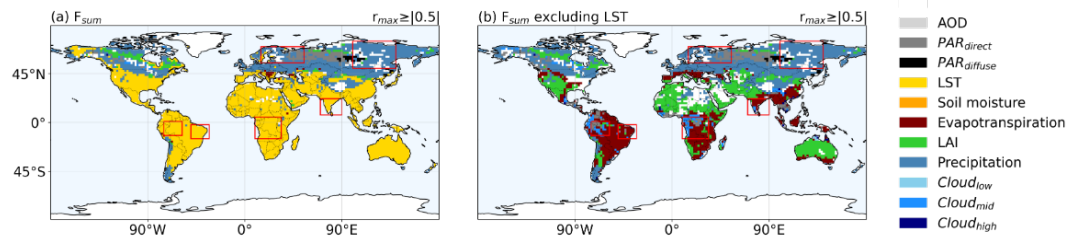


Figure 3.7: Region overview with the variable anomalies strongest correlating to the GPP Feedback including land surface temperature (LST) (a) and excluding LST (b). The values are filtered for correlations $r_{max} \geq |0.5|$ for the total GPP feedback (F_{sum}). The correlations between the GPP feedback and the variable anomalies are classified using principal component analysis.

broadleaf forests. Changes in evapotranspiration are also strongly correlated with changes in GPP in India, where JSBACH models the dominant vegetation types as C3 and C4 crops (Figure 3.2). At the southern tip of the country, predominantly covered by raingreen shrubs and receiving the highest multi-annual average precipitation within the region, the strongest correlation with GPP is observed for precipitation, similar to the Northwest Amazon. This suggests that precipitation plays a particularly important role in relation to GPP in regions with heavy rainfall. In all other regions, where LST was primarily correlated with GPP before its exclusion from the PCA, evapotranspiration now shows the strongest correlation. This shift highlights the close relationship between LST and evapotranspiration, as changes in surface temperature directly influence evaporation rates, while evapotranspiration induces surface cooling, which in turn affects LST.

Table 3.2: Global and regional average feedbacks of a twofold BBA emission. Standard deviations represent the area-weighted, year-to-year variability of the isolated feedback, integrated over all grid cells.

ΔGPP ($gCO_2m^{-2}y^{-1}$) F_{BBA}	F_{GHG}	F_{WV}	F_{VOC}	$F_{CLOUD \& RAD}$	F_{sum}	
<i>Global</i>						
($gCm^{-2}y^{-1}$)	-0.87 ± 0.05	0.56 ± 11.1	2.49 ± 5.36	-3.4 ± 8.45	-0.01 ± 11.16	-1.23 ± 10.42
($TgCy^{-1}$)	-129.24 ± 6.84	83.41 ± 1653.3	371.05 ± 798.1	-506.83 ± 1258.37	-1.98 ± 1661.55	-183.6 ± 1551.66
<i>Regions (Figure 3.7)</i>						
Central Amazon	-1.28 ± 0.1	-12.84 ± 112.67	27.89 ± 78.93	-31.27 ± 65.5	16.33 ± 192.89	-1.17 ± 195.44
Northwest Amazon	-1.44 ± 0.06	-8.63 ± 47.69	5.53 ± 44.17	7.13 ± 17.97	-8.8 ± 54.69	-6.21 ± 38.42
Central Africa	-1.96 ± 0.08	-0.92 ± 30.23	-6.68 ± 27.54	8.47 ± 10.63	-24.84 ± 42.01	-25.93 ± 30.71
North Europe	-0.24 ± 0.03	-3.17 ± 31.62	2.96 ± 11.63	2.08 ± 22.27	0.87 ± 13.23	2.49 ± 8.97
India	-1.65 ± 0.12	10.77 ± 184.77	1.6 ± 44.65	-2.89 ± 136.44	-12.52 ± 73.95	-4.69 ± 50.21
Siberia	-0.68 ± 0.06	0.99 ± 16.56	1.05 ± 7.44	-2.02 ± 9.34	1.52 ± 7.84	0.85 ± 6.4

Table 3.3: Global average feedbacks of a twofold BBA emission by Plant Functional Type (PFT). Standard deviations represent the area-weighted, year-to-year variability of the isolated feedback integrated over all grid cells.

$\Delta GPP (g(CO_2)m^{-2}y^{-1})$	F_{BBA}	F_{GHG}	F_{WV}	F_{VOC}	$F_{CLOUD\&RAD}$	F_{sum}
<i>PFTs</i>						
Tropical Broadleaf Evergreen	-0.11 ± 0.0	-0.66 ± 4.66	1.2 ± 3.74	-1.29 ± 2.71	-0.24 ± 8.53	-1.11 ± 8.36
Tropical Broadleaf Deciduous	-0.01 ± 0.0	-0.14 ± 0.83	-0.11 ± 0.75	0.18 ± 0.4	0.1 ± 1.21	0.02 ± 0.81
Extra-Tropical Evergreen	-0.03 ± 0.0	-0.03 ± 1.17	0.11 ± 0.33	-0.03 ± 0.86	0.2 ± 0.37	0.22 ± 0.41
Extra-Tropical Broadleaf Deciduous	-0.05 ± 0.0	0.1 ± 1.02	0.1 ± 0.45	-0.22 ± 0.55	0.26 ± 0.46	0.2 ± 0.29
Raingreen Shrubs	-0.16 ± 0.01	0.4 ± 2.37	0.48 ± 2.09	-0.73 ± 1.59	-1.13 ± 3.55	-1.15 ± 2.71
Deciduous Shrubs	-0.0 ± 0.0	0.01 ± 0.09	0.02 ± 0.16	-0.03 ± 0.01	0.08 ± 0.17	0.09 ± 0.13
C3 Grass	-0.0 ± 0.0	0.02 ± 0.1	0.0 ± 0.0	-0.02 ± 0.1	0.0 ± 0.0	0.0 ± 0.0
C4 Grass	-0.0 ± 0.0	0.01 ± 0.1	0.0 ± 0.0	-0.0 ± 0.1	0.0 ± 0.0	0.0 ± 0.0
C3 Pasture	-0.0 ± 0.0	0.01 ± 0.03	0.0 ± 0.0	-0.01 ± 0.03	0.0 ± 0.0	0.0 ± 0.0
C4 Pasture	-0.0 ± 0.0	0.0 ± 0.02	0.0 ± 0.0	-0.0 ± 0.02	0.0 ± 0.0	0.0 ± 0.0
C3 & C4 Crops	-0.58 ± 0.08	0.82 ± 7.55	0.75 ± 1.45	-1.16 ± 6.17	0.67 ± 1.54	0.5 ± 0.91

3.2.4 Conclusion

This study demonstrates that the EMAC/JSBACH model effectively simulates the ratio of direct and diffuse photosynthetic active radiation in relation to the fraction of incoming shortwave radiation in good agreement with with FLUXNET observations. Based on this, we find that the increase in global aerosol optical depth due to the doubling of BBA emissions leads to an year-round increase in absorbed PAR in mid an high latitudes but to an reduction in GPP when considering only the altered ratio of direct to diffuse PAR. This reduction is most pronounced in single-canopy vegetation types, such as crops and shrubs, which are more sensitive to a reduction in direct light. This result is mainly related to the parametrization of JSBACH, which calculates the absorption of plants as a function of the penetration depth of the light determined by the solar zenith angle. Note that the currently implemented version four of JSBACH differs from other models as it does not differentiate between shaded and sunlit leaves when calculating photosynthesis. This explains the variation in the result to Rap et al. 2015 and leads to the assumption that the diffuse radiation fertilization effect is only caused by the distinction between sunlit and shaded leaves and not by the penetration depth of the light. We have gradually integrated additional feedback mechanisms into our analysis, resulting in significant shifts in the overall analysis of GPP. These feedbacks introduce region-specific effects, leading to increases in GPP in some areas and decreases in others. Notably, the magnitude of these changes are significantly larger - by an order of magnitude - compared to analyses conducted without accounting for feedbacks. However, the overall impact of BBA on the biosphere including these complex interactions - especially aerosol-cloud interactions - introduces, as expected, significant uncertainties. A PCA analysis of the correlation of changes in different variables such as AOD,

PAR, cloud cover, precipitation or temperature with changes in GPP shows that the GPP feedback shows different sensitivities to these factors depending on the region and plant function type. For example, in Northern Europe and Siberia, GPP is most strongly correlated with precipitation, reflecting the importance of water availability for plant productivity in evergreen and deciduous forests. In tropical and subtropical regions, GPP is highly sensitive to LST, with small temperature changes significantly impacting photosynthesis and increasing water stress. Excluding LST from the analysis shows that in regions with higher rainfall, such as the central Amazon, central Africa and the southern tip of India, GPP is more closely linked to rainfall and PAR. In these areas, water availability and light are likely to be the key factors driving plant productivity. In all other regions, there is a strong correlation between GPP and evapotranspiration once LST is excluded. The aim of this study was to isolate individual feedback mechanisms on plant growth introduced by increased aerosol load and subsequent diffuse radiation increases using the newly coupled Earth System Model EMAC/JSBACH. Despite expected large uncertainties, the findings contribute to a better understanding of the complex interplay between aerosols, radiation, and plant productivity, highlighting the significance of feedback mechanisms and the importance of regional and vegetation-specific responses to increased aerosol loads and subsequent shifts in PAR. To minimize uncertainties, further comprehensive Earth system model studies, combined with extensive measurements and experiments, are needed. These efforts should focus on refining the physiological thresholds of plant functional types, such as grasses, trees and shrubs, by determining the critical environmental limits (e.g. light, temperature and water availability) at which they operate. Incorporating experimental data and observational evidence will improve the model's ability to simulate plant responses under varying environmental conditions, resulting in more accurate and reliable predictions. Additionally, new strategies for isolating effects independent from changes in the dynamics should be developed to better assess the processes against the system internal (larger) variability.

3.2.5 Appendix

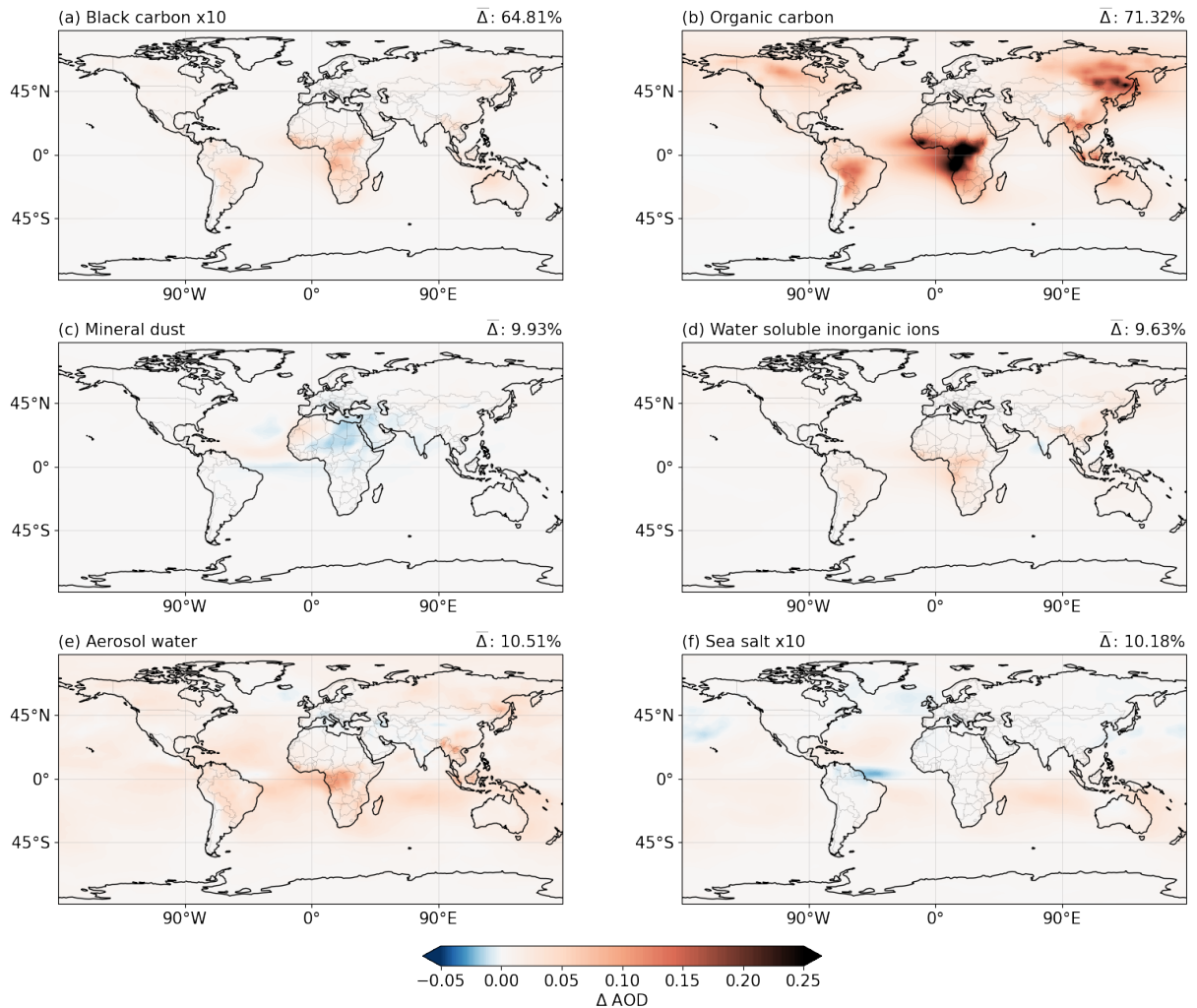


Figure 3.8: Annual average change in AOD of different Aerosol compounds due to doubled BBA emissions, derived from S5. Shown are black carbon (a), organic carbon (b), mineral dust (c), water soluble inorganic ions (d), aerosol water (e) and sea salt (f). Black carbon and sea salt are scaled by a factor of 10 to adapt it to the same colorbar as the other compounds. The data is based on monthly averages from 1992 to 2020.

Code availability.

The Modular Earth Submodel System (MESSy, <https://doi.org/10.5281/zenodo.8360186>) is continuously further developed and applied by a consortium of institutions. The usage of MESSy and access to the source code is licensed to all affiliates of institutions which are members of the MESSy Consortium. Institutions can become a member of the MESSy Consortium by signing the MESSy Memorandum of Understanding. More information can be found on the MESSy Consortium Website (<http://www.messy-interface.org>). The code presented/used here is available from <https://doi.org/10.5281/zenodo.10084186> and will be part of the next official release. It has been based on MESSy version d2.55.2 and JSBACH version 4 available via the jsbach Repository on GitLab (#7de0f9bf3b50910655f474bc23d647c6ba2a7b6f).

Data availability.

Regarding data availability, access to the FLUXNET datasets are available from the website <https://doi.org/10.1038/s41597-020-0534-3> (Baldocchi et al. 2001). The Aerosol Robotic Network (AERONET) dataset is available at <https://AERONET.gsfc.nasa.gov/> (Holben et al. 1998), and the Global Fire Emissions Database (GFED) v4.1 data is available at <https://doi.org/10.3334/ORNLDAAAC/1293> (Randerson et al. 2017).

Author contribution.

AM, AP and GC planned the research. AM further developed the model code and designed the simulation setups. AP, HT and RV contributed to the setup development. AM performed the simulations. GC provided the FLUXNET datasets. AM preprocessed the FLUXNET and AERONET datasets. AM wrote the manuscript with help of AP, RV and GC. AP, HT and JL supervised the project. All authors contributed to the manuscript reviewing and finalisation.

Acknowledgments.

The model simulations have been performed at the German Climate Computing Centre (DKRZ) through support from the Max Planck Society.

3.3 Biogenic soil deposition of methane and hydrogen in the ECHAM5/MESSy atmospheric chemistry model (EMAC)

This chapter contains a complete manuscript draft. I am the first author of and the main contributor to this work. I implemented the soil deposition submodel BIODep and performed the model simulations with Andrea Pozzer. I analyzed the model results and compared the simulation results to observations. I prepared the manuscript and made the figures. More detailed information on the Author contributions are provided at the end of the manuscript. After further coauthor exchange and optimization, it will be submitted to a peer-reviewed journal as:

Martin, A., Klingmüller, K., Steil, B., Surawski, N., Gromov, S., Lelieveld, J., and Pozzer, A.: Methane and hydrogen soil deposition in the ECHAM5/MESSy atmospheric chemistry model (EMAC) v2.55 using the newly implemented submodel BIODep, Manuscript in preparation, 2025.

Methane and hydrogen soil deposition in the ECHAM5/MESSy atmospheric chemistry model (EMAC) v2.55 using the newly implemented sub-model BIODep

Abstract Methane (CH_4) and hydrogen (H_2) play critical roles in atmospheric chemistry and climate processes. CH_4 is a powerful greenhouse gas, whereas H_2 , although not a greenhouse gas itself, indirectly affects radiative forcing by modifying the atmosphere's oxidative capacity and the concentrations of CH_4 , ozone (O_3) and stratospheric water vapor. The primary sink for methane is oxidation by hydroxyl radicals, while hydrogen is predominantly removed through microbial uptake in soils. Additionally, approximately 6% of CH_4 is taken up by soils, a factor that contributes significantly to its overall atmospheric budget. Soil uptake depends on various soil characteristics, including type, temperature, moisture, and for CH_4 , nitrogen deposition. Accurately representing these influences requires a detailed understanding of both atmospheric conditions and land surface and hydrological properties. However, many Earth system models currently use fixed soil deposition rates for H_2 and CH_4 , without accounting for variations in soil hydrology. We present BIODep, a new biogenic deposition submodel that has been integrated into the ECHAM/MESSy Atmospheric Chemistry model (EMAC). BIODep dynamically simulates the uptake of CH_4 and H_2 by soil, based on local meteorological and soil conditions. With BIODep, the soil sinks of CH_4 and H_2 are updated online based on the meteorological conditions, atmospheric composition and land surface properties provided by the EMAC model. The EMAC model is coupled to the JSBACH land surface and vegetation model. This allows for a consistent and interactive treatment of soil sinks within the atmospheric chemistry model. Modeled global mean soil uptakes of $61.22 \pm 11.63 \text{ Tg yr}^{-1}$ for H_2 and $30.88 \pm 6.97 \text{ Tg yr}^{-1}$ for CH_4 are consistent with previous studies, and the resulting atmospheric mixing ratios show good agreement with observations from the NOAA GML Carbon Cycle Cooperative Global Air Sampling Network, evaluated over the period 2009–2019. This development makes EMAC a state-of-the-art model to interactively simulate atmospheric chemistry, including both the soil sinks of CH_4 and H_2 . This enables more consistent simulation of trace gas budgets and an improved assessment of the feedbacks between land surface processes, atmospheric composition and future climate and emission scenarios.

3.3.1 Introduction

Methane (CH_4) is a highly potent greenhouse gas with a large climate warming potential through radiative forcing and an average atmospheric lifetime of approximately 9–12 years (IPCC 2023). Approximately 6% of the atmospheric CH_4 is removed via soil uptake by Methanotrophic bacteria particularly in well-aerated upland soils (Saunois et al. 2025). This sink is sensitive to environmental conditions, especially soil temperature, moisture, and nitrogen availability (Murguia-Flores et al. 2018; Singh et al. 1997; Pol-van Dasselaar et al. 1998; Wang et al. 2005). Numerous studies have quantified CH_4 uptake across various ecosystems and climatic regions (Dutaur et al. 2007; Shushi et al. 2020; Saunois et al. 2016; Ito et al. 2012; Kleinen et al. 2020; Murguia-Flores et al. 2018). Table 3.3.1 summarizes CH_4 soil uptake rates reported in selected studies as described in the recent methane budget review by Saunois et al. 2019. Estimated uptake values range from 18 Tg $\text{CH}_4 \text{ yr}^{-1}$, as reported by Kleinen et al. 2020, to 39.5 Tg $\text{CH}_4 \text{ yr}^{-1}$ according to Murguia-Flores et al. 2018. As these fluxes are strongly affected by climate change, understanding the behavior of the soil CH_4 sink under future conditions is crucial for reliable projections of atmospheric methane levels. Hydrogen (H_2) has the potential to be used as clean energy carrier, especially for hard-to-electrify sectors (Schultz et al. 2003; Tromp et al. 2003; Hauglustaine et al. 2022). However, the transition to a hydrogen-based energy system introduces new uncertainties related to atmospheric chemistry. Although H_2 itself is not a greenhouse gas, it indirectly influences climate by reacting with hydroxyl radicals (OH), thereby reducing the oxidative capacity of the atmosphere and prolonging the lifetime of CH_4 and other pollutants (Ehhalt et al. 2009; Sand et al. 2023). Under current conditions, the global hydrogen budget is approximately balanced, with the dominant removal process being soil uptake—accounting for 70–80 % of total H_2 loss (Constant et al. 2009; Ehhalt et al. 2009; Paulot et al. 2024). This soil sink is driven by similar environmental variables as the CH_4 sink, making it particularly sensitive to climate variability. Increases in H_2 emissions, particularly through leakage in future hydrogen usage scenarios, could disturb this balance, potentially enhancing climate forcing via secondary effects on methane, ozone, and stratospheric water vapor (Trapani et al. 2025; Sand et al. 2023). Recent studies have quantified the indirect warming potential of H_2 using the Global Warming Potential over 100 years (GWP_{100}) metric. Sand et al. 2023 estimate a model-mean GWP_{100} for H_2 of 11.6 ± 2.8 , with the largest contribution arising from enhanced CH_4 due to OH removal. However, they also highlight that the dominant uncertainty in this estimate stems from the poorly constrained soil sink of H_2 , motivating the need for improved process-based modeling. Given the strong atmospheric coupling between CH_4 and H_2 , particularly through shared sink processes such as soil uptake and OH

reactivity, accurately representing these interactions is critical for climate impact assessments. To address this, we present and evaluate a new BIOgenic DEPosition submodel BIODep, which dynamically calculates the soil sink fluxes of both CH₄ and H₂ based on local soil and meteorological conditions. BIODep is implemented within the EMAC (ECHAM/MESSy Atmospheric Chemistry) model. While BIODep adopts the same soil sink parametrization for microbial uptake in aerobic soils as presented by Surawski et al. 2025, it replaces the externally prescribed ERA5 reanalysis data-sets soil moisture input with interactive data from the coupled EMAC/JSBACH model. This dynamic coupling enables the online calculation of H₂ soil deposition fluxes within EMAC, allowing atmospheric H₂ dynamics to be consistently updated in response to evolving land-surface conditions. For CH₄, the sink parametrization is based on the approach of Murguia-Flores et al. 2018, incorporating dependencies on the online interactively calculated soil temperature, moisture, and nitrogen deposition. The CH₄ soil uptake fluxes are interactively calculated and coupled to EMAC's tracer budget, allowing for real-time updates of atmospheric CH₄ tendencies. This study presents the evaluation of BIODep under present-day conditions. We assess the simulated soil uptake fluxes against available observational constraints and benchmark the model performance for both CH₄ and H₂ data. By providing a dynamic and coupled treatment of these important trace gas sinks, BIODep enhances EMAC's capacity to simulate future scenarios involving hydrogen deployment and climate-driven changes in the soil environment.

Table 3.3.1 Global soil CH₄ uptake estimates from measurement and model studies

Reference	Time-frame	Description	Global soil CH ₄ uptake (Tg CH ₄ yr ⁻¹)
<i>Measurement studies</i>			
Dutaur et al. 2007	–	–	36 ± 23
<i>Combined Measurement and Model dataset</i>			
Shushi et al. 2020	2010–2018	Soil CH ₄ fluxes observed at 682 sites combined with a machine-learning algorithm for a data-driven estimate of monthly global soil CH ₄ uptake	28.65 ± 6.1
<i>Model studies</i>			
Saunois et al. 2016	–	Ridgwell et al. 1999 parametrization improved by Curry 2007	28 range: 9–4
Ito et al. 2012	–	Ensemble	25–35
Kleinen et al. 2020	2000–2020	JSBACH model	18
Ito et al. 2012	2000–2020	VISIT model	35
		MeMo model	37.5
Murguia-Flores et al. 2018	1990–2009	Ridgwell et al. 1999 parametrization	39.5
		Curry 2007 parametrization	31.3
This work	2009–2019	EMAC coupled to JSBACH and BIODep	30.88 ± 6.97

3.3.2 Evaluation datasets

We evaluate the performance of the BIODep submodel by comparing simulated atmospheric mixing ratios of hydrogen (H_2) and methane (CH_4) against observational datasets for the period 2009–2019. For hydrogen, simulated H_2 concentrations (in ppb) from BIODep are compared to observations from the NOAA GML Carbon Cycle Cooperative Global Air Sampling Network, which provides data from 52 global stations (Pétron et al. 2024). For methane, simulated CH_4 mixing ratios (in ppb) are evaluated against observations from the NOAA GML network (Lan et al. 2025), covering a global set of monitoring sites with available data between 2009 and 2019. Quality control procedures and the impact of the COVID-19 pandemic result in data gaps or missing data at some stations. These comparisons allow us to assess the model's ability to reproduce atmospheric concentration levels and spatial patterns of both trace gases.

3.3.3 Model description and setup

EMAC

The ECHAM/MESSy Atmospheric Chemistry (EMAC) model is a numerical chemistry and climate simulation system that includes sub-models describing tropospheric and middle atmosphere processes and their interaction with oceans, land and human influences (Jöckel et al. 2010a). It uses the second version of the Modular Earth Submodel System (MESSy2) to link multi-institutional computer codes. The core atmospheric model is the fifth-generation European Center Hamburg general circulation model (ECHAM5, (Roeckner et al. 2006)). The physics subroutines of the original ECHAM code have been modularized and re-implemented as MESSy submodels and have continuously been further developed. Only the spectral transform core, the flux-form semi-Lagrangian large-scale advection scheme, and the nudging routines for Newtonian relaxation remain from ECHAM. Further details on EMAC are documented by (Jöckel et al. 2016) and can be found on the MESSy website[‡]. In this study, we utilized EMAC (MESSy version 2.55.0) at a resolution of T63L31ECMWF. This configuration corresponds to a spherical truncation of T63, which translates to a quadratic Gaussian grid with approximately 1.8 by 1.8 degrees spacing in latitude and longitude, and includes 31 vertical hybrid pressure levels extending up to 10 hPa. Each simulation conducted in this study includes 10 years of simulation data from January 2009 to December 2019. Simulations are nudged towards ERA-Interim meteorological reanalysis data (Berrisford et al.

‡ <https://www.messy-interface.org>

2011) from the European Center for Medium-Range Weather Forecasts (ECMWF) (Jeuken et al. 1996; Jöckel et al. 2006). This study uses the model configuration described in (Kohl et al. 2023). EMAC has recently been coupled to version four of the Jena Scheme for Biosphere-Atmosphere Coupling in Hamburg (JSBACH) (Martin et al. 2024). JSBACH is a comprehensive land surface and vegetation model developed to simulate a wide range of biogeochemical processes within terrestrial ecosystems (Reick et al. 2021; Schneck et al. 2022). Among other improvements, JSBACH replaces the bucket soil hydrology scheme included in the former SURFACE submodel of EMAC with a comprehensive five-layer soil hydrology model, leading to improved representation of surface energy fluxes and reduction of biases related to surface temperature and vegetation stress. This updated framework allows the investigation of biogeochemical processes at finer temporal resolutions, facilitating a more detailed understanding of land-atmosphere interactions and their impact on atmospheric chemistry. JSBACH uses a vertical structure of five snow layers, three canopy layers and five soil layers to a depth of 9.8 meters. The model includes 11 plant functional types (PFTs), including tropical and extratropical broadleaf evergreen and deciduous trees, broadleaf and deciduous shrubs, C_3 and C_4 grasses, and C_3 and C_4 pastures and crops. The JSBACH model initialization is based on carbon pools, soil properties and land characteristics of the year 2005, with system equilibration expected within approximately five years (Martin et al. 2024). While atmospheric variables typically stabilize within a few days, soil moisture adjusts more slowly, with an equilibration time of up to one year (Hagemann et al. 2015; Schneck et al. 2022). The simulation setups employ the same emission inventories as Surawski et al. 2025. CH_4 emissions correspond to the year 2020 and include twelve categories (e.g., wetlands, agriculture, fossil fuel sectors), using the emission fields of the Global Atmospheric Methane Synthesis (GAMEs) inventory (Houweling et al. 1999) and the GFEDv4s emission datasets for biomass burning (Randerson et al. 2017). In the original configuration, emissions of CH_4 were scaled to match an atmospheric OH concentration in order to reproduce observed methane levels Zimmermann et al. 2020. Since the model setup has been updated to include an improved land surface and vegetation model, as well as interactive biogenic emissions and several changes to the chemistry setup, the formation of tropospheric ozone and, subsequent global oxidation capacity of the atmosphere driven by OH has changed. As OH is the dominant sink for methane, changes in its concentration directly affect the lifetime of methane. Consequently, the CH_4 emissions were scaled by a factor of 0.90 for emission sources and 1.06 for emissions responsible for long-term trends to align with the updated OH distribution and maintain consistency with observed methane levels. H_2 emissions are based on the RETRO dataset (year 2000) and include anthropogenic, biomass burning, soil, and oceanic sources

(Schultz et al. 2008). All emissions are annually repeated, excluding inter annual variability, and optimized for steady-state simulations representative of present-day conditions.

Methane deposition parametrization

The newly implemented Soil Methanotrophy Model (MeMo v1.0) (Murguia-Flores et al. 2018) in EMAC simulates soil–atmosphere CH₄ exchange by solving a steady-state, one-dimensional diffusion–reaction equation that accounts for microbial CH₄ oxidation throughout the soil profile. CH₄ uptake is controlled by the balance between gas-phase diffusion and microbial oxidation, governed by spatially variable parameters for the CH₄ diffusion coefficient (D_{CH_4}) and first-order oxidation rate constant (k_d). Following (Murguia-Flores et al. 2018), the soil uptake flux of CH₄ (J_{CH_4}) is given as:

$$J_{CH_4} = -D_{CH_4} \left(-A \sqrt{\frac{k_d}{D_{CH_4}}} + B \sqrt{\frac{k_d}{D_{CH_4}}} \right) \quad (3.11)$$

with

$$A = - \frac{C_{CH_4} \times \exp\left(\sqrt{\frac{k_d}{D_{CH_4}}} L\right) - CH_{4,\min}}{\left[\exp\left(-\sqrt{\frac{k_d}{D_{CH_4}}} L\right) - \exp\left(\sqrt{\frac{k_d}{D_{CH_4}}} L\right) \right]} \quad (3.12)$$

and

$$B = \frac{-CH_{4,\min} + C_{CH_4} \times \exp\left(-\sqrt{\frac{k_d}{D_{CH_4}}} L\right)}{\left[\exp\left(-\sqrt{\frac{k_d}{D_{CH_4}}} L\right) - \exp\left(\sqrt{\frac{k_d}{D_{CH_4}}} L\right) \right]} \quad (3.13)$$

C_{CH_4} is the atmospheric CH₄ concentration (in ppb), $CH_{4,\min}$ (in mg m⁻³) represents the threshold for the minimum CH₄ concentration within the soil. This value is set to the biological limit of 100 ppb, and L (in cm) denotes the depth of 99.9% penetration of atmospheric CH₄ into the soil.

Soil air diffusivity D_{CH_4}

The soil air diffusivity D_{CH_4} is calculated as $D_{CH_4} = D_0 CH_4 \times G_T \times G_{\text{soil}}$, where $D_0 CH_4 = 0.196 \text{ cm}^2 \text{ s}^{-1}$ is the diffusion coefficient of methane in free air at standard temperature and pressure, G_T is the temperature response factor and G_{soil} is the dimensionless soil structure factor. The temperature response is derived from the

temperature T (in °C) based on (Moldrup et al. 1996; Moldrup et al. 2013) with $G_T = 1.0 + 0.0055 \times T$. The soil structure factor G_{soil} is computed as:

$$G_{\text{soil}} = \phi^{4/3} \left(\frac{\phi_{\text{air}}}{\phi} \right)^{1.5 + \frac{3}{b}}, \quad (3.14)$$

with $b = 15.9 \times f_{\text{clay}} + 2.91$, a scalar dependent on the clay content (f_{clay} in %), ϕ the total pore volume (in $\text{cm}^3 \text{cm}^{-3}$), based on the bulk density ρ (in g cm^{-3}) and the particle density of soil $d = 2.65 \text{ g cm}^{-3}$:

$$\phi = 1 - \left(\frac{\rho}{d} \right) \quad (3.15)$$

and the air-filled porosity ϕ_{air} (in $\text{cm}^3 \text{cm}^{-3}$) which is depended on the volumetric soil water content Θ (in %):

$$\phi_{\text{air}} = \phi - \Theta. \quad (3.16)$$

Oxidation rate constant k_d

The CH_4 oxidation rate constant k_d in MeMo is calculated as:

$$k_d = k_0 \times r_{\text{SM}} \times r_T \times r_N, \quad (3.17)$$

with the base oxidation rate constant for uncultivated moist soil at 0 °C k_0 and the scaling factors accounting for the effects of soil moisture (r_{SM}), temperature (r_T), and nitrogen content (r_N) (Murguia-Flores et al. 2018) To improve accuracy, MeMo uses biome-specific k_0 values derived from time-series data on soil CH_4 uptake, temperature, and moisture from three ecosystems: temperate forest, tropical rainforest, steppe and other (Luo et al. 2013). Those ecosystems are based on the cover fraction of individual plant functional types in JSBACH. The table 3.3.3 shows the ecosystems, the corresponding k_0 values and their associated Plant Functional Types (PFTs) based on JSBACH PFT classifications. Murguia-Flores et al. 2018 note that uncertainties regarding the k_0 value persist, particularly in tropical regions, due to limited observational data. To prevent overestimation of CH_4 fluxes, lower k_0 values are typically used in these areas.

Table 3.3.3 Ecosystem classification and corresponding base oxidation rate constant k_0 in s^{-1} based on Luo et al. 2013 and JSBACH PFT

Ecosystem	k_0 in s^{-1}	JSBACH PFT
Temperate forest	4.0×10^{-5}	Extra Tropical forests
Tropical forest	1.6×10^{-5}	Tropical forests
Steppe	3.6×10^{-5}	Grass
Other ecosystems	5.0×10^{-5}	Shrubs, pasture and crops

Soil moisture contribution r_{SM}

In MeMo, the CH_4 oxidation rate constant k_d is scaled by soil moisture, temperature and soil nitrogen deposition. The influence of soil moisture is represented by the soil moisture factor r_{SM} , which quantifies the effect of moisture on methane uptake. Low moisture levels reduce microbial activity as water is required for microbial metabolism and gas diffusion. Conversely, too high moisture levels inhibit the diffusion of methane and oxygen into the soil, limiting microbial oxidation. This results in an optimum soil moisture content for methane uptake, where the soil moisture factor r_{SM} peaks for efficient microbial oxidation of CH_4 . r_{SM} is calculated based on the volumetric soil moisture fraction SM following (Murguia-Flores et al. 2018):

$$r_{SM} = \left[1 - \frac{\log_{10}(1 - SM) - \log_{10}(0.2)}{\log_{10}(100) - \log_{10}(0.2)} \right]^{0.8}, \quad \text{for } SM < 0.2 \quad (3.18)$$

and

$$r_{SM} = \frac{1}{\sqrt{2\pi}} \exp\left(-\frac{1}{2} \left(\frac{SM - 0.2}{0.2}\right)^2\right), \quad \text{for } SM > 0.2 \quad (3.19)$$

Soil temperature contribution r_T

The second scaling factor of the CH_4 oxidation rate constant k_d accounts for soil temperature and is referred to as r_T . This factor accounts for the influence of temperature on methane oxidation, reflecting the high sensitivity of microbial activity to temperature variations and is calculated following (Murguia-Flores et al. 2018) as:

$$r_T = \exp(0.1515 + 0.05238T - 5.946 \times 10^{-7}T^4) \quad \text{for } T > 0^\circ\text{C} \quad (3.20)$$

and

$$r_T = \frac{1}{\exp(-T)} \quad \text{for } T < 0^\circ\text{C} \quad (3.21)$$

The model predicts maximum CH_4 uptake at approximately 25°C , where r_T reaches its peak. The temperature dependency in MeMo captures the observed exponential decline in CH_4 uptake at subzero temperatures, aligning well with field observations that show methanotrophic activity persists even below 0°C (Murguia-Flores et al. 2018). Compared to earlier models, the r_T formulation in MeMo more accurately reflects real-world patterns of soil methane oxidation. A detailed description of the derivation of this formulation—based on the work of (Castro et al. 1995) and

(Del Grosso et al. 2000) and its comparison to other soil methanotrophy models is provided in (Murguia-Flores et al. 2018).

Soil nitrogen deposition contribution r_N

The third contributory factor is the nitrogen scaling factor r_N . It accounts for the inhibitory effect of nitrogen (N) inputs from atmospheric deposition N_{dep} and fertilizer application N_{fert} (both in $\text{kg N ha}^{-1} \text{ yr}^{-1}$) on soil CH_4 uptake. Scaled by soil bulk density ρ (in g cm^{-3}) and depth z (in cm), the total soil nitrogen deposition in soil N_{soil} (in $\text{kg N m}^{-2} \text{ yr}^{-1}$) is as follows:

$$N_{\text{soil}} = \frac{N_{\text{dep}} + N_{\text{fert}}}{\rho \times z} \quad (3.22)$$

Methanotrophic bacteria responsible for methane oxidation can be negatively affected by excess nitrogen through a number of mechanisms. These include substrate competition with ammonia-oxidizing bacteria (Gulledge et al. 1998; Bradford et al. 2001; Phillips et al. 2001), toxicity from intermediates such as hydroxylamine and nitrite (Bronson et al. 1994; MacDonald et al. 1996; Sitaula et al. 2000), and osmotic stress induced by high concentrations of ammonium salts (Whalen 2000). Although some studies have reported positive effects of N inputs on CH_4 uptake, attributed to stimulated activity of nitrifying bacteria under improved nutrient conditions (Cai et al. 2000; De Visscher et al. 2003; Rigler et al. 1999), observational datasets support a net inhibitory effect in most ecosystems (Aronson et al. 2010; Butterbach-Bahl et al. 2002; Steinkamp et al. 2001). Therefore, MeMo assumes a consistent negative effect of nitrogen inputs on CH_4 uptake. Nitrogen inhibition r_N is then calculated based on the empirical inhibition coefficient $\alpha = 0.0033$ (i.e. 0.33 % reduction in CH_4 uptake per mol N added) derived from field and laboratory studies (Zhuang et al. 2013):

$$r_N = 1 - (N_{\text{soil}} \times \alpha) \quad (3.23)$$

MeMo optionally includes the upward CH_4 flux ($F_{\text{CH}_4} > 0$) from wetlands, permafrost, or areas with anaerobic microsites, representing methane production below the surface, as a lower boundary condition. This allows the model to simulate not only the uptake of atmospheric methane but also the consumption of internally produced methane. However, due to the lack of measurement data, this feature was not evaluated and tested in this study.

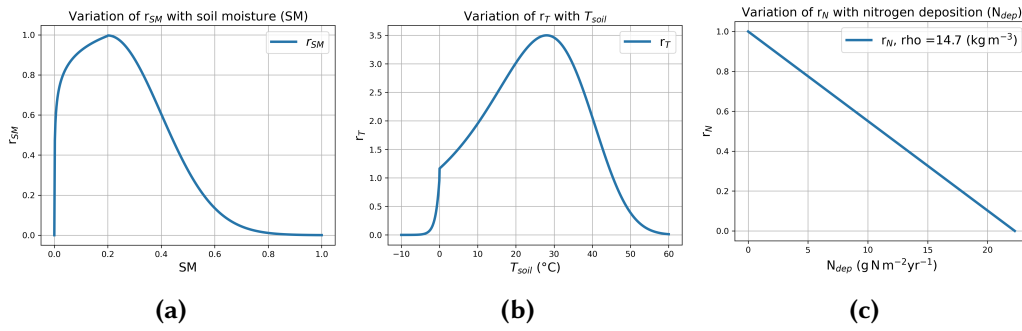


Figure 3.9: CH₄ uptake responses as a function of (a) fractional soil moisture (r_{SM} versus soil moisture, SM), (b) soil temperature (response factor r_T versus soil temperature, T_{soil} , in °C), and (c) nitrogen deposition and fertilizer application (response factor r_N versus nitrogen deposition, N_{dep} , in $\text{g N m}^{-2} \text{yr}^{-1}$). The factor r_N is derived using an initial bulk density of 14.7 kg m^{-3} .

Hydrogen deposition parametrization

The implemented soil deposition scheme is described in detail in (Surawski et al. 2025) following (Paulot et al. 2021; Ehhalt et al. 2013; Yonemura et al. 2000). It estimates the rate at which molecular hydrogen is removed from the atmosphere by the soil using a two-layer soil model that accounts for physical diffusion and microbial activity. Physical diffusion is considered in the top soil layer and depends on soil water content, temperature and surface pressure. The water content and thickness of the top layer are calculated from porosity, total column water content and empirical thresholds depending on the eolian and sand and loess loam fractions (Surawski et al. 2025) while these fractions are taken from the LDAS/GLDAS data sets (Rodell et al. 2004), porosity and total water column content are derived from the optimized soil hydrology in EMAC, provided by the JSBACH submodel. Microbial activity of hydrogen-oxidizing bacteria is considered in the second (lower) soil layer, which also depends on soil temperature and moisture of the second soil layer. The soil moisture is derived as the remaining water in the top 10 cm of the soil, derived from the JSBACH submodel. The temperature dependence is given by (Ehhalt et al. 2013). The H₂ uptake rate is then determined by the diffusion resistance of snow and the top soil layer plus the microbial uptake in layer 2. The latter is multiplied by a constant A representing bacterial activity, following Yashiro et al. 2011. This factor is used to calibrate to a global mean deposition rate over land to 0.033 cm s^{-1} (Figure 3.10).

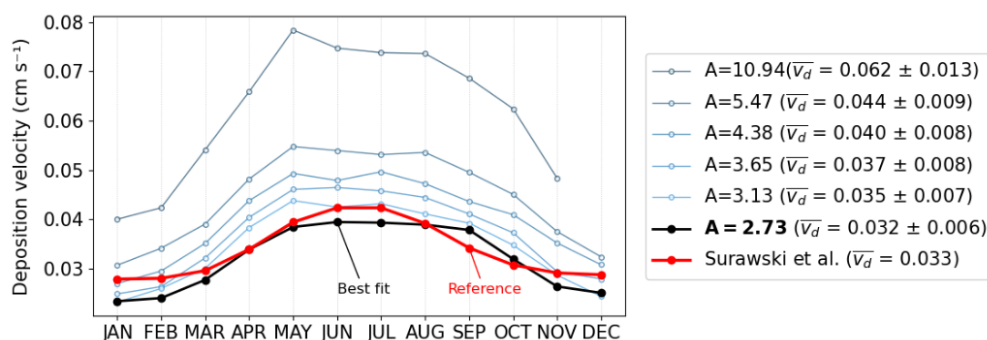


Figure 3.10: Monthly mean soil H₂ deposition velocities in 2009 from the BIODEP model with different tuning factors (A). The black dashed line shows the chosen factor $A/4$, matching the land average of 0.033 cm s^{-1} , while the red line shows data from Surawski et al. 2025.

Driving data for methane and hydrogen deposition parameterizations

The input data required for both the H₂ and CH₄ deposition subroutines are obtained from EMAC/JSBACH, which provides all relevant atmospheric and surface variables including surface temperature (T), surface pressure, atmospheric H₂ and CH₄ concentration, nitrogen deposition (N_{dep}), soil porosity (ϕ), soil moisture (SM), soil depth (z), and ecosystem properties. In addition, soil properties such as clay fraction (f_{clay}), sand fraction (f_{sand}), and bulk density (ρ) are obtained from the global soil dataset by (Shangguan et al. 2014). Following (Murguia-Flores et al. 2018), anthropogenic nitrogen input is derived from the historical global maps of NH₄⁺ and NO₃⁻ application in synthetic nitrogen fertilizers (N_{fert}), as provided by (Nishina et al. 2017).

3.3.4 Results and discussion

The following subsection presents a comparison of the results for CH₄ soil deposition (Sec.3.3.4), followed by an evaluation of H₂ deposition (Sec.3.3.4). Table 3.4 summarizes the weighted global average values (\pm standard deviation) for the deposition velocity (cm s^{-1}), soil uptake (Tg yr^{-1}), and total global atmospheric burden of H₂ and CH₄ (Tg). These values are compared with observational datasets (H₂ measurements from Pétron et al. 2024, CH₄ measurements from Lan et al. 2025), and modeled datasets by Surawski et al. 2025 (H₂ deposition velocity, uptake, and burden) and the MeMo data from 2000 (CH₄, uptake Murguia-Flores et al. 2018). Deposition velocity's and uptake are averaged only over land.

Table 3.4: Comparison summary of model results, observational data, and reference datasets. Values represent weighted global averages \pm standard deviation from the model simulations and reference data. Deposition velocities and soil uptake are averaged over land areas only.

Reference	Timeframe	Deposition velocity (cm s ⁻¹)	Soil Sink (Tg yr ⁻¹)	Atmospheric burden at surface (Tg)
<i>CH₄</i>				
Lan et al. 2025	2010–2020	–	–	5320.45 \pm 164.96
Murguia-Flores et al. 2018	2000	–	37.98 \pm 8.4	–
This work	2009–2019	0.0006 \pm 0.0001	30.88 \pm 6.97	5139.70 \pm 34.59
<i>H₂</i>				
Pétron et al. 2024	2020 (avg.)	–	–	191.42 \pm 7.33
Surawski et al. 2025	2010–2020	0.033	60.5 \pm 0.07	199.6 \pm 0.2
This work	2009–2019	0.033 \pm 0.007	61.22 \pm 11.63	201.67 \pm 7.51

Comparison of methane mixing ratio against observations

Figure 3.11 presents the trend of atmospheric CH₄ simulated by EMAC with the interactive CH₄ soil sink parametrization, compared to the global mean observations from the NOAA Global Monitoring Laboratory ((GML) 2025) for the period 2009–2019. This global mean dataset was used here specifically for tuning the model performance. EMAC successfully captures the observed CH₄ trends over this period compared to the global mean observations from the NOAA GML network ((GML) 2025).

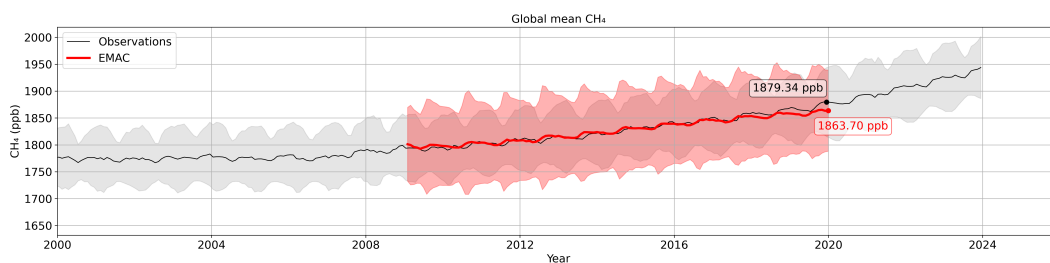
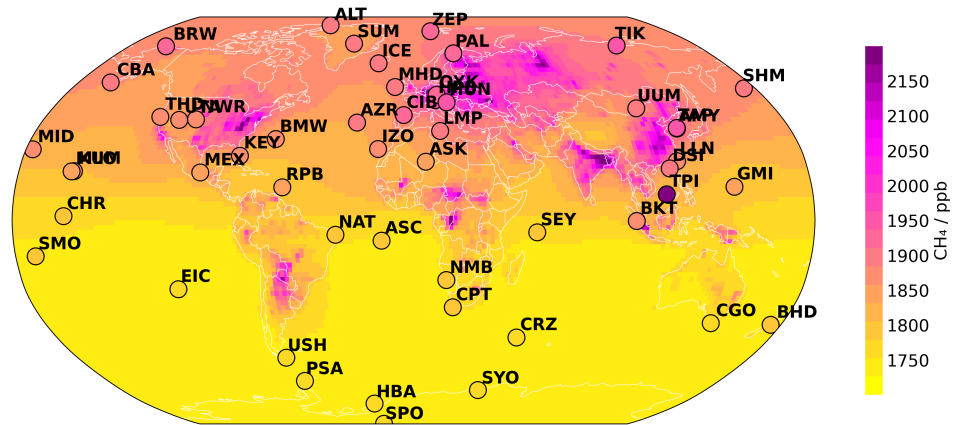
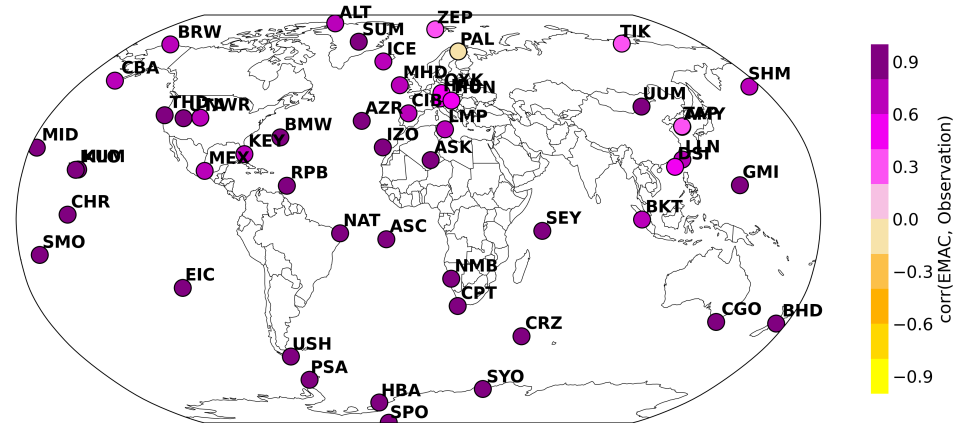
**Figure 3.11:** Global mean observations of CH₄ from the NOAA Global Monitoring Laboratory ((GML) 2025) (black), compared with the CH₄ trend simulated by EMAC (red). Shaded areas represent the spatial standard deviation of each dataset.

Figure 3.12 shows the average CH₄ mixing ratio of the EMAC model together with the individual on the site-level flask observational station data from the NOAA GML network (Lan et al. 2025) averaged over the period 2009-2019. Panel (a) illustrates the spatial distribution of mean modeled CH₄ mixing ratios, while panel (b) presents the Pearson correlation coefficients (r) between EMAC-simulated and observed CH₄ values at individual monitoring stations. A detailed summary of the number



(a)



(b)

Figure 3.12: Comparison of modeled and observed CH₄ data averaged over the years 2009-2019. Circles indicate the location of the observational stations Panel (a) shows the global distribution of mean CH₄ mixing ratio (CH₄/ppb), and panel (b) shows the corresponding Pearson correlation coefficient between the observation stations and EMAC results using the BIODEP submodel.

of available data points, mean modeled and observed CH₄ mixing ratios, and the model–observation differences is provided in Table 3.5 of the Appendix. The corresponding time series for each station are shown in Figures 3.17 of the Appendix. The CH₄ mixing ratios are well reproduced with 43 out of 51 stations showing high correlation ($r > 0.6$) between the EMAC simulations and station datasets, as shown in Figure 3.12 (a). Correlations between EMAC simulations and observational data exceeding $r > 0.90$ are found at several stations, including EIC in Chile ($r = 0.97$), HBA in Antarctica ($r = 0.97$), BHD in New Zealand ($r = 0.97$), and USH in Argentina ($r = 0.97$). These stations are predominantly situated in remote, coastal, island, or Southern Hemisphere regions, often at lower latitudes or in polar areas with low anthropogenic background emissions. EMAC captures regional-scale methane transport and background levels without being affected by local sources or sinks. In contrast, low or even negative correlations between EMAC simulations and observational CH₄ data are found at Northern Hemisphere stations (latitude > 0.55), including ZEP in Norway ($r = -0.34$), PAL in Finland ($r = -0.01$), or AMY in South Korea ($r = -0.28$). These sites are located in regions where complex local sources and sinks including wetland emissions and seasonal soil uptake contribute significantly to methane variability, which are not fully captured at the 1.8° resolution of EMAC simulations. The meridional gradient and seasonal cycle of CH₄, as derived from both EMAC model output and observational data, are shown in Figure 3.13. As illustrated in Figure 3.13 (a), both datasets show a clear inter hemispheric gradient, characterized by higher CH₄ mixing ratios in the Northern Hemisphere. This distribution is primarily driven by greater anthropogenic emissions in the Northern Hemisphere, notably from fossil fuel combustion, industrial activities, and biomass burning. The EMAC simulation accurately reflects the observed meridional gradient. The seasonal cycle (Figure 3.13 (b)) also exhibits good overall agreement between EMAC and the observational station data. The model remains within the observational standard deviation throughout the year, with slight overestimation in the summer months and minor underestimation in the winter months. Due to its long atmospheric lifetime (9–12 years) and relatively steady global sources, CH₄ exhibits only minor seasonal variations at the hemispheric and global scale. EMAC reproduces this small seasonal variability in agreement with the observations and generally within their standard deviations. In summary, results from the EMAC model accurately captures atmospheric methane variability at many remote stations, particularly in tropical and Southern Hemisphere regions, where the correlation between modeled and observed values is consistently high. These sites are characterized by cleaner air and low local anthropogenic and natural emissions. Conversely, model performance

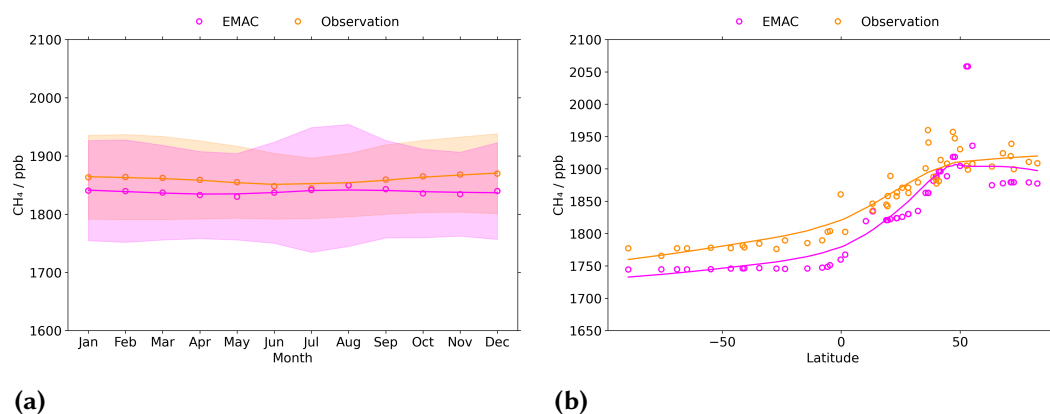


Figure 3.13: Comparison of modeled and observed CH₄ data from 2009 to 2019. Solid lines represent smoothed trends obtained using locally estimated scatterplot smoothing (LOESS) with a smoothing parameter of 2/3 and locally linear fitting. Panel (a) shows the seasonal variability of modeled and observed CH₄ data. Shaded areas represent the temporal standard deviations. Panel (b) shows the meridional distribution of CH₄ based on EMAC model outputs and observational data from stations with at least 12 monthly measurements.

is weaker at stations affected by complex topography and anthropogenic or wetland emissions where low or even negative correlations suggest discrepancies in the seasonal and inter annual patterns of methane dynamics. EMAC reproduces the latitudinal gradient and seasonal cycle of atmospheric methane as observed in measurements. Both the model and the observations show higher methane mixing ratios in the Northern Hemisphere, driven by greater anthropogenic emissions from sources such as fossil fuel use, industry, and biomass burning. The model captures seasonal variability well, remaining within the range of observational uncertainty throughout the year. A global methane soil sink of $30.88 \pm 6.97 \text{ Tg yr}^{-1}$ is estimated, which is consistent with previous literature (see Table 3.3.1).

Comparison of hydrogen mixing ratio against observations

Figure 3.14 evaluates the performance of the EMAC model using the new online soil sink submodel BIODP simulating atmospheric H₂. The comparison is based on observations of the NOAA GML Carbon Cycle Cooperative Global Air Sampling Network and model outputs averaged over the 2009–2019 period. Panel (a) shows the spatial distribution of mean modeled H₂ mixing ratios, while panel (b) displays Pearson correlation coefficients (r) between EMAC-modeled and observed H₂ values at individual monitoring stations. The corresponding overview of num-

ber of compared data points, mean model and observational H_2 mixing ratio and difference between the model and observational data are listed in Table 3.6 of the Appendix. The timelines for each station are shown in Figure 3.21, 3.22, and 3.23 of the Appendix. Mixing ratios are satisfactorily reproduced for background stations by the EMAC model with correlations higher than $r > 0.60$ for 17 out of 51 stations (Figure 3.14 (a)). Those stations include for example CHR ($r = 0.86$) or SMO ($r = 0.77$) in the central Pacific Ocean, CPT in South Africa ($r = 0.83$) or PSA

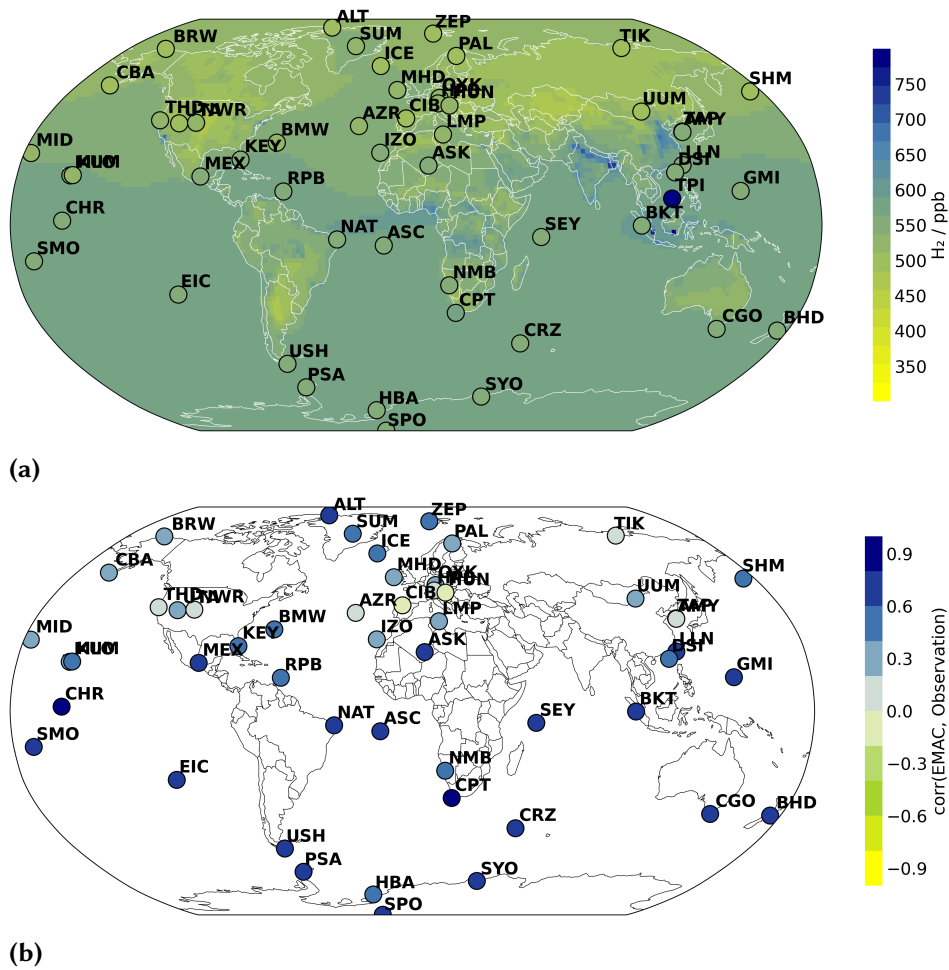


Figure 3.14: Comparison of modeled and observed H_2 data. Modeled data are averaged over 2009-2019. Circles indicate observational stations with mid-2020 values estimated using a sixth-order harmonic regression detrended fit. Panel (a) shows the global distribution of mean H_2 mixing ratio (H_2/ppb), and panel (b) shows the corresponding Pearson correlation coefficient between the observation stations and BIODEP results.

in Antarctica ($r = 0.76$). These sites show a comparable seasonal cycle and inter annual variability (see Figure 3.21), which suggests that the EMAC model with BIODP accurately represents soil sink dynamics in at remote stations. In these regions, atmospheric dynamics and transport processes tend to be smoother, with more uniform seasonal patterns and comparatively lower biomass burning emissions. This suggests that the EMAC model performs better in regions dominated by large-scale atmospheric transport and stable boundary layer conditions, as these factors minimize sub-grid scale variability. Conversely, there are stations where the seasonal cycle is not well captured by the model, as indicated by low or even negative correlation coefficients between the simulated and observed data. Notable examples include NWR in the United States ($r = 0.05$), HUN in Hungary ($r = -0.05$) or TAP in the Republic of Korea ($r = -0.08$). These stations are mainly located in the continental Northern Hemisphere, where stronger anthropogenic emissions, steep soil sink gradients and more complex boundary layer dynamics are present. Despite these discrepancies, the global average seasonal cycle (Figure 3.15 (a)) shows good overall agreement between the EMAC simulation and observational data. From April to December, EMAC values lie within the observational standard deviation, while from December to April, simulated means slightly exceed the observed variability, but the difference between model results and observations is not statistically significant. EMAC reproduces the overall seasonal pattern, though the timing of the maxima and minima is shifted about one month earlier relative to the observations. The meridional gradient derived from both EMAC model output and observational data, are presented in Figure 3.15 (b). Both datasets exhibit a distinct inter hemispheric gradient, with higher H_2 mixing ratios in the Southern Hemisphere. Although H_2 emissions, particularly from fossil fuel combustion, industrial activities, and biomass burning, are stronger in the Northern Hemisphere, this is offset by a correspondingly larger deposition flux, primarily due to more extensive and active soil sink. In contrast, the Southern Hemisphere exhibits a weaker soil sink due to lower landmass coverage, resulting in less efficient H_2 removal. EMAC generally simulates higher H_2 mixing ratios of approximately 40 ppb in both hemispheres, with increasing positive bias toward the poles and the smallest model–observation difference occurring near $25^\circ N$, where both datasets show mixing ratios of approximately 235 ppb. In summary, the implementation of the BIODP submodel within EMAC, allows a successful reproduction of the spatial and seasonal patterns of atmospheric H_2 mixing ratios across diverse regions. High correlations ($r > 0.6$) between modeled and observed values primarily occur at remote, low-emission sites, mainly island or coastal stations in the Southern Hemisphere and the tropics, where large-scale transport dominates and local sub-grid influences are minimal. Conversely, lower or negative correlations occur at

mid-latitude locations in the Northern Hemisphere characterized by complex terrain and significant anthropogenic emissions, where enhanced sub-grid variability and unresolved local processes challenge the accuracy of the model. As stated by Surawski et al. 2025, coarse resolution can lead to a limited representation of local and intermittent emission sources, thereby affecting the simulated mixing ratios. These issues related to resolutions are expected to be very pronounced in this study, since the coupled model computes soil moisture data at the same coarse resolution as the EMAC model. This is much lower than the resolution of the higher-resolution soil moisture datasets such as ERA5. On a global scale, BIODep estimates an H₂ soil sink of , which is consistent with previous estimates, including $60.05 \pm 0.07 \text{ Tg yr}^{-1}$ (Surawski et al. 2025), $44\text{--}73 \text{ Tg yr}^{-1}$ (Sand et al. 2023), $57\text{--}60 \pm 12 \text{ Tg yr}^{-1}$ (Yashiro et al. 2011), and $60^{+30}_{-20} \text{ Tg yr}^{-1}$ (Ehhalt et al. 2009).

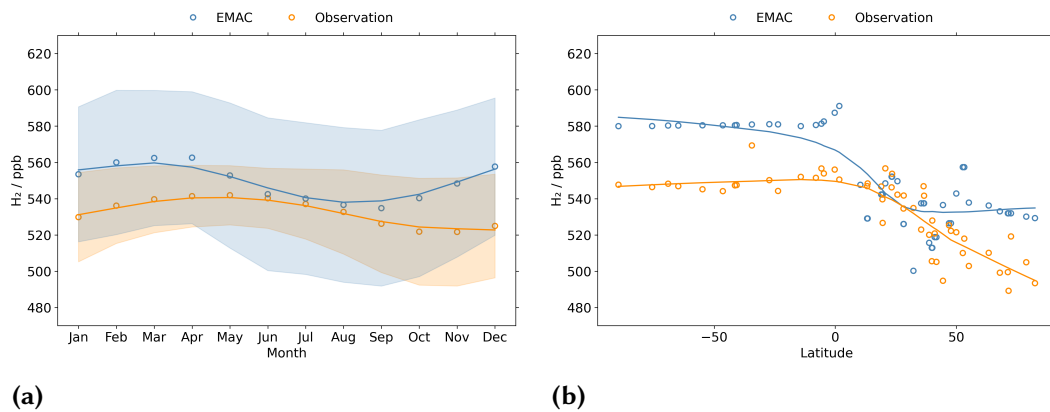


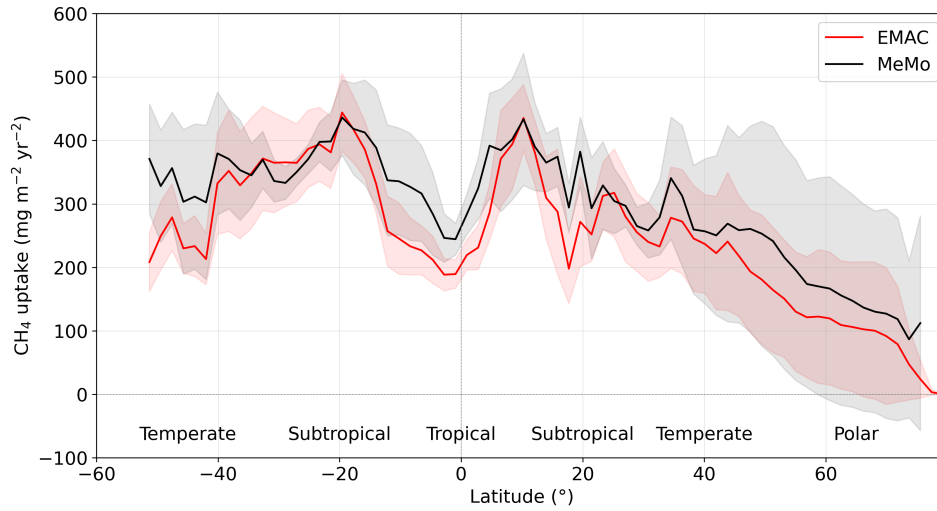
Figure 3.15: Comparison of modeled and observed H₂ data from 2009 to 2019. Solid lines represent smoothed trends obtained using locally estimated scatterplot smoothing (LOESS) with a smoothing parameter of $2/3$ and locally linear fitting. Panel (a) shows the seasonal variability of modeled and observed H₂ data. Shaded areas represent the temporal standard deviations. Panel (b) shows the meridional distribution of H₂ based on EMAC model outputs and observational data from stations with at least 12 monthly measurements.

3.3.5 Conclusion

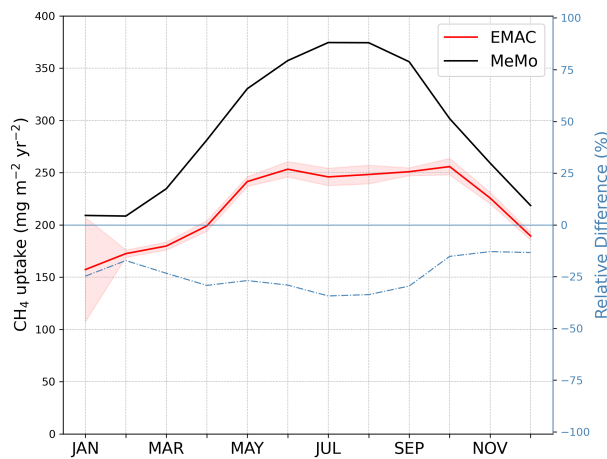
Implementing the BIODIP soil sink submodel into the MESSy framework and coupling it to EMAC has enabled the accurate simulation of global atmospheric H₂ and CH₄ mixing ratios. The model accurately reproduces the observed spatial distributions, seasonal cycles, and interhemispheric gradients of both gases, particularly at remote stations in the Southern Hemisphere where background conditions dominate, with the exception that simulated H₂ values from December to April deviate by about one standard deviation from the observations, which is a not statistically significant deviation from observations. The strong correlations between modeled and observed data in these regions highlight the model's ability to perform well in environments with low local variability. However, the model's performance is reduced at mid- to high-latitude Northern Hemisphere sites characterized by complex terrain, and stronger anthropogenic influences. This highlights the challenges of capturing localized emissions, boundary layer dynamics, and sub-grid scale processes, such as wetland emissions and soil moisture variability, at the model's coarse resolution. These limitations suggest that higher-resolution emission datasets would improve accuracy. Despite these challenges, the overall spatial and temporal consistency of EMAC simulations including the online calculations of global soil sink estimates of $61.22 \pm 11.63 \text{ Tg yr}^{-1}$ for H₂ and $30.88 \pm 6.97 \text{ Tg yr}^{-1}$ for CH₄ align with previous studies, demonstrating the capability of EMAC in representing the atmospheric budgets of both trace gases.

3.3.6 Appendix

Methane



(a)



(b)

Figure 3.16: Mean distribution of CH_4 uptake (in $\text{mg m}^{-2} \text{yr}^{-1}$) averaged over the period 2009-2019 from the new BIODP submodel coupled to EMAC/JSBACH (red) and from the MeMo average for 2000 (black). Shaded areas indicate the standard deviation for each dataset. Panel (a) shows the latitudinal distribution and panel (b) the monthly distribution.

Table 3.5: Comparison of mean model and observational CH₄ mixing ratios. Δ = Model – Observed, while r denotes the Pearson correlation coefficient.

Station	Longitude	Latitude	# values	CH ₄ EMAC (ppb)	CH ₄ Observed (ppb)	Δ (ppb)	r
ALT	-62.50	82.50	131	1889.3	1908.3	-19.01	0.66
AMY	126.00	36.50	71	2014.9	1959.6	55.30	-0.28
ASC	-14.40	-7.97	131	1771.7	1789.3	-17.54	0.97
ASK	5.63	23.30	127	1842.1	1857.5	-15.48	0.91
AZR	-27.40	38.80	102	1860.1	1887.3	-27.26	0.88
BHD	175.00	-41.40	123	1778.1	1781.2	-3.14	0.97
BKT	100.00	-0.20	108	1896.4	1859.8	36.55	0.66
BMW	-64.90	32.30	128	1859.4	1878.5	-19.08	0.91
BRW	-157.00	71.30	131	1894.3	1919.4	-25.04	0.68
CBA	-163.00	55.20	121	1884.3	1907.4	-23.14	0.75
CGO	145.00	-40.70	131	1775.1	1778.3	-3.21	0.95
CHR	-157.00	1.70	98	1778.7	1802.0	-23.33	0.90
CIB	-4.93	41.80	126	1910.0	1913.3	-3.22	0.73
CPT	18.50	-34.40	116	1782.3	1784.1	-1.75	0.93
CRZ	51.80	-46.40	130	1767.9	1777.2	-9.28	0.97
DSI	117.00	20.70	112	1889.3	1888.5	0.80	0.55
EIC	-109.00	-27.20	117	1763.2	1776.0	-12.81	0.97
GMI	145.00	13.40	114	1815.4	1834.9	-19.54	0.89
HBA	-26.20	-75.60	97	1760.3	1765.5	-5.24	0.97
HPB	11.00	47.80	131	1975.8	1947.0	28.86	0.46
HUN	16.70	47.00	131	2014.4	1956.7	57.65	0.47
ICE	-20.30	63.40	128	1892.5	1903.2	-10.71	0.61
IZO	-16.50	28.30	131	1858.1	1862.4	-4.33	0.86
KEY	-80.20	25.70	131	1906.5	1870.3	36.14	0.74
KUM	-155.00	19.60	131	1833.0	1857.5	-24.53	0.92
LLN	121.00	23.50	131	1865.1	1863.3	1.71	0.77
LMP	12.60	35.50	131	1906.6	1900.5	6.10	0.69
MEX	-97.30	19.00	131	1863.6	1844.4	19.20	0.72
MHD	-9.90	53.30	131	1907.2	1898.4	8.88	0.76
MID	-177.00	28.20	131	1846.2	1870.4	-24.12	0.94
MLO	-156.00	19.50	131	1833.0	1841.9	-8.92	0.91
NAT	-35.20	-5.68	104	1787.7	1802.4	-14.67	0.90
NMB	15.00	-23.60	125	1778.8	1789.1	-10.37	0.95
NWR	-106.00	40.10	131	1910.5	1876.8	33.66	0.79
OXK	11.80	50.00	125	1983.1	1930.3	52.74	0.48
PAL	24.10	68.00	131	1996.2	1923.8	72.41	-0.01
PSA	-64.10	-64.80	131	1768.1	1776.8	-8.72	0.98
RPB	-59.40	13.20	131	1815.8	1845.8	-30.06	0.96
SEY	55.50	-4.68	131	1786.0	1803.4	-17.36	0.93
SHM	174.00	52.70	124	1884.0	1904.4	-20.37	0.74
SMO	-171.00	-14.20	131	1769.3	1785.0	-15.67	0.96
SPO	-24.80	-89.50	131	1767.3	1776.9	-9.59	0.98
SUM	-38.40	72.60	131	1876.6	1899.0	-22.36	0.83
SYO	39.60	-69.00	131	1767.7	1776.8	-9.15	0.98
TAP	126.00	36.70	131	1994.4	1940.4	54.09	0.23
THD	-124.00	41.10	101	1860.4	1881.1	-20.71	0.85
TIK	129.00	71.60	77	1919.7	1938.7	-19.00	0.37
USH	-68.30	-54.80	127	1768.9	1777.7	-8.81	0.97
UTA	-114.00	39.90	131	1869.4	1883.4	-13.94	0.87
UUM	111.00	44.50	131	1892.1	1907.5	-15.44	0.81
ZEP	11.90	78.90	131	1906.3	1910.3	-4.00	0.34

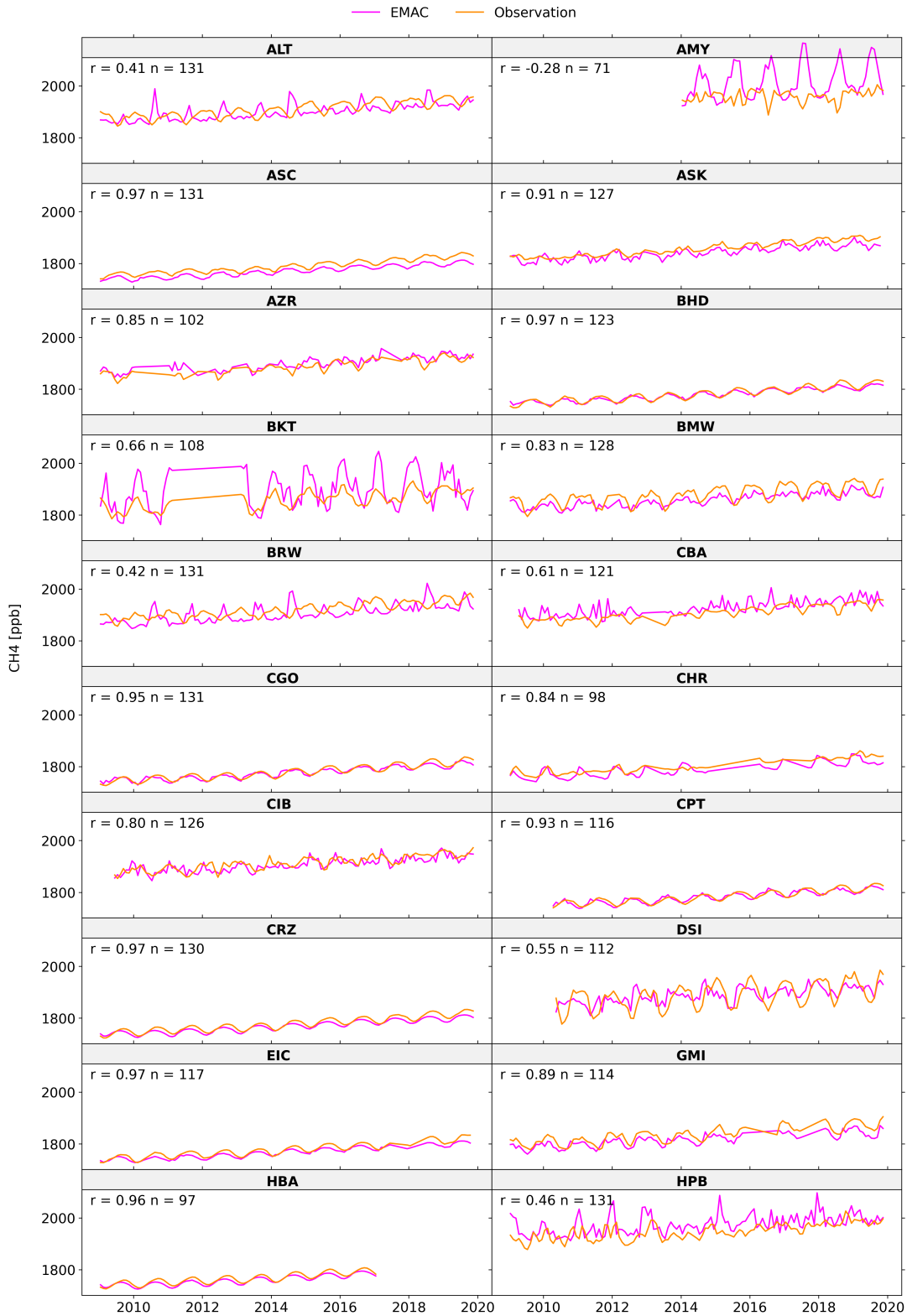


Figure 3.17: Comparison of CH₄ time series from observations and the EMAC model at 20 stations with complete monthly data between 2009-2019. The number of observational data points is indicated by *n*, and *r* represents the Pearson correlation coefficient between observed and modeled values.



Figure 3.18: Comparison of CH₄ time series from observations and the EMAC model at stations. The number of observational data points is indicated by n , and r represents the Pearson correlation coefficient between observed and modeled values, part 2

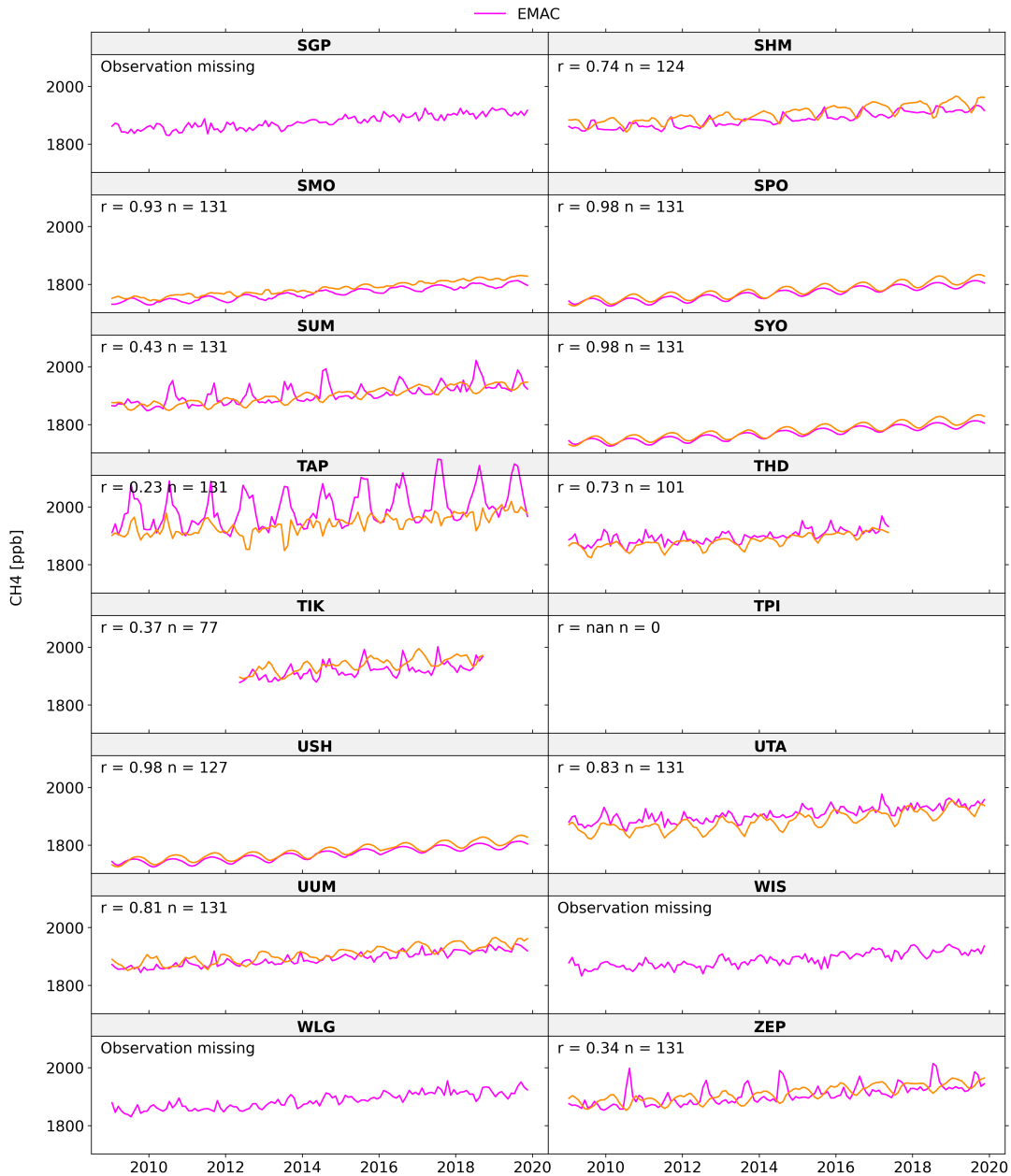
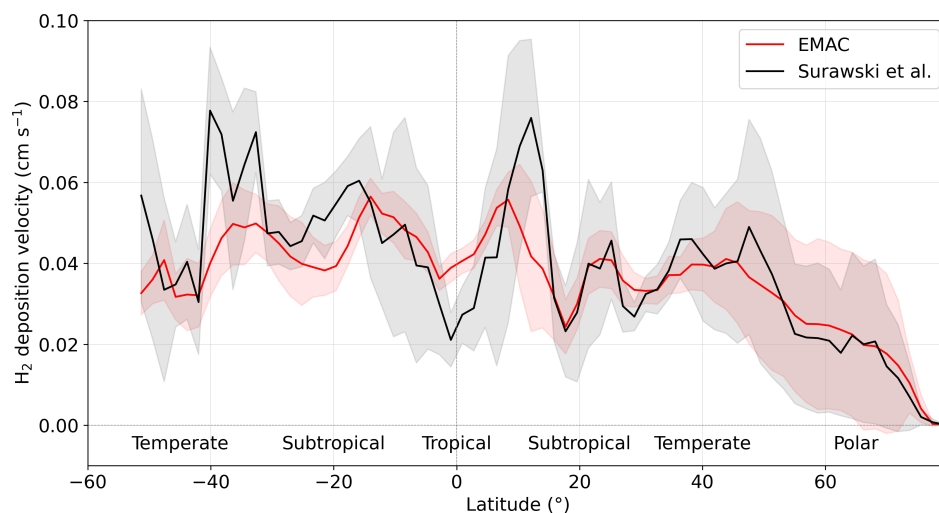
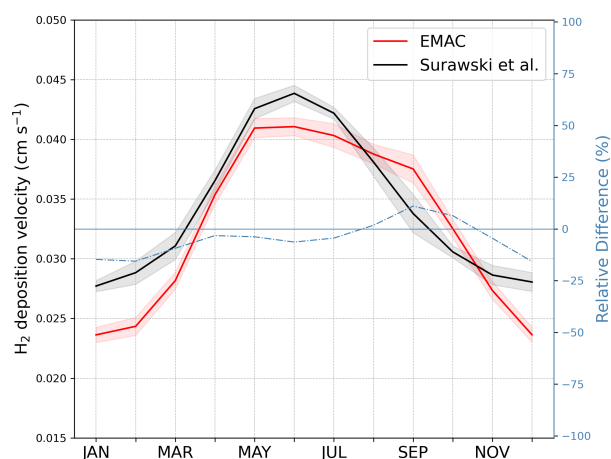


Figure 3.19: Comparison of CH₄ time series from observations and the EMAC model at stations. The number of observational data points is indicated by *n*, and *r* represents the Pearson correlation coefficient between observed and modeled values, part 3

Hydrogen



(a)



(b)

Figure 3.20: Mean distribution of H_2 deposition velocity (in $cm\ s^{-1}$) averaged over the period 2009-2019 from the new BIODP submodel coupled to EMAC/JSBACH (red) and from the Surawski et al. 2025 average for 2000 (black). Shaded areas indicate the standard deviation for each dataset. Panel (a) shows the latitudinal distribution and panel (b) the monthly distribution.

Table 3.6: Comparison of mean model and observational H₂ mixing ratios. Δ = Model – Observed, while r denotes the Pearson correlation coefficient.

Station	Longitude	Latitude	# values	H ₂ EMAC (ppb)	H ₂ Observed (ppb)	Δ (ppb)	r
ALT	-62.50	82.50	123	562.5	493.4	69.11	0.60
AMY	126.00	36.50	71	591.5	547.3	44.24	0.03
ASC	-14.40	-7.97	118	620.6	551.4	69.23	0.62
ASK	5.63	23.30	117	581.1	546.2	34.89	0.66
AZR	-27.40	38.80	98	583.1	520.2	62.95	0.17
BHD	175.00	-41.40	102	614.4	547.1	67.25	0.72
BKT	100.00	-0.20	93	637.2	556.1	81.09	0.64
BMW	-64.90	32.30	118	588.2	534.9	53.28	0.48
BRW	-157.00	71.30	121	556.2	499.6	56.59	0.34
CBA	-163.00	55.20	114	567.7	502.9	64.82	0.37
CGO	145.00	-40.70	120	612.5	547.4	65.09	0.73
CHR	-157.00	1.70	83	616.6	550.4	66.19	0.86
CIB	-4.93	41.80	121	542.2	505.4	36.75	-0.08
CPT	18.50	-34.40	105	621.7	569.1	52.63	0.83
CRZ	51.80	-46.40	118	617.7	544.0	73.66	0.73
DSI	117.00	20.70	112	612.8	556.8	55.96	0.47
EIC	-109.00	-27.20	108	620.3	550.2	70.04	0.68
GMI	145.00	13.40	102	609.4	548.4	60.96	0.67
HBA	-26.20	-75.60	96	606.4	546.4	60.01	0.51
HPB	11.00	47.80	120	559.6	522.3	37.27	0.08
HUN	16.70	47.00	124	543.1	525.5	17.62	-0.05
ICE	-20.30	63.40	122	567.1	510.2	56.97	0.49
IZO	-16.50	28.30	124	579.0	541.7	37.34	0.35
KEY	-80.20	25.70	121	607.8	542.3	65.52	0.56
KUM	-155.00	19.60	121	600.3	526.6	73.72	0.45
LLN	121.00	23.50	120	605.7	553.8	51.96	0.68
LMP	12.60	35.50	122	572.2	523.1	49.13	0.23
MEX	-97.30	19.00	120	583.5	546.7	36.81	0.64
MHD	-9.90	53.30	125	565.9	518.0	47.87	0.36
MID	-177.00	28.20	122	591.5	534.6	56.86	0.35
MLO	-156.00	19.50	121	600.3	539.6	60.63	0.35
NAT	-35.20	-5.68	102	617.9	556.5	61.31	0.63
NMB	15.00	-23.60	113	567.1	544.1	23.05	0.57
NWR	-106.00	40.10	121	544.5	528.0	16.52	0.05
OXK	11.80	50.00	116	555.4	521.5	33.91	0.24
PAL	24.10	68.00	122	540.6	499.2	41.35	0.28
PSA	-64.10	-64.80	125	616.8	546.8	70.03	0.76
RPB	-59.40	13.20	120	608.6	546.9	61.70	0.47
SEY	55.50	-4.68	123	619.7	553.8	65.93	0.62
SHM	174.00	52.70	111	564.1	510.1	54.03	0.45
SMO	-171.00	-14.20	121	622.0	551.9	70.14	0.77
SPO	-24.80	-89.50	128	615.1	547.6	67.51	0.65
SUM	-38.40	72.60	125	572.5	519.2	53.28	0.41
SYO	39.60	-69.00	129	615.1	548.1	66.93	0.65
TAP	126.00	36.70	123	580.2	541.8	38.35	-0.08
THD	-124.00	41.10	91	544.5	520.8	23.71	0.19
TIK	129.00	71.60	75	548.3	489.2	59.09	0.16
USH	-68.30	-54.80	118	609.3	545.1	64.24	0.76
UTA	-114.00	39.90	121	545.1	505.8	39.30	0.20
UUM	111.00	44.50	123	529.7	495.0	34.67	0.24
ZEP	11.90	78.90	123	559.6	505.0	54.65	0.54

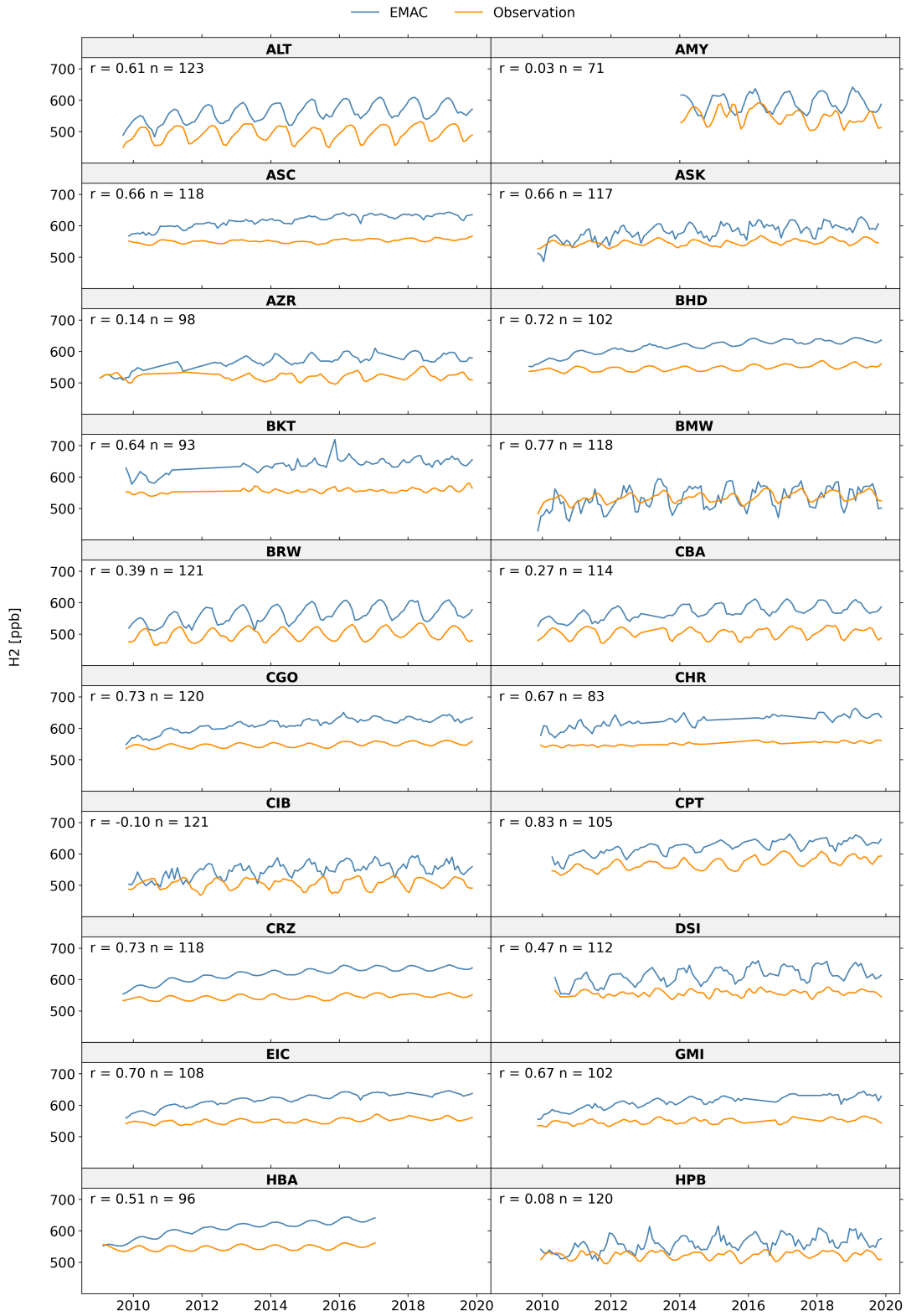


Figure 3.21: Comparison of H₂ time series from observations and the EMAC model at 20 stations with complete monthly data between 2009-2019. The number of observational data points is indicated by n , and r represents the Pearson correlation coefficient between observed and modeled values.

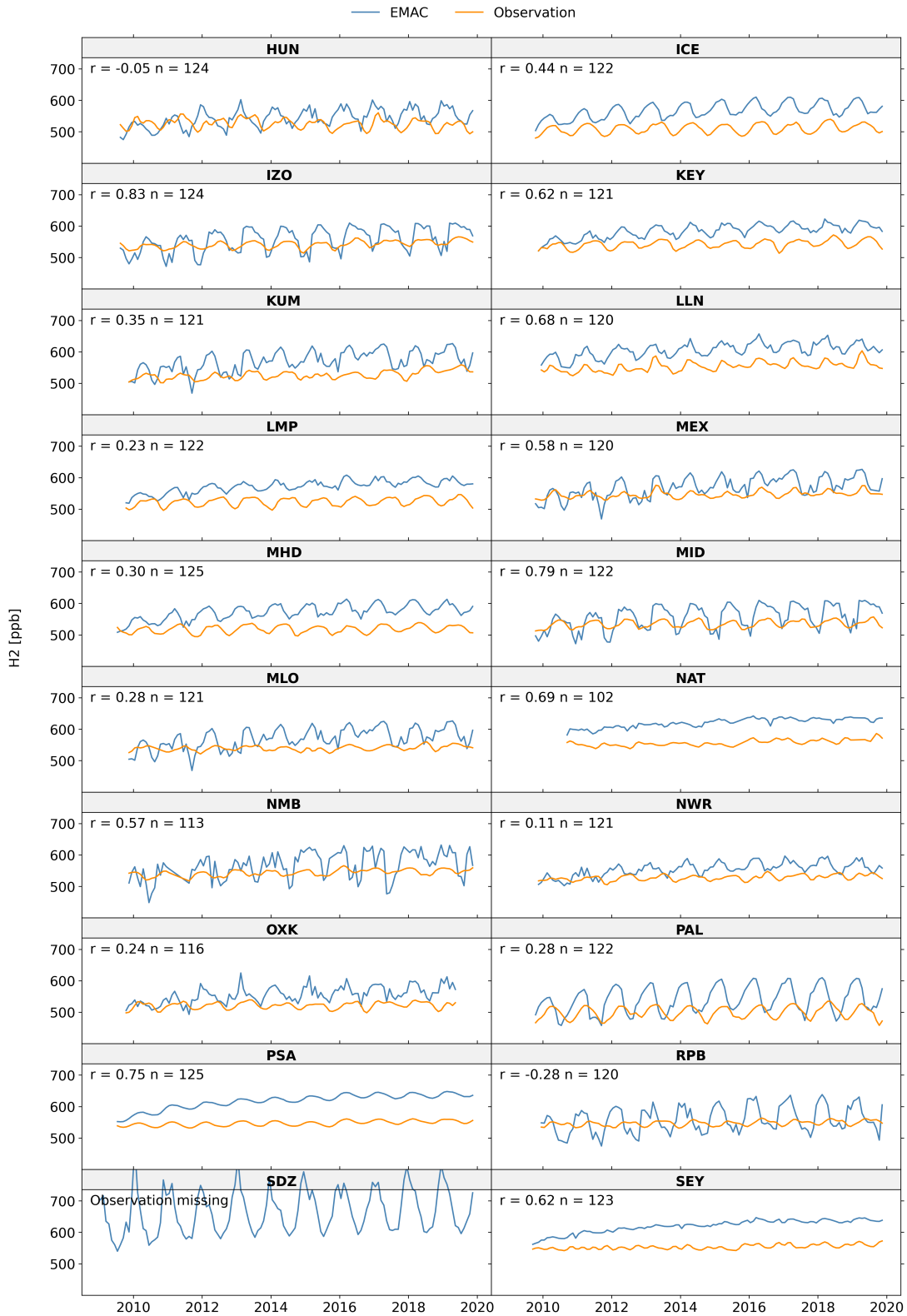


Figure 3.22: Comparison of H₂ time series from observations and the EMAC model at stations. The number of observational data points is indicated by n , and r represents the Pearson correlation coefficient between observed and modeled values, part 2

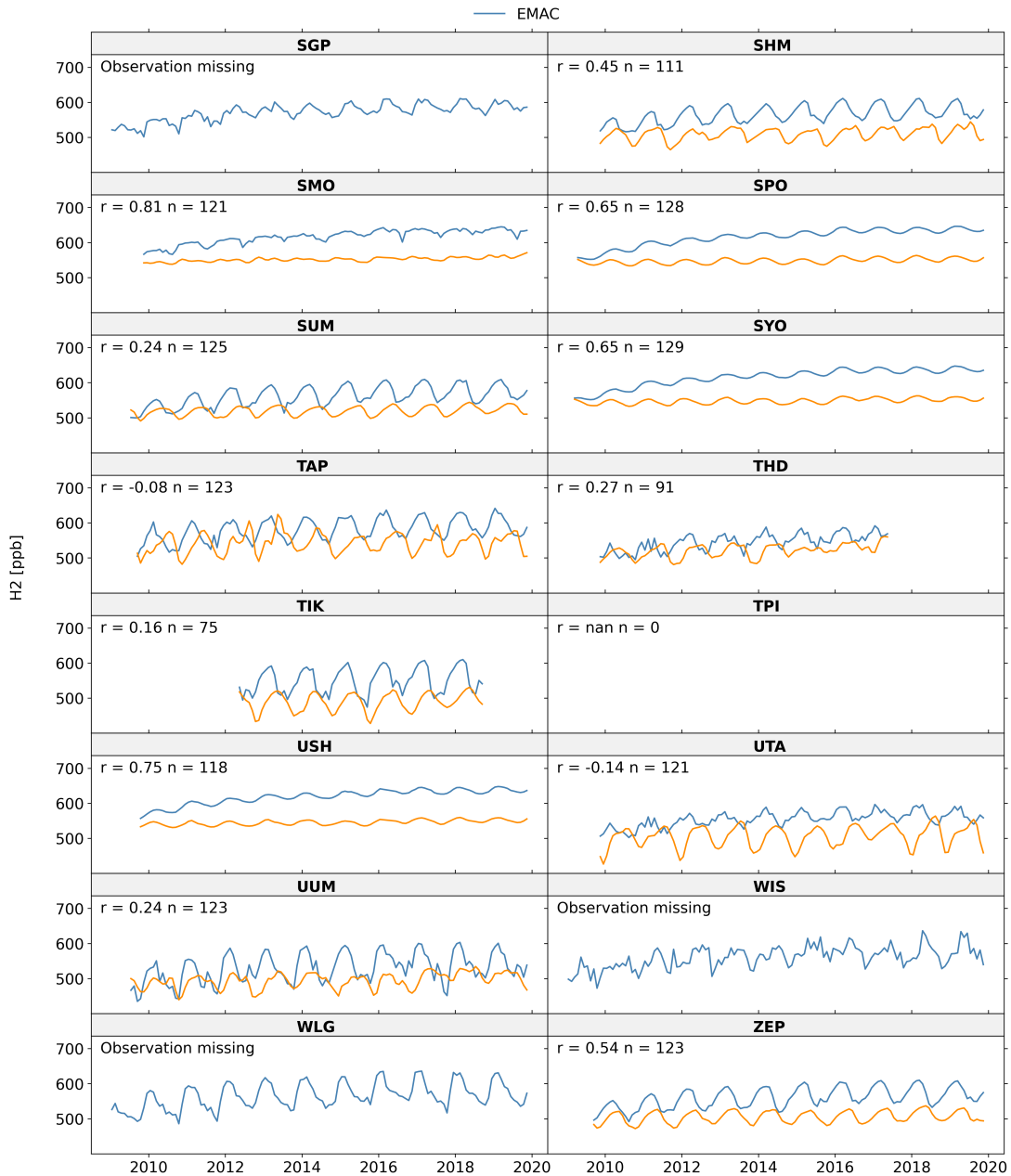


Figure 3.23: Comparison of H₂ time series from observations and the EMAC model at stations. The number of observational data points is indicated by *n*, and *r* represents the Pearson correlation coefficient between observed and modeled values, part 3

Code availability.

The Modular Earth Submodel System (MESSy, <https://doi.org/10.5281/zenodo.8360186>) is continuously further developed and applied by a consortium of institutions. The usage of MESSy and access to the source code is licensed to all affiliates of institutions which are members of the MESSy Consortium. Institutions can become a member of the MESSy Consortium by signing the MESSy Memorandum of Understanding. More information can be found on the MESSy Consortium Website (<http://www.messy-interface.org>). The code presented/used here is available from <https://doi.org/10.5281/zenodo.10084186> and will be part of the next official release. It has been based on MESSy version d2.55.2

Data availability.

Sand and loess loam fractions are taken from the LDAS/GLDAS data sets (Rodell et al. 2004). Clay fraction and bulk density are available from the global soil dataset <http://globalchange.bnu.edu.cn/research/soilw> (Shangguan et al. 2014). Anthropogenic nitrogen from fertilizers is available from <https://doi.pangaea.de/10.1594/PANGAEA.861203> (Nishina et al. 2017).

Author contribution.

AM and AP planned the research. AM developed the submodel model code and performed the simulations with the help of AP. AP, KK and BS contributed to the overall submodel model development. KK and provided the H₂ station observation datasets. BS provided the CH₄ station observation datasets. AM wrote the manuscript. AP and JL supervised the project. All authors discussed the results and contributed to the writing and editing of the manuscript.

Acknowledgments.

The model simulations have been performed at the German Climate Computing Center (DKRZ) through support from the Max Planck Society.

4.1 Numerical simulation of the impact of COVID-19 lockdown on tropospheric composition and aerosol radiative forcing in Europe

This chapter presents part of a study published in Atmospheric Chemistry and Physics. I am the second author of this work. I implemented the code corrections for aerosol-cloud interactions, analyzed the indirect aerosol effects, prepared the corresponding figures and wrote part of the manuscript as attached below in Section 4.1.1. How to cite:

Reifenberg, S. F., Martin, A., Kohl, M., Bacer, S., Hamryszczak, Z., Tadic, I., Röder, L., Crowley, D. J., Fischer, H., Kaiser, K., Schneider, J., Dörich, R., Crowley, J. N., Tomsche, L., Marsing, A., Voigt, C., Zahn, A., Pöhlker, C., Holanda, B. A., Krüger, O., Pöschl, U., Pöhlker, M., Jöckel, P., Dorf, M., Schumann, U., Williams, J., Bohn, B., Curtius, J., Harder, H., Schlager, H., Lelieveld, J., and Pozzer, A.: Numerical simulation of the impact of COVID-19 lockdown on tropospheric composition and aerosol radiative forcing in Europe, *Atmos. Chem. Phys.*, 22, 10901–10917, <https://doi.org/10.5194/acp-22-10901-2022>, 202

Abstract*

Aerosols influence the Earth's energy balance through direct radiative effects and indirectly by altering the cloud microphysics. Anthropogenic aerosol emissions dropped considerably when the global COVID-19 pandemic resulted in severe restraints on mobility, production, and public life in spring 2020. Here we assess the effects of these reduced emissions on direct and indirect aerosol radiative forcing over Europe, excluding contributions from contrails. We simulate the atmospheric composition with the ECHAM5/MESy Atmospheric Chemistry (EMAC) model in a baseline (business as usual) and a reduced emission scenario. The model results are compared to aircraft observations from the BLUESKY aircraft campaign performed in May/June 2020 over Europe. The model agrees well with most of the observations, except for sulfur dioxide, particulate sulfate and nitrate in the upper troposphere, likely due to a somewhat biased representation of stratospheric aerosol chemistry and missing information about volcanic eruptions which could have influenced the campaign. The comparison with a business as usual scenario shows that the largest relative differences for tracers and aerosols are found in the upper troposphere, around the aircraft cruise altitude, due to the reduced aircraft emissions, while the largest absolute changes are present at the surface. We also find an increase in shortwave radiation of $0.327 \pm 0.105 \text{ W m}^{-2}$ at the surface in Europe for May 2020, solely attributable to the direct aerosol effect, which is dominated by decreased aerosol scattering of sunlight, followed by reduced aerosol absorption, caused by lower concentrations of inorganic and black carbon aerosols in the troposphere. A further increase in shortwave radiation from aerosol indirect effects was found to be much smaller than its variability. Impacts on ice crystal- and cloud droplet number concentrations and effective crystal radii are found to be negligible.

4.1.1 Aerosol–cloud interactions*

In Fig. 4.1, the vertical distributions of the aerosol number concentration (N), ice crystal number concentration (ICNC), cloud droplet number concentration (CDNC) and ice crystal radius (r) are shown for Europe for both simulations, STD CLOUD and RED CLOUD. Additionally, the SW flux at the TOA and the surface have been calculated from these coupled aerosol–cloud simulations (see Table 4.1), both for the total effect (i.e. direct plus indirect) and for the indirect (i.e. neglecting any direct radiation influence of the aerosol particles). Due to the short simulation period, the difference between these simulations is much smaller than its variability, represented by its spatial and temporal standard deviation. Nevertheless, comparing the vertical distribution of number concentrations of aerosols, ice crystals and cloud droplets, the largest relative difference between STD CLOUD and RED CLOUD (i.e.

* as published in Reifenberg et al. 2022

the two simulations where the aerosol–cloud feedback is activated) is found for the aerosol number concentration between 200 and 300 hPa. These are the cruise altitudes at which the largest aircraft emissions are injected in the model and therefore these differences can be directly connected to the reduced air traffic present during the lockdown (REDCLOUD). As this altitude is somewhat higher than the typical (cold) cloud altitude, the effect on clouds is less pronounced. At the highest level of these clouds (see Fig. 4.1) the ICNC are reduced (by $\approx 30\%$ at 250 hPa, although with large variability), while no visible effect is found for CDNC. These results are in line with those obtained by (Righi et al. 2021), who showed that aircraft emissions do increase ice crystal number concentration, although their results were not statistically significant. The ice crystal effective radius seems to be the least affected by the reduced emissions during the COVID–19 lockdown, with a negligible absolute and relative difference. To investigate the effect of reduced aircraft emissions on the SW flux via the indirect aerosol effect at the TOA and surface (SRF), the mean differences in SW flux between REDCLOUD and STD CLOUD for May were calculated over Europe. Positive values indicate greater reflection of SW radiation back to space (for TOA) or more absorption through the troposphere (for surface values) in the STD CLOUD simulation, compared to the REDCLOUD. The mean surface differences are $0.307 \pm 0.115 \text{ W m}^{-2}$ for the clear sky and $0.443 \pm 1.063 \text{ W m}^{-2}$ for the all sky case. At the TOA the mean differences in shortwave fluxes are $0.186 \pm 0.106 \text{ W m}^{-2}$ (clear sky) and $0.281 \pm 0.928 \text{ W m}^{-2}$ (all sky, Table 4.1). We should notice that the clear sky results agree with the direct effect estimated in Sect.?? but with different simulations, confirming the consistency of the calculations. Thus, the indirect effect of aerosols enhances the direct effect on the SW radiation during the lockdown, even with larger intensity. This confirms the importance of the cloud–aerosol interaction, as mentioned by Hong et al. 2016, Gasparini et al. 2016 and Myhre et al. 2013. However, those values are associated with large standard deviations, related to the strong spatial variability of the upward shortwave radiation difference between the simulations.

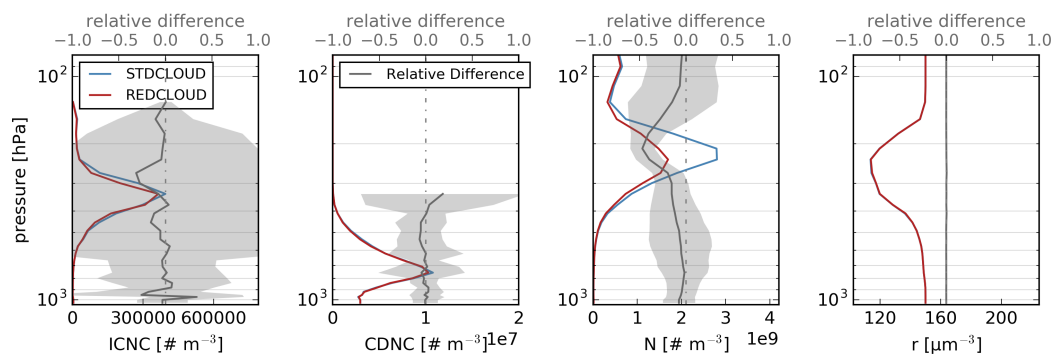


Figure 4.1: Vertical profiles of the monthly mean ice crystal number concentration (ICNC), cloud droplet number concentration (CDNC), aerosol number concentration (N) and ice crystal effective radius (r) of the reduced emission scenario REDCLOUD (red) and the standard emission scenario STDCLLOUD (blue) and their relative difference (grey line) for May 2020 over Europe. The grey area denote the spatial and temporal standard deviation of the relative difference*.

Table 4.1: Aerosol direct and indirect effects on the shortwave radiation flux at the top of atmosphere (TOA) and surface (SRF) over Europe for May. Note that direct effects are derived from STD and RED simulations, and indirect and total (i.e. direct plus indirect) effects from STDCLLOUD and REDCLOUD. The indirect effect of clear sky estimation is obviously equal to zero, but it was included to confirm the validity of the calculations*.

$\Delta F_{\text{SW}} \text{ W m}^{-2}$	RED-STD	REDCLOUD-STDCLLOUD	
	direct	indirect	total
TOA	0.090 ± 0.035	0.188 ± 0.759	0.281 ± 0.928
TOA clear sky	0.198 ± 0.092	0.000 ± 0.006	0.186 ± 0.106
SRF	0.209 ± 0.053	0.233 ± 1.089	0.443 ± 1.063
SRF clear sky	0.327 ± 0.105	0.001 ± 0.023	0.307 ± 0.115

* as published in Reifenberg et al. 2022

Code availability.

The Modular Earth Submodel System (MESSy) is continuously further developed and applied by a consortium of institutions. The usage of MESSy and access to the source code is licensed to all affiliates of institutions which are members of the MESSy Consortium. Institutions can become a member of the MESSy Consortium by signing the MESSy Memorandum of Understanding. More information can be found on the MESSy Consortium Website (<http://www.messy-interface.org>). The code presented here has been based on MESSy version 2.55 and is available as git commit #dc3ed8, in the MESSy repository.

Data availability.

Data are available from the contact author under request.

Author contribution.

A.P. and S.R. planned the research. A.P. and S.R. collected and prepared the emission data. A.M. implemented code corrections for aerosol–cloud interactions. A.P. performed the model simulations. P.J. contributed to the overall model development and helped with the preparation of the model setups. M.K. provided the script for the aerosol mass estimation in the model. Z.H., I.T., L.R., D.J.C. and H.F. provided the data for CO, NO and H₂O₂. J.S. and K.K. provided observational aerosol composition data. R.D. and J.N.C. were responsible for the PAN measurements. C.V., L.T. and A.M. provided observational data of HNO₃ and SO₂. A.Z. provided the ozone data. O.K., B.H., C.P., M.P. and U.P. were conducting, analyzing and interpreting the BC data. M.D. organized the field campaign logistically. J.C. planned the flight tracks during the campaign. H.S. coordinated the measurements on the FALCON. S.R. and A.P. performed the model evaluation and analysis of direct effects. A.M. and A.P. performed the analysis of indirect effects. U.S. and A.P. discussed the results on the radiative forcing. S.R., A.M. and A.P. wrote the manuscript with the help of J.C., M.K. and J.W.. A.P. and J.L. supervised the project. All authors discussed the results and contributed to the review and editing of the manuscript.

Acknowledgments.

Christiane Voigt, Laura Tomsche and Andreas Marsing thank funding by the HGF and by the DFG within the SPP1294 HALO under contract no Vo1504/7-1 and the TRR301-1 TP change.

5

Conclusions & Outlook

The first part of this thesis (3.1), presents the successful integration of the land surface model JSBACH version 4 into EMAC, replacing the former SURFACE sub-model. This update significantly enhances EMAC's capability by introducing a more sophisticated hydrology scheme and improved soil and vegetation processes. The new level of complexity allows EMAC to simulate new bio-geophysics parameters such as gross primary productivity. Our evaluation confirms that the new EMAC/JSBACH coupling maintains model stability and performance while improving the accuracy of land-atmosphere interactions, particularly in terms of soil moisture, groundwater storage, and LAI. Adjustments were made to tune the radiation budget in the T63L31ECMWF resolution and we find a good agreement with reanalysis and the satellite data.

Building upon this development, part (3.2) demonstrates the capability of the EMAC/JSBACH model to realistically simulate the partitioning of direct and diffuse photosynthetically active radiation, aligning well with FLUXNET observations. Based on this, we examined the impact of increased biomass burning aerosol emissions and found that, while higher aerosol loads enhance diffuse PAR absorption in mid- and high-latitudes, they can reduce gross primary productivity, particularly in single-canopy vegetation types, due to the model's current treatment of light absorption, which does not distinguish between sunlit and shaded leaves. The analysis highlights that feedback mechanisms, especially those involving clouds, precipitation, and temperature, significantly influence regional GPP responses, often amplifying the impact by an order of magnitude. Principal component analysis reveals that GPP sensitivities vary widely by region and plant functional type, driven by key environmental factors such as land surface temperature, light availability and precipitation. Although uncertainties remain, particularly concerning aerosol-cloud interactions, this work improves our understanding of the effects of aerosol-induced radiation changes on vegetation. Reducing these uncertainties will require future studies that incorporate the distinction between sunlit and shaded leaves, integrate experimental data, and refine the physiological parameters of different plant types, thereby enabling more robust predictions of ecosystem responses under changing atmospheric conditions.

Part (3.3) presents the newly implemented soil sinks for hydrogen and methane within the newly developed BIODEP sub-model, made possible by the foundational

developments in Part 3.1. Integrating BIODep into the EMAC framework enables the accurate simulation of global atmospheric H₂ and CH₄ mixing ratios. The model successfully reproduces observed spatial distributions, seasonal cycles, and inter-hemispheric gradients of both gases, particularly at remote Southern Hemisphere stations dominated by large-scale atmospheric transport and stable meteorological conditions. Strong correlations between modeled and observed data in these regions underscore EMAC's capability to perform well under low local variability conditions. Conversely, model performance declines at mid- to high-latitude Northern Hemisphere sites characterized by complex terrain, variable meteorology, and stronger anthropogenic influences, highlighting challenges in capturing localized emissions, boundary layer dynamics, and sub-grid scale processes such as wetland emissions and soil moisture variability. These limitations point to the need for higher-resolution emission datasets to enhance model accuracy. The global soil sink estimates from EMAC incorporating BIODep are $61.2 \pm 11.63 \text{ Tg yr}^{-1}$ for H₂ and $30.9 \pm 6.97 \text{ Tg yr}^{-1}$ for CH₄ are consistent with values reported in previous studies. Together with the agreement on mixing ratios and atmospheric budgets, this demonstrates EMAC's ability to accurately reproduce the atmospheric trace gas cycles of H₂ and CH₄. Integrating BIODep now provides a user-friendly option for incorporating additional terrestrial sinks and, more importantly, enables EMAC to simulate future climate scenarios.

In summary this work advances the MESSy framework and the EMAC model by integrating a detailed land surface component, allowing a more comprehensive and mechanistic representation of biosphere–atmosphere feedbacks within the Earth system. By bridging critical gaps in simulating vegetation dynamics, soil hydrology, and trace gas fluxes, EMAC is now an state-of-the-art model capable of representing coupled atmospheric chemistry, and climate–ecosystem interactions and aerosols processes. Together, these contributions aim to improve our understanding of feedback mechanisms in the Earth system and support the development of effective climate mitigation strategies.

Bibliography

- (GML), NOAA Global Monitoring Laboratory (2025). *Atmospheric Methane Data (CH₄) – Global Monthly Means*. Data freely available from NOAA GML. Contact: Xin Lan (xin.lan@noaa.gov). Please cite appropriately as recommended by NOAA GML. See Dlugokencky et al. (1994), JGR, vol. 99, pp. 17021–17043, for methodology. URL: <https://gml.noaa.gov/ccgg/trends/> (see page 85).
- Ackermann, IJ, H Hass, and B Schell (2001). **Regional Modelling of Atmospheric Aerosols**. In: *Transport and Chemical Transformation in the Troposphere: Proceedings of EUROTRAC Symposium 2000 Garmisch-Partenkirchen, Germany 27–31 March 2000 Eurotrac-2 International Scientific Secretariat GSF-National Research Center for Environment and Health Munich, Germany*. Springer, 119–122 (see page 7).
- Andreae, M. O. et al. (2004). **Smoking rain clouds over the Amazon**. *science* 303:5662, 1337–1342 (see page 50).
- Andreae, M. O. (2019). **Emission of trace gases and aerosols from biomass burning—an updated assessment**. *Atmospheric Chemistry and Physics* 19:13, 8523–8546 (see page 52).
- Andreae, M. O., C. D. Jones, and P. M. Cox (2005). **Strong present-day aerosol cooling implies a hot future**. *Nature* 435:7046, 1187–1190 (see page 6).
- Armour, K., P. Forster, T. Storelvmo, W. Collins, J.-L. Dufresne, D. Frame, D. Lunt, T. Mauritsen, M. Palmer, M. Watanabe, et al. (2021). **The Earths energy budget, climate feedbacks, and climate sensitivity**. In: *AGU Fall Meeting Abstracts*. Vol. 2021, U13B–07 (see page 9).
- Aronson, E.L. and B.R. Helliker (2010). **Methane flux in non-wetland soils in response to nitrogen addition: a meta-analysis**. *Ecology* 91:11, 3242–3251 (see page 82).
- Atkinson, R. (2000). **Atmospheric chemistry of VOCs and NO_x**. *Atmospheric Environment* 34:12–14, 2063–2101 (see page 4).
- Atkinson, R. and J. Arey (2003). **Gas-phase tropospheric chemistry of biogenic volatile organic compounds: A review**. *Atmospheric Environment* 37, 197–219 (see page 4).
- Bai, Yanfen, Jian Wang, Baocheng Zhang, Zhihui Zhang, and Ji Liang (2012). **Comparing the impact of cloudiness on carbon dioxide exchange in a grassland and a maize cropland in northwestern China**. *Ecological Research* 27, 615–623 (see page 56).
- Baldocchi, Dennis, Eva Falge, Lianhong Gu, Richard Olson, David Hollinger, Steve Running, Peter Anthoni, Ch Bernhofer, Kenneth Davis, Robert Evans, et al. (2001). **FLUXNET: A new tool to study the temporal and spatial variability of ecosystem-scale carbon dioxide, water vapor, and energy flux densities**. *Bulletin of the American Meteorological Society* 82:11, 2415–2434 (see pages 56, 72).

- Bellouin, N., J. Quaas, E. Gryspeerdt, S. Kinne, P. Stier, D. Watson-Parris, O. Boucher, K. S. Carslaw, M. Christensen, A.-L. Daniau, J.-L. Dufresne, G. Feingold, S. Fiedler, P. Forster, A. Gettelman, J. M. Haywood, U. Lohmann, F. Malavelle, T. Mauritsen, D. T. McCoy, G. Myhre, J. Mülmenstädt, D. Neubauer, A. Possner, M. Rugenstein, Y. Sato, M. Schulz, S. E. Schwartz, O. Sourdeval, T. Storelvmo, V. Toll, D. Winker, and B. Stevens (2020). **Bounding Global Aerosol Radiative Forcing of Climate Change**. *Reviews of Geophysics* 58:1. e2019RG000660 10.1029/2019RG000660, e2019RG000660. DOI: 10.1029/2019RG000660. eprint: <https://agupubs.onlinelibrary.wiley.com/doi/pdf/10.1029/2019RG000660>. URL: <https://agupubs.onlinelibrary.wiley.com/doi/abs/10.1029/2019RG000660> (see page 66).
- Berrisford, P., D.P. Dee, P. Poli, R. Brugge, Mark Fielding, Manuel Fuentes, P.W. Källberg, S. Kobayashi, S. Uppala, and Adrian Simmons (Nov. 2011). *The ERA-Interim archive Version 2.0*. eng. 1. Shinfield Park, Reading: ECMWF, 23 (see pages 51, 77).
- Bian, Huisheng, Eunjee Lee, Randal D Koster, Donifan Barahona, Mian Chin, Peter R Colarco, Anton Darmenov, Sarith Mahanama, Michael Manyin, Peter Norris, et al. (2021). **The response of the Amazon ecosystem to the photosynthetically active radiation fields: integrating impacts of biomass burning aerosol and clouds in the NASA GEOS Earth system model**. *Atmospheric Chemistry and Physics* 21:18, 14177–14197 (see page 50).
- Bradford, M. A., Phil Ineson, P. A. Wookey, and H. M. Lappin-Scott (2001). **The effects of acid nitrogen and acid sulphur deposition on CH₄ oxidation in a forest soil: a laboratory study**. *Soil Biology and Biochemistry* 33:12-13, 1695–1702 (see page 82).
- Bronson, K. F. and A. R. Mosier (1994). **Suppression of methane oxidation in aerobic soil by nitrogen fertilizers, nitrification inhibitors, and urease inhibitors**. *Biology and Fertility of Soils* 17, 263–268 (see page 82).
- Buchwitz, M. D., R. De Beek, J. P. Burrows, H. Bovensmann, T. Warneke, J. Notholt, J. F. Meirink, A. P. H. Goede, P. Bergamaschi, S. Körner, et al. (2005). **Atmospheric methane and carbon dioxide from SCIAMACHY satellite data: initial comparison with chemistry and transport models**. *Atmospheric Chemistry and Physics* 5:4, 941–962 (see page 10).
- Butterbach-Bahl, K. and H. Papen (2002). **Four years continuous record of CH₄ exchange between the atmosphere and untreated and limed soil of a N-saturated spruce and beech forest ecosystem in Germany**. *Plant and Soil* 240, 77–90 (see page 82).
- Cai, Zucong C. and Arvin R. Mosier (2000). **Effect of NH₄Cl addition on methane oxidation by paddy soils**. *Soil Biology and Biochemistry* 32:11-12, 1537–1545 (see page 82).
- Calfapietra, C., S. Fares, F. Manes, A. Morani, G. Sgrigna, and F. Loreto (2013). **Role of biogenic volatile organic compounds (BVOC) emitted by urban trees on ozone concentration in cities: A review**. *Environmental Pollution* 183, 71–80 (see pages 5, 6).

- Carslaw, K. S., O. Boucher, D. V. Spracklen, G. W. Mann, J. G. L. Rae, S. Woodward, and M. Kulmala (2010). **A review of natural aerosol interactions and feedbacks within the Earth system**. *Atmospheric Chemistry and Physics* 10:4, 1701–1737 (see pages 7, 50).
- Castro, M. S., P. A. Steudler, J. M. Melillo, J. D. Aber, and R. D. Bowden (1995). **Factors controlling atmospheric methane consumption by temperate forest soils**. *Global Biogeochemical Cycles* 9:1, 1–10 (see page 81).
- Chang, Jackson Hian-Wui, Yong Jie Wong, Maggie Chel-Gee Ooi, Saginela Ravindra Babu, Shantanu Kumar Pani, and Neng-Huei Lin (2024). **Biomass burning in critical fire region over the Maritime Continent from 2012 to 2021: A review of the meteorological influence and cloud-aerosol-radiation interactions**. *Atmospheric Environment*, 120324 (see page 50).
- Christensen, Matthew W., William K. Jones, and Philip Stier (2020). **Aerosols enhance cloud lifetime and brightness along the stratus-to-cumulus transition**. *Proceedings of the National Academy of Sciences* 117:30, 17591–17598. ISSN: 0027-8424. DOI: 10.1073/pnas.1921231117. eprint: <https://www.pnas.org/content/117/30/17591.full.pdf>. URL: <https://www.pnas.org/content/117/30/17591> (see page 66).
- Cirino, GG, RAF Souza, DK Adams, and P Artaxo (2014). **The effect of atmospheric aerosol particles and clouds on net ecosystem exchange in the Amazon**. *Atmospheric Chemistry and Physics* 14:13, 6523–6543 (see pages 50, 56).
- Cohan, D. S., J. Xu, R. Greenwald, M. H. Bergin, and W. L. Chameides (2002). **Impact of atmospheric aerosol light scattering and absorption on terrestrial net primary productivity**. *Global Biogeochemical Cycles* 16:4, 37–1 (see page 7).
- Constant, P., L. Poissant, and R. Villemur (2009). **Tropospheric H₂ budget and the response of its soil uptake under the changing environment**. *Science of the Total Environment* 407:6, 1809–1823 (see pages 11, 75).
- Cowan, N., T. Roberts, M. Hanlon, A. Bezanger, G. Toteva, A. Tweedie, K. Yeung, A. Deshpande, P. Levy, U. Skiba, et al. (2024). **Quantifying the soil sink of atmospheric Hydrogen: a full year of field measurements from grassland and forest soils in the UK**. *EGUsphere* (see page 12).
- Crutzen, P. J. (1973). “Gas-phase nitrogen and methane chemistry in the atmosphere.” In: *Physics and Chemistry of the Upper Atmosphere: Proceedings of a Symposium*. Springer, 110–124 (see page 9).
- (1979). **The role of NO and NO₂ in the chemistry of the troposphere and stratosphere**. *Annual Review of Earth and Planetary Sciences* 7, 443–472 (see page 9).
- Curry, Charles L (2007). **Modeling the soil consumption of atmospheric methane at the global scale**. *Global Biogeochemical Cycles* 21:4 (see page 76).
- De Visscher, Alex and Oswald Van Cleemput (2003). **Induction of enhanced CH₄ oxidation in soils: NH₄⁺ inhibition patterns**. *Soil Biology and Biochemistry* 35:7, 907–913 (see page 82).
- Del Grosso, S. J., W. J. Parton, A. R. Mosier, D. S. Ojima, C. S. Potter, W. Borke, R. Brumme, K. Butterbach-Bahl, P. M. Crill, K. Dobbie, et al. (2000). **General CH₄ oxidation model**

- and comparisons of CH₄ oxidation in natural and managed systems.** *Global Biogeochemical Cycles* 14:4, 999–1019 (see page 82).
- Delany, AC, P Haagensen, S Walters, AF Wartburg, and PJ Crutzen (1985). **Photochemically produced ozone in the emission from large-scale tropical vegetation fires.** *Journal of Geophysical Research: Atmospheres* 90:D1, 2425–2429 (see page 50).
- Desservettaz, Maximilien, Michael Pikridas, Iasonas Stavroulas, Aikaterini Bougiatioti, Eleni Liakakou, Nikolaos Hatzianastassiou, Jean Sciare, Nikolaos Mihalopoulos, and Efstratios Bourtsoukidis (2023). **Emission of volatile organic compounds from residential biomass burning and their rapid chemical transformations.** *Science of The Total Environment* 903, 166592 (see page 50).
- Dietmüller, Simone, Patrick Jöckel, Holger Tost, Markus Kunze, Catrin Gellhorn, Sabine Brinkop, Christine Frömming, Michael Ponater, Benedikt Steil, Axel Lauer, et al. (2016). **A new radiation infrastructure for the Modular Earth Submodel System (MESSy, based on version 2.5.1).** *Geoscientific Model Development* 9:6, 2209–2222 (see page 155).
- Dlugokencky, E. J., E. G. Nisbet, R. Fisher, and D. Lowry (2011). **Global atmospheric methane: budget, changes and dangers.** *Philosophical Transactions of the Royal Society A: Mathematical, Physical and Engineering Sciences* 369:1943, 2058–2072 (see page 10).
- Dubovik, O, A Smirnov, BN Holben, MD King, YJ Kaufman, TF Eck, and I Slutsker (2000). **Accuracy assessments of aerosol optical properties retrieved from Aerosol Robotic Network (AERONET) Sun and sky radiance measurements.** *Journal of Geophysical Research: Atmospheres* 105:D8, 9791–9806 (see page 58).
- Duce, R. A. (1986). “The impact of atmospheric nitrogen, phosphorus, and iron species on marine biological productivity.” In: *The Role of Air-Sea Exchange in Geochemical Cycling*. Springer, 497–529 (see page 7).
- Dutaur, Laure and Louis V Verchot (2007). **A global inventory of the soil CH₄ sink.** *Global biogeochemical cycles* 21:4 (see pages 75, 76).
- Ebi, K. and G. McGregor (2009). **Climate change, tropospheric ozone and particulate matter, and health impacts.** *Ciência & Saúde Coletiva* 14, 2281–2293 (see page 5).
- Ehhalt, D. H. and F. Rohrer (2013). **Deposition velocity of H₂: a new algorithm for its dependence on soil moisture and temperature.** *Tellus B: Chemical and Physical Meteorology* 65:1, 19904 (see pages 17, 83).
- Ehhalt, D.H. and L.E. Heidt (1973). **Vertical profiles of CH₄ in the troposphere and stratosphere.** *Journal of Geophysical Research* 78:24, 5265–5271 (see page 9).
- Ehhalt, D.H. and F. Rohrer (2009). **The tropospheric cycle of H₂: a critical review.** *Tellus B: Chemical and Physical Meteorology* 61:3, 500–535 (see pages 5, 11, 12, 75, 91).
- Emmerichs, Tamara, Yen-Sen Lu, and Domenico Taraborrelli (2024). **The influence of plant water stress on vegetation–atmosphere exchanges: implications for ozone modelling.** *Biogeosciences* 21:14, 3251–3269 (see page 4).
- Ezhova, E., I. Ylivinkka, J. Kuusk, K. Komsaare, M. Vana, A. Krasnova, S. Noe, M. Arshinov, B. Belan, S.-B. Park, J. V. Lavrič, M. Heimann, T. Petäjä, T. Vesala, I. Mammarella, P. Kolari, J. Bäck, Ü. Rannik, V.-M. Kerminen, and M. Kulmala (2018). **Direct effect of aerosols on**

- solar radiation and gross primary production in boreal and hemiboreal forests.** *Atmospheric Chemistry and Physics* 18:24, 17863–17881. DOI: 10.5194/acp-18-17863-2018. URL: <https://acp.copernicus.org/articles/18/17863/2018/> (see page 50).
- Farquhar, G. D., S. von Caemmerer, and J. A. Berry (1980). **A biochemical model of photosynthetic CO₂ assimilation in leaves of C₃ species.** *Planta* 149, 78–90 (see pages 52, 63).
- Feck, T., J.-U. Grooß, and M. Riese (2008). **Sensitivity of Arctic ozone loss to stratospheric H₂O.** *Geophysical Research Letters* 35:1 (see page 12).
- Flato, G. M. (2011). **Earth system models: an overview.** *WIREs Climate Change* 2:6, 783–800. DOI: 10.1002/wcc.148. URL: <https://wires.onlinelibrary.wiley.com/doi/abs/10.1002/wcc.148> (see page 2).
- Fluet-Chouinard, E., B. D. Stocker, Z. Zhang, A. Malhotra, J. R. Melton, B. Poulter, J. O. Kaplan, K. K. Goldewijk, S. Siebert, T. Minayeva, et al. (2023). **Extensive global wetland loss over the past three centuries.** *Nature* 614:7947, 281–286 (see page 8).
- Fluxnet-CRP (2015). (2001-2013) *FLUXNET2015 US-Ne3 Mead - rainfed maize-soybean rotation site, Dataset.* Downloaded on 08-04-2024. URL: <https://doi.org/10.18140/FLX/1440086> (see page 154).
- Fluxnet-DBF (2015). (1996-2010) *FLUXNET2015 CA-Oas Saskatchewan - Western Boreal, Mature Aspen, Dataset.* Downloaded on 08-04-2024. URL: <https://doi.org/10.18140/FLX/1440043> (see page 154).
- Fluxnet-EBF (2015). (2002-2011) *FLUXNET2015 BR-Sa1 Santarem-Km67-Primary Forest, Dataset.* Downloaded on 08-04-2024. URL: <https://doi.org/10.18140/FLX/1440032> (see page 154).
- Fluxnet-GRA (2015). (2004-2014) *FLUXNET2015 US-Wkg Walnut Gulch Kendall Grasslands, Dataset.* Downloaded on 08-04-2024. URL: <https://doi.org/10.18140/FLX/1440096> (see page 154).
- Fluxnet-SHR (2015). (2007-2014) *FLUXNET2015 US-Whs Walnut Gulch Lucky Hills Shrub, Dataset.* Downloaded on 08-04-2024. URL: <https://doi.org/10.18140/FLX/1440097> (see page 154).
- Forrest, M., H. Tost, J. Lelieveld, and T. Hickler (2020). **Including vegetation dynamics in an atmospheric chemistry-enabled general circulation model: linking LPJ-GUESS (v4.0) with the EMAC modelling system (v2.53).** *Geoscientific Model Development* 13:3, 1285–1309. DOI: 10.5194/gmd-13-1285-2020. URL: <https://gmd.copernicus.org/articles/13/1285/2020/> (see page 13).
- Forster, Piers, Venkatachalam Ramaswamy, Paulo Artaxo, Terje Berntsen, Richard Betts, David W Fahey, James Haywood, Judith Lean, David C Lowe, Gunnar Myhre, et al. (2007). **Changes in atmospheric constituents and in radiative forcing.** *Climate Change 2007: The Physical Science Basis. Contribution of Working Group I to the 4th Assessment Report of the Intergovernmental Panel on Climate Change* (see page 50).

- Gasparini, B. and U. Lohmann (2016). **Why cirrus cloud seeding cannot substantially cool the planet.** *Journal of Geophysical Research: Atmospheres* 121:9, 4877–4893 (see page 107).
- Gu, L. et al. (2002). **Advantages of diffuse radiation for terrestrial ecosystem productivity.** *Journal of Geophysical Research: Atmospheres* 107:D6, ACL-2 (see page 50).
- Gu, Lianhong, Jose D Fuentes, Herman H Shugart, Ralf M Staebler, and T Andrew Black (1999). **Responses of net ecosystem exchanges of carbon dioxide to changes in cloudiness: Results from two North American deciduous forests.** *Journal of Geophysical Research: Atmospheres* 104:D24, 31421–31434 (see page 56).
- Guenther, A. (2002). **The contribution of reactive carbon emissions from vegetation to the carbon balance of terrestrial ecosystems.** *Chemosphere* 49:8, 837–844 (see page 6).
- Guenther, A., T. Karl, P. Harley, C. Wiedinmyer, P. I. Palmer, and C. Geron (2006). **Estimates of global terrestrial isoprene emissions using MEGAN (Model of Emissions of Gases and Aerosols from Nature).** *Atmospheric Chemistry and Physics* 6:11, 3181–3210 (see pages 3, 16, 155).
- Gulledge, Jay and Joshua P. Schimel (1998). **Low-concentration kinetics of atmospheric CH₄ oxidation in soil and mechanism of NH₄⁺ inhibition.** *Applied and Environmental Microbiology* 64:11, 4291–4298 (see page 82).
- Hagemann, S. and T. Stacke (2015). **Impact of the soil hydrology scheme on simulated soil moisture memory.** *Climate Dynamics* 44, 1731–1750. URL: <https://doi.org/10.1007/s00382-014-2221-6> (see pages 52, 78).
- Hallquist, M., J. C. Wenger, U. Baltensperger, Y. Rudich, D. Simpson, M. Claeys, J. Dommen, N. M. Donahue, C. George, A. H. Goldstein, et al. (2009). **The formation, properties and impact of secondary organic aerosol: current and emerging issues.** *Atmospheric Chemistry and Physics* 9:14, 5155–5236 (see page 5).
- Hansen, J. and L. Nazarenko (2004). **Soot climate forcing via snow and ice albedos.** *Proceedings of the National Academy of Sciences* 101:2, 423–428 (see page 7).
- Hauglustaine, D., F. Paulot, W. Collins, R. Derwent, M. Sand, and O. Boucher (2022). **Climate benefit of a future hydrogen economy.** *Communications Earth & Environment* 3:1, 295 (see page 75).
- Haywood, J. and O. Boucher (2000). **Estimates of the direct and indirect radiative forcing due to tropospheric aerosols: A review.** *Reviews of Geophysics* 38:4, 513–543 (see pages 6, 7, 50, 66).
- Hines, Colin O (1997). **Doppler-spread parameterization of gravity-wave momentum deposition in the middle atmosphere. Part 1: Basic formulation.** *Journal of Atmospheric and Solar-Terrestrial Physics* 59:4, 371–386 (see page 155).
- Holben, Brent N, T F Eck, I al Slutsker, D Tanré, JP Buis, A Setzer, E Vermote, John A Reagan, YJ Kaufman, T Nakajima, et al. (1998). **AERONET—A federated instrument network and data archive for aerosol characterization.** *Remote sensing of environment* 66:1, 1–16 (see pages 57, 72).

- Hong, Y., G. Liu, and J.-L. F. Li (2016). **Assessing the radiative effects of global ice clouds based on CloudSat and CALIPSO measurements.** *Journal of Climate* 29:21, 7651–7674 (see page 107).
- Houweling, Sander, Thomas Kaminski, Frank Dentener, Jos Lelieveld, and Martin Heimann (1999). **Inverse modeling of methane sources and sinks using the adjoint of a global transport model.** *Journal of Geophysical Research: Atmospheres* 104:D21, 26137–26160 (see page 78).
- IPCC (2023). **Climate Change 2023: Synthesis Report. Contribution of Working Groups I, II and III to the Sixth Assessment Report of the Intergovernmental Panel on Climate Change.** Ed. by Core Writing Team, H. Lee, and J. Romero. Geneva, Switzerland: IPCC, 35–115. DOI: 10.59327/IPCC/AR6-9789291691647 (see pages 1, 75).
- Ito, A and M Inatomi (2012). **Use of a process-based model for assessing the methane budgets of global terrestrial ecosystems and evaluation of uncertainty.** *Biogeosciences* 9:2, 759–773 (see pages 75, 76).
- Jacob, D. J., D. J. Varon, D. H. Cusworth, P. E. Dennison, C. Frankenberg, R. Gautam, L. Guanter, J. Kelley, J. McKeever, L. E. Ott, et al. (2022). **Quantifying methane emissions from the global scale down to point sources using satellite observations of atmospheric methane.** *Atmospheric Chemistry and Physics Discussions* 2022, 1–44 (see page 10).
- Jeuken, A. B. M., P. C. Siegmund, L. C. Heijboer, J. Feichter, and L. Bengtsson (1996). **On the potential of assimilating meteorological analyses in a global climate model for the purpose of model validation.** *Journal of Geophysical Research: Atmospheres* 101:D12, 16939–16950 (see pages 51, 78).
- Jing, Xie, J Huang, G Wang, K Higuchi, J Bi, Y Sun, H Yu, and T Wang (2010). **The effects of clouds and aerosols on net ecosystem CO₂ exchange over semi-arid Loess Plateau of Northwest China.** *Atmospheric Chemistry and Physics* 10:17, 8205–8218 (see page 56).
- Jöckel, P., A. Kerkweg, A. Pozzer, R. Sander, H. Tost, H. Riede, A. Baumgaertner, S. Gromov, and B. Kern (2010a). **Development cycle 2 of the Modular Earth Submodel System (MESSy2).** *Geoscientific Model Development* 3:2, 717–752. DOI: 10.5194/gmd-3-717-2010. URL: <https://gmd.copernicus.org/articles/3/717/2010/> (see pages 13, 15, 51, 77, 155).
- Jöckel, P., R. Sander, A. Kerkweg, H. Tost, and J. Lelieveld (2005). **Technical Note: The Modular Earth Submodel System (MESSy) – a new approach towards Earth system modeling.** *Atmospheric Chemistry and Physics* 5:2, 433–444. DOI: 10.5194/acp-5-433-2005. URL: <https://acp.copernicus.org/articles/5/433/2005/> (see page 13).
- Jöckel, P., H. Tost, A. Pozzer, C. Brühl, J. Buchholz, L. Ganzeveld, P. Hoor, A. Kerkweg, M. G. Lawrence, R. Sander, et al. (2006). **The atmospheric chemistry general circulation model ECHAM5/MESSy1: consistent simulation of ozone from the surface to the mesosphere.** *Atmospheric Chemistry and Physics* 6:12, 5067–5104 (see pages 13, 51, 78).

- Jöckel, P., H. Tost, A. Pozzer, M. Kunze, O. Kirner, C. A. M. Brenninkmeijer, S. Brinkop, D. S. Cai, C. Dyroff, J. Eckstein, F. Frank, H. Garny, K.-D. Gottschaldt, P. Graf, V. Grewe, A. Kerkweg, B. Kern, S. Matthes, M. Mertens, S. Meul, M. Neumaier, M. Nützel, S. Oberländer-Hayn, R. Ruhnke, T. Runde, R. Sander, D. Scharffe, and A. Zahn (2016). **Earth System Chemistry integrated Modelling (ESCiMo) with the Modular Earth Submodel System (MESSy) version 2.51**. *Geoscientific Model Development* 9:3, 1153–1200. DOI: 10.5194/gmd-9-1153-2016. URL: <https://gmd.copernicus.org/articles/9/1153/2016/> (see pages 13, 15, 51, 77).
- Jöckel, Patrick, Astrid Kerkweg, Andrea Pozzer, Rolf Sander, Holger Tost, Hella Riede, Andreas Baumgaertner, Sergey Gromov, and Bastian Kern (2010b). **Development cycle 2 of the modular earth submodel system (MESSy2)**. *Geoscientific Model Development* 3:2, 717–752 (see page 155).
- Jungclaus, J.H., S.J. Lorenz, H. Schmidt, V. Brovkin, N. Brüggemann, F. Chegini, T. Crüger, P. De-Vrese, V. Gayler, M.A. Giorgetta, et al. (2022). **The ICON earth system model version 1.0**. *Journal of Advances in Modeling Earth Systems* 14:4, e2021MS002813 (see page 16).
- Kaiser, J. W., A. Heil, M. O. Andreae, A. Benedetti, N. Chubarova, L. Jones, J.-J. Morcrette, M. Razinger, M. G. Schultz, M. Suttie, et al. (2012). **Biomass burning emissions estimated with a global fire assimilation system based on observed fire radiative power**. *Biogeosciences* 9:1, 527–554 (see pages 52, 155).
- Kerkweg, A, R Sander, H Tost, and P Jöckel (2006). **Implementation of prescribed (OFFLEM), calculated (ONLEM), and pseudo-emissions (TNUDGE) of chemical species in the Modular Earth Submodel System (MESSy)**. *Atmospheric Chemistry and Physics* 6:11, 3603–3609 (see page 155).
- Kesselmeier, J., P. Ciccioli, U. Kuhn, P. Stefani, T. Biesenthal, S. Rottenberger, A. Wolf, M. Vitullo, R. Valentini, A. Nobre, et al. (2002). **Volatile organic compound emissions in relation to plant carbon fixation and the terrestrial carbon budget**. *Global Biogeochemical Cycles* 16:4, 73–1 (see page 6).
- Kleinen, T., V. Brovkin, and R. J. Schuldt (2012). **A dynamic model of wetland extent and peat accumulation: results for the Holocene**. *Biogeosciences* 9:1, 235–248 (see page 10).
- Kleinen, T., S. Gromov, B. Steil, and V. Brovkin (2023). **Atmospheric methane since the last glacial maximum was driven by wetland sources**. *Climate of the Past* 19:5, 1081–1099 (see pages 9, 10).
- Kleinen, T., U. Mikolajewicz, and V. Brovkin (2020). **Terrestrial methane emissions from the Last Glacial Maximum to the preindustrial period**. *Climate of the Past* 16:2, 575–595 (see pages 10, 75, 76).
- Kohl, M., J. Lelieveld, S. Chowdhury, S. Ehrhart, D. Sharma, Y. Cheng, S. N. Tripathi, M. Sebastian, G. Pandithurai, H. Wang, et al. (2023). **Numerical simulation and evaluation of global ultrafine particle concentrations at the Earth's surface**. *EGUsphere* 2023, 1–34 (see pages 52, 78, 155).

- Koster, R. D., Y. C. Sud, Z. Guo, P. A. Dirmeyer, G. Bonan, K. W. Oleson, E. Chan, D. Verseghy, P. Cox, H. Davies, et al. (2006). **GLACE: the global land–atmosphere coupling experiment. Part I: overview.** *Journal of Hydrometeorology* 7:4, 590–610 (see page 3).
- Kulmala, M., T. Suni, K. E. J. Lehtinen, M. Dal Maso, M. Boy, A. Reissell, Ü. Rannik, P. Aalto, P. Keronen, H. Hakola, et al. (2004). **A new feedback mechanism linking forests, aerosols, and climate.** *Atmospheric Chemistry and Physics* 4:2, 557–562 (see pages 5, 6).
- Lan, X., J.W. Mund, A.M. Croftwell, K.W. Thoning, E. Moglia, M. Madronich, K. Baugh, G. Petron, M.J. Croftwell, D. Neff, S. Wolter, T. Mefford, and S. DeVogel (2025). *Atmospheric Methane Dry Air Mole Fractions from the NOAA GML Carbon Cycle Cooperative Global Air Sampling Network, 1983–2024.* Version 2025-04-26. Accessed YYYY-MM-DD. NOAA Global Monitoring Laboratory. DOI: 10.15138/VNCZ-M766. URL: <https://doi.org/10.15138/VNCZ-M766> (see pages 77, 84–86).
- Laothawornkitkul, J., N. D. Paul, C. E. Vickers, M. Possell, J. E. Taylor, P. M. Mullineaux, and C. N. Hewitt (2008). **Isoprene emissions influence herbivore feeding decisions.** *Plant, Cell & Environment* 31:10, 1410–1415 (see page 4).
- Lelieveld, J., T. M. Butler, J. N. Crowley, T. J. Dillon, H. Fischer, L. Ganzeveld, H. Harder, M. G. Lawrence, M. Martinez, D. Taraborrelli, et al. (2008). **Atmospheric oxidation capacity sustained by a tropical forest.** *Nature* 452:7188, 737–740 (see page 3).
- Lelieveld, J., P. J. Crutzen, and F. J. Dentener (1998). **Changing concentration, lifetime and climate forcing of atmospheric methane.** *Tellus B* 50:2, 128–150 (see pages 5, 7).
- Lippmann, M. (1991). **Health effects of tropospheric ozone.** *Environmental Science & Technology* 25:12, 1954–1962 (see page 5).
- Liu, L., M. Estiarte, and J. Peñuelas (2019). **Soil moisture as the key factor of atmospheric CH₄ uptake in forest soils under environmental change.** *Geoderma* 355, 113920 (see page 10).
- Lohmann, U. and J. Feichter (2005). **Global indirect aerosol effects: a review.** *Atmospheric Chemistry and Physics* 5:3, 715–737 (see pages 6, 7, 12, 50, 66).
- Luo, G. J., R. Kiese, B. Wolf, and K. Butterbach-Bahl (2013). **Effects of soil temperature and moisture on methane uptake and nitrous oxide emissions across three different ecosystem types.** *Biogeosciences* 10:5, 3205–3219 (see pages 9, 80).
- MacDonald, Jannette A., Ute Skiba, Lucy J. Sheppard, Kenneth J. Hargreaves, Keith A. Smith, and David Fowler (1996). **Soil environmental variables affecting the flux of methane from a range of forest, moorland and agricultural soils.** *Biogeochemistry* 34, 113–132 (see page 82).
- Malavelle, Florent F, Jim M Haywood, Lina M Mercado, Gerd A Folberth, Nicolas Bellouin, Stephen Sitch, and Paulo Artaxo (2019). **Studying the impact of biomass burning aerosol radiative and climate effects on the Amazon rainforest productivity with an Earth system model.** *Atmospheric Chemistry and Physics* 19:2, 1301–1326 (see page 50).

- Martin, A., V. Gayler, B. Steil, K. Klingmüller, P. Jöckel, H. Tost, J. Lelieveld, and A. Pozzer (2024). **Evaluation of the coupling of EMACv2.55 to the land surface and vegetation model JSBACHv4**. *Geoscientific Model Development* 17:14, 5705–5732 (see pages 52, 78, 136, 155).
- Matyssek, R., A. R. Kozovits, J.-P. Schnitzler, H. Pretzsch, J. Dieler, and G. Wieser (2014). **Forest trees under air pollution as a factor of climate change**. *Trees in a Changing Environment: Ecophysiology, Adaptation, and Future Survival*, 117–163 (see pages 4, 6).
- Mauritsen, T., J. Bader, T. Becker, J. Behrens, M. Bittner, R. Brokopf, V. Brovkin, M. Claussen, T. Crueger, M. Esch, et al. (2019). **Developments in the MPI-M Earth System Model version 1.2 (MPI-ESM1.2) and its response to increasing CO₂**. *Journal of Advances in Modeling Earth Systems* 11:4, 998–1038 (see page 16).
- McKee, D. (1993). **Tropospheric ozone: human health and agricultural impacts**. CRC Press (see page 5).
- MESSy-webpage (2023). *MESSy Submodels*. URL: <https://messy-interface.org/messy/submodels/> (visited on 11/20/2023) (see page 155).
- Moldrup, P., T. K. K. Chamindu Deepagoda, S. Hamamoto, T. Komatsu, K. Kawamoto, D. E. Rolston, and L. W. de Jonge (2013). **Structure-dependent water-induced linear reduction model for predicting gas diffusivity and tortuosity in repacked and intact soil**. *Vadose Zone Journal* 12:3, vzj2013–01 (see page 80).
- Moldrup, P., C. W. Kruse, D. E. Rolston, and T. Yamaguchi (1996). **Modeling diffusion and reaction in soils: III. Predicting gas diffusivity from the Campbell soil-water retention model**. *Soil Science* 161:6, 366–375 (see page 80).
- Monks, P. S. (2005). **Gas-phase radical chemistry in the troposphere**. *Chemical Society Reviews* 34:5, 376–395 (see page 3).
- Monson, R. K., N. Trahan, T. N. Rosenstiel, P. Veres, D. Moore, M. Wilkinson, R. J. Norby, A. Volder, M. G. Tjoelker, D. D. Briske, et al. (2007). **Isoprene emission from terrestrial ecosystems in response to global change: minding the gap between models and observations**. *Philosophical Transactions of the Royal Society A: Mathematical, Physical and Engineering Sciences* 365:1856, 1677–1695 (see page 6).
- Moreira, Demerval S, Karla M Longo, Saulo R Freitas, Marcia A Yamasoe, Lina M Mercado, Nilton E Rosário, Emanuel Gloor, Rosane SM Viana, John B Miller, Luciana V Gatti, et al. (2017). **Modeling the radiative effects of biomass burning aerosols on carbon fluxes in the Amazon region**. *Atmospheric chemistry and physics* 17:23, 14785–14810 (see page 50).
- Murguia-Flores, F., S. Arndt, A. L. Ganesan, G. Murray-Tortarolo, and E. R. C. Hornibrook (2018). **Soil Methanotrophy Model (MeMo v1.0): a process-based model to quantify global uptake of atmospheric methane by soil**. *Geoscientific Model Development* 11:6, 2009–2032 (see pages 10, 17, 75, 76, 79–82, 84, 85).
- Murguia-Flores, F., A.L. Ganesan, S. Arndt, and E.R.C. Hornibrook (2021). **Global uptake of atmospheric methane by soil from 1900 to 2100**. *Global Biogeochemical Cycles* 35:7, e2020GB006774 (see page 10).

- Myhre, G., D. Shindell, F.-M. Bréon, W. Collins, J. Fuglestedt, J. Huang, D. Koch, J.-F. Lamarque, D. Lee, B. Mendoza, T. Nakajima, A. Robock, G. Stephens, T. Takemura, and H. Zhang (2013). **IPCC AR5, WG1, Chapter 8: Anthropogenic and Natural Radiative Forcing**, 659–740. URL: https://archive.ipcc.ch/pdf/assessment-report/ar5/wg1/WG1AR5_Chapter08_FINAL.pdf (see page 107).
- Nauta, A.L., M.M.P.D. Heijmans, D. Blok, J. Limpens, B.O. Elberling, A. Gallagher, B. Li, R.E. Petrov, T.C. Maximov, J. Van Huissteden, et al. (2015). **Permafrost collapse after shrub removal shifts tundra ecosystem to a methane source**. *Nature climate change* 5:1, 67–70 (see page 9).
- Nisbet, E.G., M.R. Manning, E.J. Dlugokencky, S.E. Michel, X. Lan, T. Röckmann, H.A.C. Denier van der Gon, J. Schmitt, P.I. Palmer, M.N. Dyonisius, et al. (2023). **Atmospheric methane: Comparison between methane’s record in 2006–2022 and during glacial terminations**. *Global Biogeochemical Cycles* 37:8, e2023GB007875 (see pages 8, 9).
- Nishina, K., A. Ito, N. Hanasaki, and S. Hayashi (2017). **Reconstruction of spatially detailed global map of NH_4^+ and NO_3^- application in synthetic nitrogen fertilizer**. *Earth System Science Data* 9:1. Accessed: October 31, 2024, 149–162 (see pages 84, 103).
- Noël, S., K. Weigel, K. Bramstedt, A. Rozanov, M. Weber, H. Bovensmann, and J.P. Burrows (2018). **Water vapour and methane coupling in the stratosphere observed using SCIAMACHY solar occultation measurements**. *Atmospheric Chemistry and Physics* 18:7, 4463–4476 (see page 9).
- Nützel, Matthias, Laura Stecher, Patrick Jöckel, Franziska Winterstein, Martin Dameris, Michael Ponater, Phoebe Graf, and Markus Kunze (2023). **Updating the radiation infrastructure in MESSy (based on MESSy version 2.55)**. *EGUsphere* 2023, 1–44 (see page 155).
- Oke, T. R. (2002). **Boundary layer climates**. Routledge (see page 2).
- Oliveira, Paulo HF, Paulo Artaxo, Carlos Pires, Silvia De Lucca, Aline Procópio, Brent Holben, Joel Schafer, Luiz F Cardoso, Steven C Wofsy, and Humberto R Rocha (2007). **The effects of biomass burning aerosols and clouds on the CO₂ flux in Amazonia**. *Tellus B: Chemical and Physical Meteorology* 59:3, 338–349 (see page 56).
- Pacifico, F, GA Folberth, S Sitch, JM Haywood, P Artaxo, and LV Rizzo (2014). **Biomass burning related ozone damage on vegetation over the Amazon forest**. *Atmospheric Chemistry & Physics Discussions* 14:14 (see page 50).
- Paulot, F., D. Paynter, V. Naik, S. Malyshev, R. Menzel, and L. W. Horowitz (2021). **Global modeling of hydrogen using GFDL-AM4.1: Sensitivity of soil removal and radiative forcing**. *International Journal of Hydrogen Energy* 46:24, 13446–13460 (see pages 17, 83).
- Paulot, F., G. Pétron, A.M. Crotwell, and M.B. Bertagni (2024). **Reanalysis of NOAA H₂ observations: implications for the H₂ budget**. *Atmospheric Chemistry and Physics* 24:7, 4217–4229 (see pages 11, 75).
- Penner, J. E., M. O. Andreae, H. Annegarn, L. Barrie, J. Feichter, D. Hegg, A. Jayaraman, R. Leaitch, D. Murphy, J. Nganga, et al. (2001). “Aerosols, their direct and indirect effects.”

- In: *Climate Change 2001: The Scientific Basis. Contribution of Working Group I to the Third Assessment Report of the Intergovernmental Panel on Climate Change*. Cambridge University Press, 289–348 (see pages 6, 7).
- Peñuelas, J. and J. Llusà (2003). **BVOCs: plant defense against climate warming?** *Trends in Plant Science* 8:3, 105–109 (see page 5).
- Peñuelas, J., T. Rutishauser, and I. Filella (2009). **Phenology feedbacks on climate change.** *Science* 324:5929, 887–888 (see page 6).
- Peñuelas, J. and M. Staudt (2010a). **BVOCs and global change.** *Trends in Plant Science* 15:3, 133–144 (see pages 3, 4, 6).
- Peñuelas, Josep and Michael Staudt (2010b). **BVOCs and global change.** *Trends in plant science* 15:3, 133–144 (see page 4).
- Pétron, Gabrielle, Andrew M Crotwell, John Mund, Molly Crotwell, Thomas Mefford, Kirk Thoning, Bradley Hall, Duane Kitzis, Monica Madronich, Eric Moglia, et al. (2024). **Atmospheric H₂ observations from the NOAA Cooperative Global Air Sampling Network.** *Atmospheric Measurement Techniques* 17:16, 4803–4823 (see pages 77, 84, 85).
- Phillips, Rebecca L., Stephen C. Whalen, and William H. Schlesinger (2001). **Response of soil methanotrophic activity to carbon dioxide enrichment in a North Carolina coniferous forest.** *Soil Biology and Biochemistry* 33:6, 793–800 (see page 82).
- Pol-van Dasselaar, A. Van den, M.L. Van Beusichem, and O. Oenema (1998). **Effects of soil moisture content and temperature on methane uptake by grasslands on sandy soils.** *Plant and Soil* 204:2, 213–222 (see page 75).
- Pozzer, A, P Jöckel, R Sander, J Williams, L Ganzeveld, and J Lelieveld (2006). **The MESSy-submodel AIRSEA calculating the air-sea exchange of chemical species.** *Atmospheric Chemistry and Physics* 6:12, 5435–5444 (see page 155).
- Pozzer, A., S.C. Anenberg, S. Dey, A. Haines, J. Lelieveld, and S. Chowdhury (2023). **Mortality attributable to ambient air pollution: A review of global estimates.** *GeoHealth* 7:1, e2022GH000711 (see page 5).
- Pringle, KJ, H Tost, B Steil, D Giannadaki, Athanasios Nenes, C Fountoukis, P Stier, E Vignati, J Lelieveld, et al. (2010). **Description and evaluation of GMXe: a new aerosol submodel for global simulations (v1).** *Geoscientific Model Development* 3:2, 391–412 (see page 155).
- Rabl, A. and J. V. Spadaro (2000). **Public health impact of air pollution and implications for the energy system.** *Annual Review of Energy and the Environment* 25:1, 601–627 (see page 7).
- Randerson, J. T., G. R. van der Werf, L. Giglio, G. J. Collatz, and P. S. Kasibhatla (Jan. 2017). *Global Fire Emissions Database, Version 4.1 (GFEDv4)*. DOI: 10.3334/ORNLDAAC/1293 (see pages 52, 72, 78).
- Rap, A. et al. (2015). **Fires increase Amazon forest productivity through increases in diffuse radiation.** *Geophysical Research Letters* 42:11, 4654–4662 (see pages 7, 50, 63, 69).

- (2018). **Enhanced global primary production by biogenic aerosol via diffuse radiation fertilization**. *Nature Geoscience* 11:9, 640–644 (see page 50).
- Rap, A., C. E. Scott, D. V. Spracklen, N. Bellouin, P. M. Forster, K. S. Carslaw, A. Schmidt, and G. Mann (2013). **Natural aerosol direct and indirect radiative effects**. *Geophysical Research Letters* 40:12, 3297–3301 (see page 5).
- Reick, C. H., V. Gayler, D. Goll, S. Hagemann, M. Heidkamp, J. E. M. S. Nabel, et al. (2021). **JSBACH 3 - The land component of the MPI Earth System Model: documentation of version 3.2. Hamburg: MPI für Meteorologie**. DOI: 10.17617/2.3279802 (see pages 13, 16, 52, 63, 78).
- Reick, C.H., T. Raddatz, V. Brovkin, and V. Gayler (2013). **Representation of natural and anthropogenic land cover change in MPI-ESM**. *Journal of Advances in Modeling Earth Systems* 5:3, 459–482 (see pages 2, 13, 16).
- Reid, JS, R Koppmann, TF Eck, and DP Eleuterio (2005). **A review of biomass burning emissions part II: intensive physical properties of biomass burning particles**. *Atmospheric chemistry and physics* 5:3, 799–825 (see page 50).
- Reifenberg, S. F., A. Martin, M. Kohl, S. Bacer, Z. Hamryszczak, I. Tadic, L. Röder, D. J. Crowley, H. Fischer, K. Kaiser, et al. (2022). **Numerical simulation of the impact of COVID-19 lockdown on tropospheric composition and aerosol radiative forcing in Europe**. *Atmospheric Chemistry and Physics* 22:16, 10901–10917 (see pages 14, 106, 108).
- Reindl, Douglas T, William A Beckman, and John A Duffie (1990). **Diffuse fraction correlations**. *Solar energy* 45:1, 1–7 (see pages 56, 57).
- Ridgwell, Andy J, Stewart J Marshall, and Keith Gregson (1999). **Consumption of atmospheric methane by soils: A process-based model**. *Global Biogeochemical Cycles* 13:1, 59–70 (see page 76).
- Righi, M., J. Hendricks, and C. G. Beer (2021). **Exploring the uncertainties in the aviation soot-cirrus effect**. *Atmospheric Chemistry and Physics Discussions* 2021, 1–31. DOI: 10.5194/acp-2021-329. URL: <https://acp.copernicus.org/preprints/acp-2021-329/> (see page 107).
- Rigler, Elisabeth and Sophie Zechmeister-Boltenstern (1999). **Oxidation of ethylene and methane in forest soils—effect of CO₂ and mineral nitrogen**. *Geoderma* 90:1-2, 147–159 (see page 82).
- Rodell, M., P. R. Houser, U. E. A. Jambor, J. Gottschalck, K. Mitchell, C.-J. Meng, K. Arsenault, B. Cosgrove, J. Radakovich, M. Bosilovich, et al. (2004). **The global land data assimilation system**. *Bulletin of the American Meteorological Society* 85:3, 381–394 (see pages 83, 103).
- Rodrigues, Simone, Glauber Cirino, Demerval Moreira, Rafael Palácios, José Nogueira, Maria Isabel Vitorino, and George Vourlitis (2023). **Enhanced net CO₂ exchange of a semi-deciduous forest in the southern Amazon due to diffuse radiation from biomass burning**. *EGUsphere* 2023, 1–33 (see pages 50, 56).

- Roeckner, E., R. Brokopf, M. Esch, M. A. Giorgetta, S. Hagemann, L. Kornblueh, E. Manzini, U. Schlese, and U. Schulzweida (2006). **Sensitivity of simulated climate to horizontal and vertical resolution in the ECHAM5 atmosphere model.** *Journal of Climate* 19:16, 3771–3791 (see pages 15, 51, 77, 155).
- Roeckner, Erich, G Bäuml, Luca Bonaventura, Renate Brokopf, Monika Esch, Marco Giorgetta, Stefan Hagemann, Ingo Kirchner, Luis Kornblueh, Elisa Manzini, et al. (2003). **The atmospheric general circulation model ECHAM 5. PART I: Model description** (see page 155).
- Sand, M., R. B. Skeie, M. Sandstad, S. Krishnan, G. Myhre, H. Bryant, R. Derwent, D. Hauglustaine, F. Paulot, M. Prather, et al. (2023). **A multi-model assessment of the Global Warming Potential of hydrogen.** *Communications Earth & Environment* 4:1, 203 (see pages 5, 12, 75, 91).
- Sander, R, A Baumgaertner, D Cabrera-Perez, F Frank, S Gromov, JU Grooss, H Harder, V Huijnen, P Jöckel, VA Karydis, et al. (2019). *The community atmospheric chemistry box model CAABA/MECCA-4.0*, *Geosci. Model Dev.*, 12, 1365–1385 (see page 155).
- Sander, Rolf, Patrick Jöckel, Oliver Kirner, AT Kunert, Jochen Landgraf, and Andrea Pozzer (2014). **The photolysis module JVAL-14, compatible with the MESSy standard, and the JVal PreProcessor (JVPP).** *Geoscientific Model Development* 7:6, 2653–2662 (see page 155).
- Sanderson, M. G., C. D. Jones, W. J. Collins, C. E. Johnson, and R. G. Derwent (2003). **Effect of climate change on isoprene emissions and surface ozone levels.** *Geophysical Research Letters* 30:18 (see page 3).
- Saunio, M., A. Martinez, B. Poulter, Z. Zhang, P.A. Raymond, P. Regnier, J.G. Canadell, R.B. Jackson, P.K. Patra, P. Bousquet, et al. (2025). **Global methane budget 2000–2020.** *Earth System Science Data* 17:5, 1873–1958 (see pages 3, 8–10, 75).
- Saunio, Marielle, Philippe Bousquet, Ben Poulter, Anna Peregon, Philippe Ciais, Josep G Canadell, Edward J Dlugokencky, Giuseppe Etiope, David Bastviken, Sander Houweling, et al. (2016). **The global methane budget: 2000–2012.** *Earth System Science Data Discussions* 2016, 1–79 (see pages 75, 76).
- Saunio, Marielle, Ann R Stavert, Ben Poulter, Philippe Bousquet, Joseph G Canadell, Robert B Jackson, Peter A Raymond, Edward J Dlugokencky, Sander Houweling, Prabir K Patra, et al. (2019). **The global methane budget 2000–2017.** *Earth System Science Data Discussions* 2019, 1–136 (see page 75).
- Schaefer, K., H. Lantuit, V.E. Romanovsky, E.A.G. Schuur, and R. Witt (2014). **The impact of the permafrost carbon feedback on global climate.** *Environmental Research Letters* 9:8, 085003 (see page 9).
- Schneck, R., V. Gayler, J. E. M. S. Nabel, T. Raddatz, C. H. Reick, and R. Schnur (2022). **Assessment of JSBACHv4.30 as land component of ICON-ESM-V1 in comparison to its predecessor JSBACHv3.2 of MPI-ESM1.2.** *Geoscientific Model Development Discussions* 2022, 1–45. DOI: 10.5194/gmd-2022-74. URL: <https://gmd.copernicus.org/preprints/gmd-2022-74/> (see pages 16, 52, 78).

- Schultz, M.G., T. Diehl, G.P. Brasseur, and W. Zittel (2003). **Air pollution and climate-forcing impacts of a global hydrogen economy**. *Science* 302:5645, 624–627 (see page 75).
- Schultz, Martin G, Angelika Heil, Judith J Hoelzemann, Allan Spessa, Kirsten Thonicke, Johann G Goldammer, Alexander C Held, Jose MC Pereira, and Maarten van Het Bolscher (2008). **Global wildland fire emissions from 1960 to 2000**. *Global Biogeochemical Cycles* 22:2 (see page 79).
- Scott, C. E., A. Rap, D. V. Spracklen, P. M. Forster, K. S. Carslaw, G. W. Mann, K. J. Pringle, N. Kivekäs, M. Kulmala, H. Lihavainen, et al. (2014). **The direct and indirect radiative effects of biogenic secondary organic aerosol**. *Atmospheric Chemistry and Physics* 14:1, 447–470 (see page 5).
- Sellers, P. J. (1985). **Canopy reflectance, photosynthesis and transpiration**. *International Journal of Remote Sensing* 6:8, 1335–1372. DOI: 10.1080/01431168508948283. eprint: <https://doi.org/10.1080/01431168508948283>. URL: <https://doi.org/10.1080/01431168508948283> (see page 52).
- Seneviratne, S. I., T. Corti, E. L. Davin, M. Hirschi, E. B. Jaeger, I. Lehner, B. Orlowsky, and A. J. Teuling (2010). **Investigating soil moisture–climate interactions in a changing climate: A review**. *Earth-Science Reviews* 99:3-4, 125–161 (see page 3).
- Seneviratne, S. I., D. Lüthi, M. Litschi, and C. Schär (2006). **Land–atmosphere coupling and climate change in Europe**. *Nature* 443:7108, 205–209 (see page 3).
- Shangguan, W., Y. Dai, Q. Duan, B. Liu, and H. Yuan (2014). **A global soil data set for earth system modeling**. *Journal of Advances in Modeling Earth Systems* 6:1. Accessed: October 31, 2024, 249–263 (see pages 84, 103).
- Shindell, D.T. (2001). **Climate and ozone response to increased stratospheric water vapor**. *Geophysical Research Letters* 28:8, 1551–1554 (see page 12).
- Shushi, Peng, Lu Zihan, Liu Gang, and Chen Anping (Sept. 2020). *Global soil methane uptake inferred from global field measurements*. Version v1. Zenodo. DOI: 10.5281/zenodo.4019118. URL: <https://doi.org/10.5281/zenodo.4019118> (see pages 75, 76).
- Singh, J.S., S. Singh, A.S. Raghubanshi, S. Singh, A.K. Kashyap, and V.S. Reddy (1997). **Effect of soil nitrogen, carbon and moisture on methane uptake by dry tropical forest soils**. *Plant and Soil* 196, 115–121 (see page 75).
- Sinyuk, Alexander, Brent N Holben, Alexander Smirnov, Thomas F Eck, Ilya Slutsker, Joel S Schafer, David M Giles, and Mikhail Sorokin (2012). **Assessment of error in aerosol optical depth measured by AERONET due to aerosol forward scattering**. *Geophysical Research Letters* 39:23 (see page 58).
- Sitaula, Bishal K., Sissel Hansen, J. Ileana Bonilla Sitaula, and Lars R. Bakken (2000). **Methane oxidation potentials and fluxes in agricultural soil: Effects of fertilisation and soil compaction**. *Biogeochemistry* 48, 323–339 (see page 82).
- Solomon, S., K.H. Rosenlof, R.W. Portmann, J.S. Daniel, S.M. Davis, T.J. Sanford, and G.-K. Plattner (2010). **Contributions of stratospheric water vapor to decadal changes in the rate of global warming**. *science* 327:5970, 1219–1223 (see page 12).

- Spitters, CJT, HAJM Toussaint, and J Goudriaan (1986). **Separating the diffuse and direct component of global radiation and its implications for modeling canopy photosynthesis Part I. Components of incoming radiation.** *Agricultural and Forest Meteorology* 38:1-3, 217–229 (see pages 56, 57).
- Sporre, M. K., S. M. Blichner, I. H. H. Karset, R. Makkonen, and T. K. Berntsen (2019). **BVOC–aerosol–climate feedbacks investigated using NorESM.** *Atmospheric Chemistry and Physics* 19:7, 4763–4782 (see page 6).
- Spracklen, Dominick V, Steve R Arnold, and CM Taylor (2012). **Observations of increased tropical rainfall preceded by air passage over forests.** *Nature* 489:7415, 282–285 (see page 50).
- Steinkamp, R., K. Butterbach-Bahl, and H. Papen (2001). **Methane oxidation by soils of an N limited and N fertilized spruce forest in the Black Forest, Germany.** *Soil Biology and Biochemistry* 33:2, 145–153 (see page 82).
- Strada, Susanna and Nadine Unger (2016). **Potential sensitivity of photosynthesis and isoprene emission to direct radiative effects of atmospheric aerosol pollution.** *Atmospheric Chemistry and Physics* 16:7, 4213–4234 (see pages 50, 63).
- Surawski, N., B. Steil, C. Brühl, S. Gromov, K. Klingmüller, A. Martin, A. Pozzer, and J. Lelieveld (2025). **Global atmospheric hydrogen chemistry and long-term source-sink budget simulation with the EMAC v2.55 model.** In: vol. 2025, 1–29 (see pages 17, 76, 78, 83–85, 91, 98).
- Swap, R., M. Garstang, S. Greco, R. Talbot, and P. Kållberg (1992). **Saharan dust in the Amazon Basin.** *Tellus B* 44:2, 133–149 (see page 7).
- Tardito Chaudhri, A. K. and D. S. Stevenson (2024). **Soil Deposition of Atmospheric Hydrogen Constrained using Planetary Scale Observations.** *EGUsphere* 2024, 1–22 (see page 12).
- Tosca, MG, JT Randerson, and CS Zender (2013). **Global impact of smoke aerosols from landscape fires on climate and the Hadley circulation.** *Atmospheric Chemistry and Physics* 13:10, 5227–5241 (see page 50).
- Tost, H, P Jöckel, A Kerkweg, R Sander, and J Lelieveld (2006a). **A new comprehensive SCAVenging submodel for global atmospheric chemistry modelling.** *Atmospheric Chemistry and Physics* 6:3, 565–574 (see page 155).
- Tost, H, P Jöckel, and J Lelieveld (2006b). **Influence of different convection parameterisations in a GCM.** *Atmospheric Chemistry and Physics* 6:12, 5475–5493 (see page 155).
- (2007). **Lightning and convection parameterisations–uncertainties in global modelling.** *Atmospheric Chemistry and Physics* 7:17, 4553–4568 (see page 155).
- Tost, H. (2023). *ECHAM5 cloud scheme.* URL: <https://envmodel.ipa.uni-mainz.de/submodels-cloud/> (visited on 10/12/2023) (see page 155).
- Trapani, D., P. Marocco, M. Gandiglio, and M. Santarelli (2025). **Hydrogen leakages across the supply chain: Current estimates and future scenarios.** Available at SSRN 5241128 (see pages 11, 75).

- Tromp, T.K., R.-L. Shia, M. Allen, J.M. Eiler, and Y.L. Yung (2003). **Potential environmental impact of a hydrogen economy on the stratosphere**. *Science* 300:5626, 1740–1742 (see pages 12, 75).
- Tsimpidi, AP, VA Karydis, A Pozzer, SN Pandis, and J Lelieveld (2014). **ORACLE (v1.0): module to simulate the organic aerosol composition and evolution in the atmosphere**. *Geoscientific Model Development* 7:6, 3153–3172 (see page 155).
- Twomey, S. (1959a). **The nuclei of natural cloud formation part II: The supersaturation in natural clouds and the variation of cloud droplet concentration**. *Geofisica Pura e Applicata* 43:1, 243–249 (see page 7).
- (May 1959b). **The nuclei of natural cloud formation part II: The supersaturation in natural clouds and the variation of cloud droplet concentration**. en. *Geofisica pura e applicata* 43:1, 243–249. ISSN: 1420-9136. DOI: 10.1007/BF01993560. URL: <https://doi.org/10.1007/BF01993560> (visited on 06/11/2021) (see page 66).
- (1959c). **The nuclei of natural cloud formation. PART I**. *Geofisica Pura e Applicata* 43, 227–242 (see page 7).
- Unger, N, X Yue, and KL Harper (2017). **Aerosol climate change effects on land ecosystem services**. *Faraday discussions* 200, 121–142 (see pages 50, 63).
- Vella, Ryan, Matthew Forrest, Jos Lelieveld, and Holger Tost (2023a). **Isoprene and monoterpene simulations using the chemistry–climate model EMAC (v2. 55) with interactive vegetation from LPJ-GUESS (v4. 0)**. *Geoscientific Model Development* 16:3, 885–906 (see page 13).
- Vella, Ryan, Andrea Pozzer, Matthew Forrest, Jos Lelieveld, Thomas Hickler, and Holger Tost (2023b). **Changes in biogenic volatile organic compound emissions in response to the El Niño–Southern Oscillation**. *Biogeosciences* 20:20, 4391–4412 (see page 4).
- Wang, P., Q. Ying, H. Zhang, J. Hu, Y. Lin, and H. Mao (2018). **Source apportionment of secondary organic aerosol in China using a regional source-oriented chemical transport model and two emission inventories**. *Environmental Pollution* 237, 756–766 (see page 5).
- Wang, Y., M. Xue, X. Zheng, B. Ji, R. Du, and Y. Wang (2005). **Effects of environmental factors on N₂O emission from and CH₄ uptake by the typical grasslands in the Inner Mongolia**. *Chemosphere* 58:2, 205–215 (see page 75).
- Weber, James, Scott Archer-Nicholls, Nathan Luke Abraham, Youngsub Matthew Shin, Paul Griffiths, Daniel P Grosvenor, Catherine E Scott, and Alex T Archibald (2022). **Chemistry-driven changes strongly influence climate forcing from vegetation emissions**. *Nature Communications* 13:1, 7202 (see page 65).
- Whalen, Stephen C. (2000). **Influence of N and non-N salts on atmospheric methane oxidation by upland boreal forest and tundra soils**. *Biology and Fertility of Soils* 31, 279–287 (see page 82).
- Williams, Mathew, Andrew D Richardson, M Reichstein, Paul C Stoy, Philippe Peylin, Hans Verbeeck, N Carvalhais, Martin Jung, David Y Hollinger, J Kattge, et al. (2009).

- Improving land surface models with FLUXNET data.** *Biogeosciences* 6:7, 1341–1359 (see page 56).
- Woodward, G., D. M. Perkins, and L. E. Brown (2010). **Climate change and freshwater ecosystems: impacts across multiple levels of organization.** *Philosophical Transactions of the Royal Society B: Biological Sciences* 365:1549, 2093–2106 (see page 8).
- Wu, K., X. Yang, D. Chen, S. Gu, Y. Lu, Q. Jiang, K. Wang, Y. Ou, Y. Qian, P. Shao, et al. (2020). **Estimation of biogenic VOC emissions and their corresponding impact on ozone and secondary organic aerosol formation in China.** *Atmospheric Research* 231, 104656 (see page 5).
- Yang, Yiming, Fengbin Sun, Yusheng Chen, Shiyue Yang, Yuan Dai, Yiming Qin, Ning Zhang, Zhifeng Shu, Han Yan, Xinlei Ge, et al. (2025). **Impact of temperature on the biogenic volatile organic compound (BVOC) emissions in China: A review.** *Journal of Environmental Sciences* (see pages 4, 5).
- Yao, Wanying, Yixuan Zhao, Ruihan Chen, Mengying Wang, Weiwei Song, and Dajiang Yu (2023). **Emissions of toxic substances from biomass burning: a review of methods and technical influencing factors.** *Processes* 11:3, 853 (see page 50).
- Yashiro, H., K. Sudo, S. Yonemura, and M. Takigawa (2011). **The impact of soil uptake on the global distribution of molecular hydrogen: chemical transport model simulation.** *Atmospheric Chemistry and Physics* 11:13, 6701–6719 (see pages 83, 91).
- Yonemura, S., M. Yokozawa, S. Kawashima, and H. Tsuruta (2000). **Model analysis of the influence of gas diffusivity in soil on CO and H₂ uptake.** *Tellus B: Chemical and Physical Meteorology* 52:3, 919–933 (see pages 17, 83).
- Zhang, M., G-R Yu, L-M Zhang, X-M Sun, X-F Wen, S-J Han, and J-H Yan (2010). **Impact of cloudiness on net ecosystem exchange of carbon dioxide in different types of forest ecosystems in China.** *Biogeosciences* 7:2, 711–722 (see page 56).
- Zhang, Z., B. Poulter, A.F. Feldman, Q. Ying, P. Ciais, S. Peng, and X. Li (2023). **Recent intensification of wetland methane feedback.** *Nature Climate Change* 13:5, 430–433 (see page 9).
- Zhao, Y., M. Saunio, P. Bousquet, X. Lin, A. Berchet, M. I. Hegglin, J. G. Canadell, R. B. Jackson, D. A. Hauglustaine, S. Szopa, et al. (2019). **Inter-model comparison of global hydroxyl radical (OH) distributions and their impact on atmospheric methane over the 2000–2016 period.** *Atmospheric Chemistry and Physics* 19:21, 13701–13723 (see page 8).
- Zhou, Y., X. Wu, W. Ju, L. Zhang, Z. Chen, W. He, Y. Liu, and Y. Shen (2020). **Modeling the effects of global and diffuse radiation on terrestrial gross primary productivity in China based on a two-leaf light use efficiency model.** *Remote Sensing* 12:20, 3355 (see pages 7, 50).
- Zhuang, Q., M. Chen, K. Xu, J. Tang, E. Saikawa, Y. Lu, J.M. Melillo, R.G. Prinn, and A.D. McGuire (2013). **Response of global soil consumption of atmospheric methane to changes in atmospheric climate and nitrogen deposition.** *Global Biogeochemical Cycles* 27:3, 650–663 (see page 82).

Zimmermann, Peter H, Carl AM Brenninkmeijer, Andrea Pozzer, Patrick Jöckel, Franziska Winterstein, Andreas Zahn, Sander Houweling, and Jos Lelieveld (2020). **Model simulations of atmospheric methane (1997–2016) and their evaluation using NOAA and AGAGE surface and IAGOS-CARIBIC aircraft observations.** *Atmospheric Chemistry and Physics* 20:9, 5787–5809 (see page 78).

List of Publications

Articles in Refereed Journals

- Martin, A., V. Gayler, B. Steil, K. Klingmüller, P. Jöckel, H. Tost, J. Lelieveld, and A. Pozzer (2024). **Evaluation of the coupling of EMACv2.55 to the land surface and vegetation model JSBACHv4**. *Geoscientific Model Development* 17:14, 5705–5732.
- Reifenberg, S. F., A. Martin, M. Kohl, S. Bacer, Z. Hamryszczak, I. Tadic, L. Röder, D. J. Crowley, H. Fischer, K. Kaiser, et al. (2022). **Numerical simulation of the impact of COVID-19 lockdown on tropospheric composition and aerosol radiative forcing in Europe**. *Atmospheric Chemistry and Physics* 22:16, 10901–10917.
- Voigt, C., J. Lelieveld, H. Schlager, J. Schneider, J. Curtius, R. Meerkötter, D. Sauer, L. Bugliaro, B. Bohn, J. N. Crowley, et al. (2022). **Cleaner skies during the COVID-19 lockdown**. *Bulletin of the American Meteorological Society* 103:8, E1796–E1827.

Further contributions and proceedings

- Cirino, G., A. Martin, R. Vella, S. Rodrigues, R. Palacios, D. Galbraith, and A. Pozzer (2025). **Optimal physiological thresholds of pan-tropical forests using surface measurements and ECHAM/MESy atmospheric chemistry numerical modeling**. In: *EGU General Assembly Conference Abstracts*.
- Klingmüller, K., J. Arns, A. Martin, A. Pozzer, and J. Lelieveld (2024). **Combined machine learning model of aeolian dust and surface soil moisture**. In: *EGU General Assembly Conference Abstracts*, 9208.
- Kohl, M., C. Brühl, H. Tost, C. Xenofontos, T. Christoudias, S. Gromov, O. Appel, O. Eppers, P. Jöckel, P. Joppe, K. Kaiser, K. Klingmüller, F. Köllner, A. Martin, S. Ruhl, J. Schneider, C. Schulz, R. Vella, J. Lelieveld, and A. Pozzer (2025). **Global atmospheric aerosol distributions and composition from the surface to the stratosphere**. In: Manuscript to be submitted to *Atmospheric Chemistry and Physics*.

Surawski, N., B. Steil, C. Brühl, S. Gromov, K. Klingmüller, A. Martin, A. Pozzer, and J. Lelieveld (2025). **Global atmospheric hydrogen chemistry and long-term source-sink budget simulation with the EMAC v2.55 model**. In: vol. 2025, 1–29.

Appendix A

Evaluation of the coupling of EMACv2.55 and the land surface and vegetation model JSBACHv4

as published in Martin et al. 2024*

Content

Table A1: JSBACH input file overview

A1: Example namelist for EMAC/JSBACH: *jsbach.nml*

Figure A1: Schematic of JSBACH in EMAC

Parameter optimization:

Table A2: List of optimized parameters

Table A3: Results of parameter optimization

Table A4: Results of parameter optimization

Table A6: Lists of newly available output parameters

Table A1: JSBACH input file overview. *grid* corresponds to the simulation gridsize and *year* to the reference year.

Initial conditions	filename
Initial data for the Carbon Pools	cpools_vga0218_18991231_tiles.nc
Initial data for soil and land properties	ic_land_soil_grid_1976_tsrf_clim.nc
	jsbach_grid_11tiles_5layers_year_no-dynveg_layer_moist.nc
	jsbach_grid_11tiles_5layers_year_no-dynveg_albedo.nc
	jsbach_grid_11tiles_5layers_year_no-dynveg_cover_fract.nc
	jsbach_grid_11tiles_5layers_year_no-dynveg_cover_type.nc
	jsbach_grid_11tiles_5layers_year_no-dynveg_nn.nc
	jsbach_grid_11tiles_5layers_year_no-dynveg_soil_layer_depth.nc
	jsbach_grid_11tiles_5layers_year_no-dynveg_veg_fract.nc
	bc_land_soil_grid_year_fract_org.nc
	bc_land_soil_grid_year_nn.nc

* <https://gmd.copernicus.org/articles/17/5705/2024/gmd-17-5705-2024-supplement.pdf>

A1 Example namelist for EMAC/JSBACH: *jsbach.nml*

The following snippets of the *jsbach* namelist show the default simulation setup for the JSBACH submodel.

```
1 ! *- f90 *-
2 &CTRL
3 l_verbose= F      ! verbose output of model (debugging)
4 /
5 &CPL
6 !#####
7 !## JSBACH switches for PROCESS in CALL ORDER FOR DEBUGGING
8 !## DEFAULT = .true.
9 !#####
10      L_CARBON                      = T,
11      L_FUEL                        = T,
12      L_RADIATION                   = T,
13      L_PHENOLOGY                   = T,
14      L_HYDROLOGY                   = T,
15      L_SEB                         = T,
16      L_SSE                         = T,
17      L_ASSIMILATION                = T,
18      L_TURBULENCE                 = T,
19      L_DISTURB                     = T,
20      !#FUEL
21      L_update_fuel                 = .true.,
22      !#DISTURBANCE
23      L_update_natural_disturbances = .true.,
24      !#RADIATION
25      L_update_surface_radiation    = .true.,
26      !#PHENOLOGY
27      L_update_phenology_logrop     = .true.,
28      L_update_fpc                  = .true.,
29      !#HYDROLOGY
30      L_update_snow_and_skin_fraction = .true.,
31      L_update_soil_properties      = .true.,
32      !#SURFACE ENERGY BALANCE
33      L_update_surface_energy_land  = .true.,
34      L_update_surface_energy_lake  = .true.,
35      !#HYDROLOGY
36      L_update_evaporation          = .true.,
```

```

37      !#SURFACE ENERGY BALANCE
38          L_update_surface_fluxes_land           = .true. ,
39          L_update_surface_fluxes_lake          = .true. ,
40      !#RADIATION
41          L_update_radiation_par                 = .true. ,
42      !#HYDROLOGY
43          L_update_surface_hydrology            = .true. ,
44          L_update_snow_and_skin_fraction       = .true. ,
45      !#SOIL and SNOW ENERGY
46          L_update_soil_and_snow_properties     = .true. ,
47          L_update_soil_and_snow_temperature    = .true. ,
48      !#HYDROLOG
49          L_update_soil_hydrology              = .true. ,
50      !#SURFACE ENERGY BALANCE
51          L_update_snowmelt_correction          = .true. ,
52      !#ASSIMILATION
53          L_update_assimilation_scaling_factors = .true. ,
54          L_update_canopy_cond_unstressed_assimilation = .true. ,
55          L_update_canopy_cond_stressed_assimilation = .true. ,
56          L_update_assimilation                = .true. ,
57      !#HYDROLOGY
58          L_update_canopy_cond_unstressed       = .true. ,
59          L_update_water_stress                 = .true. ,
60          L_update_canopy_cond_stressed        = .true. ,
61      !#CARBON
62      ! warning CO2 gas tracer must be present!
63          L_update_C_NPP_pot_allocation         = .true. ,
64      !#TURBULENCE
65          L_update_humidity_scaling            = .true. ,
66          L_update_roughness                   = .true. ,
67      !#RADIATION
68          L_update_albedo                       = .true. ,
69      !#HYDROLOGY
70          L_update_water_balance               = .true. ,
71      #####
72      ### JSBACH logical switches
73      #####
74          l_freeze                             = T,
75          l_supercool                           = T,
76          l_dynsnow                             = T,
77          l_heat_cap_dyn                        = T,

```

```

78     l_heat_cond_dyn           = T,
79     l_ice_on_lakes           = T,
80     l_snow                   = T,
81     l_organic                = T,
82     ltpe_closed              = F,
83     ltpe_open                = F,
84     l_forestRegrowth         = T,
85     l_use_alb_canopy         = T,
86     l_use_alb_veg_simple     = T,
87     l_use_alb_soil_scheme    = F,
88     l_use_alb_soil_litter    = T,
89     l_use_alb_mineralsoil_const = T,
90     l_use_alb_soil_organic_C = T,   !T:
        \ 'linear', F: 'log'
91     l_burn_pasture           = T,
92     l_use_quincy             = F,   !QUINCY
        \not implemented
93 !#####
94 !## EMAC INPUT DATA
95 !#####
96 ! The following channel objects are just input.
97 ! JSBACH will not modify them.
98 input_fract_lake           = 'ECHAM5', 'alake',   ! [1]
99 input_land_mask           = 'ECHAM5', 'slm',     ! [1]
100 input_slf                 = 'ECHAM5', 'slf',     ! [1]
101 input_fract_glacier       = 'g3b', 'glac',      ! [1]
102 input_press_srf           = 'g3b', 'aps',       ! [Pa]
103 input_t_air               = 'e5vdiff', 'temp2', ! [K]
104 input_t_acoef             = 'e5vdiff', 'zetnl', !
        \[1]Richtmyer-morton-coefficients, t=dry static energy,
        \q=moisture
105 input_t_bcoef             = 'e5vdiff', 'zftnl', ! [J/kg]
106 input_t_acoef_wtr         = 'e5vdiff', 'zetnw', ! [1]
107 input_t_bcoef_wtr         = 'e5vdiff', 'zftnw', ! [J/kg]
108 input_t_acoef_ice         = 'e5vdiff', 'zetni', ! [1]
109 input_t_bcoef_ice         = 'e5vdiff', 'zftni', ! [J/kg]
110 input_q_acoef             = 'e5vdiff', 'zeqnl', ! [1]
111 input_q_bcoef             = 'e5vdiff', 'zfqnl', ! [kg/kg]
112 input_q_acoef_wtr         = 'e5vdiff', 'zeqnw', ! [1]
113 input_q_bcoef_wtr         = 'e5vdiff', 'zfqnw', ! [kg/kg]
114 input_q_acoef_ice         = 'e5vdiff', 'zeqni', ! [1]

```

```

115 input_q_bcoef_ice           = 'e5vdiff', 'zfqni',      ! [kg/kg]
116 input_drag_srf             = 'e5vdiff', 'cfhl',      !
      \(\neutral)/ drag coefficients, was cdnl, cdnw, cdni
117 input_drag_wtr             = 'e5vdiff', 'cfhw',      ! [-]
118 input_drag_ice             = 'e5vdiff', 'cfhi',      ! [-]
119 input_pch                   = 'e5vdiff', 'chl',        ! surface
      \drag [1]
120 input_wind_10m             = 'e5vdiff', 'wind10',     ! [m s-1]
121 input_cos_zenith_angle     = 'orbit', 'cossza',     ! [-]
122 input_declination          = 'orbit', 'dec_off',      ! [degrees,
      \angle sun at equator]
123 input_rad_sw_lwtr         = 'rad01', 'soflw',      ! [W m-2]
124 input_rad_sw_lice         = 'rad01', 'sofli',      ! [W m-2]
125 input_rad_lw_lwtr         = 'rad01', 'trflw',      ! [W m-2]
126 input_rad_lw_lice         = 'rad01', 'trflw',      ! [W m-2]
127 input_q_rel_air_climbuf   = 'e5vdiff', 'rh_2m',      ! [-]
128 input_oro_stddev          = 'g3b', 'orostd',      ! [m]
129
130 ! The following channel objects are just input.
131 ! Only srf level is used.
132 input_wind_u               = 'ECHAM5', 'um1',        ! [m/s]
133 input_wind_v               = 'ECHAM5', 'vm1',        ! [m/s]
134 input_cv_rain              = 'ECHAM5', 'rsfc_2d',     ! [kg m-2]
      \s-1]
135 input_ls_rain              = 'ECHAM5', 'rsfl_2d',     ! [kg m-2]
      \s-1]
136 input_cv_snow              = 'ECHAM5', 'ssfc_2d',     ! [kg m-2]
      \s-1]
137 input_ls_snow              = 'ECHAM5', 'ssfl_2d',     ! [kg m-2]
      \s-1]
138 input_lwflx               = 'rad01', 'flxt',        ! [W m-2]
139 input_swflx               = 'rad01', 'flxs',        ! shortwave
      \flux [W m-2]
140 input_swnirflx            = 'rad01', 'flxnir',      ! NIR flux
      \all sky [W m-2]
141 input_swvisflx            = 'rad01', 'flxsw1',      ! SW1 flux
      \all sky (VIS) [W m-2]
142 input_lwflx_up            = 'rad01', 'flxut',        ! longwave
      \flux [W m-2]
143 input_swflx_up            = 'rad01', 'flxus',        ! shortwave
      \flux [W m-2]

```

```

144
145
146 ! The following channel objects exist already in MESSy.
147 ! SURFACE did not update those variables, but JSBACH will update
    \them (only over land and lakes)
148 ! either via calculation or according to the jsbach input files.
149 input_vol_heat_cap      = 'g3b',      'rgcgn',      !
    \Volumetric heat capacity of the soil [j/m**3/K]
150 input_az0              = 'g3b',      'az0',        ! roughness
    \length orography [m]
151 input_fract_forest     = 'ECHAM5',   'forest',     ! forest
    \fraction [1]
152 input_fract_fpc       = 'ECHAM5',   'vgrat',     !
    \vegetation fraction rel to land [1]
153 input_fract_fpc_mon   = 'ECHAM5',   'vgrat',     !
    \vegetation fraction rel to land, monthly [1]
154 input_latent_hflx     = 'e5vdiff',  'ahfl',      ! latent
    \heat flux [W m-2]
155 input_latent_hflx_lnd = 'e5vdiff',  'ahfl1',    ! latent
    \heat flux over land [W m-2]
156 input_latent_hflx_wtr = 'e5vdiff',  'ahflw',    ! latent
    \heat flux over water [W m-2]
157 input_latent_hflx_ice = 'e5vdiff',  'ahfli',    ! latent
    \heat flux over ice [W m-2]
158 input_sensible_hflx  = 'e5vdiff',  'ahfs',     ! sensible
    \heat flux [W m-2]
159 input_sensible_hflx_lnd = 'e5vdiff',  'ahfsl',   ! sensible
    \heat flux over land [W m-2]
160 input_sensible_hflx_wtr = 'e5vdiff',  'ahfsw',   ! sensible
    \heat flux over water [W m-2]
161 input_sensible_hflx_ice = 'e5vdiff',  'ahfsi',   ! sensible
    \heat flux over ice [W m-2]
162 input_evapo_wtr      = 'e5vdiff',  'evapw',    !
    \evaporation over water [kg m-2 s-1]
163 input_evapo_ice      = 'e5vdiff',  'evapi',    !
    \evaporation over ice [kg m-2 s-1]
164 input_evapopot       = 'e5vdiff',  'evapot_2d', ! potential
    \evaporation/sublimation [kg m-2 s-1]
165 input_evapl          = 'e5vdiff',  'evapl_2d', !
    \evaporation land

```

```

166 input_evap          = 'e5vdiff', 'evap', !
      \evaporation
167
168 ! The following channel objects exist already in MESSy and will be
      \updated by JSBACH
169 ! SURFACE did update them before.
170 input_depth_lice    = 'g3b', 'siced', ! seaice
      \depth [m]
171 input_seaice        = 'g3b', 'seaice', ! seaice
      \fraction rel to ocean [1]
172 input_seacov        = 'ECHAM5', 'seacov', ! sea cover
      \ (fraction of grid box) [1]
173 input_landcov       = 'ECHAM5', 'landcov', ! land
      \cover (fraction of grid box) [1]
174 input_fract_lice    = 'ECHAM5', 'icecov', ! ice cover
      \ (fract of gb) only over water [1]
175 input_water_content = 'g3b', 'ws', ! Soil
      \water content [m]
176 input_w_skin        = 'g3b', 'wl', ! Water
      \content skin reservoir (soil&canopy)[m]
177 input_t_unfilt      = 'g3b', 'tslm', ! T(t)
      \Surface temperature, unfiltered [K]
178 input_t_old         = 'g3b', 'tslm1', ! T(t-dt)
      \Surface temperature t-dt [K]
179 input_t_soil        = 'g3b', 'tsoil', !
      \Temperature [K] in the five soil layers [K]
180 input_tsi           = 'g3b', 'tsi', ! Lake
      \surface temperature (ice) [K]
181 input_t_lwtr        = 'g3b', 'tsw', ! surface
      \temperature of water [K]
182 input_t             = 'ECHAM5', 'tsurf', ! surface
      \temperature [K]
183 input_snowmelt      = 'g3b', 'snmel', ! Snow melt
      \[kg/m**2]
184 input_w_snow_can    = 'g3b', 'snc', ! Snow
      \depth canopy [m water equivalent]
185 input_w_snow_soil   = 'g3b', 'sn', ! Snow
      \depth ground [m water equivalent]
186 input_w_snow_lice   = 'g3b', 'sni', ! Snow
      \depth ice [m water equivalent]

```

```

187 input_snow_accum      = 'g3b',      'snacl',      ! Snow
      \budget at non-glacier points [kg/m**2]
188 input_w_glac         = 'g3b',      'gld',        ! Glacier
      \depth (including snow) [m water equivalent]
189 input_runoff_glac    = 'g3b',      'rogl',        ! Glacier
      \runoff (rain+snow/ice melt) [kg/m**2]
190 input_adrain         = 'ECHAM5',    'adrain',     ! Drainage
      \at non-glacier points [m]
191 input_aros           = 'ECHAM5',    'aros',        !
      \atmospheric runoff [m]
192 input_hcap_grnd      = 'g3b',      'grndcapc',   ! Heat
      \capacity of the uppermost soil layer [J/m**2/K]
193 input_grnd_hflx      = 'g3b',      'grndhflx',   ! Ground
      \heat flux [J m-2 s-1]
194 input_evapo_skin     = 'ECHAM5',    'evwsd',      !
      \Evaporation from skin reservoir [1]
195 input_hflx_cond_ice  = 'g3b',      'ahfice',     !
      \conductive heat flux [W m-2]
196 input_fract_snow_lice = 'ECHAM5',    'cvsi',        ! snow
      \cover over ice (fraction of grid box) [1]
197 input_fract_snow_can = 'ECHAM5',    'cvsc',        !
      \Fractional snow cover canopy [1]
198 input_fract_snow     = 'ECHAM5',    'cvs',         !
      \Fractional snow cover [1]
199 input_lai            = 'ECHAM5',    'vlt',         ! leaf area
      \index [1]
200 input_wsmx           = 'g3b',      'wsmx',        ! field
      \capacity (water holding capacity) of soil [m]
201 input_grndflux       = 'g3b',      'grndflux',    !
      \grndflux+grndhflx*slm*dtime [W/m**2]
202 input_cvw            = 'ECHAM5',    'cvw',         ! Skin
      \reservoir fraction (= pwl/pwlmx, see *vdiff*)
203 input_runoff_hd      = 'g3b',      'runoff',      ! Total
      \runoff non-glacier points (acc.) [kg/m**2s]
204 input_drainage_hd    = 'ECHAM5',    'adrain',     ! Drainage
      \at non-glacier points [m/s]
205 input_albedo         = 'rad',      'albedo',     ! surface
      \albedo [1]
206
207 !#####
208 !##JSBACH input data /pool/data/JSBACH/...

```

```

209 !#####
210 ! The following channel objects exist already in MESSy.
211 ! JSBACH will use input data and overwrite the channel objects for
    \the first timestep.
212 input_lai_init          =   'import_grid','in_lai_cl_lai_clim',
    \!initial LAI from climatology [1]
213 ! The following channel objects don't exist in MESSy.
214 ! JSBACH will use input data and create new channel objects.
215 input_fract_fpc_max    =
    \ 'import_grid','in_jsb_veg_ratio_max',    ! [1]
216 input_rough_m          =
    \ 'import_grid','in_alb_roughness_length',! [m]
217 input_vol_field_cap    =
    \ 'import_grid','in_jsb_soil_field_cap',    ! [m/m]
218 input_cover_type_ti    =
    \ 'import_grid','in_jsb_ct_cover_type',    ! [1]
219 input_cover_fract_ti   =
    \ 'import_grid','in_jsb_lc_cover_fract',    ! [1]
220 input_w_soil_sl        =
    \ 'import_grid','in_jsb_lm_layer_moist',    ! [m]
221 input_soil_depth       =   'import_grid','in_jsb_soil_depth',
    \      ! [m]
222 input_vol_porosity     =
    \ 'import_grid','in_jsb_soil_porosity',    ! [m/m]
223 input_pore_size_index  =
    \ 'import_grid','in_jsb_pore_size_index',    ! [-]
224 input_heat_cond        =
    \ 'import_grid','in_jsb_heat_conductivity',! [J m-1 s-1 K-1]
225 input_hyd_cond_sat     =
    \ 'import_grid','in_jsb_hyd_cond_sat',    ! [m/s]
226 input_vol_p_wilt       =
    \ 'import_grid','in_jsb_wilting_point',    ! [m/m]
227 input_bclapp           =   'import_grid','in_jsb_bclapp',
    \      ! [-]
228 input_w_soil_column    =   'import_grid','in_jsb_init_moist',
    \      ! [m]
229 input_max_moist        =   'import_grid','in_jsb_maxmoist',
    \      ! [m]
230 input_root_depth       =   'import_grid','in_jsb_root_depth',
    \      ! [m]

```

```

231 input_matrix_pot           =
    \ 'import_grid', 'in_jsb_moisture_pot',      ! [m]
232 input_albedo_veg_vis      =
    \ 'import_grid', 'in_alb_albedo_veg_vis',    ! [1]
233 input_albedo_veg_nir      =
    \ 'import_grid', 'in_alb_albedo_veg_nir',    ! [1]
234 input_albedo_soil_vis     =
    \ 'import_grid', 'in_alb_albedo_soil_vis',   ! [1]
235 input_albedo_soil_nir     =
    \ 'import_grid', 'in_alb_albedo_soil_nir',   ! [1]
236 input_tclim               =
    \ 'import_grid', 'in_jsb_ic_surf_temp',      ! [K]
237 input_tclim_sum           =
    \ 'import_grid', 'in_jsb_tc_tclim_sum',      ! [K]
238 input_tclim_max           =
    \ 'import_grid', 'in_jsb_tc_tclim_max',      ! [K]
239 input_tclim_min           =
    \ 'import_grid', 'in_jsb_tc_tclim_min',      ! [K]
240 input_tclim_idx           =   'import_grid', 'in_jsb_tc_tidc',
    \           ! [-]
241 input_fract_org_sl        =
    \ 'import_grid', 'in_fosl_fract_org_sl',      ! [1]
242 input_NPP_pot_yDayMean    =   'import_grid', 'j_NPP_run_mean',
    \           ! [mol(CO2)/m2 (canopy) s]
243 !#####
244 !## JSBACH Input Carbon from cpools
245 !#####
246 ! Initial conditions for carbon pools, all in [mol(C)/m^2(canopy)]
    \if not stated otherwise.
247 input_c_green             =   'import_grid', 'j_Cpool_green',
    \           ! Green carbon pool: on input last value;
    \updated on output [mol(C)/m^2(canopy) s]:
248 input_c_reserve           =   'import_grid', 'j_Cpool_reserve',
    \           ! C-pool for carbohydrate reserve (sugars,
    \starches) that allows plants to survive
249 input_c_woods             =   'import_grid', 'j_Cpool_woods',
    \           ! C-pool for stems, thick roots and other
    \ (dead) structural
250 input_c_crop_harvest      =
    \ 'import_grid', 'j_Cpool_crop_harvest',      ! C-pool for
    \ biomass harvested from crops [mol(C)/m^2(grid box)]

```

```

251 input_c_acid_ag1          = 'import_grid','j_YCpool_acid_ag1',
    \          ! Above ground litter-pool for acid soluble litter
252 input_c_water_ag1       = 'import_grid','j_YCpool_water_ag1',
    \          ! - for water soluble litter
253 input_c_ethanol_ag1     =
    \ 'import_grid','j_YCpool_ethanol_ag1',          ! - for ethanol
    \soluble litter
254 input_c_nonsoluble_ag1  =
    \ 'import_grid','j_YCpool_nonsoluble_ag1',      ! - non-soluble
    \soluble litter
255 input_c_acid_bg1        = 'import_grid','j_YCpool_acid_bg1',
    \          ! Below ground litter-pool for acid soluble litter
256 input_c_water_bg1       = 'import_grid','j_YCpool_water_bg1',
    \          ! - for water soluble litter
257 input_c_ethanol_bg1     =
    \ 'import_grid','j_YCpool_ethanol_bg1',          ! - for ethanol
    \soluble litter
258 input_c_nonsoluble_bg1  =
    \ 'import_grid','j_YCpool_nonsoluble_bg1',      ! - for
    \non-soluble litter
259 input_c_humus_1         = 'import_grid','j_YCpool_humus_1',
260 input_c_acid_ag2        = 'import_grid','j_YCpool_acid_ag2',
261 input_c_water_ag2       = 'import_grid','j_YCpool_water_ag2',
262 input_c_ethanol_ag2     =
    \ 'import_grid','j_YCpool_ethanol_ag2',
263 input_c_nonsoluble_ag2  =
    \ 'import_grid','j_YCpool_nonsoluble_ag2',
264 input_c_acid_bg2        = 'import_grid','j_YCpool_acid_bg2',
265 input_c_water_bg2       = 'import_grid','j_YCpool_water_bg2',
266 input_c_ethanol_bg2     =
    \ 'import_grid','j_YCpool_ethanol_bg2',
267 input_c_nonsoluble_bg2  =
    \ 'import_grid','j_YCpool_nonsoluble_bg2',
268 input_c_humus_2         = 'import_grid','j_YCpool_humus_2',
269 /

```

Schematic of JSBACH in EMAC

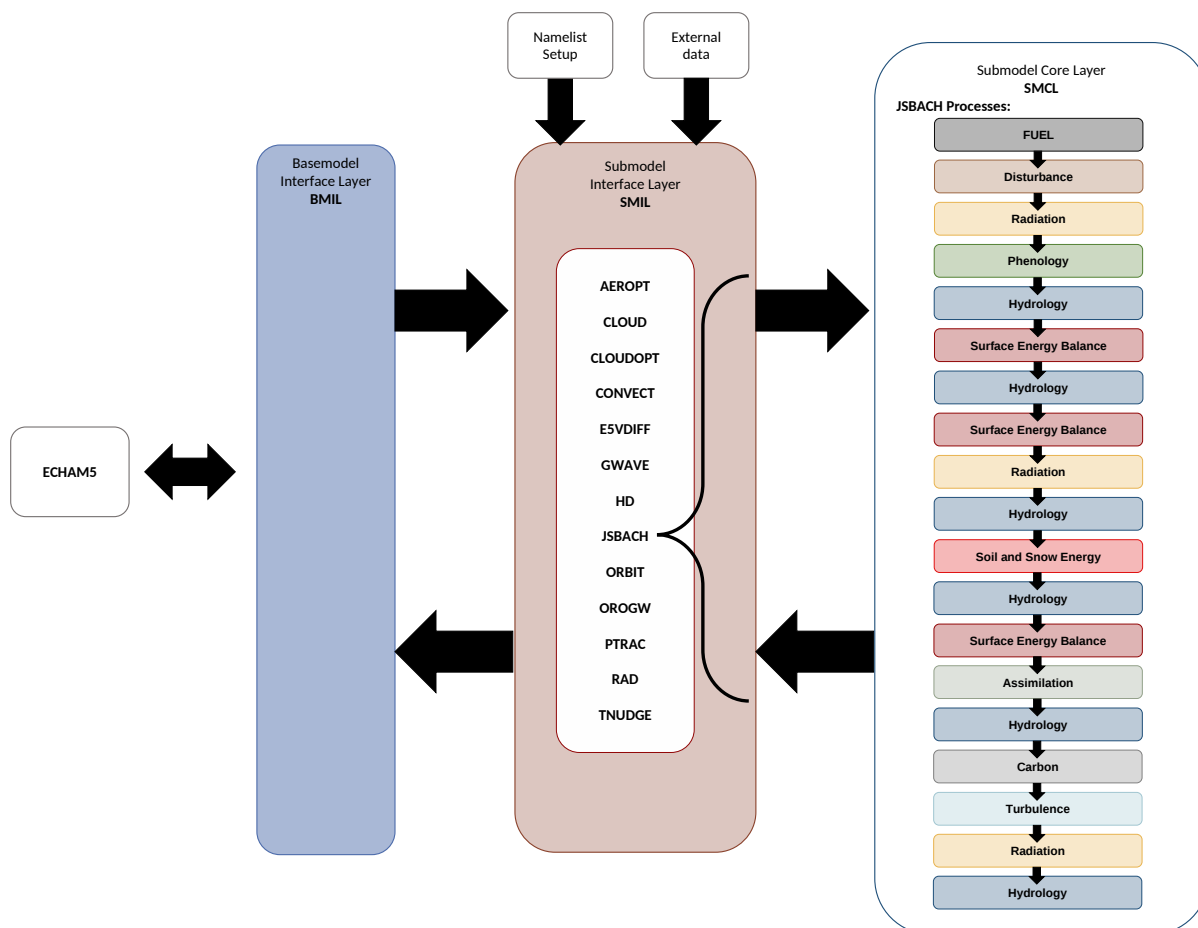


Figure A1: Schematic overview of JSBACH as new submodel in EMAC with corresponding processes.

Parameter optimisation

Table A2: List of optimised parameters of the control simulation (CTRL) and the 35 Simulations with varying parameters. Simulation 1 (EMAC/SRF) is performed with the SURFACE submodel, while simulation 2 to 35 are performed with the JSBACH submodel. The simulation with the parameters used for the EMAC/JSBACH setup is indicated in bold.

Run	zasic	zinhomi	zinhoml	cmfctop	cprcon [$e-04s^2 m^{-2}$]
1 (EMAC/SRF)	0.85 (default)	0.85 (default)	zinhoml _{default}	0.3 (default)	1 (default)
2 (CTRL)	default	default	default	default	default
3	0.8	default	default	default	default
4	default	default	default	default	default
5	0.89	default	default	default	default
6	0.91	default	default	default	default
7	default	0.8	default	default	default
8	default	default	default	default	default
9	default	0.9	default	default	default
10	default	0.95	default	default	default
11	default	1	default	default	default
12	default	default	0.7	default	default
13	default	default	0.77	default	default
14	default	default	0.8	default	default
15	default	default	0.9	default	default
16 (EMAC/JSBACH)	default	default	0.92	default	default
17	default	default	default	0.2	default
18	default	default	default	0.23	default
19	default	default	default	0.26	default
20	default	default	default	default	default
21	default	default	default	0.35	default
22	default	default	default	default	default
23	default	default	default	default	2
24	default	default	default	default	3
25	default	default	default	default	4
26	default	default	default	default	5
27	default	default	default	default	6
28	default	default	default	default	8
29	default	default	default	default	9
30	0.75	1	0.88	default	4
32	0.75	1	0.88	default	8
33	0.75	1	0.88	default	10
34	0.7	1	0.92	default	4
35	default	default	0.92	default	4

Table A3: Table of the temporally and globally averaged results \pm inter annual variability as standard deviation of the CTRL and 35 Simulations with varying tuning parameters (1990 to 2010). Simulation 1 (EMAC/SRF) is performed with the SURFACE submodel, while simulation 2 to 35 are performed with the JSBACH submodel. Additionally, the corresponding reanalysis or observational results are listed as "REF". For precipitation REF refers to the GPCP monthly precipitation dataset (Adler et al. (2003)), while for the remaining variables REF refers to ERA5/ERA5-Land reanalysis datasets (Hersbach (2023);Muñoz Sabater(2019,2021)). The simulation with the parameters used for the EMAC/JSBACH setup is indicated in bold.

Run	LST [K]	TOA _{net} [W m ⁻²]	TOA _{sw} [W m ⁻²]	TOA _{lw} [W m ⁻²]	SRF _{net} [W m ⁻²]	SRF _{sw} [W m ⁻²]	SRF _{lw} [W m ⁻²]	HFLX _{net} [W m ⁻²]	HFLX _{sensible} [W m ⁻²]	HFLX _{latent} [W m ⁻²]	Precip [mm day ⁻¹]	ACLC	LWC [kg m ⁻²]	IWC [kg m ⁻²]	TWS [m]
REF	282.25 ± 0.27	0.45 ± 0.65	242.67 ± 0.65	-242.22 ± 0.29	105.91 ± 0.45	163.76 ± 0.54	-57.85 ± 0.31	-69.92 ± 0.57	-28.15 ± 0.68	-41.76 ± 0.43	2.7 ± 0.03	0.553 ± 0.00405	0.04707 ± 0.00098	0.02166 ± 0.00033	1.06012 ± 0.00947
1 (EMAC/SRF)	283.09 ± 0.27	3.56 ± 0.39	234.33 ± 0.27	-230.77 ± 0.34	107.92 ± 0.24	161.74 ± 0.31	-53.83 ± 0.3	-104.24 ± 0.35	-16.74 ± 0.18	-87.5 ± 0.42	2.83 ± 0.02	1.06067 ± 0.00444	0.10394 ± 0.00115	0.04972 ± 0.00068	0.34995 ± 0.00425
2 (CTRL)	280.66 ± 0.26	6.61 ± 0.5	237.22 ± 0.3	-230.61 ± 0.42	108.08 ± 0.28	165.97 ± 0.36	-57.88 ± 0.35	-110.92 ± 0.65	-11.59 ± 0.15	-99.33 ± 0.6	2.77 ± 0.02	0.6462 ± 0.0025	0.09594 ± 0.00114	0.04945 ± 0.00067	1.00362 ± 0.00761
3	280.54 ± 0.28	5.06 ± 0.51	235.54 ± 0.29	-230.48 ± 0.38	106.76 ± 0.25	164.66 ± 0.39	-57.91 ± 0.43	-111.01 ± 0.59	-11.7 ± 0.16	-99.31 ± 0.55	2.77 ± 0.02	0.6466 ± 0.0025	0.0959 ± 0.00159	0.04976 ± 0.00066	1.00345 ± 0.00823
4	280.66 ± 0.26	6.61 ± 0.5	237.22 ± 0.3	-230.61 ± 0.42	108.08 ± 0.28	165.97 ± 0.36	-57.88 ± 0.35	-110.92 ± 0.65	-11.59 ± 0.15	-99.33 ± 0.6	2.77 ± 0.02	0.6462 ± 0.0025	0.09594 ± 0.00114	0.04945 ± 0.00067	1.00362 ± 0.00761
5	280.73 ± 0.27	8.06 ± 0.43	238.78 ± 0.31	-230.72 ± 0.37	109.31 ± 0.26	167.24 ± 0.38	-57.93 ± 0.36	-110.81 ± 0.64	-11.6 ± 0.12	-99.21 ± 0.62	2.76 ± 0.02	0.646 ± 0.0022	0.09552 ± 0.00114	0.04936 ± 0.00063	1.00336 ± 0.00878
6	280.85 ± 0.29	8.63 ± 0.53	239.5 ± 0.31	-230.87 ± 0.39	109.92 ± 0.25	167.76 ± 0.4	-57.83 ± 0.37	-110.84 ± 0.64	-11.6 ± 0.15	-99.24 ± 0.65	2.76 ± 0.02	0.6453 ± 0.0022	0.09582 ± 0.00127	0.04919 ± 0.00059	1.0033 ± 0.0086
7	280.6 ± 0.29	6.67 ± 0.42	237.87 ± 0.35	-231.2 ± 0.41	108.53 ± 0.32	166.66 ± 0.39	-58.14 ± 0.37	-111.28 ± 0.61	-11.72 ± 0.14	-99.56 ± 0.59	2.77 ± 0.02	0.6465 ± 0.0027	0.09529 ± 0.00098	0.04955 ± 0.00061	1.00326 ± 0.00943
8	280.66 ± 0.26	6.61 ± 0.5	237.22 ± 0.3	-230.61 ± 0.42	108.08 ± 0.28	165.97 ± 0.36	-57.88 ± 0.35	-110.92 ± 0.65	-11.59 ± 0.15	-99.33 ± 0.6	2.77 ± 0.02	0.6462 ± 0.0025	0.09594 ± 0.00114	0.04945 ± 0.00067	1.00362 ± 0.00761
9	280.73 ± 0.27	6.35 ± 0.42	236.5 ± 0.24	-230.15 ± 0.34	107.56 ± 0.26	165.2 ± 0.3	-57.64 ± 0.35	-110.55 ± 0.6	-11.58 ± 0.11	-98.97 ± 0.58	2.76 ± 0.02	0.6462 ± 0.0018	0.09652 ± 0.00112	0.04933 ± 0.00055	1.0034 ± 0.00672
10	280.73 ± 0.27	6.48 ± 0.46	236.0 ± 0.31	-229.52 ± 0.45	107.19 ± 0.29	164.69 ± 0.34	-57.5 ± 0.33	-110.04 ± 0.59	-11.55 ± 0.14	-98.48 ± 0.58	2.74 ± 0.02	0.6465 ± 0.0028	0.09637 ± 0.00111	0.04942 ± 0.00057	1.00328 ± 0.00819
11	280.75 ± 0.26	6.34 ± 0.49	235.32 ± 0.36	-228.98 ± 0.33	106.71 ± 0.31	163.97 ± 0.43	-57.26 ± 0.39	-109.6 ± 0.58	-11.49 ± 0.14	-98.1 ± 0.55	2.73 ± 0.02	0.6474 ± 0.0024	0.09708 ± 0.00096	0.049 ± 0.00052	1.00239 ± 0.00791
12	280.58 ± 0.28	5.66 ± 0.44	236.32 ± 0.32	-230.65 ± 0.39	106.91 ± 0.33	164.94 ± 0.37	-58.02 ± 0.35	-110.57 ± 0.62	-11.59 ± 0.17	-98.97 ± 0.61	2.76 ± 0.02	0.6456 ± 0.0026	0.09557 ± 0.00096	0.04952 ± 0.00049	1.00348 ± 0.00838
13	280.57 ± 0.28	4.84 ± 0.42	235.5 ± 0.34	-230.67 ± 0.35	106.06 ± 0.27	164.01 ± 0.43	-57.95 ± 0.4	-110.55 ± 0.54	-11.63 ± 0.17	-98.93 ± 0.53	2.76 ± 0.02	0.6455 ± 0.0031	0.09529 ± 0.00108	0.04946 ± 0.00061	1.00356 ± 0.00795
14	280.53 ± 0.28	4.4 ± 0.47	235.04 ± 0.3	-230.64 ± 0.39	105.67 ± 0.24	163.47 ± 0.38	-57.8 ± 0.36	-110.57 ± 0.59	-11.65 ± 0.13	-98.92 ± 0.57	2.76 ± 0.02	0.6462 ± 0.0027	0.09533 ± 0.00104	0.04946 ± 0.00058	1.00368 ± 0.0075
15	280.55 ± 0.26	3.48 ± 0.39	234.1 ± 0.37	-230.62 ± 0.41	104.62 ± 0.29	162.42 ± 0.44	-57.79 ± 0.39	-110.5 ± 0.67	-11.57 ± 0.13	-98.93 ± 0.63	2.76 ± 0.02	0.6457 ± 0.0035	0.09531 ± 0.00098	0.04942 ± 0.00049	1.00327 ± 0.00821
16 (EMAC/JSBACH)	280.48 ± 0.23	3.23 ± 0.38	233.86 ± 0.29	-230.63 ± 0.38	104.43 ± 0.3	162.14 ± 0.34	-57.71 ± 0.35	-110.47 ± 0.67	-11.67 ± 0.14	-98.79 ± 0.61	2.76 ± 0.02	0.6464 ± 0.0028	0.09519 ± 0.0009	0.04936 ± 0.00054	1.00385 ± 0.00815
17	280.6 ± 0.23	3.89 ± 0.46	234.27 ± 0.31	-230.38 ± 0.37	105.94 ± 0.28	162.71 ± 0.38	-56.77 ± 0.37	-111.4 ± 0.58	-11.82 ± 0.14	-99.58 ± 0.55	2.78 ± 0.02	0.6578 ± 0.0025	0.09687 ± 0.00121	0.04916 ± 0.00063	1.00379 ± 0.00819
18	280.63 ± 0.23	4.81 ± 0.4	235.27 ± 0.33	-230.46 ± 0.37	106.67 ± 0.27	163.83 ± 0.41	-57.16 ± 0.41	-111.22 ± 0.6	-11.78 ± 0.15	-99.44 ± 0.58	2.77 ± 0.02	0.654 ± 0.0027	0.09656 ± 0.00118	0.04918 ± 0.0006	1.00344 ± 0.00751
19	280.64 ± 0.21	5.59 ± 0.44	236.14 ± 0.29	-230.56 ± 0.42	107.32 ± 0.24	164.77 ± 0.41	-57.45 ± 0.44	-111.11 ± 0.67	-11.72 ± 0.16	-99.39 ± 0.63	2.77 ± 0.02	0.6506 ± 0.0026	0.09622 ± 0.00136	0.04941 ± 0.00068	1.00382 ± 0.0075
20	280.66 ± 0.26	6.61 ± 0.5	237.22 ± 0.3	-230.61 ± 0.42	108.08 ± 0.28	165.97 ± 0.36	-57.88 ± 0.35	-110.92 ± 0.65	-11.59 ± 0.15	-99.33 ± 0.6	2.77 ± 0.02	0.6462 ± 0.0025	0.09594 ± 0.00114	0.04945 ± 0.00067	1.00362 ± 0.00761
21	280.69 ± 0.28	7.64 ± 0.37	238.32 ± 0.24	-230.68 ± 0.34	108.9 ± 0.26	167.18 ± 0.27	-58.27 ± 0.32	-110.69 ± 0.61	-11.6 ± 0.17	-99.09 ± 0.61	2.76 ± 0.02	0.6424 ± 0.0025	0.09519 ± 0.00094	0.04968 ± 0.00063	1.00316 ± 0.00774
22	280.66 ± 0.26	6.61 ± 0.5	237.22 ± 0.3	-230.61 ± 0.42	108.08 ± 0.28	165.97 ± 0.36	-57.88 ± 0.35	-110.92 ± 0.65	-11.59 ± 0.15	-99.33 ± 0.6	2.77 ± 0.02	0.6462 ± 0.0025	0.09594 ± 0.00114	0.04945 ± 0.00067	1.00362 ± 0.00761
23	280.49 ± 0.26	6.85 ± 0.48	241.36 ± 0.35	-234.51 ± 0.32	111.04 ± 0.22	170.57 ± 0.48	-59.53 ± 0.48	-113.5 ± 0.66	-11.91 ± 0.13	-101.59 ± 0.63	2.84 ± 0.02	0.6267 ± 0.0029	0.08383 ± 0.00098	0.03996 ± 0.00057	1.00189 ± 0.00737
24	280.41 ± 0.22	6.29 ± 0.41	242.5 ± 0.28	-236.21 ± 0.33	111.74 ± 0.26	171.84 ± 0.35	-60.09 ± 0.36	-114.76 ± 0.56	-12.06 ± 0.12	-102.7 ± 0.57	2.87 ± 0.02	0.619 ± 0.0026	0.07962 ± 0.00066	0.0366 ± 0.00056	1.0015 ± 0.00797
25	280.4 ± 0.27	5.88 ± 0.43	243.13 ± 0.32	-237.25 ± 0.33	112.06 ± 0.23	172.56 ± 0.46	-60.51 ± 0.48	-115.45 ± 0.65	-12.16 ± 0.14	-103.29 ± 0.63	2.89 ± 0.02	0.6133 ± 0.0028	0.07735 ± 0.00073	0.0349 ± 0.00056	1.00089 ± 0.00818
26	280.35 ± 0.26	5.59 ± 0.39	243.44 ± 0.29	-237.85 ± 0.36	112.25 ± 0.25	172.9 ± 0.37	-60.65 ± 0.35	-115.92 ± 0.59	-12.18 ± 0.1	-103.74 ± 0.61	2.91 ± 0.02	0.6099 ± 0.0026	0.07629 ± 0.00061	0.03385 ± 0.00087	1.00167 ± 0.00813
27	280.34 ± 0.25	5.31 ± 0.38	243.62 ± 0.31	-238.31 ± 0.29	112.33 ± 0.24	173.11 ± 0.41	-60.78 ± 0.43	-116.21 ± 0.56	-12.26 ± 0.13	-103.95 ± 0.6	2.92 ± 0.02	0.6069 ± 0.0034	0.07533 ± 0.00071	0.03305 ± 0.00042	1.0011 ± 0.00768
28	280.28 ± 0.28	5.11 ± 0.37	243.93 ± 0.37	-238.82 ± 0.28	112.48 ± 0.26	173.47 ± 0.47	-60.99 ± 0.47	-116.58 ± 0.61	-12.36 ± 0.16	-104.22 ± 0.61	2.92 ± 0.02	0.6036 ± 0.0033	0.07422 ± 0.00081	0.03216 ± 0.00043	1.00115 ± 0.00858
29	280.32 ± 0.3	4.95 ± 0.43	244.0 ± 0.35	-239.05 ± 0.35	112.49 ± 0.27	173.54 ± 0.46	-61.05 ± 0.45	-116.73 ± 0.59	-12.32 ± 0.18	-104.41 ± 0.58	2.93 ± 0.02	0.6018 ± 0.0033	0.07398 ± 0.00073	0.03186 ± 0.00042	1.00108 ± 0.00824
30	280.17 ± 0.31	0.54 ± 0.41	236.07 ± 0.28	-235.53 ± 0.36	105.78 ± 0.26	165.57 ± 0.35	-59.79 ± 0.39	-114.13 ± 0.62	-11.99 ± 0.14	-102.14 ± 0.61	2.87 ± 0.02	0.6146 ± 0.0025	0.07776 ± 0.00067	0.03467 ± 0.0005	1.00037 ± 0.00886
32	280.08 ± 0.28	-0.08 ± 0.43	237.09 ± 0.34	-237.17 ± 0.27	106.35 ± 0.23	166.66 ± 0.46	-60.31 ± 0.47	-115.27 ± 0.55	-12.13 ± 0.13	-103.13 ± 0.6	2.9 ± 0.02	0.6062 ± 0.0024	0.07447 ± 0.0008	0.03201 ± 0.00055	1.00072 ± 0.00858
33	280.07 ± 0.28	-0.19 ± 0.45	237.34 ± 0.42	-237.52 ± 0.35	106.52 ± 0.29	166.92 ± 0.52	-60.4 ± 0.42	-115.57 ± 0.61	-12.16 ± 0.14	-103.41 ± 0.58	2.91 ± 0.02	0.6028 ± 0.0037	0.07393 ± 0.00063	0.03153 ± 0.00041	1.00103 ± 0.00849
34	280.06 ± 0.25	-0.89 ± 0.36	234.44 ± 0.36	-235.33 ± 0.35	104.42 ± 0.28	164.15 ± 0.44	-59.73 ± 0.41	-114.11 ± 0.54	-12.01 ± 0.16	-102.09 ± 0.52	2.87 ± 0.01	0.6168 ± 0.0031	0.07773 ± 0.00069	0.03483 ± 0.0005	1.00153 ± 0.00794
35	280.21 ± 0.25	2.53 ± 0.44	239.73 ± 0.39	-237.2 ± 0.33	108.41 ± 0.26	168.65 ± 0.51	-60.24 ± 0.44	-114.97 ± 0.58	-12.15 ± 0.13	-102.82 ± 0.58	2.88 ± 0.02	0.6129 ± 0.003	0.0771 ± 0.00081	0.03461 ± 0.00046	1.00171 ± 0.00781

Table A4: Root mean square error (RMSE) and normalised RMSE by the range of the reference data (NRMSE) of reference data minus simulation for the analysed time period (1990 to 2010).

Run	LST [K]	TOA _{net} [W m ⁻²]	TOA _{sw} [W m ⁻²]	TOA _{lw} [W m ⁻²]	SRF _{net} [W m ⁻²]	SRF _{sw} [W m ⁻²]	SRF _{lw} [W m ⁻²]	HFLX _{net} [W m ⁻²]	HFLX _{sensible} [W m ⁻²]	HFLX _{latent} [W m ⁻²]	Precip [mm day ⁻¹]	ACLC	LWC [kg m ⁻²]	IWC [kg m ⁻²]	TWS [m]
2 (CTRL) RMSE	4.88	9.044	7.131	11.839	5.6	5.441	0.909	42.858	5.205	15.966	0.092	0.02	0.042	0.027	0.06
2 (CTRL) NRMSE	0.349	0.411	0.411	1.535	0.308	0.312	0.209	1.129	1.136	1.227	0.28	0.554	2.936	10.765	0.66
3 RMSE	4.919	8.068	8.49	11.971	5.228	5.055	0.942	42.944	5.101	15.948	0.097	0.02	0.042	0.028	0.06
3 NRMSE	0.351	0.366	0.49	1.552	0.288	0.29	0.217	1.132	1.114	1.226	0.295	0.564	2.934	10.888	0.663
4 RMSE	4.88	9.044	7.131	11.839	5.6	5.441	0.909	42.858	5.205	15.966	0.092	0.02	0.042	0.027	0.06
4 NRMSE	0.349	0.411	0.411	1.535	0.308	0.312	0.209	1.129	1.136	1.227	0.28	0.554	2.936	10.765	0.66
5 RMSE	4.856	10.086	6.024	11.731	6.18	6.069	0.915	42.753	5.189	15.844	0.086	0.019	0.042	0.027	0.06
5 NRMSE	0.347	0.458	0.348	1.521	0.34	0.348	0.21	1.127	1.133	1.218	0.261	0.548	2.907	10.727	0.664
6 RMSE	4.822	10.524	5.586	11.58	6.537	6.382	0.917	42.781	5.198	15.882	0.088	0.019	0.042	0.027	0.06
6 NRMSE	0.345	0.478	0.322	1.501	0.36	0.366	0.211	1.127	1.135	1.221	0.268	0.53	2.928	10.661	0.665
7 RMSE	4.9	9.08	6.651	11.261	5.789	5.76	0.961	43.206	5.073	16.191	0.099	0.02	0.027	0.042	0.06
7 NRSME	0.35	0.412	0.384	1.46	0.319	0.33	0.221	1.139	1.108	1.245	0.3	0.562	2.891	10.802	0.667
8 RMSE	4.88	9.044	7.131	11.839	5.6	5.441	0.909	42.858	5.205	15.966	0.092	0.02	0.042	0.027	0.06
8 NRMSE	0.349	0.411	0.411	1.535	0.308	0.312	0.209	1.129	1.136	1.227	0.28	0.554	2.936	10.765	0.66
9 RMSE	4.858	8.864	7.698	12.292	5.417	5.172	0.935	42.505	5.215	15.614	0.087	0.02	0.043	0.027	0.06
9 NRMSE	0.347	0.403	0.444	1.593	0.298	0.296	0.215	1.12	1.139	1.2	0.264	0.554	2.976	10.716	0.661
10 RMSE	4.858	8.95	8.106	12.909	5.318	5.058	0.968	42.013	5.241	15.133	0.076	0.02	0.043	0.027	0.06
10 NRMSE	0.347	0.406	0.468	1.674	0.293	0.29	0.222	1.107	1.144	1.163	0.232	0.562	2.965	10.751	0.664
11 RMSE	4.851	8.861	8.676	13.442	5.223	4.981	1.098	41.593	5.297	14.757	0.07	0.021	0.043	0.027	0.061
11 NRMSE	0.347	0.402	0.501	1.743	0.288	0.285	0.252	1.096	1.157	1.134	0.213	0.585	3.014	10.584	0.673
12 RMSE	4.904	8.424	7.847	11.798	5.259	5.11	0.925	42.521	5.201	15.616	0.087	0.019	0.042	0.027	0.06
12 NRMSE	0.35	0.383	0.453	1.529	0.29	0.293	0.213	1.121	1.135	1.2	0.265	0.538	2.91	10.789	0.663
13 RMSE	4.909	7.938	8.519	11.782	5.161	4.983	0.932	42.506	5.167	15.565	0.085	0.019	0.042	0.027	0.06
13 NRMSE	0.351	0.36	0.491	1.527	0.284	0.285	0.214	1.12	1.128	1.196	0.26	0.535	2.891	10.766	0.661
14 RMSE	4.925	7.706	8.913	11.809	5.162	4.98	0.914	42.523	5.147	15.564	0.086	0.02	0.042	0.027	0.06
14 NRMSE	0.352	0.35	0.514	1.531	0.284	0.285	0.21	1.121	1.124	1.196	0.263	0.554	2.894	10.767	0.659
15 RMSE	4.916	7.277	9.732	11.834	5.317	5.154	0.926	42.457	5.219	15.569	0.085	0.019	0.042	0.027	0.06
15 NRMSE	0.351	0.33	0.561	1.534	0.293	0.295	0.213	1.119	1.139	1.197	0.257	0.541	2.892	10.75	0.665
16 (EMAC/JSBACH) RMSE	4.939	7.175	9.943	11.822	5.367	5.225	0.919	42.426	5.123	15.439	0.084	0.02	0.042	0.027	0.06
16 (EMAC/JSBACH) NRMSE	0.353	0.326	0.574	1.533	0.296	0.299	0.211	1.118	1.118	1.187	0.255	0.559	2.884	10.728	0.658
17 RMSE	4.897	7.46	9.58	12.068	5.159	5.08	1.414	43.32	4.976	16.21	0.102	0.031	0.043	0.027	0.06
17 NRMSE	0.35	0.339	0.553	1.564	0.284	0.291	0.325	1.142	1.086	1.246	0.311	0.867	3.001	10.651	0.659
18 RMSE	4.886	7.923	8.713	11.983	5.215	4.976	1.159	43.144	5.019	16.072	0.098	0.027	0.043	0.027	0.06
18 NRMSE	0.349	0.36	0.503	1.553	0.287	0.285	0.267	1.137	1.096	1.235	0.296	0.763	2.979	10.657	0.662
19 RMSE	4.881	8.376	7.986	11.892	5.349	5.078	1.03	43.044	5.074	16.026	0.097	0.024	0.043	0.027	0.06
19 NRMSE	0.349	0.38	0.461	1.542	0.295	0.291	0.237	1.134	1.108	1.232	0.296	0.671	2.956	10.749	0.658
20 RMSE	4.88	9.044	7.131	11.839	5.6	5.441	0.909	42.858	5.205	15.966	0.092	0.02	0.042	0.027	0.06
20 NRSME	0.349	0.411	0.411	1.535	0.308	0.312	0.209	1.129	1.136	1.227	0.28	0.554	2.936	10.765	0.66
21 RMSE	4.869	9.771	6.328	11.77	5.967	6.029	0.991	42.64	5.193	15.73	0.086	0.016	0.042	0.027	0.06
21 NRSME	0.348	0.444	0.365	1.526	0.329	0.345	0.228	1.124	1.134	1.209	0.261	0.455	2.883	10.853	0.665
22 RMSE	4.88	9.044	7.131	11.839	5.6	5.441	0.909	42.858	5.205	15.966	0.092	0.02	0.042	0.027	0.06
22 NRSME	0.349	0.411	0.411	1.535	0.308	0.312	0.209	1.129	1.136	1.227	0.28	0.554	2.936	10.765	0.66
23 RMSE	4.935	9.206	4.79	8.052	7.276	8.439	1.936	45.337	4.89	18.198	0.151	0.007	0.03	0.018	0.061
23 NRSME	0.353	0.418	0.276	1.044	0.401	0.483	0.445	1.195	1.068	1.399	0.458	0.198	2.099	7.021	0.678
24 RMSE	4.965	8.823	4.604	6.443	7.79	9.486	2.422	46.54	4.746	19.287	0.184	0.011	0.026	0.014	0.062
24 NRSME	0.355	0.401	0.266	0.835	0.429	0.543	0.557	1.226	1.036	1.483	0.559	0.316	1.809	5.697	0.683
25 RMSE	4.969	8.561	4.626	5.488	8.026	10.118	2.827	47.213	4.649	19.878	0.203	0.016	0.024	0.013	0.062
25 NRSME	0.355	0.389	0.267	0.711	0.442	0.579	0.65	1.244	1.015	1.528	0.615	0.453	1.653	5.024	0.689
26 RMSE	4.987	8.377	4.666	4.949	8.176	10.407	2.944	47.659	4.635	20.322	0.217	0.019	0.023	0.012	0.062
26 NRSME	0.356	0.38	0.269	0.642	0.45	0.596	0.677	1.256	1.012	1.562	0.66	0.541	1.58	4.618	0.681
27 RMSE	4.992	8.209	4.7	4.545	8.235	10.59	3.077	47.941	4.557	20.531	0.226	0.022	0.022	0.011	0.062
27 NRSME	0.357	0.373	0.271	0.589	0.453	0.607	0.707	1.263	0.995	1.578	0.686	0.621	1.514	4.293	0.686
28 RMSE	5.016	8.089	4.777	4.111	8.355	10.912	3.28	48.299	4.46	20.798	0.236	0.025	0.021	0.01	0.062
28 NRSME	0.358	0.367	0.276	0.533	0.46	0.625	0.754	1.273	0.974	1.599	0.716	0.709	1.438	3.944	0.687
29 RMSE	5.001	8.001	4.794	3.931	8.362	10.975	3.338	48.444	4.494	20.98	0.24	0.027	0.021	0.01	0.062
29 NRSME	0.357	0.363	0.277	0.51	0.46	0.629	0.767	1.277	0.981	1.613	0.73	0.758	1.421	3.825	0.687
30 RMSE	5.061	6.618	8.048	7.085	5.16	5.29	2.148	45.935	4.814	18.735	0.18	0.015	0.024	0.012	0.063
30 NRSME	0.362	0.301	0.464	0.918	0.284	0.303	0.494	1.21	1.051	1.44	0.547	0.42	1.681	4.933	0.696
32 RMSE	5.096	6.641	7.234	5.55	5.176	5.763	2.639	47.032	4.675	19.72	0.213	0.023	0.021	0.01	0.063
32 NRSME	0.364	0.302	0.417	0.72	0.285	0.33	0.607	1.239	1.021	1.516	0.646	0.639	1.455	3.888	0.692
33 RMSE	5.103	6.652	7.05	5.239	5.196	5.901	2.715	47.327	4.649	19.994	0.221	0.026	0.02	0.009	0.062
33 NRSME	0.365	0.302	0.407	0.679	0.286	0.338	0.624	1.247	1.015	1.537	0.67	0.731	1.417	3.696	0.688
34 RMSE	5.106	6.75	9.431	7.269	5.368	4.993	2.097	45.914	4.795	18.691	0.182	0.013	0.024	0.013	0.062
34 NRSME	0.365	0.307	0.544	0.942	0.296	0.286	0.482	1.21	1.047	1.437	0.554	0.367	1.678	4.995	0.682
35 RMSE	5.044	6.939	5.466	5.533	5.733	6.987	2.575	46.752	4.658	19.413	0.194	0.016	0.024	0.012	0.062
35 NRSME	0.36	0.315	0.315	0.717	0.316	0.4	0.592	1.232	1.017	1.492	0.59	0.463	1.636	4.909	0.68

Table A5: Selection of newly available output variables and diagnostics of the JSBACH submodel.

<i>Process</i>	Variable	Additional information
<i>Radiation</i>		
	Surface albedo	Available in the visible and near infrared range for soil, snow, ice, water, canopy and separately for each Plant Functional Type (PFT).
	Photosynthetic active radiation (PAR)	Available are total, direct and diffuse parts for each canopy layer and PFT.
	Fraction of absorbed PAR	Available are total, direct and diffuse parts for each canopy layer and PFT.
<i>Surface Energy Balance</i>		
	Surface temperature	Available for land, ice, water, snow, five soil and three snow levels.
	Sensible and latent heatflux	Available for land, ice and water.
	Heat capacity of soil	Available for land and water.
<i>Turbulence</i>		
	Surface roughness length	Available for Orography, momentum and heat. All are available for each PFT.
<i>Soil and Snow Energy</i>		
	Ground heat conductivity	Available for each soil and snow layer.
	Ground heat capacity	Available for each soil and snow layer.
	Ground heat flux	Available for each soil and snow layer.
	Volumetric soil field capacity	Available for each soil layer.
	Volumetric porosity of ground	Available for each soil layer.
	Density of snow on soil	Available for each snow layer.
	Snow depth	Available for each snow layer.
	Thawing depth	Available for each snow layer.
<i>Assimilation</i>		
	CO ₂ concentration at surface level	
	Dark respiration	Available for each canopy level and PFT.
<i>Disturbance</i>		
	Fraction of burned foliage projective cover (FPC)	Available for each PFT.
	Fraction of damaged FPC from wind	Available for each PFT.
	Amount of carbon relocated by wind and fire damage	

Table A6: Selection of newly available output variables and diagnostics of the JSBACH submodel.

<i>Process</i>	
Variable	Additional information
<i>Hydrology</i>	
Fraction of organic material in soil layers	
Volume fraction of frozen water	Available for each soil layer.
Wet (skin reservoir) fraction	Available for each soil layer and canopy level.
Water and ice content	Available for each soil and snow layer and the total columns.
Water content in root zone	
Water stress factor of canopy	
Depth of each soil layer that can be saturated with water	
Rooted depth per soil layer (until rooting depth)	
Volumetric permanent wilting point	
Evapotranspiration	Available for land, water, ice, vegetation, soil, snow and skin reservoir.
Humidity at lowest atmospheric level	
Surface drag coefficients	Available for land, water and ice.
<i>Carbon</i>	
Plant carbon pools	Available for carbohydrate reserve (sugars, starches) that allows plants to survive. Additional for stems, thick roots and other (dead) structural matter and last for biomass harvested from crops.
Above ground and below ground litter carbon pools	Available for green and woody litter, plus acid, water and ethanol soluble litter and non soluble litter.
Gross assimilation	Available for each canopy layer and PFT.
Soil heterotrophic respiration	Available for each canopy layer and PFT.
Gross primary productivity	Available for each canopy layer and PFT.
Net primary productivity	Available for each canopy layer and PFT.
<i>Phenology</i>	
Leaf area index (LAI)	Available for each canopy layer and PFT.
<i>Fuel</i>	
Amount of fuel available for fire	Available for each PFT.

Appendix B

The Effect of Biomass Burning Aerosol Emissions on Global Gross Primary Productivity

Content

Table B7: Overview of plant functional types at measurement sites

Table B8: Overview of the submodels comprising the simulations

Table B7: Overview of the analyzed the measurement sites with corresponding Plant Functional Type (PFT) coverage of the EMAC/JSBACH simulation.

Aeronet Site	Fluxnet Site	Fluxnet PFT	EMAC/JSBACH PFTs and their cover frac- tion	(%)
Alta Floesta (10S, 56W)	BR-Sa1 (2.8S, 54.9W) Fluxnet-EBF 2015	Evergreen Broadleaf Forest (EBF)	Tropical Broadleaf Evergreen	92.86
			Raingreen Shrubs	2.42
			C3 Grass	0.36
			C4 Grass	1.74
			C3 Pasture	0.06
			C4 Pasture	0.31
			C3 & C4 Crops	2.24
Wasekesu (53N, 106W)	CA-Oas (53.6N, 106.2W) Fluxnet-DBF 2015	Deciduous Broadleaf Forest (DBF)	Extra-Tropical Evergreen	18.24
			Extra-Tropical Broadleaf Deciduous	8.28
			C3 Grass	7.11
			C4 Grass	0.82
			C3 Pasture	0.85
			C4 Pasture	0.1
			C3 & C4 Crops	64.6
Konza EDC (39N, 96W)	US-Ne3 (41.2N, 96.4W) Fluxnet-CRP 2015	Crops (CRP)	Extra-Tropical Evergreen	1.52
			Extra-Tropical Broadleaf Deciduous	1.52
			C3 Grass	7.18
			C4 Grass	8.37
			C3 Pasture	4.05
			C4 Pasture	4.72
			C3 & C4 Crops	72.6
Tuscon (32N, 111W)	US-Whs (31.7N, 110.1W) Fluxnet-SHR 2015 & US-Wkg (31.7N, 109.9W) Fluxnet-GRA 2015	Shrubs (SHR)	Tropical Broadleaf Deciduous	8.85
			Extra-Tropical Evergreen	6.35
			Extra-Tropical Broadleaf Deciduous	0.44
		Grass (GRA)	Raingreen Shrubs	28.36
			C3 Grass	8.2
			C4 Grass	22.7
			C3 Pasture	0.06
			C4 Pasture	0.17
			C3 & C4 Crops	24.87

Table B8: Overview of the submodels comprising the simulations including short description and reference.

PROCESS SUBMODELS	Short Description	Reference
AEROPT	Calculation of aerosol optical properties.	(Dietmüller et al. 2016)
AIRSEA	Deposition and emission of tracers over the ocean and the ocean surface water.	(Pozzer et al. 2006)
ALBEDO	Solar zenith angle dependent and satellite-based background (white-sky) albedo.	(Nützel et al. 2023)
BIOBURN	Biomass burning fluxes based on Global Fire Assimilatin System data.	(Kaiser et al. 2012)
CLOUD	ECHAM5 cloud scheme as MESSy submodel.	(Roeckner et al. 2006; Tost 2023)
CLOUDOPT	Calculation of cloud optical properties.	(Dietmüller et al. 2016)
CONVECT	Convection parametrisations.	(Tost et al. 2006b)
CVTRANS	Convection transport of tracers due to convection.	(MESSy-webpage 2023)
DDEP	Gas phase and aerosol tracer dry deposition based on the big leaf approach.	(Kerkweg et al. 2006)
DRADON	Emission and decay of ²²² Rn, optionally the complete decay chain up to ²¹⁰ Pb.	(Jöckel et al. 2010a)
E5VDIFF	Land-atmosphere exchange and vertical diffusion based on ECHAM5.	(Roeckner et al. 2003; MESSy-webpage 2023)
EVER	Aerosol emissions in different vertical ranges and shapes.	(Kohl et al. 2023)
GMXE	Mircophysical processes including nucleation, coagulation and aerosol properties.	(Pringle et al. 2010)
GWAVE	ECHAM5 non-orographic gravity wave routines plus additional drag parametrisations.	(Hines 1997; MESSy-webpage 2023)
HD	Hydrological Discharge model for present day rivers.	(MESSy-webpage 2023)
IONS	Ion pair production rates from Radon decay and Galactic Cosmic Rays.	(MESSy-webpage 2023)
JSBACH	Land surface and vegetation model.	(Martin et al. 2024)
JVAL	Photolysis rate coefficients based on clouds, ozone concentration and aerosols.	(Sander et al. 2014)
LNOX	Parameterisation of NO _x produced by lightning.	(Tost et al. 2007)
MECCA	Tropospheric and stratospheric chemistry calculation.	(Sander et al. 2019)
MEGAN	Ecosystem emissions, implemented in EMAC via the PCEEA algorithm.	(Guenther et al. 2006)
NAN	Calculation of aerosol nucleation rates.	(MESSy-webpage 2023)
OFFEMIS	Reading 2D/3D emissions from netCDF and updating tracer tendencies.	(Kerkweg et al. 2006)
ONEMIS	2D emission fluxes of gas-phase tracers.	(Kerkweg et al. 2006)
ORACLE	Organic aerosol composition and evolution in the atmosphere.	(Tsimpidi et al. 2014)
ORBIT	Calculation of orbital parameters of the Earth orbit around the sun.	(Dietmüller et al. 2016)
OROGW	Parameterisation of drag from subgrid orography and gravity waves.	Chapter 7 of (Roeckner et al. 2003)
QBO	Assimilation of QBO zonal wind observations.	(MESSy-webpage 2023)
RAD	ECHAM5 radiation code with extended features.	(Dietmüller et al. 2016)
SCAV	Wet deposition and liquid phase chemistry in precipitation fluxes.	(Tost et al. 2006a)
SEDI	Aerosol sedimentation.	(Kerkweg et al. 2006)
SCOUT	High-frequency output of model data at the position of stationary observatories.	(Jöckel et al. 2010b)
TNUDGE	Newtonian relaxation of species as pseudo-emission.	(Kerkweg et al. 2006)
TROPOP	Tropopause (WMO + PV) and other diagnostics.	(MESSy-webpage 2023)

